DISSERTATION

TOWARDS A PHYSICALLY INFORMED UNDERSTANDING OF NEW PARTICLE FORMATION AND GROWTH IN THE ATMOSPHERE

Submitted by
Samuel Emmart O'Donnell
Department of Atmospheric Science

In partial fulfillment of the requirements
For the Degree of Doctor of Philosophy
Colorado State University
Fort Collins, Colorado
Fall 2025

Doctoral Committee:

Advisor: Jeffrey R. Pierce

Shantanu H. Jathar
Sonia M. Kreidenweis
Emily V. Fischer

ABSTRACT

TOWARDS A PHYSICALLY INFORMED UNDERSTANDING OF NEW PARTICLE FORMATION AND GROWTH IN THE ATMOSPHERE

Aerosol particles are among the most uncertain yet influential components of Earth's radiative balance, influencing it directly through interactions with radiation and indirectly by serving as the formation sites for cloud droplets and ice crystals. Understanding the size and composition of the aerosol particles is critical for understanding their climate impacts. The majority of aerosol particles in the atmosphere form through the process of new particle formation and growth (NPF&G), the process by which new small particles form from the clustering of low-volatility vapors. These newly formed particles may grow to climatically relevant sizes through condensation of vapors or be lost through collisions with pre-existing larger particles. NPF&G events are time periods where NPF&G occurs, and the particles grow substantially over the following several hours. This dissertation examines the processes governing NPF&G in the atmosphere.

First, we investigate the implications of stationary-site observations of NPF&G events by contrasting them with a Lagrangian perspective. Most observations of NPF&G events are conducted at stationary sites; however, NPF&G observed from stationary sites is influenced by gradual or rapid changes in the air masses passing over the site, complicating NPF&G analysis. In this work, we use observations and a 3D aerosol model to compare aerosol size distributions at a stationary site (Southern Great Plains (SGP) observatory, Oklahoma, USA) and along Lagrangian trajectories crossing the site. The model simulates the NPF&G events reasonably well compared

to observations at SGP. Using the model to compare the Lagrangian and stationary perspectives, we can explain previously unanalyzable days with some evidence of NPF&G as either non-event or analyzable NPF&G days. We find most of the unanalyzable NPF&G days are due to isolated and inhomogeneous NPF&G occurring upwind of the stationary site, often in the outflow of urban regions. Finally, we compare formation rates of 3 nm particles, growth rates, and the survival probability of 3 nm particles growing to 25 nm between the stationary and Lagrangian perspectives. Due to the much larger number of analyzable days along the Lagrangian trajectories, this perspective potentially provides more robust statistics and better characterization of NPF&G event extremes. Our method for extracting chemical/physical properties along Lagrangian trajectories from 3D models can be applied to a wide range of science questions.

Second, to better understand NPF&G in urban environments, we examine NPF&G occurring in a unique environmental chamber. While our understanding of NPF&G in certain environments has advanced, the processes that govern NPF&G in some urban environments are still poorly understood. As part of the Tracking Aerosol Convection Interactions Experiment (TRACER) Ultrafine Aerosol Formation and Impacts (UFI; together TRACER-UFI) campaign, the University of California, Riverside's Captive Aerosol Growth and Evolution (CAGE) chamber operated during July and August of 2022. The CAGE chamber filters out ambient particles, allowing only ambient vapors to enter. On most days during TRACER-UFI, NPF&G events occurred in the chamber, providing the unique opportunity to assess what chemical species and mechanisms have the potential to drive secondary aerosol processes in Houston. In this work, we use the SOM-TOMAS chemistry and aerosol-microphysics model to represent the CAGE chamber to better understand the governing processes within it. We calculate that aerosol mass in the chamber is primarily derived from toluene, trimethylbenzene, styrene, and monoterpene products.

Aerosol measurements in the chamber corroborate the contribution of anthropogenic species to aerosol particles; however, because of challenges of simulating the unique particle and vapor loss mechanisms in the chamber (wall losses, instrument flows, diffusional membrane), other conclusions are less robust.

Finally, we examine the effects of particle phase state (i.e., liquid or solid) on the global size-dependent condensation and growth of aerosol particles. The phase state of atmospheric aerosol particles ranges from liquid-like to solid-like, which can profoundly affect size-dependent secondary organic aerosol (SOA) partitioning. In this work, we examine some of the effects of phase state and size-dependent SOA condensation on aerosol size distributions, with a specific focus on NPF&G events. To this end, we use the 3D chemical transport model, GEOS-Chem with the TwO-Moment Aerosol Sectional (TOMAS) microphysics module to test the size-distribution effects from including an updated phase-state-dependent SOA condensation scheme that depends on humidity, temperature, and aerosol composition. Compared to a liquid-like-aerosol assumption, using the phase-state scheme shows a global decrease in the surface number concentration of 3-20 nm particles, likely due to faster growth and increased survival of small particles growing to larger sizes, which consequently hinders further new particle formation (NPF). We find increases in the number concentrations of 20-80 and 80-200 nm particles, with the largest increases occurring in low-relative-humidity regions where particles are more solid-like. Zonally averaged changes in the number concentration of particles mirror the changes at the surface, but the greatest changes are in regions of large-scale subsidence, which generally have low relative humidity. We also investigate regional changes over the south-central United States, where, again, we see the greatest changes in number concentration in dry, cool regions. Finally, we compare average size distributions between the model and several observational datasets, and we highlight several

NPF&G event case studies from the Southern Great Plains (SGP) observatory, where the inclusion of size-dependent SOA condensation in the model led to better model-measurement agreement. This work provides novel insights into the global, regional, and site-specific impacts of phase state on size-dependent SOA condensation and aerosol size distributions.

ACKNOWLEDGEMENTS

This work would not exist without the love and support of so many people. From friends and family who supported my well-being throughout my graduate studies, to the amazing scientist whose insights and ideas about the atmosphere inspired me to learn more and dig deeper – I am deeply grateful.

I would first like to thank my wife, Whitney, for her never-ending support throughout these years in Colorado. She was always there when I was feeling the stress of graduate school, reminding me to close my computer and go outside. I would not have made it through this program without her. I would also like to thank my friends and family. My mom and brother were always curious about what I was working on and they always found ways to make me feel valued. For all the friends I have made in Fort Collins, I cannot thank you enough for making my time here so enjoyable. The hardest part of finishing this dissertation is knowing that it marks the end of an era, but hopefully not the end of our friendships.

I extend my gratitude to all the members of the Pierce Group, as they have all shaped my journey to becoming a better scientist. I wish my plots, code, and writing could remotely measure up to theirs. I also thank my committee members for their guidance and support as I have navigated this dissertation. Shantanu's research guidance and class (MECH577) provided me with great perspectives on aerosols and atmospheric chemistry. Sonia's depth of knowledge is unparalleled, and I have appreciated her humble feedback throughout my studies. Emily's class (ATS716) was a formative experience for me as it showed me the power and impact of community-based research. Their feedback has always been supportive and growth-oriented and has undoubtedly made me a better scientist. I would like to thank all the members of the CSU Atmospheric Science Department

for their support throughout this program, and to the members of The Cloud Covers, whose musical talent and friendship has made the past year simply spectacular.

I would be remiss to not thank my undergraduate mentors for instilling in me a love of research. Drs. Miller, Hennon, Godfrey, and Huang each played an integral part in my appreciation for atmospheric science. I am especially indebted to Dr. Evan Couzo for both introducing me to the topic of atmospheric chemistry as well as reaching out to his network when I expressed interest in going to grad school.

Finally, I thank my advisor, Jeff. Your patience, kindness, curiosity, and overwhelming scientific knowledge have been my guiding beacon over the past six years. Through our conversations about food, music, aerosol microphysics, and so many other topics, I have learned how to think as a scientist – something for which I am eternally grateful.

“I know I'm far away from home, but I know I'm not alone”

– Michael Franti & Spearhead

DEDICATION

I would like to dedicate this work to my niece, Maggie O'Donnell; my late father-in-law, John McCurry; and my two pups, Davos and Bailey.

TABLE OF CONTENTS

CHAPTER 1

INTRODUCTION TO AEROSOLS AND NEW PARTICLE FORMATION

The mean temperature of Earth's atmosphere is regulated by the delicate balance of incoming shortwave and outgoing longwave radiation. Aerosol particles, suspended solids or liquids in the atmosphere, can affect this balance through two broad mechanisms: (1) direct absorption and scattering of either longwave or shortwave radiation, which is known as the aerosol direct effect, and (2) serving as the sites for cloud droplet or ice crystal formation, which in turn interact with both longwave and shortwave radiation and is known as the aerosol indirect effect. For context, the 2001-2025 average top of atmosphere (TOA) energy imbalance (incoming - outgoing) associated with anthropogenic climate change is on the order of ~0.75 W m^{-2} (Mauritsen et al., 2025), whereas the globally and annually averaged net top of atmosphere direct aerosol effect is -0.22 [-0.47 to 0.04] W m^{-2} (Forster et al., 2021). While the net radiative forcing from the direct aerosol effect serves to cool the Earth system, more localized effects can exist. In general, particles that appear visibly lighter (e.g., sulfate aerosols or dust) will scatter or reflect in the shortwave bands with an overall net cooling of the Earth system. Conversely, particles that are visibly darker (e.g., soot from diesel exhaust) will absorb in the shortwave and reemit in the longwave, generally having a localized warming effect (Bond et al., 2013).

The net effect of aerosol particles on warm cloud properties is more uncertain than the direct aerosol radiation effects, in part due to a more complex dependence on aerosol composition and size, as well as regime-dependent dynamics of warm cloud formation. The global average total shortwave TOA energy reflected by clouds is about -47.5±3 W m^{-2}, however, clouds also interact strongly with longwave reflecting about 26.6±5 W m^{-2} back towards Earth's surface (Stephens et

al., 2012). Since aerosol particles serve as cloud condensation nuclei (CCN), the concentration of aerosol particles directly affects the number of cloud droplets for a given amount of water, in turn affecting the radiative properties of clouds. The estimated instantaneous change in TOA energy from 1750 to 2019 due to changes in cloud properties by anthropogenic aerosols is estimated to be ~-0.84 [-1.45 to -0.25] W m^{-2} (Forster et al., 2021). Understanding how aerosol particles come to serve as the activation sites for cloud formation is of great importance for understanding Earth's radiative balance.

For a given supersaturation of water vapor, the ability of an aerosol particle to act as a CCN is dictated by its size and composition. Studies have found that CCN activity tends to be more sensitive to fractional changes in particle size than fractional changes in particle hygroscopicity (Farmer et al., 2015; McFiggans et al., 2006). Particles with diameters larger than ~200 nm generally have enough soluble material to readily activate into cloud droplets at moderate supersaturations (0.5%); however, for particles in the ~30-200 nm diameter range, particle composition plays a greater role in determining which particles activate at what supersaturation (Farmer et al., 2015). The aerosol size distribution in the 30-200 nm diameter range often contains a significant number of particles and is shaped by both primary emissions and secondary aerosol processes (Seinfeld and Pandis, 2016), further complicating the ability to fully understand the effects of aerosols on cloud droplet activation.

The process of new particle formation (NPF), the process by which new ~1 nm aerosol particles are formed from vapors, is a significant contributor to global cloud-level CCN concentrations at 0.5% supersaturation as well as the dominant contributor to global aerosol number (Gordon et al., 2017; Zhao et al., 2024). The exact mechanisms by which new particles form and grow to larger sizes in different environments is still an active area of research. In most

scenarios, NPF involves sulfuric acid due to its extremely low vapor pressure and relative abundance in the atmosphere. Sulfuric acid can form clusters with water (Vehkamäki et al., 2002), ammonia (Dunne et al., 2016), amines (Johnson and Jen, 2023; Olenius et al., 2017), low-volatility organics (Riccobono et al., 2014; Zhao et al., 2024), and iodine oxoacids (He et al., 2023). Some NPF mechanisms may interact synergistically in ways that are difficult to quantify both in chamber experiments and models (Wang et al., 2022). The dominant NPF mechanism varies greatly with surface location and altitude, and the inclusion of many NPF mechanisms into models has been shown to improve model-measurement comparisons of aerosol size distributions in specific regions (Zhao et al., 2024).

Once formed, the ~1 nm particles can collide with larger existing particles, thus reducing the total number of particles and the potential contribution of NPF to CCN concentrations. The freshly nucleated particles are subject to Brownian diffusion and generally have high velocities, whereas larger particles (≳50 nm) have lower velocities and greater cross-sectional area, making them perfect targets for collisions with smaller particles. The aerosol size distribution is often represented by discretized bins that represent the number or mass of particles within a given diameter range, hence the following discussion will focus on aerosol processes in the context of this bin framework. The first-order timescale for the loss of small particles via collisions with larger particles is described by the coagulation timescale (s), which is the inverse of the coagulation sink (s^{-1}) (Pierce and Adams, 2007):

$$\tau_k^{coag} = \frac{1}{\frac{1}{2}K(D_{p,k}, D_{p,k})N_k + \sum_{j=k+1}^{k_{max}} K(D_{p,k}, D_{p,j})N_j} \quad (1)$$

Where K is the coagulation kernel, N_k and N_j are the number of particles in bins k and j, respectively. Hence, the loss rate of freshly nucleated particles by coagulation depends strongly on the number of pre-existing particles.

The less time small particles spend as small particles, the less likely they are to be lost by coagulation, therefore, rapid particle growth is necessary for the survival to CCN sizes. Further nuances will be discussed in later paragraphs, but particle growth at the smallest sizes (diameter, $D_p \lesssim 10$ nm) is driven by species with extremely low saturation vapor pressures ($C^* < 10^{-4}\ \mu g\ m^{-3}$), principally sulfuric acid and extremely low-volatility organic compounds (ELVOC). Once particles are slightly larger, particle curvature (Kelvin effect) plays less of a role, therefore, species with higher C* values can contribute to particle growth. Unfortunately for the small particles, they must compete with the existing particles for condensable vapors in order to grow. The first-order rate for uptake of vapors to the Fuchs-corrected surface area can be described by the condensation sink (CS; s^{-1}; Pierce and Adams, 2007):

$$CS = 2\pi D \sum_{i=1}^{max} \beta_i D_{p,i} N_i \quad (2)$$

Where D is the gas-phase diffusion constant, $D_{p,i}$ is the particle diameter in bin i, N_i is the particle number concentration in bin i, and β_i is the transition regime correction factor (Seinfeld and Pandis, 2016). Given that larger particles have greater surface area, their presence increases the condensation sink, lowering the ambient vapor pressure of the condensing material and reducing the growth rate of the freshly nucleated particles.

The rate of change in particle diameter, or "growth rate" (GR), as a function of the vapor pressure of low-volatility species is expressed as follows:

$$GR = \frac{dD_p}{dt} = \frac{4D_g}{\rho D_p}(C_\infty - C_S)\beta \quad (3)$$

In the above equation, D_p is the particle diameter, D_g is the diffusion coefficient of the condensing vapor, ρ is the density of the condensing vapor, C_∞ is the ambient partial pressure of the condensing vapor, C_S is the vapor pressure of the condensing vapor over the particle surface, and β is a correction factor for non-continuum-regime effects. The greater the difference between the partial pressure of the vapor and the vapor pressure at the particle surface, the faster mass will condense. For low-volatility species, the vapor pressure at the surface of the particle approaches ~0.0 Pa, therefore, the driving force for condensation is dictated by the partial pressure of the vapor and particle surface area (i.e., CS, Equation 2).

For these low-volatility vapors, such as sulfuric acid, accurate representation of the ambient vapor concentrations is important for the accurate representation of NPF and early particle growth. The concentration of low-volatility species can be found through a balance between gas-phase chemical production and loss by condensation. Pierce and Adams (2009a) developed a computationally efficient pseudo-steady-state approximation for vapor concentrations that can be used for calculations of condensation and nucleation dynamics in aerosol models. The pseudo-steady-state concentration of the low-volatility vapor (*PSSV*) is expressed as follows:

$$[PSSV] = \frac{P_V}{CS + J_{nuc}M_{nuc}} \quad (4)$$

In the above equation, P_V is the production rate of the low-volatility vapor, CS is the condensation sink (Equation 2), J_{nuc} is the nucleation rate of particles at some diameter, and M_{nuc} is the mass of each nucleated particle. In the absence of nucleation or if the vapor does not participate in nucleation (i.e., J_{nuc}= 0), the above equation converges to $[PSSV] = P_V/CS$. The pseudo-steady-state approximation provides a useful means to understand the potential growth of freshly nucleated particles. Assuming the gas-phase production does not change ($P_V = 0$), a high CS (i.e., more pre-existing particles) reduces the vapor concentration, and thus reduces the growth rate of small particles. Conversely, a low CS increases the vapor concentration, leading to faster growth of small particles and, in the case of sulfuric acid, increases the vapor available for NPF. It is also apparent that faster gas-phase production leads to higher vapor concentrations which can accelerate growth and production of small particles.

While the CS describes the rate of vapor condensation, the condensation timescale describes the time it takes a particle to grow in a given size range (Pierce and Adams, 2007):

$$\tau_{k,k+1}^{cond} = \frac{D_{p,k+1} - D_{p,k}}{GR_{k,k+1}} \quad (5)$$

Where D_p is the particle diameter in bins *k* and *k*+1, and GR is the average diameter growth rate between bins *k* and *k*+1. The condensation and coagulation timescales can be used to envisage the two competing forces for small particle survival. For a given size range, a shorter condensation timescale means particles will grow faster to the larger size, while a shorter coagulation timescale increases the likelihood of collisions with larger particles. This competition between these two processes can be represented by the survival probability (SP) (Pierce and Adams, 2007):

$$SP_{m,n} = \prod_{k=m}^{n-1} exp\left(-\frac{\tau_{k,k+1}^{cond}}{\tau_k^{coag}}\right) \quad (6)$$

Where $SP_{m,n}$ is the probability of a particle in diameter bin m surviving to diameter bin n. The SP parameter is a useful means to quantify the potential contribution of NPF to particles in a specific size range (e.g., CCN).

Equations 1-6 describe how freshly nucleated particles grow and survive to sizes at which they can act as CCN and interact with radiation, processes that need to be constrained to reduce uncertainty in global radiative forcing. Equations 1 and 5 express the timescales for coagulation and condensation, the two most important processes impacting freshly nucleated particles. The pseudo-steady-state approximation (Equation 4) provides a useful means to understand the availability of low-volatility vapor for NPF and growth based on the number of pre-existing particles (i.e., CS, Equation 2) and vapor production rate. We can also quantify the likelihood of a particle growing to CCN sizes using Equation 6. While Equations 1-6 broadly capture the pertinent processes for NPF&G in the atmosphere, many complicating factors influencing aerosol formation and growth that are not accounted for, necessitating further research to better develop a physically informed understanding of NPF&G in the atmosphere.

Up until now, we have treated vapor condensation as that of extremely low-volatility compounds (i.e., sulfuric acid and ELVOCs) condensing onto liquid-like particles, where the vapors condense according to the Fuchs-corrected particle surface area size distribution. While this treatment has led to good agreement between modeled and measured size distributions (D'Andrea et al., 2013; Pierce and Adams, 2007, 2009a; Westervelt et al., 2013), there is evidence of another bounding regime for size-dependent vapor condensation (Pierce et al., 2011; Zaveri et

al., 2014; Shiraiwa et al., 2011, 2017). This second regime involves the equilibrium partitioning of semi-volatile organic compounds (SVOC; $0.3 < C^* < 300\ \mu g\ m^{-3}$) onto either liquid- or solid-like particles (Pierce et al., 2011; Riiponen et al., 2011; Zaveri et al., 2014). For liquid-like particles, SVOCs partition into the particle phase proportional to the aerosol mass size distribution, similar to how water partitions into aerosols. Given that large particles contain significantly more mass than smaller particles, SVOCs partition favorably to the larger particles, hindering the growth of smaller particles.

Beyond the two limiting cases described above (and the continuum between them), solid-like particles exhibit slow intraparticle mixing timescales that scale with the square of particle diameter (Zaveri et al., 2014, 2018; Luu et al., 2025). The slow internal mixing effectively limits the available aerosol mass for SVOCs to partition into, and this limitation affects larger particles more than the smaller particles, thereby favoring the growth of smaller particles. The influence of particle phase state (i.e., liquid- or solid-like particles) on size-dependent vapor condensation has implications for early particle growth by the reduction of the effective CS, which increases the vapor available for small-particle growth. Particle phase-state effects on the aerosol size distribution have been investigated theoretically (Zaveri et al., 2014), in chamber experiments (He et al., 2021; Hodshire et al., 2018; Zaveri et al., 2018), and in urban outflow over the Amazon (Zaveri et al., 2022; He et al., 2025). Additionally, particle phase state, intraparticle mixing timescales, and SOA equilibrium timescales have been modeled at the global scale (Shiraiwa et al., 2017; Luu et al., 2025); however, the effects of particle phase state on aerosol size distributions have not been examined in a global context, nor have the specific impacts on NPF&G events been explored. The effects of particle phase state on NPF&G and global aerosol number concentrations will be examined in ***Chapter 4***.

Much of our understanding of NPF&G (e.g., Equations 1-6) has been derived from measurements of NPF&G events at stationary surface sites across the globe. While observations from stationary sites have been integral for developing a theoretical framework for NPF&G in the atmosphere, as well as serving as the benchmark for model evaluation, an analysis of such observations often presumes horizontal and vertical homogeneity in the process rates (e.g., emissions, chemistry, particle growth) affecting the aerosol size distribution around the site. This is because air moves over the site due to winds, and hence, spatial inhomogeneities lead to temporal variability in aerosol properties at the stationary site. In other words, deriving statistics, such as nucleation rates, from a NPF&G event measured at a stationary site may lead to erroneous conclusions due to unaccounted for changes in the air mass passing over the stationary site. Additionally, many days at stationary sites show partial or interrupted NPF or particle growth, indicating the NPF or growth is occurring elsewhere in the atmosphere and making deriving statistics impossible. There is evidence that these less-clear NPF events may have non-trivial contributions to aerosol number (Kulmala et al., 2022).

It has long been acknowledged that, in order to derive nucleation rates in the atmosphere, the Lagrangian perspective (i.e., tracking changes following a moving air parcel) must be considered (O'Dowd et al., 1998). Unfortunately, measuring aerosol size distributions from the Lagrangian perspective is often logistically prohibitive, therefore, we rely on models to help interpret stationary observations (Hakala et al., 2023). This issue is the focus of ***Chapter 2***, where we use a 3D chemistry-aerosol along with Lagrangian trajectories to investigate the stationary and Lagrangian perspectives of NPF&G events.

While modeling the Lagrangian perspective of NPF&G events may provide a better means to interpret ambient NPF&G events, semi-ambient environmental chambers that partially parallel

the ambient atmosphere can isolate and control the conditions under which particles form (Sickles et al., 1979; Jeffries et al., 2013; Sirmollo et al., 2021). This approach is particularly powerful for highly polluted regions where large numbers of vapor and particle emissions sources can confound an analysis of chemical or aerosol processes. These chambers often utilize sunlight to drive photochemistry, and the conditions (i.e., temperature, relative humidity, etc.) in the chambers are often close to those in the ambient atmosphere. The goal of these chambers is to isolate certain chemical or aerosol processes while retaining relevance and applicability to the ambient atmosphere.

The Captive Aerosol Growth and Evolution (CAGE) chamber is one such chamber that filters out ambient particles but allows vapors to diffuse into the reactor chamber. The CAGE chamber removes the direct effects of aerosol transport on the aerosol size distribution, while retaining the local time-varying gas-phase species and atmospheric conditions. ***Chapter 3*** focuses on a modeling analysis of the CAGE chamber during the Tracking Aerosol Convection Interactions Experiment (TRACER) Ultrafine Aerosol Formation and Impacts (UFI; together TRACER-UFI) in Houston Texas during the summer of 2022. The surrounding area of Houston is home to many petrochemical plants with numerous sources of particles, VOCs and inorganic vapors. Isolation of the secondary aerosol processes is important for a better understanding of the chemical and physical drivers of aerosol concentrations in Houston as well as other highly polluted urban areas.

REFERENCES

Bond TC, Doherty SJ, Fahey DW, et al (2013) Bounding the role of black carbon in the climate system: A scientific assessment. Journal of Geophysical Research: Atmospheres 118:5380–5552. https://doi.org/10.1002/jgrd.50171

Dunne EM, Gordon H, Kürten A, et al (2016) Global atmospheric particle formation from CERN CLOUD measurements. Science 354:1119–1124. https://doi.org/10.1126/science.aaf2649

D'Andrea SD, Häkkinen S a. K, Westervelt DM, et al (2013) Understanding global secondary organic aerosol amount and size-resolved condensational behavior. Atmospheric Chemistry and Physics 13:11519–11534. https://doi.org/10.5194/acp-13-11519-2013

Farmer DK, Cappa CD, Kreidenweis SM (2015) Atmospheric Processes and Their Controlling Influence on Cloud Condensation Nuclei Activity. Chem Rev 115:4199–4217. https://doi.org/10.1021/cr5006292

Forster, PT, Storelvmo K, Armour W, et al (2021) The Earth's Energy Budget, Climate Feedbacks, and Climate Sensitivity. In Climate Change 2021: The Physical Science Basis. Contribution of Working Group I to the Sixth Assessment Report of the Intergovernmental Panel on Climate Change. Cambridge University Press, Cambridge, pp. 923–1054, doi: 10.1017/9781009157896.009.

Gordon H, Kirkby J, Baltensperger U, et al (2017) Causes and importance of new particle formation in the present-day and preindustrial atmospheres. Journal of Geophysical Research: Atmospheres 122:8739–8760. https://doi.org/10.1002/2017JD026844

Hakala S, Vakkari V, Lihavainen H, et al (2023) Explaining apparent particle shrinkage related to new particle formation events in western Saudi Arabia does not require evaporation. Atmospheric Chemistry and Physics 23:9287–9321. https://doi.org/10.5194/acp-23-9287-2023

He X-C, Simon M, Iyer S, et al (2023) Iodine oxoacids enhance nucleation of sulfuric acid particles in the atmosphere. Science 382:1308–1314. https://doi.org/10.1126/science.adh2526

He Y, Akherati A, Nah T, et al (2021) Particle Size Distribution Dynamics Can Help Constrain the Phase State of Secondary Organic Aerosol. Environ Sci Technol 55:1466–1476. https://doi.org/10.1021/acs.est.0c05796

He Y, Bilsback KR, Shrivastava M, et al (2025) Kinetic Modeling of Secondary Organic Aerosol in a Weather-Chemistry Model: Parameterizations, Processes, and Predictions for GOAmazon. ACS EST Air 2:249–263. https://doi.org/10.1021/acsestair.4c00240

Hodshire AL, Palm BB, Alexander ML, et al (2018) Constraining nucleation, condensation, and chemistry in oxidation flow reactors using size-distribution measurements and aerosol microphysical modeling. Atmospheric Chemistry and Physics 18:12433–12460. https://doi.org/10.5194/acp-18-12433-2018

Jeffries HE, Kamens RM, Sexton K (2013) Early history and rationale for outdoor chamber work at the University of North Carolina. Environ Chem 10:349–364. https://doi.org/10.1071/EN13901

Johnson JS, Jen CN (2023) Role of Methanesulfonic Acid in Sulfuric Acid–Amine and Ammonia New Particle Formation. ACS Earth Space Chem. https://doi.org/10.1021/acsearthspacechem.3c00017

Kulmala M, Junninen H, Dada L, et al (2022) Quiet New Particle Formation in the Atmosphere. Frontiers in Environmental Science 10:

Luu R, Schervish M, June NA, et al (2025) Global Simulations of Phase State and Equilibration Time Scales of Secondary Organic Aerosols with GEOS-Chem. ACS Earth Space Chem 9:288–302. https://doi.org/10.1021/acsearthspacechem.4c00281

Mauritsen T, Tsushima Y, Meyssignac B, et al (2025) Earth's Energy Imbalance More Than Doubled in Recent Decades. AGU Advances 6:e2024AV001636. https://doi.org/10.1029/2024AV001636

McFiggans G, Artaxo P, Baltensperger U, et al (2006) The effect of physical and chemical aerosol properties on warm cloud droplet activation. Atmospheric Chemistry and Physics 6:2593–2649. https://doi.org/10.5194/acp-6-2593-2006

Olenius T, Halonen R, Kurtén T, et al (2017) New particle formation from sulfuric acid and amines: Comparison of monomethylamine, dimethylamine, and trimethylamine. Journal of Geophysical Research: Atmospheres 122:7103–7118. https://doi.org/10.1002/2017JD026501

O'Dowd CD, Geever M, Hill MK, et al (1998) New particle formation: Nucleation rates and spatial scales in the clean marine coastal environment. Geophysical Research Letters 25:1661–1664. https://doi.org/10.1029/98GL01005

Pierce JR, Adams PJ (2007) Efficiency of cloud condensation nuclei formation from ultrafine particles. Atmospheric Chemistry and Physics 7:1367–1379. https://doi.org/10.5194/acp-7-1367-2007

Pierce JR, Adams PJ (2009a) A Computationally Efficient Aerosol Nucleation/ Condensation Method: Pseudo-Steady-State Sulfuric Acid. Aerosol Science and Technology 43:216–226. https://doi.org/10.1080/02786820802587896

Pierce JR, Riipinen I, Kulmala M, et al (2011) Quantification of the volatility of secondary organic compounds in ultrafine particles during nucleation events. Atmospheric Chemistry and Physics 11:9019–9036. https://doi.org/10.5194/acp-11-9019-2011

Riccobono F, Schobesberger S, Scott CE, et al (2014) Oxidation Products of Biogenic Emissions Contribute to Nucleation of Atmospheric Particles. Science 344:717–721. https://doi.org/10.1126/science.1243527

Riipinen I, Pierce JR, Yli-Juuti T, et al (2011) Organic condensation: a vital link connecting aerosol formation to cloud condensation nuclei (CCN) concentrations. Atmos Chem Phys 11:3865–3878. https://doi.org/10.5194/acp-11-3865-2011

Seinfeld JH, Pandis SN (2016) Atmospheric Chemistry and Physics: From air pollution to climate change (3rd ed.). John Wiley and Sons.

Shiraiwa M, Ammann M, Koop T, Pöschl U (2011) Gas uptake and chemical aging of semisolid organic aerosol particles. Proceedings of the National Academy of Sciences 108:11003–11008. https://doi.org/10.1073/pnas.1103045108

Shiraiwa M, Li Y, Tsimpidi AP, et al (2017) Global distribution of particle phase state in atmospheric secondary organic aerosols. Nat Commun 8:15002. https://doi.org/10.1038/ncomms15002

Sickles JE, Ripperton LA, Eaton WC, Wright RS (1979) Oxidant-precursor relationships under pollutant transport conditions: outdoor smog chamber study. Volume II.

Appendixes. Final report, June 1975-June 1978. Research Triangle Inst., Research Triangle Park, NC (USA)

Sirmollo CL, Collins DR, McCormick JM, et al (2021) Captive Aerosol Growth and Evolution (CAGE) chamber system to investigate particle growth due to secondary aerosol formation. Atmospheric Measurement Techniques 14:3351–3370. https://doi.org/10.5194/amt-14-3351-2021

Stephens GL, Li J, Wild M, et al (2012) An update on Earth's energy balance in light of the latest global observations. Nature Geosci 5:691–696. https://doi.org/10.1038/ngeo1580

Vehkamäki H, Kulmala M, Napari I, et al (2002) An improved parameterization for sulfuric acid–water nucleation rates for tropospheric and stratospheric conditions. Journal of Geophysical Research: Atmospheres 107:AAC 3-1-AAC 3-10. https://doi.org/10.1029/2002JD002184

Wang M, Xiao M, Bertozzi B, et al (2022) Synergistic HNO3–H2SO4–NH3 upper tropospheric particle formation. Nature 605:483–489. https://doi.org/10.1038/s41586-022-04605-4

Westervelt DM, Pierce JR, Riipinen I, et al (2013) Formation and growth of nucleated particles into cloud condensation nuclei: model–measurement comparison. Atmospheric Chemistry and Physics 13:7645–7663. https://doi.org/10.5194/acp-13-7645-2013

Zaveri RA, Easter RC, Shilling JE, Seinfeld JH (2014) Modeling kinetic partitioning of secondary organic aerosol and size distribution dynamics: representing effects of volatility, phase state, and particle-phase reaction. Atmospheric Chemistry and Physics 14:5153–5181. https://doi.org/10.5194/acp-14-5153-2014

Zaveri RA, Shilling JE, Zelenyuk A, et al (2018) Growth Kinetics and Size Distribution Dynamics of Viscous Secondary Organic Aerosol. Environ Sci Technol 52:1191–1199. https://doi.org/10.1021/acs.est.7b04623

Zaveri RA, Wang J, Fan J, et al (2022) Rapid growth of anthropogenic organic nanoparticles greatly alters cloud life cycle in the Amazon rainforest. Science Advances 8:eabj0329. https://doi.org/10.1126/sciadv.abj0329

Zhao B, Donahue NM, Zhang K, et al (2024) Global variability in atmospheric new particle formation mechanisms. Nature 1–8. https://doi.org/10.1038/s41586-024-07547-1

CHAPTER 2

GOING OFF GRID: A COMPARATIVE STUDY OF THE LAGRANGIAN AND EULERIAN PERSPECTIVES OF NEW PARTICLE FORMATION EVENTS[1]

2.1. Introduction

Aerosol particles in the atmosphere, if large enough, can alter Earth's radiative balance directly by scattering and absorbing light, and indirectly by acting as cloud condensation nuclei (CCN; Charlson et al., 1992; Myhre et al., 2013; Bulatovic et al., 2021). The number of CCN can directly alter cloud properties such as albedo, lifetime, and precipitation efficiency, and the effects are enhanced in regions where CCN concentrations are low (Albrecht, 1989; Clement et al., 2009; Gryspeerdt et al., 2014; Rosenfeld et al., 2014; B. Stevens & Feingold, 2009; Twomey, 1974). By most estimates, the majority of global aerosol number and ~50% of cloud-level CCN are produced via the process of new particle formation (NPF) and growth (NPF&G: Gordon et al., 2017; Pierce & Adams, 2009b; Dunne et al., 2016). The combined uncertainty of the direct and indirect aerosol effects remains the largest uncertainty among the radiative forcings (Forster et al., 2021). Many of the uncertainties associated with aerosol forcings stem from the lack of knowledge of pre-industrial aerosol characteristics, which serves as the baseline for radiative forcing calculations (Forster et al., 2021). This pre-industrial uncertainty highlights the need for understanding the processes that govern aerosol formation, to enable prediction of aerosol concentrations when measurements are not possible.

[1]This chapter accepted as: Samuel E. O'Donnell, Betty Croft, Bonne Ford, Nicole A. June, Chongai Kuang, Ashish Singh, Rachel Y.-W. Chang, Don R. Collins, Simo Hakala, Shantanu H. Jathar, Pauli Paasonen, Manish Shrivastava, James N. Smith, Jeffrey R. Pierce: "Going Off Grid: A Comparative Study of the Lagrangian and Eulerian Perspectives of New Particle Formation Events", submitted to Journal of Geophysical Research, 2025.

The process of NPF involves the formation of new ~1 nm particles through the clustering of low-volatility vapors, principally sulfuric acid (Ball et al., 1999) with one or more vapor molecules(s) of other species, including ammonia/amines (Dunne et al., 2016; Napari et al., 2002; Vehkamäki et al., 2002), low-volatility organics (Riccobono et al., 2014; Bianchi et al., 2019) and iodine oxoacids (He et al., 2023; Baccarini et al., 2020). These new particles are thermodynamically stable; however, in order to avoid being lost by collisions with existing particles, they must grow rapidly through continued condensation of low-volatility molecules (Kuang et al., 2008; Westervelt et al., 2014). The faster the newly formed particles grow, the less likely they are to be lost via coagulation with larger particles (Pierce and Adams, 2007). Additionally, existing particles compete with the freshly nucleated particles for condensable gases, inhibiting the growth and survival of nucleated clusters to larger sizes (Westervelt et al., 2014). The condensation sink describes this first-order uptake of condensable gases to existing particles, and it is proportional to particle surface area in the kinetic regime (~1-100 nm) and diameter in the continuum regime (≥10 μm; Kuang et al., 2008; Westervelt et al., 2014; Seinfeld and Pandis, 2016). Environments that are favorable for NPF&G are those with lower condensation sink and high production rates of low-volatility compounds (Wang et al., 2020; Lee et al., 2024; Kirkby et al., 2023). This complexity makes understanding NPF&G in different environments difficult given the spatial and temporal variability in existing particle concentrations and production rates of low-volatility gases.

Much of our understanding of NPF&G in the atmosphere has relied on ambient aerosol size distribution measurements. From these measurements, NPF&G events have been observed in many regions and environments, from megacity complexes (Deng et al., 2020; Hussein et al., 2008; Qian et al., 2007; Sebastian et al., 2022) to the remote Arctic (Collins et al., 2017; Croft et al.,

2016), and from the surface (Lee et al., 2019; Kerminen et al., 2018) up to the upper troposphere (Weigel et al., 2021; Williamson et al., 2019; Xiao et al., 2023). Multi-year size distribution measurements at stationary ground sites provide long term statistics about NPF frequency, nucleation rates, growth rates, and CCN production (Nieminen et al., 2018; Parworth et al., 2015; Shen et al., 2022). These long-term measurements have been crucial for our understanding of NPF&G; however, NPF&G rates are regionally dependent and measurement sites have limitations in how well they represent the surrounding areas (Fast et al., 2022). Different sites report varying frequencies of NPF events (see Section 2.2.1 in the Methods), and many sites report frequent "undefined" days (Pierce et al., 2014; Shen et al., 2022; Deng et al., 2020). Undefined days are days where there is evidence that some part of the NPF&G process was observed, but extracting meaningful statistics (e.g., particle growth rates, nucleation rates, and survival probabilities) is close to impossible due to incongruencies and rapid changes in the nucleation mode of the size distribution. Additionally, many NPF&G events show fluctuations in particle formation and growth that makes deriving meaningful statistics difficult, and such events are classified as class II NPF&G events. In other words, there are many days where the conditions driving NPF&G are varying in space and/or time in such a way that understanding the underlying processes is difficult. Given the non-trivial number of undefined days (~5% to ≥ 40%, Deng et al., 2020; Buenrostro Mazon et al., 2009; Aktypis et al., 2023) and class II events (~12% to ≥ 23%, Dal Maso et al., 2005) observed at different locations, a large number of days are likely ignored in any analysis of NPF&G. In the analysis in this manuscript, we combine both the traditional undefined days with class II days referring to both under the umbrella term of "undefined/class II days".

In addition to long-term fixed-site observations of NPF events, there have been many targeted short-term studies to investigate the regionality and spatial gradients of NPF, often

involving multiple sites, vehicles, and aircraft (e.g., O'Donnell et al., 2023; Chen et al., 2018; Carnerero et al., 2018). Large piloted aircraft can carry suites of instruments to characterize the chemical and microphysical properties of aerosols as well as gas-phase species; however, aircraft flights are often too short to capture the full progression of NPF&G events (Fast et al., 2019; Lampilahti et al., 2021; Leino et al., 2019). Unmanned aerial vehicles and tethered aerostats have also been used to characterize NPF closer to the surface ($\lesssim$ 1000 m), often finding large vertical gradients in NPF&G rates (Platis et al., 2016; Chen et al., 2018; Lampilahti et al., 2020). Observations from surface sites and aerial platforms during intensive campaigns have provided important site-specific information about NPF spatial gradients and chemical drivers, along with detailed particle property measurements (Hodshire et al., 2016; Wehner et al., 2007; O'Donnell et al., 2023). In conjunction with the long-term measurements, intensive campaigns have proved an invaluable tool for our understanding of NPF&G in the atmosphere, especially as it pertains to the spatial extent of NPF events. However, as mentioned, these intensive NPF&G studies are often limited in the extent to which they capture the full lifecycle of NPF&G events, often only capturing a snapshot of spatial gradients or a subset of NPF events during a season.

It has long been hypothesized that in order to fully understand aerosol processes (including NPF&G), observations must be made from the Lagrangian perspective (i.e., following along the wind; O'Dowd et al., 1998; Hoppel et al., 1994). Notably, several campaigns in the 1990's used a combination of ships, aircraft and stationary observations to characterize aerosol and cloud interactions from this perspective. The Atlantic Stratocumulus Transition Experiment (ASTEX; Albrecht et al., 1995), the Aerosol Characterization Experiment (ACE; Raes et al., 2000), and the Marine Aerosol and Gas Exchange (MAGE) campaigns (Huebert et al., 1996) used GPS tracked balloons in order to follow and sample air masses in the European outflow over the Azores.

Overall, these experiments were some of the largest and most comprehensive efforts to characterize continental aerosol and chemical processes for an extended period of time from the Lagrangian perspective, but measurements pertaining to NPF&G were limited or non-existent. Since ASTEX/MAGE and ACE, there have been targeted aircraft campaigns using a pseudo-Lagrangian framework to investigate urban outflow (Borbon et al., 2013; Zaveri et al., 2022), wildfire plumes (Juncosa Calahorrano et al., 2021; Kleinman and Sedlacek, 2016; June et al., 2022), and aerosol-cloud interactions (Zaveri et al., 2022; Fan et al., 2018). However, to our knowledge, there has not been an NPF specific campaign to understand NPF&G in the atmosphere from the Lagrangian perspective.

While there have been several aerosol-focused Lagrangian field campaigns (with many other campaigns utilizing pseudo-Lagrangian techniques as well), there have been more modeling efforts to investigate aerosols and aerosol processes using a variety of different Lagrangian modeling frameworks. Lagrangian particle dispersion models have been used to provide particle or air mass trajectories. These trajectories are commonly used to understand the air mass history at stationary sites, but they have also been used in conjunction with 0-D box models to understand aerosol processes (including NPF&G). Notably, the FLEXible PARTicle (FLEXPART) model was used in conjunction with an aerosol formation and growth model to explain apparent particle shrinkage events in Hada Al Sham, Saudi Arabia (Hakala et al., 2023). Hakala et al. (2023) found that the apparent shrinking (or evaporation) of particles could be explained by air masses with different origins passing by their observation site (i.e., different aerosol characteristics and particle growth history, so that the observed decrease in mode diameter is due to decreasing net growth instead of shrinkage).

A number of other studies have used box and column models representing aerosol microphysics and chemistry along Lagrangian trajectories to explain aerosol mass (Emmerson et al., 2004; Murphy et al., 2012), aerosol partitioning and volatility (Murphy et al., 2011), volcanic and wildfire plumes (Sellitto et al., 2016; Alvarado and Prinn, 2009; June et al., 2022), transport of dust and microplastics (Kim and Lee, 2013; Tatsii et al., 2024), aerosol sources (Derwent et al., 2003), and aerosol size distributions (Tunved et al., 2010). Additionally, Lagrangian particle dispersion models (like FLEXPART) have been used within 3D Earth system models. This framework has been used extensively to investigate aerosol source/receptor regions (Fairlie et al., 2009; Kuhn et al., 2010), aerosol cloud interactions (Christensen et al. 2023; Van Leuven et al., 2023; Talvinen et al., 2025), and chemical budgets (Bergamaschi et al., 2022; Che et al., 2022; Khan et al., 2015). However, utilizing Lagrangian trajectories within a 3D model has only been employed very recently for a couple of NPF event days to understand NPF&G processes in the atmosphere (Shrivastava et al., 2024). Additionally, Talvinen et al., (2025) utilized Lagrangian trajectories in several general circulation models to investigate the effects of clouds and precipitation on aerosol lifecycles. However, to our knowledge, the combination of 3D models with trajectories has not been used to understand the Lagrangian perspective NPF&G and issues with stationary NPF&G measurements. Our study addresses this gap.

In this work, we seek to understand the source of undefined/class II NPF days in stationary measurements by examining Lagrangian trajectories through a 3D model. Specifically, we interpolate aerosol size distributions along Lagrangian trajectories within the GEOS-Chem-TOMAS chemical transport model with online aerosol microphysics to interpret NPF&G events simulated at the SGP observatory. Section 2.2 outlines the methods of our work, including observational data and modeling tools. In Section 2.3, we evaluate the model's ability to represent

NPF events at the SGP site, and then we show three case studies (three undefined/class II days) comparing the Lagrangian and Eulerian perspectives. For all the simulated days, we compare the event classification between the stationary and Lagrangian perspectives. For days where the model simulates NPF events, we compare formation rates of 3 nm particles, growth rates, and survival probabilities to 25 nm between the Eulerian and Lagrangian perspectives. Finally, in Section 2.4 we discuss the implications and limitations of our work as well as future research directions.

2.2. Methods

2.2.1 Observations

Measurement data were taken from the Atmospheric Radiation Measurement (ARM) Southern Great Plains (SGP) observatory, located in north-central Oklahoma (36.60°N, 97.48°W). The SGP observatory has a long-term record ($>$20 years) of aerosol, chemical, and meteorological observations. SGP is primarily surrounded by agricultural land with intermittent agricultural and rangeland burning, but the site is influenced by air masses from a diversity of rural and anthropogenic origins (Liu et al., 2021; Shrivastava et al., 2024). Organic aerosol (OA) is a significant contributor to the submicron aerosol mass at the SGP site with non-trivial portions of OA being attributed to biomass burning in fall, winter, and springtime (Parworth et al., 2015). Based on available data, both from the SGP site and for the model (Section 2.2.2), and computational constraints, we investigate NPF&G events from 10 April 2019, through 30 September 2019. This analysis period generally encompasses the peak period of NPF (spring and summer; Fast et al., 2019), but we recognize this short analysis period is a limitation, especially regarding the robustness of our statistics. This work is intended to serve as an initial exploration of analyzing NPF&G events from the Lagrangian perspective in a 3D model.

The current generation of Aerosol Observing System (AOS) has been stationed at the SGP observatory since November 15, 2016, and has been making semi-continuous measurements of particle size distributions since then to the present day. As part of the AOS, a TSI, Inc. Model 3938 scanning mobility particle sizer (SMPS) was deployed to measure particles with electrical mobility diameters between 10 and 500 nm. Particles entering the AOS SMPS system are given a known charge distribution by a bipolar aerosol charger (TSI, Inc. Model 3077A). Particles are then classified by a long column differential mobility analyzer (DMA; TSI, Inc. Model 3081a) based on their electrical mobility. Finally, a TSI, Inc. Model 3772 condensation particle counter (CPC) counts the total number of particles at the given electrical mobility. The measurement cycle for the SMPS was 5 min, and the sample flow was dried to a relative humidity below ~40% using a Nafion dryer (Perma Pure Inc. PD-07018T).

2.2.1.1 NPF&G event classification

Daily size-distribution data from the SMPS at the SGP site are classified into three categories based on the potential to derive NPF&G statistics. Our method is similar to the method in Dal Maso et al. (2005), except we have combined the class II and undefined event categories. Doing this, we end up separating the clearest NPF&G events (class I), the non-event days, and the days where NPF is occurring but derivation of reliable nucleation and growth statistics is not possible (undefined/class II). Each day in the analysis period is classified visually as one of the three aforementioned categories. The criteria for an NPF-event day are (Dal Maso et al., 2005):

1. A distinctly new mode of particles must appear in the size distribution;
2. The mode must start in the nucleation mode size range (we define the nucleation mode as the 10 - 25 nm diameter range in this study);
3. The mode must prevail over a time span of hours (≥ 4 h);

4. The new mode must show signs of uninterrupted growth.

These criteria are designed to filter out events where only a portion of the NPF&G is observed, cases where nucleation or growth is interrupted, cases when ultrafine primary emissions might be the source of small particles and days where no apparent new nucleation mode particles are seen (non-event days), while retaining the NPF events from which growth rate, nucleation rate, and survival probability statistics can be calculated. Non-event days are days where little to no nucleation mode particles are present throughout the day, indicating there is no influence from emission sources or NPF&G. We combine the undefined event days and the class II event days because both event classes indicate that there are some inhomogeneities in the air mass causing either nucleation or growth rates to vary in time. In doing this, our goal is to explain peculiar aerosol size distribution behaviour by looking at the Lagrangian perspective. While this category analysis is not perfect, similar methods have been utilized in many prior NPF studies (e.g. Zhang et al., 2012; Kerminen et al., 2018; Kulmala et al., 2013; Wang et al., 2020; Pierce et al., 2014), and it provides us with understanding of the number of undefined and class II days, which are of interest for this work. Recent studies have utilized newer methods to analyze NPF events, such as nanoparticle ranking analysis (Aliaga et al., 2023). However, such methods make it difficult to distinguish between the different types of event classes, as undefined/class II event days can be associated with large changes in the ultrafine mode and thus rank in the top percentiles of the NPF ranking. For this work, only one individual performed the event classification (as opposed to three in Dal Maso et a., 2005), and that is a limitation of our work. We employ the same categorization method for the modeling (discussed in section 2.2.3).

In addition to the SMPS data, we used aerosol chemical speciation monitor (ACSM) data from the AOS to compare aerosol mass and composition from our modeling (Section 2.2.2; Figure

A1). The ACSM measures the chemical mass concentration of non-refractory submicron (diameter 80 nm to 1 μm) aerosol species including sulfate, ammonium, chloride, nitrate, and organic matter (Parworth et al., 2015; Uin et al., 2019) with a measurement accuracy of ±30% (Ng et al., 2011). Similar to the SMPS systems, samples were dried using a Nafion dryer (Perma Pure Inc. PD-07018T). Finally, we utilized wind speed and direction data from the surface meteorological system which had a RM Young 05103/05106 Wind Monitor. Wind speeds are measured in the range of 0-100 m/s with a manufacturer reported accuracy of ±0.3 m/s or 1% of reading, whichever is greater. Wind direction data are reported in the range of 0°-360° with a manufacturer reported accuracy of ±3°. The surface wind data serves as a "ground truth" check for our modeling involving Lagrangian trajectories.

2.2.2 GEOS-Chem-TOMAS

To simulate NPF&G events regionally, we used the GEOS-Chem (version 14.3.0, 2024) chemical transport model with the TwO Moment Aerosol Sectional (TOMAS; described next) microphysics module (GC-TOMAS; Kodros and Pierce, 2017). GC-TOMAS has been used to investigate many chemical and aerosol processes including NPF&G (e.g., Croft et al., 2021; Westervelt et al., 2013; Williamson et al., 2019), aerosol-cloud interactions (e.g., Kodros and Pierce, 2017), aerosol direct radiative effects (e.g., Kodros et al., 2016a), and SOA condensation (e.g., D'Andrea et al., 2013). We ran a global simulation at 4° x 5° resolution with 47 vertical levels from March to September 2019 with a chemistry time step of 1 h and a transport time step of 0.5 h. Output from the 4° x 5° simulation serves as the boundary conditions for the high resolution (nested) simulation over the central United States. The nested simulation was run using a 0.25° x 0.3125° grid starting two weeks after the 4° x 5° simulation in order for aerosol species' concentrations to be adequately spun up in the troposphere, and the chemistry time step 600 s and

the transport time step is 300 s. The bounds of the nested simulation are -110°E to -85°E and 45°N to 25°N in order to adequately capture the regional processes impacting the SGP site. The 4° x 5° simulation was driven using NASA's Global Modeling and Assimilation Office (GMAO) MERRA-2 meteorology, and the 0.25° x 0.3125° degree simulation was run using GEOS Forward Processing meteorology (GEOS-FP).

We used the TwO Moment Aerosol Sectional (TOMAS) aerosol microphysics package to simulate size-resolved aerosol microphysics (Adams and Seinfeld, 2002; Lee and Adams, 2012). TOMAS is set up with 13 logarithmically spaced mass-quadrupling size sections ranging from diameters of 3 nm to 1 μm with 2 additional size sections between 1-10 μm. Both particle number and the mass of each species are tracked in each bin. The sectional scheme in TOMAS is based on Tzivion et al., (1987) which has been shown to be more accurate than single-moment sectional schemes (van Salzen, 2006) in representing aerosol processes. Our simulations include sulfate, hydrophilic and hydrophobic organic aerosol, internally and externally mixed black carbon, sea salt, dust, nitrate, ammonium, and aerosol water tracked across the size bins. TOMAS represents changes due to nucleation (discussed next), coagulation, irreversible sulfate and secondary organic aerosol (SOA) condensation, primary emissions, and dry and wet deposition (Trivitayanurak et al. 2008; Westervelt et al. 2013). TOMAS uses GEOS-Chem's "simple scheme" for organic aerosol (OA) which represents primary OA (POA) as non-volatile and it uses a fixed-yield approach for SOA (Pai et al., 2020). Size-dependent SOA condensation is driven by altering the accommodation coefficient following the methods outlined in Shiraiwa and Pöschl (2021). We assume that aerosol particles at all sizes have a bulk diffusion coefficient of $1x10^{-15}$ cm^2 s^{-1} (solid), the condensing SOA has a volatility of C* = 1.0 μg m^{-3}, and the condensing species do not react in the particle phase. The size-dependent accommodation coefficient used in this work is shown in the

Supplement (Figure A3). The accommodation coefficient for sulfate is a constant value of 0.65 for all sizes.

In TOMAS, the inorganic nucleation rates have been updated to those from Dunne et al. (2016), and organic nucleation rates have been added from Riccobono et al. (2014). The inorganic nucleation scheme represents both binary (sulfuric acid and water) and ternary (sulfuric acid, water, and ammonia) nucleation with ion mediated and neutral versions of each (four mechanisms total). For ion-mediated NPF mechanisms, we used an ion-pair formation rate of 10 pairs cm^{-3} s^{-1}, representative of the continental boundary layer. We found that using the inorganic nucleation schemes as outlined in Dunne et al. (2016) produced too little nucleation, therefore, we added a 10^3 scalar to the total inorganic nucleation rate. The necessity of the 10^3 scalar is likely due to not accounting for nucleation mechanisms involving amines (not represented in GEOS-Chem), which have been shown to be important for nucleation in this region (Hodshire et al., 2016; Shrivastava et al., 2024), or other species reacting with sulfuric acid. Further details of the inorganic nucleation rates can be found in Dunne et al. (2016). The organic nucleation rates are parameterized based on sulfuric acid clustering with low-volatility organic species. We include the temperature dependence of the organic nucleation rates from Yu et al. (2017). GEOS-Chem does not explicitly track low-volatility organic compounds. Therefore, in our simulations, we assume that 1% of condensing SOA has a low-enough volatility to participate in NPF, and we calculate the pseudo-steady-state concentration of these low-volatility organics using the condensation sink calculated for these species (Pierce and Adams, 2009a) and an assumed molecular mass of 200 g mol^{-1}. Similar to the inorganic nucleation scheme, we found that the organic nucleation rate required a 10^2 scalar in order to see appreciable nucleation. Again, this may be due to not accounting for other organic nucleation mechanisms that have been included in other work (Zhao et al., 2024; Lehtipalo

et al., 2018). We recognize the limitations in scaling the inorganic and organic nucleation rates, and, because of these limitations, we do not draw any conclusions about the dominant nucleation mechanism in our study region. Additionally, with scaling the nucleation rates, but not accounting for additional nucleation mechanisms, we are likely reducing the model's ability to represent variability in NPF&G events across different days. Fortunately, NPF&G is a buffered system as shown in Westervelt et al. (2014) where a two order of magnitude change in nucleation rates leads to a relatively smaller change in CCN concentrations at a 0.2% supersaturation. In other words, scaling the nucleation rates is a limitation of this work, however, the scaling has a lesser effect on the production of accumulation-mode particles (diameter > ~100 nm).

GEOS-Chem can be run with a variety of source-specific emission inventories for different aerosol and gas-phase compounds. For anthropogenic emissions, we used the Community Emissions Data System version 2, which is the default option in GEOS-Chem v14.3.0. For biomass burning emissions, we used the Quick Fire Emissions Dataset (QFED) which uses fire radiative power (FRP) from the Moderate Resolution Imaging Spectroradiometer (MODIS) satellite to derive daily-mean emissions of several aerosol and gas-phase species. We found using the QFED biomass burning emissions led to better agreement with SMPS data at the SGP site, seemingly due to QFED estimating the emissions from the small prescribed and agricultural fires in the US Great Plains and Midwest compared to the other biomass-burning inventories (Pan et al., 2020). Size dependent and source specific black carbon and organic aerosol emissions follow Kodros and Pierce (2017). Temperature dependent sea salt emissions follow Jaeglé et al. (2011), and dust emissions are parameterized based on the Dust Entrainment and Deposition (DEAD) model from Zender et al. (2003).

2.2.3 HYSPLIT

To extract aerosol size distributions along Lagrangian trajectories passing through SGP within the model, we used the HYbrid Single-Particle Lagrangian Integrated Trajectory (HYSPLIT) model (Stein et al., 2015; Rolph et al., 2017). HYSPLIT represents the forward or backward transport of a single particle or "puff" emission starting at a point and advects that particle based on the mean of the 3D velocity vectors provided by reanalysis meteorology. For each of the 174 days simulated with GEOS-Chem, we ran 24 h forward and backward trajectories every 3 h starting at 250 m over the SGP observatory. We chose 250 m as the initial height because this height is generally within the planetary boundary layer (PBL) at SGP, and 250 m is the optimal starting height for ensemble trajectories as recommended by the HYSPLIT website (Draxler, 2003). Additionally, trajectories that intersect the ground surface are not realistic, as the vertical velocity is by definition zero, thus trajectories will remain at the surface once they reach it (Rolph et al., 2017). Therefore, starting trajectories at 250 m helps to avoid this intersection from happening. Figure A2 compares the simulated hourly average total number concentration of particles at the SGP site at the surface and 250 m, and there is little difference between the two heights. The forward and backward trajectories (initialized at the same time) are combined to create a continuous "flyby" trajectory that is used for offline analysis of the aerosol fields in GEOS-Chem. For this work, we used MERRA-2 meteorology data to drive the HYSPLIT model. We recognize that comparing HYSPLIT trajectories driven by MERRA-2 meteorology (at 0.5° x 0.625° resolution) with our GC-TOMAS simulations, which were driven by GEOS-FP (at 0.25° x 0.3125° resolution), may lead to discrepancies; however, at the time of writing, there is currently no method for running HYSPLIT with GEOS-FP meteorology; both MERRA-2 and GEOS-FP are produced by NASA's Global Modeling and Assimilation Office (GMAO) and the two models

have similar resolutions. For the case studies chosen in this analysis (discussed later in this section), we ran 27 ensemble HYSPLIT trajectories with slightly different initial meteorological conditions (Draxler, 2003) in order to test the sensitivity of our results to the trajectory path (Figures A4-6 and A8-13). We recognize that utilizing single trajectories for the bulk of this analysis leads to greater uncertainty, especially if NPF&G is spatially inhomogeneous; however, our current computational power prohibits utilizing ensemble trajectories for all analysis days. Although our focus is on comparing data below the PBL height, we do not remove trajectories that go above the PBL from our analysis. These trajectories are likely in the residual layer (layer between the PBL and the free Troposphere), and we specifically note these occurrences in the results.

2.2.3.1 Lagrangian size distributions along trajectories

To extract the simulated aerosol size distributions along the HYSPLIT trajectories, we used a distance-weighted average between the trajectory location and the eight (in 3 dimensions) closest GEOS-Chem grid point centers. The aerosol number concentration for a given aerosol size bin can be expressed as the following equation:

$$N_{new} = \sum_{i=1}^{2}\sum_{j=1}^{2}\sum_{k=1}^{2} N_{i,j,k}\left(1-\frac{|x_i-x|}{0.3125^\circ}\right)\left(1-\frac{|y_j-y|}{0.25^\circ}\right)\left(1-\frac{|z_k-z|}{dz}\right) \quad (1)$$

Where N_{new} is the number concentration in a given size bin along the trajectory; k, i and j are counters for the closest model grid point centers in the horizontal (i and j) and vertical (k) directions; $N_{k,i,j}$is the number concentration in a given diameter bin for the closest model grid points; z_k is the height of the close by grid point centers; x_i is the longitude of close by grid point

centers; y_j is the latitude of close by grid point centers; z is the height along the HYSPLIT trajectory; x is the longitude along the HYSPLIT trajectory; and y is the latitude along the HYSPLIT trajectory.

2.2.3.2 NPF classification along Lagrangian trajectories

To explore the simulated size distributions at the SGP site and along trajectories, we employ the same manual categorization method (Sect. 2.1) that was used with the SGP SMPS data. While the model produces size distributions with diameters starting at ~3 nm, we only used size distribution data above 10 nm for the categorization for consistency with the SMPS data. The HYSPLIT trajectories pass over the stationary site every 3 h; however, we use the trajectory that looks most like an NPF event to make the daily event categorization. In other words, if one of the trajectories had an aerosol size distribution that looked like an NPF event, we classified that day as an NPF-event day from the Lagrangian perspective. Similarly, if no trajectories had a clear NPF event but at least one would be classified as undefined or class II, this day would be undefined/class II from a Lagrangian perspective. This methodology enables us to explore how NPF events along the trajectories might appear as undefined/class II days or non-event days at the stationary site. Examining only the trajectories that pass over the SGP site at 12:00 CDT, we found a higher fraction of undefined/class II days became non-event days because the use of only one trajectory per day sometimes missed the NPF&G that caused the undefined/class II day.

2.2.4 Nucleation rates, growth rates, and survival probability

Finally, we calculate particle formation rates, growth rates, and survival probability to 25 nm during NPF events from the modeled size distributions at the stationary site and from the modeled size distributions along the Lagrangian trajectories, and compare these apparent values

at the stationary site and physical values within the moving air mass. Growth rates, formation rates of 3 nm particles, and survival probabilities are calculated using similar methods to those outlined in Westervelt et al. (2013), which we summarize here. The formation rate of 3 nm particles (J_3, the rate of appearance of 3 nm particles [cm^{-3} s^{-1}]), is calculated using a time derivative of the nucleation mode (3 - 25 nm) number concentration ($N_{3\text{-}25}$) with a correction for coagulational losses (F_{coag}). As in Dal Maso et al. (2005), we do not include the additional condensational growth (F_{cond}) correction term to account for growth out of the nucleation mode as the influence should be minor for short time periods. As a note, assuming there are limited anthropogenic sources of sub-25 nm particles near the SGP site in the model is a reasonable assumption; however, this assumption likely breaks down along the Lagrangian trajectories. Emissions of sub-25 particles along the trajectories can potentially skew NPF&G statistics if the trajectories pass over a source area, but the number of cases is likely few and the classification method along the trajectories will filter out extreme cases. The formulation of J_3 is thus as follows:

$$J_3 = \frac{dN_{3-25}}{dt} + F_{coag} \quad (2)$$

Diameter growth rates are derived by applying a linear fit to the mode diameter of the growing nucleation mode from 3-25 nm where the slope of the fit is the growth rate [nm hr^{-1}]. The growth rate is used to calculate the condensation timescale which is used in the calculation of the survival probability of 3 nm particles to 25 nm following Pierce and Adams (2007). The timescale for condensational growth between TOMAS size sections (τ^{cond}) is calculated as:

$$\tau_{k,k+1}^{cond} = \frac{D_{p,k+1} - D_{p,k}}{GR_{k,k+1}} \quad (3)$$

Where D_p is the particle diameter in bin k, and GR is the average growth rate from 3-25 nm. The timescale for the loss of particles by coagulation in each size section is given by:

$$\tau_k^{coag} = \frac{1}{\frac{1}{2}K(D_{p,k}, D_{p,k})N_k + \sum_{j=k+1}^{k_{max}} K(D_{p,k}, D_{p,j})N_j} \quad (4)$$

Where K is the coagulation kernel, N_k and N_j is the number of particles in bins k and j respectively, the first term in the denominator represents coagulational losses of particles with the same diameter, and the second term in the denominator represents the loss of particles in bin k with particles in bin j.

Finally, the 25 nm survival probability (i.e. the probability of a given particle to survive to 25 nm) is given by:

$$SP_{m,n} = \prod_{k=m}^{n-1} exp\left(-\frac{\tau_{k,k+1}^{cond}}{\tau_k^{coag}}\right) \quad (5)$$

Where $SP_{m,n}$ is the probability of a particle in diameter bin m surviving to diameter bin n. The survival probability equation essentially calculates the probability of a particle surviving growth from one TOMAS size section to the next, and the overall survival probability is the product of all the single-growth-step probabilities. Note, the linear fit to the growing aerosol mode, not the number of particles at 25 nm, is used to calculate the survival probability.

2.3. Results

2.3.1 Frequency of NPF days in the observations and the model

The number of days classified into different event categories for the observations at the SGP site and for the stationary model results at the SGP site is shown in Figure 2.1. Based on our classification, the SGP observations showed 54 (31.0%) non-event, 114 (65.5%) undefined/class II event, and 6 (3.4%) NPF event days, while GC-TOMAS simulated 86 (49.4%) non-event, 83 (47.7%) undefined/class II event, and 5 (2.9%) NPF event days. Our analysis of GC-TOMAS output shows that the model accurately represents the event class for 125 (71.8%) of the specific days indicated by the green boxes in Figure 2.1. Notably, our classification using both the model and observations show a significant portion of days being undefined/class II, although using the model produced 31 fewer undefined/class II days than the observations. The discrepancy in undefined/class II days is expected given the limitations of the model to fully resolve sub-grid scale emissions sources that might influence the SGP observatory. For 47 (27.0%) of the 174 days, the model was one category off, indicated by the yellow colored boxes in Figure 2.1. For only two days, the model produced days with no NPF events when the observations visually showed NPF events, indicated by the red boxes (Figure 2.1). The 71.8% agreement between classifications using the model and observations aligns with previous work investigating NPF using GC-TOMAS (Westervelt et al., 2013), where agreement between the model and observations on simulating specific event/non-event days was generally between 50-60%. The model generally produces the correct number of NPF&G events, but the model produces more non-event days and fewer undefined/class II event days than the observations indicated by the numbers outside of the boxes in Figure 2.1. Additionally, the model does lack skill in reproducing the range of variability in the condensation sink (Figure A14). The model underrepresenting the number of undefined/class II

events is expected given the ~25 km horizontal resolution of the model, which is likely too coarse to resolve localized sources of gas and particle emissions. The number of undefined/class II days classified using the model and observations is a significant motivation for this work in attempting to understand what causes undefined/class II days, and we step through several case studies of undefined/class II days in the next section.

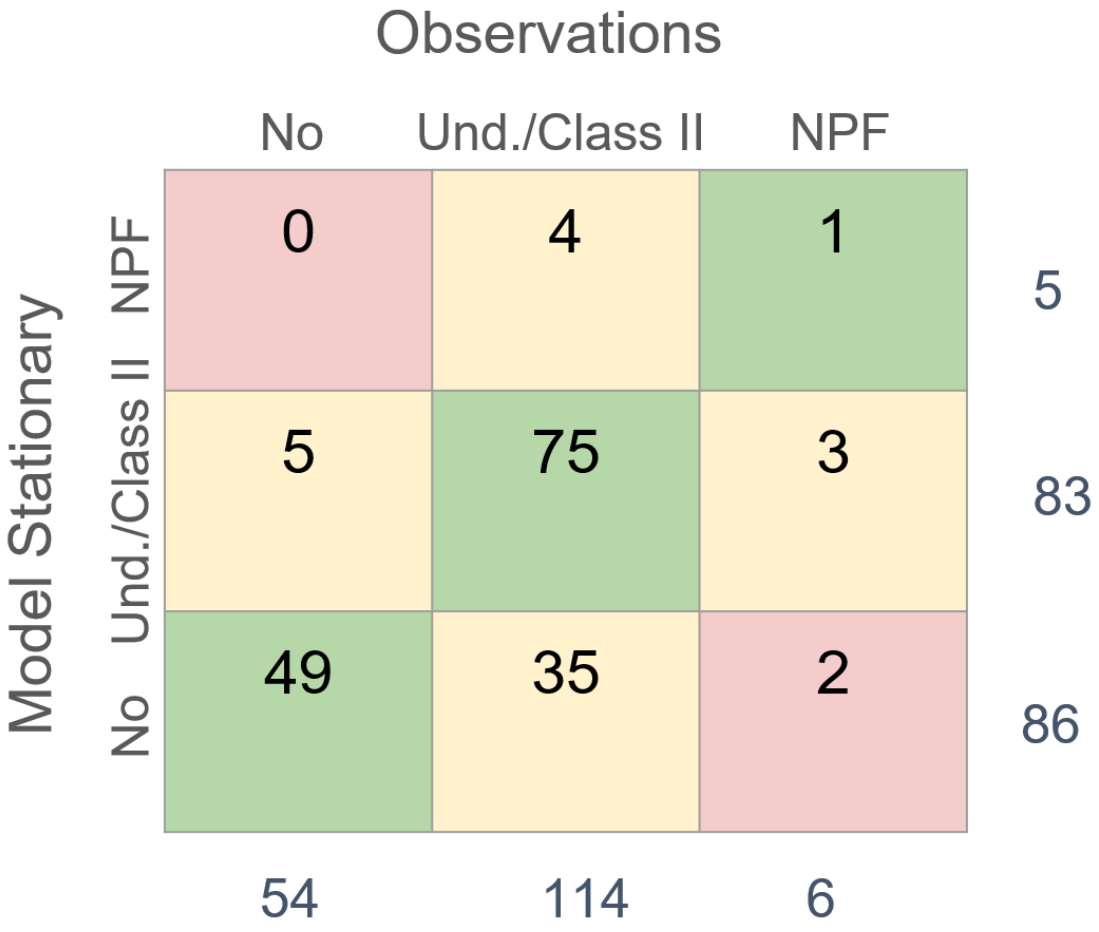

Figure 2.1. Agreement of NPF, undefined/class II, and non-event days as determined using the observations from the SGP site compared with the model. Each of the 174 days is categorized as an NPF, undefined/class II, or non-event day for both the model and observations. Categorization method described in Sect. 2.1. The green boxes represent agreement between the model and observation classifications, the yellow boxes are days where the model was off by one category, and the red boxes are days where the model produced an NPF event or non-event when the observations showed a non-event or NPF event, respectively. The numbers at the far right and bottom indicate the sum across the rows and columns, respectively.

2.3.2 Case Studies of Lagrangian trajectories on undefined/class II days

To further develop our analysis, we have chosen three case studies when there were undefined/class II days classified using both the model and observations. Notably, we chose three days where the model and observations agree well in the characteristics of the undefined/class II days (e.g. particles appearing or disappearing around the same sizes and times). The findings of these case studies generally apply for most of the undefined/class II days, as will be shown in Section 2.3.3. The first case study is one where the model and observations show particles appearing already grown at the SGP observatory. The second case study resembles a class II type NPF&G event where there appears to be nucleation occurring but the particles show little growth and then disappear. The third case study is one where the model and observations suggest significant biomass burning influence as well as potential NPF.

2.3.2.1 Already grown event

For the undefined day of 6 May 2019, we find that the appearance of already grown particles can be attributed to NPF&G in the outflow of Dallas, TX (Figure 2.2). The SMPS measurements show particles appearing at SGP around 20:00 CDT with diameters of ~40 nm (Figure 2.2b), and the model shows particles appearing after 21:00 CDT with diameters of ~40 nm (Figure 2.2a). Notably, the modeled and observed size distributions agree well with the exception of the high number concentration of ~40 nm particles in the model in the early morning. Figure 2.2c shows the six different HYSPLIT trajectories that pass over the SGP observatory at 3 h intervals. The six trajectories are consistently from the south, passing over a mix of crop land, rangeland, and urban centers. The direction of these trajectories matches well with the wind direction data at the SGP observatory (Figure A15). The six panels on the right side of Figure 2.2 (2.2d.1-6), shows the simulated size distributions along the six HYSPLIT trajectories. We also ran

27 ensemble trajectories (described in Sect 2.3) for the case studies. The size distributions for these trajectories are included in the supplementary material for 6 May 2019 at 9:00, 15:00, and 21:00 CDT (Figures A4-S6). The aerosol size distributions along the ensemble trajectories show more variation in the aerosol number given the location differences of the trajectories, both at the starting locations and up/down wind; however, the qualitative result of the later-arriving trajectories having stronger NPF events remains the same.

The aerosol size distributions along the trajectories show little to no nucleation occurring except for the last trajectory, which has a typical NPF&G event leading to particles appearing already grown at the stationary site late in the evening. The size distributions for the trajectories that pass over the SGP site at 9:00 AM and 12:00 PM show little to no nucleation occurring. The subsequent two trajectories (15:00 and 18:00 CDT) show a small amount of nucleation occurring, starting around 11:00 CDT and continuing until about 16:00 CDT. These two trajectories show similar nucleation behavior as the modeled stationary site during the afternoon, indicating that there might be some weak regional nucleation occurring over a large area during that time and that the air mass transport remained very similar for the afternoon. Maps of the number concentration of 3-22 nm particles (Figure A16) show there is a large area of seemingly weak NPF occurring with other areas of enhanced nucleation, primarily in the outflow of urban centers. The trajectory that passes over the SGP site at 21:00 CDT shows more nucleation occurring than any of the earlier trajectories (Figure 2.2d.1).

When looking at the maps of 3-22 nm particles (Figure A16), the 21:00 CDT trajectory passes over the Dallas, TX area just before nucleation initiates. The trajectory location is essentially on the leading edge of the nucleation occurring in the outflow of Dallas, hence we see considerably more nucleation occurring in that trajectory. The final trajectory passing over the

SGP observatory at 00:00 CDT on 7 May, shows the most significant NPF&G event compared to the prior trajectories. The 00:00 CDT trajectory (Figure 2.2d.6) passes over the Dallas, TX area around 13:00 CDT, when peak NPF is occurring in the urban outflow. As the air parcel is advected toward the SGP site, the particles continue to grow until they pass over the SGP site where they are observed as the appearance of ~40 nm particles.

The modeled stationary aerosol size distribution located in Dallas, TX (Figure A7a) area shows NPF&G occurring, but the particle number concentration decreases significantly above 40 nm indicating particles are advecting away. Additionally, the modeled size distribution in Houston, TX shows nucleation and limited growth (Figure A7b), and there is weaker NPF occurring between Houston and Dallas (Figure 2.2c). Our results indicate that the undefined NPF event observed at the SGP site on 6 May 2019 can be attributed to spatially inhomogeneous nucleation occurring in the air masses passing over the SGP site. On this day, it seems that weak regional NPF occurred over much of Texas and Oklahoma, and more vigorous NPF occurred in the outflow regions of large cities (Figure 2.2c).

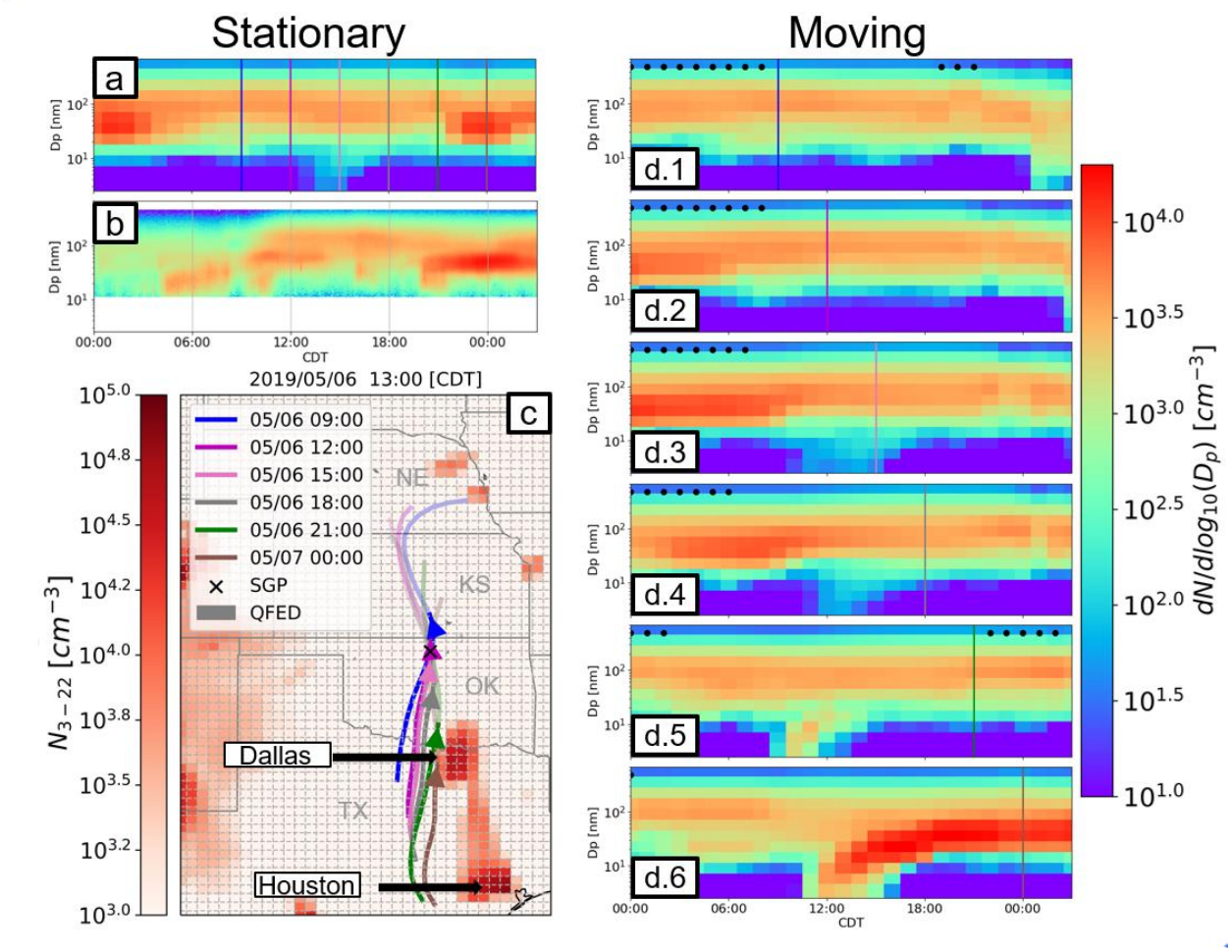

Figure 2.2. Example case on 6 May 2019, where the model correctly predicts the appearance of already grown particles at the SGP observatory. (a) The modeled aerosol size distribution at the SGP observatory where particles appear around 21:00 CDT with diameters ~40 nm. (b) The corresponding aerosol size distribution measured by the SMPS at the SGP observatory. The colored vertical lines indicate the time at which the trajectories pass over the SGP site (matching color with vertical lines on d). (c) The HYSPLIT trajectories passing over the SGP observatory with the location of the trajectories at 13:00 CDT indicated by the triangles. The red colors indicate the number concentration of 3-22 particles (N_{3-22}) at 13:00 CDT, and the grey spots indicate QFED fire hotspots. The time at which the trajectories pass over the SGP observatory is indicated by the time listed in the legend. (d) The interpolated modeled aerosol size distributions along the HYSPLIT trajectories shown in panel c. Each size distribution time series has a vertical line that shows the time at which the trajectory passes over the SGP observatory (matching lines on panel a). The black dots indicate times at which the trajectory is out of the planetary boundary layer.

2.3.2.2 Class II type event

Figure 2.3a shows the modeled aerosol size distribution on 15 April 2019, and Figure 2.3b shows the observed size distribution on the same day, both showing what we classify as a class II NPF event. We classified this day as a class II event because it illustrates signs of NPF with interrupted particle growth, shown by the mode mean diameter decrease after 14:00 CDT. While the time series of the aerosol size distributions do not exactly agree between the observations and the model on the event timing and magnitude, both show evidence that NPF&G is regionally inhomogeneous due to the rapid enhancement and reduction in the number of particles in the nucleation mode. The model at SGP does show nucleation and limited growth occurring below 10 nm sizes between 9:00 and 14:00, but these particles appear to never grow into the SMPS size range. The model shows particles appearing above 10 nm around 15:00 CDT while the observations have particles appearing around 11:00 CDT.

We cannot definitively say what process in the model is leading to the later appearance of 10 nm particles, but it is likely due to a combination of weak NPF&G occurring in the 12:00 and 15:00 trajectories, the linear interpolation method used, and the use of a single trajectory within a region of spatially inhomogeneous NPF&G. Similar to the event on 6 May, the HYSPLIT trajectories are all approaching the SGP observatory from the south on 15 April 2019 (Figure 2.3c) and then proceed northward over KS where there are biomass burning hotspots. Again, the directions of the trajectories align well with the surface winds at the SGP site (Figure A17). Finally, Figure 2.3d shows the aerosol size distributions along the six trajectories. The size distributions along the ensemble trajectories are included in the supplementary material for 15 April 2019 at 9:00, 15:00, and 21:00 CDT (Figures A8-S10; only three times chosen for each case study to limit the number of Supplementary figures). The aerosol size distributions along the ensemble

trajectories show some variation, with some of the size distributions showing discontinuous NPF events due to some of the ensemble trajectories entering and leaving regions of enhanced nucleation at different times. All ensemble trajectory members remain within the planetary boundary layer during the day, and the variation is caused by the steep gradients in NPF&G occurring between 12:00 and 18:00 CDT around the SGP site. Additionally, the variation in the ensemble size distributions could be attributed to slight disagreement between MERRA2 and GEOS-FP meteorology (along with variability of NPF&G); however, the size distributions along the ensemble trajectories are qualitatively similar to the single trajectory approach.

The Lagrangian trajectories on 15 April 2019 show varying degrees of NPF&G occurring, indicating that NPF&G is regionally inhomogeneous (Figure A18). The size distribution for the earliest, 09:00 CDT HYSPLIT trajectory (blue line, Figure 2.3d.1) shows an NPF event that resembles a typical "banana" type event that begins as the trajectory passes over the SGP site. After the 9:00 CDT trajectory passes the SGP site, we see the influence of biomass burning emissions in Kansas around 15:00 CDT (of the 9:00 CDT trajectory time series), when the ~100 nm particles increase in concentration (Figure 2.3d.1). The 12:00 CDT trajectory also shows NPF occurring (Figure 2.3d.2), though weaker than the earlier 9:00 CDT trajectory size distribution (Figure 2.3d.1). Similar to the 9:00 CDT trajectory, the 12:00 CDT trajectory shows the influence of biomass burning emissions after the trajectory passes over the SGP site. The 15:00 (Figure 2.3d.3) and 18:00 CDT (Figure 2.3d.4) trajectories do not deviate significantly from the 9:00 and 12:00 CDT trajectories, both showing more typical NPF&G events when compared to the stationary size distributions.

Notably, the 15:00 CDT trajectory has weaker NPF occurring as the trajectory passes over the SGP site, and the 18:00 CDT trajectory shows a strong NPF event occurring upwind of the

SGP site. The contrast between the 15:00 and 18:00 CDT trajectory size distributions is consistent with the sudden appearance of the particles in the stationary size distribution at 15:00 CDT (Figure 2.2a). These trajectories indicate that the <10 nm particles seen in the stationary size distribution just after 9:00 CDT indeed continue to grow, but the growth is not captured from the stationary perspective. Finally, the last two trajectories (21:00 CDT and 00:00 CDT on 16 April) show very limited NPF&G occurring upwind of the SGP site, leading to the rapid disappearance of the nucleation mode particles in the stationary size distribution. The appearance and disappearance of particles at the stationary site is again driven by horizontal variations in NPF&G occurring upwind of the site (Figure A18). Based on the back trajectories, the NPF&G observed is potentially driven by anthropogenic emissions from San Antonio, TX and the Central Termoeléctrica José López Portillo power station (28.482°N, 100.692°W) which is a >1200-megawatt coal fired power plant in Nava, Coahuila, Mexico. As mentioned, the SGP observations and the stationary modeled size distribution do not precisely agree; however, their behavior is consistent with variability in the strength of NPF&G in the trajectories passing over the site, likely due to heterogeneity in upwind sources.

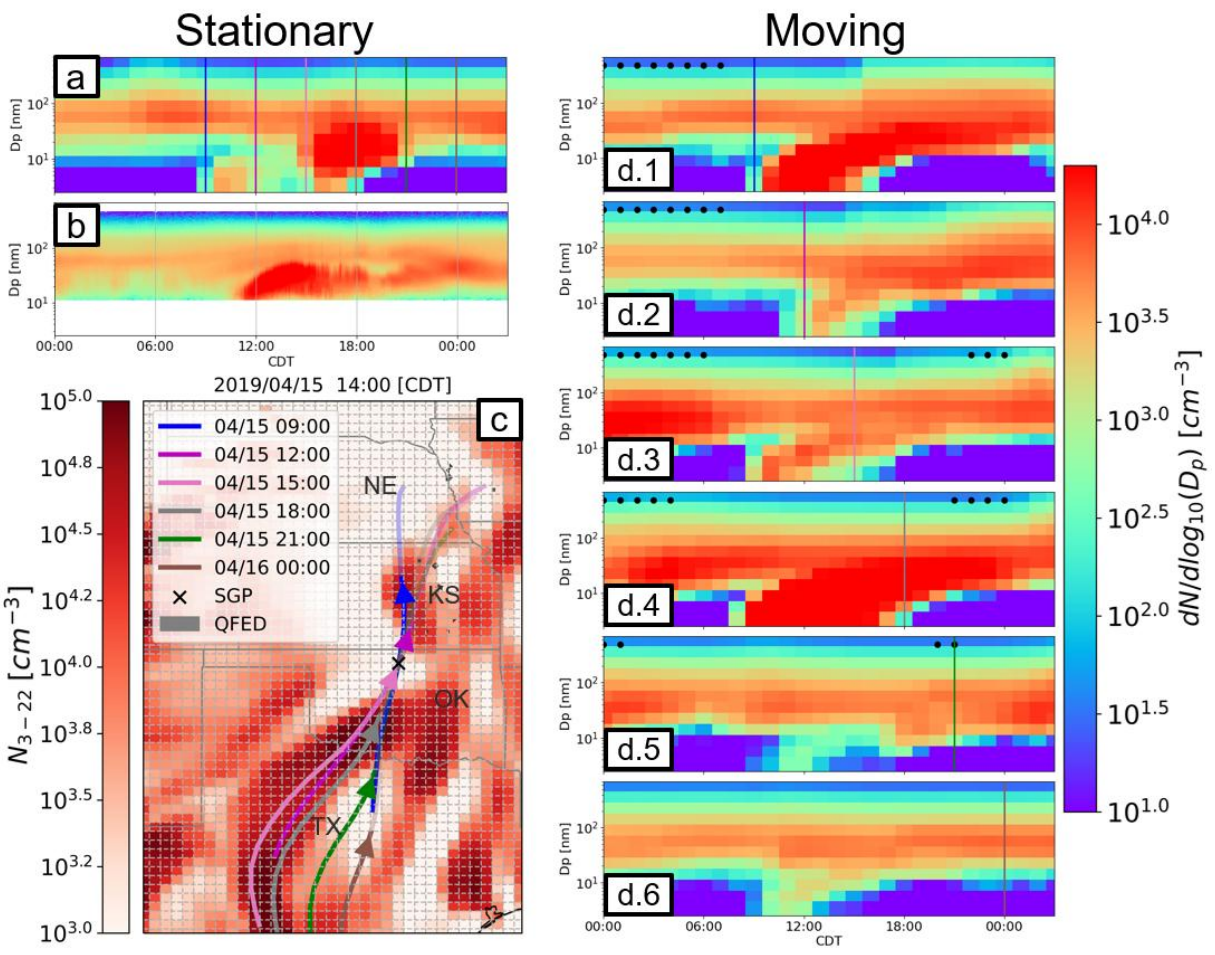

Figure 2.3. Example case on 15 April 2019 where both the model and observations show a class II NPF event. (a) The modeled aerosol size distribution at the SGP observatory. (b) The corresponding aerosol size distribution measured by the SMPS at the SGP observatory. The colored vertical lines indicate the time at which the trajectories pass over the SGP site (matching color with vertical lines on d). (c) The HYSPLIT trajectories passing over the SGP observatory with the location of the trajectories at 14:00 CDT indicated by the triangles. The red colors indicate the number concentration of 3-22 nm particles ($N_{3\text{-}22}$) at 14:00 CDT, and the grey spots indicate QFED fire hotspots. The time at which the trajectories pass over the SGP observatory is indicated by the time listed in the legend. (d) The interpolated aerosol size distributions along the HYSPLIT trajectories shown in panel c. Each size distribution time series has a vertical line that shows the time at which the trajectory passes over the SGP observatory (matching lines on panel a). The black dots indicate times at which the trajectory is out of the planetary boundary layer.

2.3.2.3 Smoke and NPF event

The third example is outlined in Figure 2.4 and illustrates a day (13 April 2019) when there was significant biomass burning influence on the aerosol size distribution at the SGP site, both in the model and observations. Figure 2.4a shows the modeled size distribution at the SGP site, where the number of particles with diameters of 40-200 nm fluctuates significantly (greater than an order of magnitude change in total number over the course of several hours). We ran GEOS-Chem-TOMAS without QFED biomass burning emissions, and there was little fluctuation in the aforementioned size range on this day and the number of particles in this mode was greatly reduced. Figure 2.4b shows the observed aerosol size distribution at the SGP site on 13 April 2019, and there is significant fluctuation in the 40-200 nm number concentration indicative of intermittent biomass burning influence at the SGP site. The QFED biomass burning hotspots can be seen on Figure 2.4c, primarily in eastern Kansas (KS) and Nebraska (NE). Recent work has highlighted the significant prescribed and agricultural burning in this region in the springtime (e.g., Sablan et al., 2024). As with the other case studies, size distributions along the ensemble trajectories are in the supplementary material for 13 April, 2019 at 9:00, 15:00, and 21:00 CDT, and the size distributions broadly agree with the findings of our single trajectory analysis (Figures A11-A13).

All six trajectories on 13 April 2019 are originally traveling from the northwest, but their directions change over eastern KS (where there is significant biomass burning) to approach the SGP site from the northeast. As with the other case studies, the trajectory directions align well with surface winds at the SGP site (Figure A19). The aerosol size distributions along the first two HYSPLIT trajectories (Figure 2.4d.1-2) show little influence of biomass burning as evidenced by the limited changes in the accumulation-mode particle number concentration and no NPF

occurring. The QFED emissions inventory prescribes a diurnal cycle of emission rates, therefore we would expect little influence of biomass burning until the afternoon when springtime fire activity in this region usually peaks (Sablan et al., 2024).

The 15:00 CDT trajectory shows an increase in the accumulation mode around 12:00 CDT, roughly three hours prior to passing over the SGP site. While the increase in the accumulation-mode particle number concentration is abrupt from the Lagrangian perspective, we see a gradual increase in the stationary size distribution as fire activity increases and wind direction changes. The 18:00 CDT trajectory shows peak influence of biomass burning as it passes over the QFED hotspots in addition to some weak NPF occurring around 12:00 CDT. The 21:00 CDT trajectory (Figure 2.4d.5) shows more NPF occurring than the previous trajectory, but slightly less biomass burning influence after the NPF has occurred as evidenced by the lesser change in the accumulation-mode number concentration. Finally, the 00:00 CDT trajectory (Figure 2.4d.6) on 14 April 2019 shows the most NPF&G occurring, but still some influence from biomass burning. The transition from biomass burning influence to NPF influence contributes to the shift in the stationary size distribution to smaller sizes around midnight CDT (Figure 2.4a). It appears that the NPF&G is occurring in the outflow of Omaha, NE. This analysis shows that air masses passing over different land types (e.g. urban and agricultural) at different times are influenced by different aerosol sources, leading to changes in the observed size distribution at a fixed location downstream of the different aerosol regimes (Figure A20).

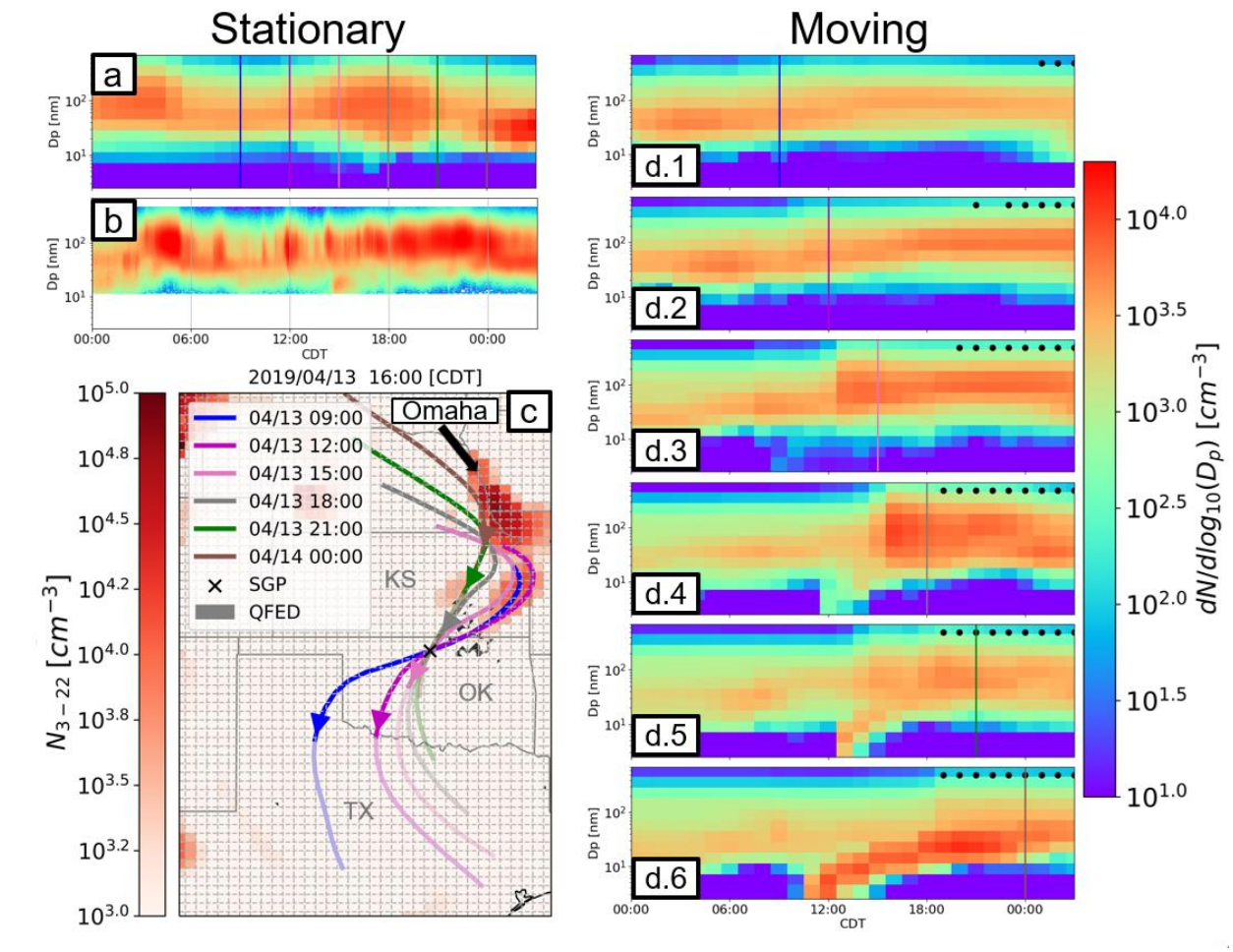

Figure 2.4 Example case on 13 April 2019 where both the model and observations show smoke influence. (a) The modeled aerosol size distribution at the SGP observatory. (b) The corresponding aerosol size distribution measured by the SMPS at the SGP observatory. The colored vertical lines indicate the time at which the trajectories pass over the SGP site (matching color with vertical lines on d). (c) The HYSPLIT trajectories passing over the SGP observatory with the location of the trajectories at 16:00 CDT indicated by the triangles. The red colors indicate the number concentration of 3-22 nm particles ($N_{3\text{-}22}$) at 16:00 CDT, and the grey spots indicate QFED fire hotspots. The black arrow indicates the location of Omaha, NE. The time at which the trajectories pass over the SGP observatory is indicated by the time listed in the legend. (d) The interpolated aerosol size distributions along the HYSPLIT trajectories shown in panel c. Each size distribution time series has a vertical line that shows the time at which the trajectory passes over the SGP observatory (matching lines on panel a). The black dots indicate times at which the trajectory is out of the planetary boundary layer.

2.3.3. Analysis of NPF and growth along Lagrangian trajectories for spring and summer 2019 at SGP

For the 174 simulated days, our event classification methodology (described in Sect 2.1) was applied to the aerosol size distributions along the trajectories. Consistent with our methodology, each day was categorized based on the "most NPF"-looking trajectory upwind of the stationary site. The purpose of this analysis is to understand the potential for information gain in analyzing aerosol size distributions along Lagrangian trajectories.

The results in Figure 2.5 compare the number of days categorized in each event class for the stationary perspective and for the Lagrangian perspective. The numbers on the outside of the boxes show the total number of events in each category from the two perspectives (the red numbers in the parentheses are the numbers of each event class analyzed including the downwind portion of the particle size distribution). As in Figure 2.1, our stationary classification of the model produced 5, 83, and 86 NPF, undefined/class II, and non-NPF days, respectively from the stationary perspective. However, from the Lagrangian perspective, our classification produces 44, 13, and 117 NPF, undefined/class II, and non-NPF days, respectively. This shows that for almost one third of the simulated days, clear NPF events happen within the domain of the forward and backward HYSPLIT trajectories during that day. Our analysis finds ~90% of these NPF events are not clearly observed at the SGP location in the model because they are occurring upwind of the site and are not occurring over a large enough region to appear at the SGP site (similar to the case study outlined in Section 2.3.2.1). The number of undefined/class II days decreases from 83 to 13, indicating that the majority of the undefined/class II days in the model can be explained as either NPF occurring at sub-regional scales or non-NPF days. The number of non-NPF days increases, driven by days where changes in the stationary size distribution, that look like undefined/class II

NPF events, can be explained by trajectories with different aerosol characteristics (but no NPF) passing by the stationary site.

The rapid changes in aerosol characteristics between successive trajectories could be explained in part by the changes in the single trajectory paths throughout the days. In addition to the spatial variability of emissions, the temporal variations of certain emissions sources (e.g., biomass burning) changes the aerosol characteristics for consecutive trajectories (exemplified by the third case study outlined in Section 2.3.2.3). In other words, a trajectory passing over an emission source in the morning may have different characteristics than a similar trajectory passing over in the afternoon. Further, the timing of a trajectory passing over an emissions site relative to the timing of photolysis rates and boundary-layer heights also affects the aerosol evolution along the trajectories. Notably, the bulk of our analysis is done using single HYSPLIT trajectories (i.e., not ensembles), so changes in consecutive single trajectory paths can lead to particle size distribution changes that are unphysical. Using this framework, due to resolution and process limitations of the GC-TOMAS model, we cannot fully constrain all influences on stationary observations of NPF&G; however, we can explain the majority of undefined/class II event days as either non-NPF days or inhomogeneous NPF&G.

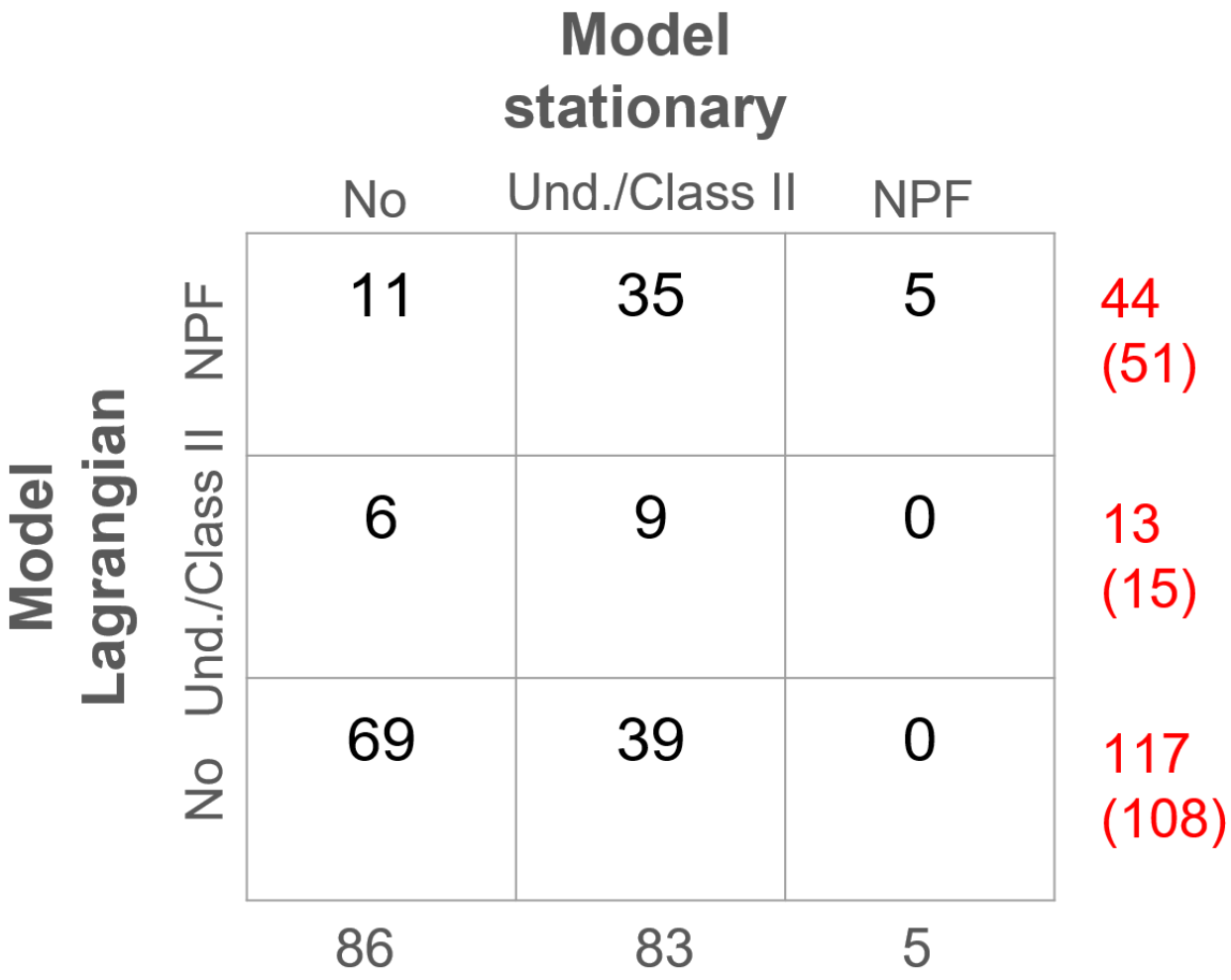

Figure 2.5. Comparison of the number of NPF, undefined/class II, and non-event days in the model at the stationary site (SGP) and along the Lagrangian trajectories. The red numbers on the right indicate the total number of NPF events in each category when looking along the Lagrangian trajectories. The gray numbers on the bottom indicate the total number of each event class based on our classification from the stationary perspective. The red numbers on the right show the total number of events in each class based on our classification of the Lagrangian perspective, and the red numbers in the parentheses show the numbers of each class including an analysis of particle size distributions downwind of the SGP site.

2.3.3.1 Formation rates, growth rates, and survival probability results

The data in Figure 2.6 show the distribution of 3 nm particle formation rates, growth rates, and survival probabilities for the stationary view from GC-TOMAS model as well as along trajectories. There is a slight increase in the median formation rate of 3 nm particles between the

Lagrangian and stationary perspectives for the five NPF&G events, but there is virtually no change in the mean formation rates between the two perspectives. The black lines on Figure 2.6a between the red and blue violin plots connect the same NPF&G events, and we see that three of the events show a decrease in formation rate of 3 nm particles from the Lagrangian perspectives and two of the events show an increase. For all 44 Lagrangian NPF&G events (Figure 2.6a, green violin plot), the mean and median formation rates of 3 nm particles are 0.39 cm^{-3} s^{-1} and 0.18 cm^{-3} s^{-1}, respectively with values spanning more than two orders of magnitude (0.017 - 2.737 cm^{-3} s^{-1}). The range of 3 nm particle formation rates is much wider than the range of five stationary NPF&G events, and we show several events with formation rates exceeding 1 $cm^{-3}s^{-1}$ that are not captured from the stationary perspective. There is no significant difference in the mean and median formation rates of 3 nm particles between the stationary and Lagrangian perspectives, but the latter perspective provides more robust statistics, especially of the extremes.

For the five stationary NPF&G events captured by the model, mean and median particle growth rates differ by ~0.5 nm hr^{-1} between the stationary and the "most NPF&G looking" Lagrangian trajectory (Figure 2.6b). The mean and median growth rates for the five NPF&G events captured by the model from the stationary perspective are 3.04 nm hr^{-1} and 3.16 nm hr^{-1}, respectively. However, when looking along the Lagrangian trajectories, the mean and median growth rates are 2.43 nm hr^{-1} and 2.57 nm hr^{-1}, respectively. These changes in the particle growth rates are consistent with the findings from Hakala et al., (2023) who found similar growth rate differences downwind of strong emission sources; however, with only 5 days in our study, this change is not significant. The black lines between the red and blue violin plots on Figure 2.6b connect the same NPF&G events. Four of the five NPF&G events have a decrease in growth rate when looking along the Lagrangian perspective and one event shows no change. Finally, for the

44 Lagrangian NPF&G events, the mean growth rate (2.49 nm hr^{-1}, Figure 2.6b green violin plot) is similar to the mean of the five NPF&G events mentioned earlier, but the median growth rate is lower at 2.07 nm hr^{-1}. Overall, there is no significant difference in the mean or median growth rates; however, our analysis of the Lagrangian perspectives provides more robust statistics (e.g., better sampling of fast- and slow-growth events) and a more comprehensive view of growth rate extremes.

Our final point of comparison between the stationary and Lagrangian perspectives is the survival probability (SP) of 3 nm particles to 25 nm. As with the growth and 3 nm particle formation rates, we do not see substantial differences between the two perspectives (Figure 2.6c) for the 5 NPF&G events, but there are differences looking at all 44 Lagrangian NPF&G events. The mean and median SP are both just below 0.4 for the five NPF&G events (Figure 2.6c, red violin plot), and the mean and median SP for the five corresponding Lagrangian trajectories are 0.3 and 0.41, respectively (Figure 2.6c, blue violin plot). Two NPF&G events show increases in SP and two events show decreases in SP when looking from the Lagrangian perspective (one event is unchanged). Finally, the green violin plot shows the SP for all 44 Lagrangian NPF&G events. As with the nucleation and growth rates, there are no significant differences between the mean values; however, the SP values derived from the Lagrangian perspective span a wider range and are potentially more statistically representative.

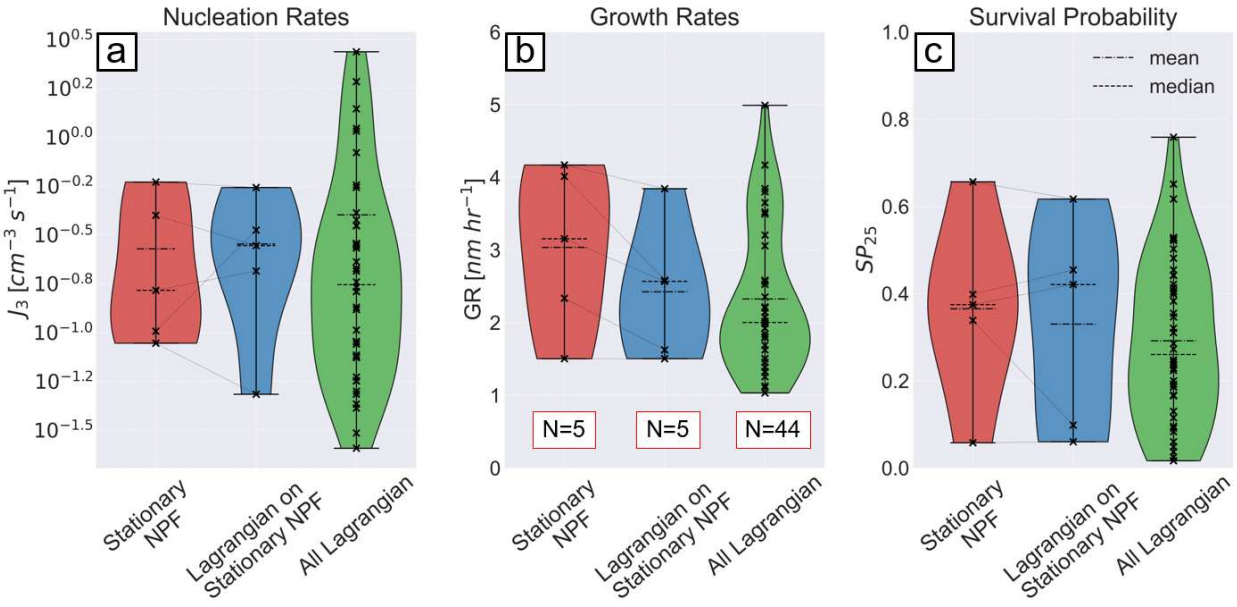

Figure 2.6. (a) Violin plots of the model 3 nm particle formation rates [cm^{-3} s^{-1}]. Color-coded as follows: Red: for the five NPF&G events that the model produces at the stationary SGP site. Blue: for the same five NPF&G events but along the most NPF&G looking Lagrangian trajectories; and Green: for all 44 Lagrangian NPF events. The black lines connecting the points on the red and blue violin plots connect the same NPF&G events. (b) Violin plots of model particle growth rates [nm hr^{-1}] with the same color-code as 3a). (c) Violin plots of the survival probability of 3 nm particles to 25 nm following the same color-code as 3a).

2.4. Discussion

In this work, we have presented a novel approach to interpreting stationary observations of aerosol size distributions based on the analysis of successive Lagrangian trajectories within a 3D model. This framework can serve as a means of better understanding and improving our mechanistic understanding of NPF&G in the atmosphere by allowing for a more complete understanding of the spatiotemporal evolution of aerosol particles in the atmosphere and their influence on stationary observation sites. This analysis was performed for the SGP observatory in northern Oklahoma, which is a regional background site. A similar analysis of other sites

influenced by spatially and temporally varying emissions of aerosols and vapors is likely to lead to different conclusions than those found in this manuscript.

The 3D model used in this work can reasonably represent NPF&G events, undefined/class II days (in terms of NPF or not), non-NPF days, and biomass burning influences, relative to previous studies (Westervelt et al., 2013), at the SGP observatory. Considering the Lagrangian trajectories for all simulated days, we see a substantial reduction in the number of undefined/class II days (relative to the Eulerian perspective) because these events become either NPF or non-NPF days. The days with an undefined/class II-to-NPF transition (Eulerian versus Lagrangian) can be explained by regionally inhomogeneous NPF&G. These days, the Lagrangian trajectories show typical banana-like NPF&G events. Finally, we analyzed and compared particle growth rates, formation rates of 3 nm particles and SP of 3 nm particles to 25 nm between the five stationary NPF&G events with the Lagrangian perspectives. We found differences (some increases and some decreases) between the perspectives for the same events but negligible differences in the mean values. Finally, in our analysis, the mean and median 3 nm particle formation rates, growth rates, and survival probability of 3 nm particles to 25 nm for all 44 Lagrangian NPF&G events were negligibly different from the mean and median values for the five stationary NPF&G events. However, based on the sample size of our analysis, we cannot robustly discard potentially significant differences between the stationary and Lagrangian perspectives. Regardless, the 44 events provide more robust statistics and a better understanding of extreme values than with only 5 events.

Our findings suggest that the majority of undefined/class II days can be explained and analyzed from the Lagrangian perspective at the SGP site. However, there are several real and potential limitations that prevent closure on this problem. The first limitation stems from the

horizontal resolution of the GC-TOMAS model (0.25x0.3125° or ~27.5x27.7 km at the latitudes near SGP). This scale cannot resolve many small sources (e.g., nearby prescribed/agricultural burning) of particles and aerosol precursors that could potentially influence the SGP site (and the trajectories). Any future analysis following a similar framework as the one presented in this work should carefully consider the horizontal resolution of the model, especially if investigating aerosol processes in a region where sources of aerosols and vapors are spatially inhomogeneous. Our simulation will also suffer from numerical diffusion, though reduced due their relatively fine resolution (Eastham and Jacob, 2017). A second limitation stems from our assumptions about and scaling of the nucleation mechanisms. While scaling the nucleation rates has been employed in previous studies, it limits our understanding of the mechanisms driving NPF&G in the atmosphere and may yield better agreement with the observations for the wrong reasons. While the nucleation mechanisms used in this work are consistent with current state-of-the-science, they are a source of uncertainty, and future work will benefit from the inclusion of more nucleation mechanisms in GC-TOMAS. A further limitation of this work is the use of the simple SOA scheme (Pai et al., 2020). Currently, the complex SOA scheme in GEOS-Chem is not compatible with TOMAS, but such coupling could be future work. An SOA scheme that considers the volatility of the condensing material will potentially capture peculiar NPF&G behavior (e.g. evaporation) that the current simple SOA scheme misses. Additionally, accurate predictions of low-volatility (e.g. $C^* < 1$ μg m^{-3}) SOA will help constrain the NPF&G process in the atmosphere.

Along with the limitations in how GC-TOMAS represent aerosol processes, limitations also arise from our event categorization method when applied within the model's grid. To explore this issue, for our three case studies, we ran ensemble (27) trajectories in order to test the sensitivity of our results to the trajectory path. However, running ensemble trajectories every three hours for

all 174 simulated days exceeded our computational resources. We recognize that the bulk of our analysis hinges on the HYSPLIT trajectories, however, we consider that the number of days and trajectories considered here provide reasonable confidence in the mean. Future investments in software to streamline the trajectory generation and analysis will greatly improve the utility and robustness of the methodology that we have developed here.

This work presents a framework for interpreting NPF&G events through the analysis of Lagrangian trajectories within a 3D model. Considering the Lagrangian perspective is important as potentially any measurement taken at a stationary site could be influenced by horizontal and vertical mixing and advection; therefore, careful consideration of the potential influences on stationary measurements should be taken. This is especially important for measurements from which process rates are derived, and considering the Lagrangian perspective using a model may be helpful in this regard. There are many potential future applications of this framework to aerosol, chemistry, and aerosol-cloud interaction problems. Interpreting stationary observations of atmospheric phenomena can be difficult, and analyzing the Lagrangian perspective provides a unique lens into understanding NPF&G upwind and downwind of a given stationary site. The Lagrangian perspective allows for discerning the role of chemical and microphysical processes compared to advection and mixing processes along the trajectory. Future work should include continued analysis of NPF&G events in different environments, and it can be extended to investigate chemical processes such as ozone formation in the outflow of urban centers. Additionally, with potential improvements to workflow, future work can utilize tools such as nanoparticle ranking analysis (Aliaga et al., 2023) to compare large numbers of days from the stationary and Lagrangian perspectives. Our analysis framework could also help reach better

closure for air quality studies looking at source-receptor regions, and it could help to constrain how representative stationary observational sites are.

REFERENCES

Adams PJ, Seinfeld JH (2002) Predicting global aerosol size distributions in general circulation models. Journal of Geophysical Research: Atmospheres 107:AAC 4-1-AAC 4-23. https://doi.org/10.1029/2001JD001010

Aktypis A, Kaltsonoudis C, Skyllakou K, et al (2023) Infrequent new particle formation in a coastal Mediterranean city during the summer. Atmospheric Environment 302:119732. https://doi.org/10.1016/j.atmosenv.2023.119732

Albrecht BA, Bretherton CS, Johnson D, et al (1995) The Atlantic Stratocumulus Transition Experiment—ASTEX

Albrecht BA (1989) Aerosols, Cloud Microphysics, and Fractional Cloudiness. Science 245:1227–1230. https://doi.org/10.1126/science.245.4923.1227

Aliaga D, Tuovinen S, Zhang T, et al (2023) Nanoparticle ranking analysis: determining new particle formation (NPF) event occurrence and intensity based on the concentration spectrum of formed (sub-5 nm) particles. Aerosol Research 1:81–92. https://doi.org/10.5194/ar-1-81-2023

Alvarado MJ, Prinn RG (2009) Formation of ozone and growth of aerosols in young smoke plumes from biomass burning: 1. Lagrangian parcel studies. Journal of Geophysical Research: Atmospheres 114:. https://doi.org/10.1029/2008JD011144

Baccarini A, Karlsson L, Dommen J, et al (2020) Frequent new particle formation over the high Arctic pack ice by enhanced iodine emissions. Nat Commun 11:4924. https://doi.org/10.1038/s41467-020-18551-0

Ball SM, Hanson DR, Eisele FL, McMurry PH (1999) Laboratory studies of particle nucleation: Initial results for H2SO4, H2O, and NH3 vapors. Journal of Geophysical Research: Atmospheres 104:23709–23718. https://doi.org/10.1029/1999JD900411

Bergamaschi P, Segers A, Brunner D, et al (2022) High-resolution inverse modelling of European CH_4 emissions using the novel FLEXPART-COSMO TM5 4DVAR inverse modelling system. Atmospheric Chemistry and Physics 22:13243–13268. https://doi.org/10.5194/acp-22-13243-2022

Bianchi F, Kurtén T, Riva M, et al (2019) Highly Oxygenated Organic Molecules (HOM) from Gas-Phase Autoxidation Involving Peroxy Radicals: A Key Contributor to Atmospheric Aerosol. Chem Rev 119:3472–3509. https://doi.org/10.1021/acs.chemrev.8b00395

Borbon A, Gilman JB, Kuster WC, et al (2013) Emission ratios of anthropogenic volatile organic compounds in northern mid-latitude megacities: Observations versus emission inventories in Los Angeles and Paris. Journal of Geophysical Research: Atmospheres 118:2041–2057. https://doi.org/10.1002/jgrd.50059

Buenrostro Mazon S, Riipinen I, Schultz DM, et al (2009) Classifying previously undefined days from eleven years of aerosol-particle-size distribution data from the SMEAR II station, Hyytiälä, Finland. Atmospheric Chemistry and Physics 9:667–676. https://doi.org/10.5194/acp-9-667-2009

Bulatovic I, Igel AL, Leck C, et al (2021) The importance of Aitken mode aerosol particles for cloud sustenance in the summertime high Arctic – a simulation study supported by observational data. Atmospheric Chemistry and Physics 21:3871–3897. https://doi.org/10.5194/acp-21-3871-2021

Carnerero C, Pérez N, Reche C, et al (2018) Vertical and horizontal distribution of regional new particle formation events in Madrid. Atmospheric Chemistry and Physics 18:16601–16618. https://doi.org/10.5194/acp-18-16601-2018

Charlson RJ, Schwartz SE, Hales JM, et al (1992) Climate Forcing by Anthropogenic Aerosols. Science 255:423–430. https://doi.org/10.1126/science.255.5043.423

Che K, Cai Z, Liu Y, et al (2022) Lagrangian inversion of anthropogenic CO2 emissions from Beijing using differential column measurements. Environ Res Lett 17:075001. https://doi.org/10.1088/1748-9326/ac7477

Chen H, Hodshire AL, Ortega J, et al (2018) Vertically resolved concentration and liquid water content of atmospheric nanoparticles at the US DOE Southern Great Plains site. Atmospheric Chemistry and Physics 18:311–326. https://doi.org/10.5194/acp-18-311-2018

Christensen MW, Ma P-L, Wu P, et al (2023) Evaluation of aerosol–cloud interactions in E3SM using a Lagrangian framework. Atmospheric Chemistry and Physics 23:2789–2812. https://doi.org/10.5194/acp-23-2789-2023

Clement AC, Burgman R, Norris JR (2009) Observational and Model Evidence for Positive Low-Level Cloud Feedback. Science 325:460–464. https://doi.org/10.1126/science.1171255

Collins DB, Burkart J, Chang RY-W, et al (2017) Frequent ultrafine particle formation and growth in Canadian Arctic marine and coastal environments. Atmospheric Chemistry and Physics 17:13119–13138. https://doi.org/10.5194/acp-17-13119-2017

Croft B, Wentworth GR, Martin RV, et al (2016) Contribution of Arctic seabird-colony ammonia to atmospheric particles and cloud-albedo radiative effect. Nat Commun 7:13444. https://doi.org/10.1038/ncomms13444

Dal Maso M, Kulmala M, Riipinen I, Wagner R (2005) Formation and growth of fresh atmospheric aerosols: Eight years of aerosol size distribution data from SMEAR II, Hyytiälä, Finland. Boreal Environment Research 10:323–336

Deng C, Fu Y, Dada L, et al (2020) Seasonal Characteristics of New Particle Formation and Growth in Urban Beijing. Environ Sci Technol 54:8547–8557. https://doi.org/10.1021/acs.est.0c00808

Derwent RG, Collins WJ, Jenkin ME, et al (2003) The Global Distribution of Secondary Particulate Matter in a 3-D Lagrangian Chemistry Transport Model. Journal of Atmospheric Chemistry 44:57–95. https://doi.org/10.1023/A:1022139814102

Draxler RR (2003) Evaluation of an Ensemble Dispersion Calculation, Bulletin of the American Meteorological Society, https://doi.org/10.1175/1520-0450(2003)042<0308:EOAEDC>2.0.CO;2

Dunne EM, Gordon H, Kurten A, et al (2016) Global atmospheric particle formation from CERN CLOUD measurements. Science 354:1119–1124. https://doi.org/10.1126/science.aaf2649

D'Andrea SD, Häkkinen S a. K, Westervelt DM, et al (2013) Understanding global secondary organic aerosol amount and size-resolved condensational behavior. Atmospheric Chemistry and Physics 13:11519–11534. https://doi.org/10.5194/acp-13-11519-2013

Eastham SD, Jacob DJ (2017) Limits on the ability of global Eulerian models to resolve intercontinental transport of chemical plumes. Atmospheric Chemistry and Physics 17:2543–2553. https://doi.org/10.5194/acp-17-2543-2017

Emmerson KM, MacKenzie AR, Owen SM, et al (2004) A Lagrangian model with simple primary and secondary aerosol scheme 1: comparison with UK PM_{10} data. Atmospheric Chemistry and Physics 4:2161–2170. https://doi.org/10.5194/acp-4-2161-2004

Fairlie TD, Szykman J, Gilliland A, et al (2009) Lagrangian sampling of 3-D air quality model results for regional transport contributions to sulfate aerosol concentrations at Baltimore, MD, in summer 2004. Atmospheric Environment 43:3275–3288. https://doi.org/10.1016/j.atmosenv.2009.02.026

Fan J, Rosenfeld D, Zhang Y, et al (2018) Substantial convection and precipitation enhancements by ultrafine aerosol particles. Science 359:411–418. https://doi.org/10.1126/science.aan8461

Fast JD, Bell DM, Kulkarni G, et al (2022) Using aircraft measurements to characterize subgrid-scale variability of aerosol properties near the Atmospheric Radiation Measurement Southern Great Plains site. Atmospheric Chemistry and Physics 22:11217–11238. https://doi.org/10.5194/acp-22-11217-2022

Fast JD, Berg LK, Alexander L, et al (2019) Overview of the HI-SCALE Field Campaign: A New Perspective on Shallow Convective Clouds. Bulletin of the American Meteorological Society 100:821–840. https://doi.org/10.1175/BAMS-D-18-0030.1

Forster, PT, Storelvmo K, Armour W, et al (2021) The Earth's Energy Budget, Climate Feedbacks, and Climate Sensitivity. In Climate Change 2021: The Physical Science Basis. Contribution of Working Group I to the Sixth Assessment Report of the

Intergovernmental Panel on Climate Change. Cambridge University Press, Cambridge, pp. 923–1054, doi: 10.1017/9781009157896.009.

Gordon H, Kirkby J, Baltensperger U, et al (2017) Causes and importance of new particle formation in the present-day and preindustrial atmospheres. Journal of Geophysical Research: Atmospheres 122:8739–8760. https://doi.org/10.1002/2017JD026844

Gryspeerdt E, Stier P, Partridge DG (2014) Satellite observations of cloud regime development: the role of aerosol processes. Atmos Chem Phys 14:1141–1158. https://doi.org/10.5194/acp-14-1141-2014

Hakala S, Vakkari V, Lihavainen H, et al (2023) Explaining apparent particle shrinkage related to new particle formation events in western Saudi Arabia does not require evaporation. Atmospheric Chemistry and Physics 23:9287–9321. https://doi.org/10.5194/acp-23-9287-2023

He X-C, Simon M, Iyer S, et al (2023) Iodine oxoacids enhance nucleation of sulfuric acid particles in the atmosphere. Science 382:1308–1314. https://doi.org/10.1126/science.adh2526

Hodshire AL, Lawler MJ, Zhao J, et al (2016) Multiple new-particle growth pathways observed at the US DOE Southern Great Plains field site. Atmos Chem Phys 16:9321–9348. https://doi.org/10.5194/acp-16-9321-2016

Hoppel WA, Frick GM, Fitzgerald JW, Larson RE (1994) Marine boundary layer measurements of new particle formation and the effects nonprecipitating clouds have on aerosol size distribution. Journal of Geophysical Research: Atmospheres 99:14443–14459. https://doi.org/10.1029/94JD00797

Huebert BJ, Zhuang L, Howell S, et al (1996) Sulfate, nitrate, methanesulfonate, chloride, ammonium, and sodium measurements from ship, island, and aircraft during the Atlantic Stratocumulus Transition Experiment/Marine Aerosol Gas Exchange. Journal of Geophysical Research: Atmospheres 101:4413–4423. https://doi.org/10.1029/95JD02044

Hussein T, Martikainen J, Junninen H, et al (2008) Observation of regional new particle formation in the urban atmosphere. Tellus B 60:509–521. https://doi.org/10.1111/j.1600-0889.2008.00365.x

Jaeglé L, Quinn PK, Bates TS, et al (2011) Global distribution of sea salt aerosols: new constraints from in situ and remote sensing observations. Atmospheric Chemistry and Physics 11:3137–3157. https://doi.org/10.5194/acp-11-3137-2011

Juncosa Calahorrano JF, Lindaas J, O'Dell K, et al (2021) Daytime Oxidized Reactive Nitrogen Partitioning in Western U.S. Wildfire Smoke Plumes. Journal of Geophysical Research: Atmospheres 126:e2020JD033484. https://doi.org/10.1029/2020JD033484

June NA, Hodshire AL, Wiggins EB, et al (2022) Aerosol size distribution changes in FIREX-AQ biomass burning plumes: the impact of plume concentration on coagulation and OA condensation/evaporation. Atmospheric Chemistry and Physics 22:12803–12825. https://doi.org/10.5194/acp-22-12803-2022

Kerminen V-M, Chen X, Vakkari V, et al (2018) Atmospheric new particle formation and growth: review of field observations. Environ Res Lett 13:103003. https://doi.org/10.1088/1748-9326/aadf3c

Khan MAH, Cooke MC, Utembe SR, et al (2015) A study of global atmospheric budget and distribution of acetone using global atmospheric model STOCHEM-CRI. Atmospheric Environment 112:269–277. https://doi.org/10.1016/j.atmosenv.2015.04.056

Kim C-H, Lee H-J (2013) Numerical simulations of Asian dust events: A Lagrangian Dust Model and its applications. Asia-Pacific J Atmos Sci 49:571–586. https://doi.org/10.1007/s13143-013-0051-9

Kirkby J, Amorim A, Baltensperger U, et al (2023) Atmospheric new particle formation from the CERN CLOUD experiment. Nat Geosci 16:948–957. https://doi.org/10.1038/s41561-023-01305-0

Kleinman L, Sedlacek AJ (2016) Biomass Burning Observation Project (BBOP) Final Campaign Report

Kodros JK, Cucinotta R, Ridley DA, et al (2016a) The aerosol radiative effects of uncontrolled combustion of domestic waste. Atmospheric Chemistry and Physics 16:6771–6784. https://doi.org/10.5194/acp-16-6771-2016

Kodros JK, Pierce JR (2017) Important global and regional differences in aerosol cloud-albedo effect estimates between simulations with and without prognostic aerosol microphysics. Journal of Geophysical Research: Atmospheres 122:4003–4018. https://doi.org/10.1002/2016JD025886

Kuang C, McMurry PH, McCormick AV, Eisele FL (2008) Dependence of nucleation rates on sulfuric acid vapor concentration in diverse atmospheric locations. Journal of Geophysical Research: Atmospheres 113:. https://doi.org/10.1029/2007JD009253

Kuang, C., Singh, A., Howie, J., Salwen, C., & Hayes, C. Scanning mobility particle sizer (AOSSMPS), 2016-11-15 to 2025-07-03, Southern Great Plains (SGP), Lamont, OK

(Extended and Co-located with C1) (E13). Atmospheric Radiation Measurement (ARM) User Facility. https://doi.org/10.5439/1476898. [Collection].

Kuhn T, Damoah R, Bacak A, Sloan JJ (2010) Characterising aerosol transport into the Canadian High Arctic using aerosol mass spectrometry and Lagrangian modelling. Atmospheric Chemistry and Physics 10:10489–10502. https://doi.org/10.5194/acp-10-10489-2010

Kulmala M, Kontkanen J, Junninen H, et al (2013) Direct Observations of Atmospheric Aerosol Nucleation. Science 339:943–946. https://doi.org/10.1126/science.1227385

Lampilahti J, Leino K, Manninen A, et al (2020) Aerosol particle formation in the upper residual layer. Atmospheric Chemistry and Physics Discussions 1–24. https://doi.org/10.5194/acp-2020-923

Lampilahti J, Manninen HE, Nieminen T, et al (2021) Zeppelin-led study on the onset of new particle formation in the planetary boundary layer. Atmospheric Chemistry and Physics 21:12649–12663. https://doi.org/10.5194/acp-21-12649-2021

Lee H, Cho H, Yoon YJ, et al (2024) Comparison of new particle formation events in urban, agricultural, and arctic environments. Atmospheric Environment 333:120634. https://doi.org/10.1016/j.atmosenv.2024.120634

Lee S-H, Gordon H, Yu H, et al (2019) New Particle Formation in the Atmosphere: From Molecular Clusters to Global Climate. Journal of Geophysical Research: Atmospheres 124:7098–7146. https://doi.org/10.1029/2018JD029356

Lee YH, Adams PJ (2012) A Fast and Efficient Version of the TwO-Moment Aerosol Sectional (TOMAS) Global Aerosol Microphysics Model. Aerosol Science and Technology 46:678–689. https://doi.org/10.1080/02786826.2011.643259

Lehtipalo K, Yan C, Dada L, et al (2018) Multicomponent new particle formation from sulfuric acid, ammonia, and biogenic vapors. Science Advances 4:eaau5363. https://doi.org/10.1126/sciadv.aau5363

Leino K, Lampilahti J, Poutanen P, et al (2019) Vertical profiles of sub-3 nm particles over the boreal forest. Atmospheric Chemistry and Physics 19:4127–4138. https://doi.org/10.5194/acp-19-4127-2019

Liu J, Alexander L, Fast JD, et al (2021) Aerosol characteristics at the Southern Great Plains site during the HI-SCALE campaign. Atmospheric Chemistry and Physics 21:5101–5116. https://doi.org/10.5194/acp-21-5101-2021

Murphy BN, Donahue NM, Fountoukis C, et al (2012) Functionalization and fragmentation during ambient organic aerosol aging: application of the 2-D volatility basis set to field studies. Atmospheric Chemistry and Physics 12:10797–10816. https://doi.org/10.5194/acp-12-10797-2012

Murphy BN, Donahue NM, Fountoukis C, Pandis SN (2011) Simulating the oxygen content of ambient organic aerosol with the 2D volatility basis set. Atmospheric Chemistry and Physics 11:7859–7873. https://doi.org/10.5194/acp-11-7859-2011

Myhre G, Samset BH, Schulz M, et al (2013) Radiative forcing of the direct aerosol effect from AeroCom Phase II simulations. Atmospheric Chemistry and Physics 13:1853–1877. https://doi.org/10.5194/acp-13-1853-2013

Napari I, Noppel M, Vehkamäki H, Kulmala M (2002) Parametrization of ternary nucleation rates for H2SO4-NH3-H2O vapors. Journal of Geophysical Research: Atmospheres 107:AAC 6-1-AAC 6-6. https://doi.org/10.1029/2002JD002132

Ng NL, Herndon SC, Trimborn A, et al (2011) An Aerosol Chemical Speciation Monitor (ACSM) for Routine Monitoring of the Composition and Mass Concentrations of Ambient Aerosol. Aerosol Science and Technology 45:780–794. https://doi.org/10.1080/02786826.2011.560211

Nieminen T, Kerminen V-M, Petäjä T, et al (2018) Global analysis of continental boundary layer new particle formation based on long-term measurements. Atmospheric Chemistry and Physics 18:14737–14756. https://doi.org/10.5194/acp-18-14737-2018

O'Donnell SE, Akherati A, He Y, et al (2023) Look Up: Probing the Vertical Profile of New Particle Formation and Growth in the Planetary Boundary Layer With Models and Observations. Journal of Geophysical Research: Atmospheres 128:e2022JD037525. https://doi.org/10.1029/2022JD037525

O'Donnell, S. (2025). Data to reproduce main text figures for "Going Off Grid: A Comparative Study of the Lagrangian and Eulerian Perspectives of New Particle Formation Events". Zenodo. https://doi.org/10.5281/zenodo.15832035. [Dataset; Software].

O'Dowd CD, Geever M, Hill MK, et al (1998) New particle formation: Nucleation rates and spatial scales in the clean marine coastal environment. Geophysical Research Letters 25:1661–1664. https://doi.org/10.1029/98GL01005

Pai SJ, Heald CL, Pierce JR, et al (2020) An evaluation of global organic aerosol schemes using airborne observations. Atmospheric Chemistry and Physics 20:2637–2665. https://doi.org/10.5194/acp-20-2637-2020

Pan X, Ichoku C, Chin M, et al (2020) Six global biomass burning emission datasets: intercomparison and application in one global aerosol model. Atmospheric Chemistry and Physics 20:969–994. https://doi.org/10.5194/acp-20-969-2020

Parworth C, Fast J, Mei F, et al (2015) Long-term measurements of submicrometer aerosol chemistry at the Southern Great Plains (SGP) using an Aerosol Chemical Speciation Monitor (ACSM). Atmospheric Environment 106:43–55. https://doi.org/10.1016/j.atmosenv.2015.01.060

Pierce JR, Adams PJ (2007) Efficiency of cloud condensation nuclei formation from ultrafine particles. Atmospheric Chemistry and Physics 7:1367–1379. https://doi.org/10.5194/acp-7-1367-2007

Pierce JR, Adams PJ (2009a) A Computationally Efficient Aerosol Nucleation/ Condensation Method: Pseudo-Steady-State Sulfuric Acid. Aerosol Science and Technology 43:216–226. https://doi.org/10.1080/02786820802587896

Pierce JR, Adams PJ (2009b) Uncertainty in global CCN concentrations from uncertain aerosol nucleation and primary emission rates. Atmospheric Chemistry and Physics 9:1339–1356. https://doi.org/10.5194/acp-9-1339-2009

Pierce JR, Westervelt DM, Atwood SA, et al (2014) New-particle formation, growth and climate-relevant particle production in Egbert, Canada: analysis from 1 year of size-distribution observations. Atmospheric Chemistry and Physics 14:8647–8663. https://doi.org/10.5194/acp-14-8647-2014

Platis A, Altstädter B, Wehner B, et al (2016) An Observational Case Study on the Influence of Atmospheric Boundary-Layer Dynamics on New Particle Formation. Boundary-Layer Meteorol 158:67–92. https://doi.org/10.1007/s10546-015-0084-y

Qian S, Sakurai H, McMurry PH (2007) Characteristics of regional nucleation events in urban East St. Louis. Atmospheric Environment 41:4119–4127. https://doi.org/10.1016/j.atmosenv.2007.01.011

Raes F, Bates T, McGovern F, Van Liedekerke M (2000) The 2nd Aerosol Characterization Experiment (ACE-2): general overview and main results. Tellus B: Chemical and Physical Meteorology 52:111–125. https://doi.org/10.3402/tellusb.v52i2.16088

Riccobono F, Schobesberger S, Scott CE, et al (2014) Oxidation Products of Biogenic Emissions Contribute to Nucleation of Atmospheric Particles. Science 344:717–721. https://doi.org/10.1126/science.1243527

Rolph G, Stein A, Stunder B (2017) Real-time Environmental Applications and Display sYstem: READY. Environmental Modelling & Software 95:210–228. https://doi.org/10.1016/j.envsoft.2017.06.025

Rosenfeld D, Andreae MO, Asmi A, et al (2014) Global observations of aerosol-cloud-precipitation-climate interactions. Reviews of Geophysics 52:750–808. https://doi.org/10.1002/2013RG000441

Sablan O, Ford B, Gargulinski E, et al (2024) Quantifying Prescribed-Fire Smoke Exposure Using Low-Cost Sensors and Satellites: Springtime Burning in Eastern Kansas. GeoHealth 8:e2023GH000982. https://doi.org/10.1029/2023GH000982

Sebastian M, Kompalli SK, Kumar VA, et al (2022) Observations of particle number size distributions and new particle formation in six Indian locations. Atmospheric Chemistry and Physics 22:4491–4508. https://doi.org/10.5194/acp-22-4491-2022

Seinfeld JH, Pandis SN (2016) Atmospheric Chemistry and Physics: From air pollution to climate change (3rd ed.). John Wiley and Sons.

Sellitto P, di Sarra A, Corradini S, et al (2016) Synergistic use of Lagrangian dispersion and radiative transfer modelling with satellite and surface remote sensing measurements for the investigation of volcanic plumes: the Mount Etna eruption of 25–27 October 2013.

Atmospheric Chemistry and Physics 16:6841–6861. https://doi.org/10.5194/acp-16-6841-2016

Shen X, Sun J, Ma Q, et al (2022) Long-term trend of new particle formation events in the Yangtze River Delta, China and its influencing factors: 7-year dataset analysis. Science of The Total Environment 807:150783. https://doi.org/10.1016/j.scitotenv.2021.150783

Shiraiwa M, Pöschl U (2021) Mass accommodation and gas–particle partitioning in secondary organic aerosols: dependence on diffusivity, volatility, particle-phase reactions, and penetration depth. Atmospheric Chemistry and Physics 21:1565–1580. https://doi.org/10.5194/acp-21-1565-2021

Shrivastava M, Zhang J, Zaveri RA, et al (2024) Anthropogenic Extremely Low Volatility Organics (ELVOCs) Govern the Growth of Molecular Clusters Over the Southern Great Plains During the Springtime. Journal of Geophysical Research: Atmospheres 129:e2024JD041212. https://doi.org/10.1029/2024JD041212

Stein AF, Draxler RR, Rolph GD, et al (2015) NOAA's HYSPLIT Atmospheric Transport and Dispersion Modeling System. https://doi.org/10.1175/BAMS-D-14-00110.1

Stevens B, Feingold G (2009) Untangling aerosol effects on clouds and precipitation in a buffered system. Nature 461:607–613. https://doi.org/10.1038/nature08281

Talvinen S, Kim P, Tovazzi E, et al (2025) Towards an improved understanding of the impact of clouds and precipitation on the representation of aerosols over the Boreal Forest in GCMs. https://doi.org/10.5194/egusphere-2025-721

Tatsii D, Bucci S, Bhowmick T, et al (2024) Shape Matters: Long-Range Transport of Microplastic Fibers in the Atmosphere. Environ Sci Technol 58:671–682. https://doi.org/10.1021/acs.est.3c08209

The International GEOS-Chem User Community. (2024). geoschem/GCClassic: GCClassic 14.3.0 (14.3.0). Zenodo. https://doi.org/10.5281/zenodo.10640536. [Software].

Trivitayanurak W, Adams PJ, Spracklen DV, Carslaw KS (2008) Tropospheric aerosol microphysics simulation with assimilated meteorology: model description and intermodel comparison. Atmospheric Chemistry and Physics 8:3149–3168. https://doi.org/10.5194/acp-8-3149-2008

Tunved P, Partridge DG, Korhonen H (2010) New trajectory-driven aerosol and chemical process model Chemical and Aerosol Lagrangian Model (CALM). Atmospheric Chemistry and Physics 10:10161–10185. https://doi.org/10.5194/acp-10-10161-2010

Twomey S (1974) Pollution and the planetary albedo. Atmospheric Environment (1967) 8:1251–1256. https://doi.org/10.1016/0004-6981(74)90004-3

Tzivion S, Feingold G, Levin Z (1987) An Efficient Numerical Solution to the Stochastic Collection Equation

Uin J, Aiken AC, Dubey MK, et al (2019) Atmospheric Radiation Measurement (ARM) Aerosol Observing Systems (AOS) for Surface-Based In Situ Atmospheric Aerosol and Trace Gas Measurements. Journal of Atmospheric and Oceanic Technology 36:2429–2447. https://doi.org/10.1175/JTECH-D-19-0077.1

Van Leuven S, De Meutter P, Camps J, et al (2023) An optimisation method to improve modelling of wet deposition in atmospheric transport models: applied to FLEXPART v10.4. Geoscientific Model Development 16:5323–5338. https://doi.org/10.5194/gmd-16-5323-2023

von Salzen K (2006) Piecewise log-normal approximation of size distributions for aerosol modelling. Atmospheric Chemistry and Physics 6:1351–1372. https://doi.org/10.5194/acp-6-1351-2006

Vehkamäki H, Kulmala M, Napari I, et al (2002) An improved parameterization for sulfuric acid–water nucleation rates for tropospheric and stratospheric conditions. Journal of Geophysical Research: Atmospheres 107:AAC 3-1-AAC 3-10. https://doi.org/10.1029/2002JD002184

Wang M, Kong W, Marten R, et al (2020) Rapid growth of new atmospheric particles by nitric acid and ammonia condensation. Nature 581:184–189. https://doi.org/10.1038/s41586-020-2270-4

Wehner B, Siebert H, Stratmann F, et al (2007) Horizontal homogeneity and vertical extent of new particle formation events. Tellus B: Chemical and Physical Meteorology 59:362–371. https://doi.org/10.1111/j.1600-0889.2007.00260.x

Weigel R, Mahnke C, Baumgartner M, et al (2021) In situ observation of new particle formation (NPF) in the tropical tropopause layer of the 2017 Asian monsoon anticyclone – Part 2: NPF inside ice clouds. Atmospheric Chemistry and Physics 21:13455–13481. https://doi.org/10.5194/acp-21-13455-2021

Westervelt DM, Pierce JR, Adams PJ (2014) Analysis of feedbacks between nucleation rate, survival probability and cloud condensation nuclei formation. Atmospheric Chemistry and Physics 14:5577–5597. https://doi.org/10.5194/acp-14-5577-2014

Westervelt DM, Pierce JR, Riipinen I, et al (2013) Formation and growth of nucleated particles into cloud condensation nuclei: model–measurement comparison. Atmospheric Chemistry and Physics 13:7645–7663. https://doi.org/10.5194/acp-13-7645-2013

Williamson CJ, Kupc A, Axisa D, et al (2019) A large source of cloud condensation nuclei from new particle formation in the tropics. Nature 574:399–403. https://doi.org/10.1038/s41586-019-1638-9

Xiao Q, Zhang J, Wang Y, et al (2023) New particle formation in the tropical free troposphere during CAMP^{2}Ex: statistics and impact of emission sources, convective activity, and synoptic conditions. Atmospheric Chemistry and Physics 23:9853–9871. https://doi.org/10.5194/acp-23-9853-2023

Yu F, Luo G, Nadykto AB, Herb J (2017) Impact of temperature dependence on the possible contribution of organics to new particle formation in the atmosphere. Atmospheric Chemistry and Physics 17:4997–5005. https://doi.org/10.5194/acp-17-4997-2017

Zaveri RA, Wang J, Fan J, et al (2022) Rapid growth of anthropogenic organic nanoparticles greatly alters cloud life cycle in the Amazon rainforest. Science Advances 8:eabj0329. https://doi.org/10.1126/sciadv.abj0329

Zender CS, Bian H, Newman D (2003) Mineral Dust Entrainment and Deposition (DEAD) model: Description and 1990s dust climatology. Journal of Geophysical Research: Atmospheres 108:. https://doi.org/10.1029/2002JD002775

Zhang R, Khalizov A, Wang L, et al (2012) Nucleation and Growth of Nanoparticles in the Atmosphere. Chem Rev 112:1957–2011. https://doi.org/10.1021/cr2001756

Zhao B, Donahue NM, Zhang K, et al (2024) Global variability in atmospheric new particle formation mechanisms. Nature 1–8. https://doi.org/10.1038/s41586-024-07547-1

CHAPTER 3

PROBING THE POTENTIAL DRIVERS OF NEW PARTICLE FORMATION AND GROWTH DURING TRACER IN HOUSTON, TX[2]

3.1. Introduction

The process of new particle formation and growth (NPF&G) is recognized as the dominant contributor to global aerosol number in the atmosphere (Fanourgakis et al., 2019; Kulmala & Kerminen, 2008; Westervelt et al., 2014; Williamson et al., 2019), and it contributes roughly half of global cloud condensation nuclei (CCN) concentrations at cloud level (Gordon et al., 2017). The abundance of CCN is important for climate due to the ability of CCN to alter cloud properties such as brightness, lifetime, and precipitation efficiency (Andreae & Rosenfeld, 2008; Petters & Kreidenweis, 2007; Albrecht, 1989; Clement et al., 2009; Gryspeerdt et al., 2014; Rosenfeld et al., 2014; B. Stevens & Feingold, 2009; Twomey, 1974). While NPF&G is important for aerosol concentrations globally, the relative contribution of NPF&G varies in different environments due to the abundance of precursor vapors and the concentrations of existing particles. NPF&G is principally driven by reactions of sulfuric acid with one or more species, including of ammonia (Dunne et al., 2016), amines (Johnson and Jen, 2023; Yu et al., 2012; Yu et al., 2025), low-volatility organics (Riccobono et al., 2014; Bianchi et al., 2019; Zhao et al., 2020; Williamson et al., 2019), and iodine oxoacids (Baccarini et al., 2020; He et al., 2023; Zhang et al., 2024), therefore the abundance of these vapors, in part, dictates the importance NPF&G. Additionally, high pre-existing particle surface area can inhibit NPF&G by scavenging small particles in addition to

[2]This chapter to be submitted as: "Probing the potential drivers of new particle formation and growth during TRACER in Houston, TX", Samuel E. O'Donnell, Xuanlin Du, Jeremy Wakeen, Abraham Dearden, Yicong He, Rebecca J. Sheesley, James N. Smith, Don R. Collins, Shantanu H. Jathar, Jeffrey R. Pierce.

competing with freshly nucleated particles for condensable vapors (Westervelt et al., 2014). Disentangling the processes that govern NPF&G in the ambient atmosphere is difficult given advection and mixing of particles and vapors, along with the feedbacks between precursor concentrations, nucleation rates, particle growth, and coagulation rates.

Urban environments exemplify the complexities of NPF&G due to generally having elevated emission rates of both NPF precursors and primary particles (Yang et al., 2021; Wu et al., 2011; Wiedensohler et al., 2009). Additionally, urban areas are often spatially inhomogeneous, meaning measurements of precursor vapors at a fixed site may not be representative of the environment in which particles measured at the same site formed. Understanding time series measurements at any stationary site is difficult given mixing and advection of air masses with different properties over time, likely confounding any interpretation of underlying processes and rates. NPF&G has been observed at many urban sites (Xiao et al., 2021; Hussein et al., 2008; Wu et al., 2021b; Li et al., 2023); however, deriving the driving mechanisms is difficult given the complications of vapor emissions, particle emissions, and spatial inhomogeneity.

To isolate processes that govern NPF&G, many studies have used batch laboratory chambers that replicate a simplified set of chemical species and processes in the real atmosphere (Kirkby et al., 2011; Chu et al., 2022; Dunne et al., 2016; Dada et al., 2020; Deng et al., 2020). While there is no strict definition of a batch chamber, here, we are referring to chambers where vapor and particle injections occur at the beginning of the experiment and are not replenished. Commonly, studies will investigate the nucleating ability of a vapor precursor when it is oxidized by the hydroxyl radical (OH), ozone, or NO_3 while controlling the environmental conditions such as temperature, radiation, and humidity. There are virtually infinite combinations of parameters that can be tested using batch chambers (e.g., vapor species, seed particles, oxidants, temperature,

humidity); however, applying findings from highly controlled environments to the ambient atmosphere can be difficult due to non-linear interactions between many species and processes as well as spatiotemporal variability. There are also many chamber sizes, shapes, and materials, all of which influence how the vapors and particles behave, further complicating comparisons between individual chambers and between chambers and the ambient environment. Notably, outdoor batch chambers may somewhat more closely replicate the ambient atmosphere as they often use sunlight to drive photochemistry and temperature and humidity in the chambers are similar to the ambient air (Sickles et al., 1979; Jeffries et al., 2013; Sirmollo et al. 2021). Outdoor chambers have been regularly used to investigate chemical and aerosol processes starting in the 1970s, often running multi-day experiments with a controlled set of chemical species (Sickles et al., 1979). However, outdoor chambers often have fewer constraints which can limit research findings for target processes of variables (Hidy, 2019). Additionally, outdoor chambers are often not accounting for changes in chemistry or vapor concentrations that are often seen in the ambient environment due to advection, mixing, and temporally varying emissions.

Recently, a unique continuous-flow outdoor chamber has been developed to isolate some NPF&G processes in the ambient environment (Sirmollo et al., 2021; Zhu et al., 2025). Similar to other outdoor chambers, the chamber replicates ambient atmospheric conditions, but ambient vapors can diffuse into the chamber while ambient particles are filtered out. This chamber setup allows for experiments that more closely match the vapors, temperature, and humidity in the ambient atmosphere. Additionally, since ambient particles are filtered out, the conditions under when the aerosol particles were formed in the chamber are known (as opposed to observations of recently formed particles in ambient urban environments). Outdoor chambers that utilize ambient gases allow for longer experiments relative to typical batch chambers due to the replenishing of

vapor concentrations in the chamber, but longer experiments can be subject to compounding ambiguities and uncertainties due to wall effects (Hidy, 2019; Sickles et al., 1979). However, these ambient, continuous-flow chambers provide an opportunity to gain insight into NPF&G processes in urban locations.

In this work, we endeavor to understand the potential drivers for three NPF&G events that occurred in the Captive Aerosol Growth and Evolution (CAGE) chamber in Houston, TX. We use a chemistry-aerosol model driven by observations to represent the CAGE chamber to investigate the various processes driving NPF&G events in the chamber. Specifically, we attempt to understand the unique chemistry and aerosol processes in the CAGE chamber, to reveal the important vapor precursors for NPF&G in the chamber, and understand how chamber artifacts affect our understanding of aerosol measurements in the chamber. Section 3.2 outlines the methods used in this work, including descriptions of the CAGE chamber and the model. Section 3.3 shows how well the model performs compared with observations. We evaluate the aerosol mass produced by the model during different events, pointing to several key vapor precursors. We then delve into details of different timescales within the chamber and how gas-aerosol partitioning is affected by some of these timescales. Finally, we test the sensitivity of NPF&G in our model to several processes and parameters, including chamber wall losses, temperature, and relative humidity. Section 3.4 discusses the main sources of uncertainty in this work, and Section 3.5 includes our conclusions and future outlook.

3.2. Methods

3.2.1 Captive Aerosol Growth and Evolution (CAGE) chamber

The Tracking Aerosol Convection Interactions Experiment (TRACER) Ultrafine Aerosol Formation and Impacts (UFI; together TRACER-UFI) campaign took place between July 1 and August 31, 2022 at the Atmospheric Radiation Measurement (ARM) Mobil Facility (AMF1) main site in La Porte, Texas. As part of TRACER-UFI, the University of California, Riverside (UCR) Captive Aerosol Growth and Evolution (CAGE) chamber was deployed. Details of the CAGE chamber can be found in Zhu et al., (2025) and Sirmollo et al., (2021), but we will provide an overview here.

The CAGE chamber is a ~2 m^3 cylindrical reactor primarily made of UV-transmitting perfluoroalkoxy (PFA; Saint-Gobain) film (Figure B1). The chamber rotates at approximately 3 rpm around an axle that is made of a cylindrical channel with a diameter of 18 cm wrapped with an expanded polytetrafluoroethylene membrane (ePTFE; Phillips Scientific). Ambient gases (see Section 3.2.1.2) diffuse through the ePTFE membrane between the main chamber volume and the cylindrical channel, hereafter referred to the *gas exchange channel*, at a rate of ~33.3 lpm. When no sample flow is drawn from the chamber, the gas lifetime is ~1.0 h in the reactor. The *gas exchange channel* is continuously flushed with ambient air at 75 lpm in an effort to keep gas concentrations in the chamber close to those in the ambient atmosphere. Ambient air passing through the *gas exchange channel* first passes through a Teflon filter where particles are filtered out. The chamber is maintained with a positive pressure of 1 mbar to prevent deformation and contamination from ambient air.

The PFA CAGE reactor is positioned inside a rectangular enclosure made of white powder coated stainless steel and UV-transmitting acrylic sheets. The UV sheets are sealed to the frame

using PTFE gasket tape (Inertech, UHF), and a variable speed blower (Ametek DFS, R304C) pulls air from inside the enclosure to create lower pressure around the CAGE reactor which helps to keep the PFA taught. The bottom of the rectangular enclosure is a sheet of UV- and visible light-reflective PTFE (Inertech, SQ-S) which reflects sunlight back up into the reactor, in part to compensate for light attenuation of the enclosure and CAGE reactor. Temperature inside the chamber was monitored using two thermistors, and an additional two thermistors were placed just outside the chamber as a reference for ambient temperature.

A monodisperse distribution of ammonium sulfate seed particles were continuously injected into the chamber, primarily during the nighttime hours throughout the campaign. Seed particles were produced using an atomizer (TSI, 3076), dried using a silica gel diffusion dryer, and size selected using a differential mobility analyzer (DMA) for a narrow particle size distribution with a mode ~30 nm. The flow rate of air with the injected particles is 3.0 lpm, however, the exact number or mass of particles per time was not tracked. While quantified injection rates, mostly at night, are not necessary for understanding NPF&G during the day, it provides a constraint on the modeled particle wall loss rates (Section 3.2.2.4).

The sample flow to instruments alternated every ~30 minutes between the CAGE chamber and the ambient environment by using a solenoid valve. The rate of flow to the instruments was 15.0 lpm, which increases the inward diffusion of gases in the *gas exchange channel* by 15.0 lpm, leading to a chamber lifetime of ~41 minutes for gases when sampling from the chamber. Additionally, the seed particles were injected with a flow rate of 3.0 lpm, increasing the diffusion rate out of the ePTFE membrane.

3.2.1.1 Aerosol Measurements

Aerosol size distribution measurements in the CAGE chamber and in the ambient atmosphere were taken using a scanning mobility particle sizer (SMPS). The sample flow to the SMPS was switched every ~30 minutes between the chamber and ambient. The sample aerosol was dried using a Nafion tube bundle (Perma Pure, PD-070-18T) and charge neutralized using a soft x-ray neutralizer (made in house at UC Riverside using a Hamamatsu L12535 source). The SMPS system was constructed in-house at UCR using a high flow DMA and a TSI 3762 condensation particle counter (CPC). The lower and upper dry diameter bounds for the SMPS system are 0.013 μm to 0.40 μm, respectively, and the total scan time across the diameter range was 90 s.

A thermal desorption chemical ionization mass spectrometer (TD-CIMS; Voisin et al., 2003; Smith et al., 2004) was used to measure the chemical composition of ultrafine particles during TRACER-UFI. The TD-CIMS was operated in "bulk collection mode" where pre-charged particles are collected on a high-voltage-biased Pt filament which is then heated to vaporize the collected particles. The vaporized particles are then measured using a chemical ionization high-resolution time-of-flight mass spectrometer (CI-HTOF; Aerodyne Research Inc. and Tofwerk AG) with O_2^- serving as the reagent ion. The collection efficiency of particles dramatically decreases with increasing particle size due to the decreased electrical mobility of larger particles; however, some larger particles will likely still influence the results. In this configuration, the TD-CIMS provides measurements of oxidized organic molecules, sulfur- and nitrogen-containing organics, inorganic sulfate, nitrate, and chloride. As a note, the CPC used as part of the TD-CIMS system had issues on August 4 and 5, therefore, we can only reliably use the TD-CIMS measurements for

our analysis of August 6. The TD-CIMS data shown in this dissertation are still somewhat preliminary, and finalized data are expected for publication.

3.2.1.2 Ambient VOC, SO_2 and ozone measurements

Concurrent with TRACER-UFI, the TRACER-MAP (Mapping Aerosol across Houston) campaign took place at several locations around the Houston metropolitan area. TRACER-MAP utilized a mobile facility to investigate gas and aerosol processes, and the mobile facility was stationed at the AMF1 main site from August 1 to August 8, 2022. The TRACER-MAP mobile facility was equipped with a quadrupole proton-transfer reaction mass spectrometer (PTR-MS Q300; Ionicon Analytik) which was used to measure several VOCs in the ambient atmosphere. The PTR-MS uses protonated water (H_3O^+) to ionize target VOCs through proton transfer. The ionized VOCs are then detected and quantified using the mass spectrometer. The sample flow was dried using a system similar to that in Jobson and McCoskey (2010) to reduce the effects of water vapor on the samples. Details of the PTR-MS calibration and operation can be found in Shrestha et al. (2022). In this study, we used benzene, toluene, styrene, xylene, trimethylbenzene, monoterpene, and isoprene measurements from the PTR-MS for our modeling work (Section 3.2.2). PTR-MS measurements at the AMF1 main site began late morning on August 1, 2022, and ended the morning of August 8, 2022. Data between August 2 at 16:15 CST and August 3 at 11:50 CST were largely missing, therefore we focus our analysis on the three NPF&G events occurring on August 4, 5, and 6.

Sulfur dioxide (SO_2) was measured using a Thermo Scientific (Model 43C-TLE) SO_2 analyzer. SO_2 molecules absorb ultraviolet radiation and then floresce in the 220-240 nm wavelength range. The single measurement detection limit of the instrument is 0.12 [ppbv] and the combined uncertainty is 3.7% (Guo et al., 2021).

Along with VOCs and SO_2, TRACER-MAP included measurements of ambient ozone using a modified Thermo Environmental, Inc. (Model 42C) ozone monitor. The ozone monitor relies on chemiluminescence with nitrogen monoxide to measure ozone. Ozone data were smoothed using a Savitzky-Golay filter with a smoothing window of ~1 h.

3.2.1.3 T, RH, and shortwave radiation

Ambient temperature and relative humidity were measured at the AMF1 main site using Vaisala HMP155 probes. The probes use a Pt100 resistive platinum sensor to measure temperature in the range of -80-60°C with a reported accuracy of ± (0.1 + 0.00167 |temperature|) °C. Relative humidity was measured using the Vaisala HUMICAP 180 capacitive thin film polymer sensor in the range of 0-100% with a reported accuracy of ± (1.0 + 0.008 x reading) % in the temperature range of -20-40°C. For this work, we assume that temperature and relative humidity in the CAGE chamber is the same as ambient, which is a reasonable assumption given previous work characterizing the CAGE and similar chambers (Zhu et al., 2025; Sirmollo et al., 2021).

Downwelling shortwave radiation (total hemispheric, 0.3 to 3.0 μm) was measured using a pyranometer (Precision Spectral Pyranometer, The Eppley Laboratory Inc.). Data reported by the pyranometer have a single measurement uncertainty of ±4% to -(4% + 20 Wm^{-2}) for zenith angles < 80°. Shortwave radiation is used for the hydroxyl radical proxy in the modeling work (Section 3.2.2.5).

3.2.2 Modeling

3.2.2.1 Model overview and representation of CAGE

In this study, we use a version of the Statistical Oxidation Model-TwO Moment Aerosol Sectional (SOM-TOMAS) chemistry and microphysics model to represent the CAGE chamber.

SOM-TOMAS is a 0D model that represents semi-explicit gas-phase oxidation chemistry, thermodynamics of SOA partitioning, and kinetic aerosol microphysics. SOM-TOMAS has been structured to best represent the CAGE chamber in terms of reactor volume, gas exchange, instrument flows, and wall effects. Previous work has used SOM-TOMAS to investigate SOA formation in indoor, batch laboratory chambers (Akherati et al., 2020; Garofalo et al., 2021; He et al., 2020, 2021, 2022), organic aerosol evolution in biomass burning plumes (Akherati et al., 2022), and the vertical profile of NPF&G (O'Donnell et al., 2023).

In SOM-TOMAS, the *gas exchange channel* is modeled using Euler's method, by which the VOC and SO_2 concentrations in the chamber are updated based on ambient concentrations and diffusion rate through the ePTFE membrane. The formulation goes as the following:

$$C_{t+1} = C_t + \left(\frac{C_{amb}(F_{m-in} + F_i) - C_t(F_{m-out} + F_i + F_{seed})}{V}\right)\Delta t \quad (1)$$

Where C_{t+1} is the VOC or SO_2 concentration in the chamber for the next time step, C_t is the concentration in the chamber at the current time step, C_{amb} is the ambient VOC (SO_2) concentration measured by the PTR-MS (SO_2 analyzer), F_i is the flow rate [lpm] to instruments (which also causes an net pull of air through the ePTFE membrane), F_{m-in} is the gross diffusional flow rate into the chamber via the ePTFE membrane, F_{m-out} is the gross diffusional flow rate out [lpm] of the membrane, F_{seed} is the flow rate for the injected particles which brings in an extra 3 lpm of air (only at night), dt is the model time step [s], and V is the chamber volume [l]. The flow rate into the chamber through the membrane is greater than the flow rate out when instruments are pulling. As a note, we can only perform this operation for the VOCs measured by the PTR-MS and used by the model (See next section). However, as will be discussed next, SOM-TOMAS

statistically represents many oxidation products of VOCs of which we lack ambient and chamber observations. Therefore, we made the assumption that only the VOCs measured by the PTR-MS diffuse through the membrane. This assumption implies that ambient concentrations of VOC oxidation products are the same as those in the chamber, and only the parent VOC concentrations are changing. We tested assuming ambient concentrations of the VOC oxidation products were zero (i.e., only diffusion out) which led to a significant and unrealistic reduction in aerosol mass (not shown).

3.2.2.2 SOM

The Statistical Oxidation Model (SOM) is set up as several two-dimensional carbon and oxygen grids that are used to track multigenerational oxidation, thermodynamics, and volatility of several VOC classes. For this work, five SOM grids are used that are representative of VOCs with the properties of or similar to benzene, toluene, xylenes, isoprene, and α-pinene. For each representative grid, SOM uses six pre-fitted parameters (Table S1) that dictate the movement of mass through and properties at each grid cell, and we chose to use the high-NO_X parameters outlined in Bilsback et al., (2023). The first parameter, ΔLVP, is the logarithmic change in equilibrium vapor concentration (C*) for the addition of an oxygen atom. The C* of the species in each grid cell is determined by $C^* = 10^{(-0.0337 \times MW\_hc + 11.56 - No \times \Delta LVP}$, where MW_hc is the molecular weight of the hydrocarbon backbone (accounting for only carbon and hydrogen atoms). The next four parameters, *P1*, *P2*, *P3*, and *P4*, dictate the molar yields of the functionalized reaction products from the addition of one, two, three, or four oxygen atoms to the existing molecule, respectively. Finally, mFRAG is a fitted exponent for the calculation of the probability of fragmentation (P_{frag}) for each reaction with OH, defined as $P_{frag} = (N_O:N_C)^{mFRAG}$. Each SOM grid cell emulates the average properties of organic species with the corresponding oxygen and

carbon numbers, and each SOM grid represents the average oxidation pathway of a given VOC class. Each SOM grid is empty at the beginning of each simulation, therefore, we initialize the model using available PTR-MS from August 3, and run the model for a whole day to "spin up" the SOM grids. Notably, OH chemistry virtually stops overnight, so initializing the model on August 3 is likely not necessary.

SOM is coupled with the SAPRC-11 chemical mechanism, which represents explicit reactions of the VOC species measured by the PTR-MS with the hydroxyl radical (OH) and ozone, and the subsequent reaction products enter the SOM grids. Additionally, SAPRC-11 includes reactions of OH with SO_2 to produce sulfuric acid, which is the principal driver of NPF. As mentioned, since NO_X concentrations in Houston are generally high (August 1 - 6 mean = ~5.2 ppb), we used the high NO_X SOM parameters that include a highly-oxygenated organic molecule (HOM) yield of 0.0 for all VOC species. Therefore, we are effectively ignoring HOM formation that could contribute to NPF&G in the chamber, and this is a potential limitation of this work.

3.2.2.3 TOMAS

TOMAS represents aerosol processes across 40 logarithmically spaced, mass-doubling size bins spanning the dry diameter range of 1.0 nm to 10 μm. TOMAS is a two-moment sectional model, meaning the total number of particles and the mass of sulfate, water, and organic species are tracked for each size section. The processes implemented in the model are reversible organic condensation, irreversible sulfuric acid condensation, coagulation, and nucleation. Condensation and evaporation of organic species in the SOM grids are size, volatility, and particle-phase diffusivity dependent (He et al., 2021). The relative humidity and O:C dependent particle-phase diffusivity is modeled following the diffusion-reaction framework outlined in Zaveri et al. (2014) and implemented in He et al. (2021). Sulfuric acid is assumed to condense irreversibly and the size

dependence of the condensation rate is therefore proportional to the Fuchs-corrected particle surface area. Particle coagulation is modeled between all size sections, and details of the coagulation and condensation routines can be found in Adams and Seinfeld (2002). The TOMAS bins are initialized using lognormal fits to the SMPS data at the beginning of each simulation, however, this is likely unnecessary given the length of model spinup and the chamber timescales.

TOMAS represents inorganic nucleation mechanisms from Dunne et al., (2016), which includes both neutral and ion-mediated, binary and ternary nucleation for a total of four mechanisms. An ion formation rate of 8.0 cm^{-3} s^{-1} was used for the ion-mediated mechanisms (Dunne et al., 2016). The nucleated particles are assumed to have a diameter of 1 nm and are composed entirely of sulfate. TOMAS does have the ability to represent organic nucleation (Riccobono et al., 2014), but, as mentioned in Section 3.2.2.2, we do not produce HOMs, which are necessary for organic nucleation. Only including four, of potentially many (Zhao et al., 2024), NPF mechanisms is a limitation of this work, therefore we do not attempt to differentiate nucleation mechanisms in this work. Additionally, we found the best model-measurement agreement by multiplying the total inorganic nucleation rate by 100.0, but we also tested scaling by 10.0 and 1000.0 (Figure B2). Scaling the inorganic nucleation rate from Dunne et al., (2016) has been done in previous work for better agreement with observations (O'Donnell et al., 2025). The implications of this scaling are discussed more in Section 3.4.2.

3.2.2.4 Wall losses

In order to best represent the CAGE chamber with SOM-TOMAS, we had to make several assumptions to derive the rate of particle loss to the chamber walls. As mentioned in Section 3.2.1, the exact injection rate of seed particles was not quantified, making constraining particle wall losses during those times difficult. Additionally, if particle wall loss rates were different during

peak NPF&G periods, fitting to the night time injections would be misleading. Unfortunately, deriving size-dependent wall loss rates is difficult during NPF&G events due to the confounding processes (e.g., condensation, coagulation, and nucleation) that make isolating particle loss processes uncertain. To best tackle this problem, we chose several NPF&G events throughout the campaign where the new particle mode stopped growing in the 60-100 nm diameter range. We then fit a first order exponential decay function of the following form $k = -\log_{10}(N_2/N_1)/(t_2-t_1)$ where N_1 and N_2 are the total number of particles at time t_1 and t_2. The k term is the first order loss rate for particles in the 60-100 nm diameter range, and we averaged the k values for the chosen NPF&G events to get k = 8.0e-5 [s^{-1}]. For size dependence, we used the functional form $k = A/D_p$, where A is a scalar [nm s^{-1}] and D_p is particle diameter, which assumes Brownian diffusion near the chamber walls limits the rate of particle wall losses (Crump and Seinfeld, 1981; Pierce et al., 2008; Trump et al., 2016). From the exponential decay fit, we can assume that k for 80 nm particles is 8.0e-5 [s^{-1}], therefore A = 1e-3 [nm s^{-1}]. To account for the kinetic limit of particle turbulent diffusion from the center of the chamber to near the walls, where Brownian diffusion dominates, we assume that particles below D_p = 3 nm have a constant loss rate. Figure B3 shows the size dependent loss rate coefficient (k), and Figure B4 shows the modeled aerosol size distributions from several sensitivity tests where A is scaled up and down by two.

The implementation of vapor wall losses in SOM-TOMAS is outlined in He et al. (2020) and Akherati et al. (2020), and is based on Zhang et al. (2014) and Krechmer et al. (2016). The first-order uptake of vapors to the chamber walls (k_{on}) is assumed to be the same as k for small particles, with the implicit assumption that Brownian diffusion limits wall uptake for gases and small particles. The release of vapors from the chamber walls follows absorptive partitioning theory where the chamber walls serve as the absorbing medium. The effective mass concentration

of the chamber walls (C_w) is varied based on the volatility of the modeled species with higher values being used for higher volatilities and vice versa (i.e., C_w = 10000 μg m^{-3} for $C^* > 10^4$ μg m^{-3}, $C_w = 16 \times (C^*)^{0.6}$ μg m^{-3} for $1 < C^* < 10^4$ μg m^{-3}, and C_w = 16 μg m^{-3} for $C^* < 1$ μg m^{-3}). The rate of release of vapors from the chamber walls is then:

$$k_{off} = \frac{C^*}{C_w} k_{on} \quad (2)$$

3.2.2.5 OH proxy

To estimate the concentration of the hydroxyl radical (OH), we used a combination of two OH proxies based on the intensity downwelling shortwave radiation (Figure B5). The first proxy is from Pietikäinen et al., (2014), which was derived for ambient OH concentrations in Finland. We found this proxy to generate lower OH concentrations, with peak values approaching 1×10^6 [molecules cm^{-3}] at 1000 [W m^{-2}] shortwave. The second proxy that we utilized was from Stevens et al., (2012), which was developed for investigating SOA production in power plant plumes. The Stevens et al. proxy has a NO_X dependence and has peak OH concentrations around 2×10^7 [molecules cm^{-3}] at 1000 [W m^{-2}] shortwave. We found using the Stevens et al. proxy led to a slower increase in OH in the morning hours, subsequently leading to later NPF&G in the model than observations. The details of how we combined the two OH proxies can be found in the Supplemental text, but, in short, we scaled the Pietikäinen et al. proxy up to have a similar peak OH concentration as the Stevens et al., proxy. This scaling led to faster morning increases in OH and better NPF event timing. Additionally, we scaled the night time OH to be the minimum value from the Stevens et al. proxy. Figure B6 shows modeled aerosol size distributions where OH is scaled down in order to test the model sensitivity.

3.2.2.6 Particle growth rates

For the three NPF&G events in the CAGE chamber, we calculated particle growth rates from the SMPS and modeled size distributions. Growth rates are derived using a similar method to that in Westervelt et al., (2013); however, we do not calculate particle formation rates or survival probabilities due to the uncertainties associated with wall losses. Particle growth rates are derived by applying a linear fit to the growing mode diameter in the 3-25 nm diameter range, and the slope of the fit is the particle growth rate [nm hr^{-1}].

3.3. Results

3.3.1 NPF&G in the CAGE and model

3.3.1.1 Characteristics of NPF&G in the CAGE chamber

NPF&G events were observed almost daily in the CAGE chamber during the campaign (Figure B7); however, we focus here on the events that occurred on August 4, 5, and 6 due to available observations. Figure 3.1 shows several time series of observed and modeled aerosol, chemical, and state variables, with Figure 3.1a showing the aerosol size distribution measured in the CAGE chamber. The atmospheric conditions on August 4 were typical of Houston in August, with temperatures reaching approximately 306 K and some fair-weather cumulus clouds intermittently reducing the afternoon sunlight (See OH profile based on shortwave radiation in Figure 3.1c). On August 4, a narrow mode of small particles appeared in the chamber just before 9:00 CST and grew to ~40 nm over ~6 hours. It is worth noting the atomizer for the injected particles experienced an issue the night before the August 4 NPF&G event, resulting in the seed particles having a larger mean diameter and a broader distribution. There is no apparent growth of

the injected particles overnight; however, they appear to grow in the early morning, concurrent with the likely start of the NPF&G event.

The NPF&G event on August 5 in the chamber was significantly weaker than those on August 4 and 6, likely due to the cloud cover observed at the AMF1 main site starting around 10:00 CST (Figure 3.1c). Freshly nucleated particles appeared around 08:30 CST and grew to ~20 nm by 10:00 CST, but further growth was inhibited, likely from reduced photochemical production of condensable species and losses to the chamber walls and instruments. The seed particles injected on the morning of August 5 also appeared to grow close to sunrise, indicating photochemically driven SOA or sulfate production. The peak temperature on August 5 was ~304 K, and relative humidity was mostly above 90%.

The NPF&G event on August 6 was the most intense, with the highest number concentration and fastest particle growth. The new nucleation mode appeared around 10:00 CST and grew to ~50 nm by 14:00 CST. This event followed a period of cloud cover where temperatures were low and relative humidity was high. The peak temperature on August 6 was around 304 K, and relative humidity was ~70% during the NPF&G event.

3.3.1.2 Model representation of NPF&G in the CAGE chamber

SOM-TOMAS generally captures both the intensity of and variability between the three NPF&G events in the CAGE chamber (Figure 3.1b). However, the model does miss certain features of specific events (e.g., overpredicting number concentration on August 5 and particle growth rate on August 4), likely as a result of missing measurements of key species (i.e., ammonia, amines, and some organics) and some model assumptions and structural limitations (see Section 3.3.4.2).

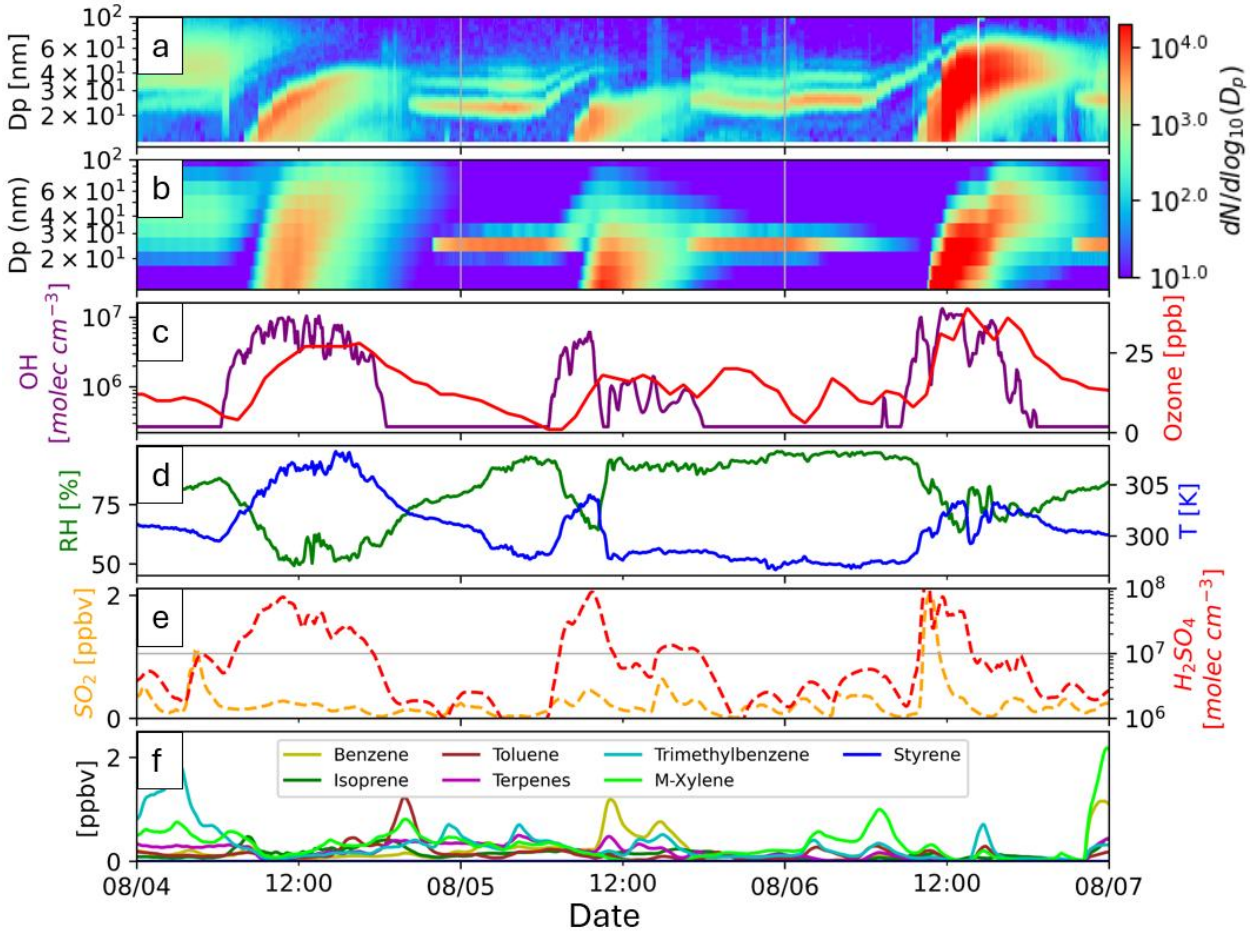

Figure 3.1. (a) Aerosol size distribution in CAGE measured by the SMPS. (b) Modeled aerosol size distribution from SOM-TOMAS. (c) Time series of OH and measured ozone multiplied by 0.9. (d) Time series of ambient temperature and relative humidity. (e) Time series of modeled sulfur dioxide and sulfuric acid. (f) Time series of VOC concentrations in the model.

On August 4, the model captures the timing of the NPF&G event, but the simulated aerosol mode is broader than the one observed in the chamber. Additionally, particles in the model grow to larger sizes than those in the chamber. This day exhibited more continuously higher OH concentrations relative to the other two days (Figure 3.1c), contributing to elevated sulfuric acid concentrations throughout the day (Figure 3.1e). The high OH concentrations have the potential to drive higher SOA production as well, potentially leading to the overprediction of particle growth.

Notably, VOC concentrations during the August 4 NPF&G event were not particularly elevated (Figure 3.1f) relative to the other events.

For the event on August 5, the model reasonably captures the event timing and growth, but the simulated nucleation is more intense and persists longer than the observations indicate. The initial nucleation appears to be driven by a morning spike in sulfuric acid (Figure 3.1e). Around 10:00 CST, OH and sulfuric acid decrease substantially, likely inhibiting continued NPF&G. However, the concentrations of some VOCs (principally benzene) are elevated around 11:00, which may contribute to continued growth of freshly nucleated particles in the model.

Finally, the August 6 event is well represented by the model in terms of event timing and the number concentration of the growing aerosol mode. However, the model simulates interrupted particle growth whereas the observations show more continuous growth. A small peak in trimethylbenzene around 15:00 CST is likely contributing to the variable growth pattern, as trimethylbenzene has the highest SOA yield of any of the VOCs used in this work (discussed in Section 3.3.2). The interrupted growth is also potentially due to the variability of OH and ozone (Figure 3.1c), which modulates SOA production over time.

3.3.2 Aerosol speciation

3.3.2.1 Contributions from different VOCs in the model

Figure 3.2a shows the total organic aerosol mass in each SOM grid and the total sulfate mass, and Figure 3.2b shows the fraction of aerosol mass in each of the same categories. Notably, during the night (gray shading in Figure 3.2b), the total aerosol mass is dominated by sulfate due to the seed injections (gold shading in Figure 3.2a). For the NPF&G events on August 4 and 5, the model indicates that the majority of SOA mass is derived from trimethylbenzene, toluene, and

styrene (Figure 3.2), all of which are modeled in the toluene SOM grid (Table S1). We tested simulating trimethylbenzene in the benzene SOM grid instead of the toluene grid which led to the benzene grid instead being the largest contributor to the SOA mass (not shown). Trimethylbenzene is a key contributor to SOA due to (1) its higher carbon number than other VOCs (e.g., toluene and styrene) leading to a higher SOA yield and (2) its generally higher ambient concentrations measured by the PTR-MS.

On August 6, the model shows sulfate as the dominant contributor to particle mass during the first several hours of the event. After 15:00 CST, however, SOA mass in the toluene SOM grid increases corresponding to an increase in particle growth (Figure 3.1b). As mentioned in Section 3.3.1.2, the sudden increase in particle growth is likely due to the afternoon spike in OH (Figure 3.1c) and the spike in trimethylbenzene concentrations. There is also a spike in afternoon ozone concentrations, but an increase in ozone would likely lead to a proportionally larger increase in SOA mass in the terpene SOM grid due to their faster ozone reaction rate coefficients.

Figure B8 shows classified subgroups (i.e., CHO, CHON, CHOS, CHONS) as measured by the TD-CIMS instrument separated by Double Bond Equivalence (DBE) above and below 4. A DBE of 4 or greater suggests that the compound contains an aromatic ring, while a DBE under 4 is typically indicative of aliphatic (straight-chained) compounds. Aromatic compounds are often linked to anthropogenic sources, including combustion and industrial processes (Calvert et al., 2002). Figure B8 shows that the aromatic fraction of each subgroup increased during the NPF&G event with the largest contribution occurring from 14:00-16:00 CDT, coinciding with the spike in TMB shown in Figure 3.1e. The aromatic fractions of CHON, CHOS, and CHONS subgroups were consistently above 50%, and CHO only reached over 50% once the TMB spike occurred, further suggesting anthropogenic aromatic influence during the event. In general, the high aromatic

fractions throughout are consistent with the large simulated contribution of aromatic compounds to SOA.

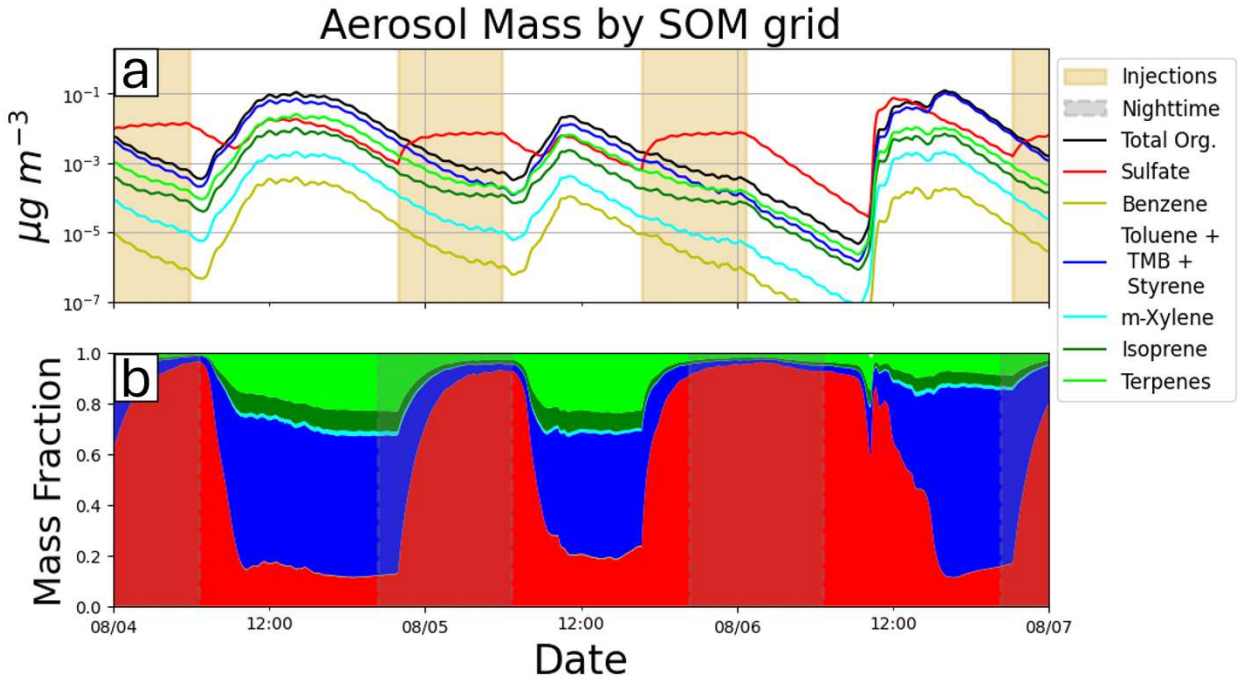

Figure 3.2. (a) Time series of modeled aerosol mass colored by SOM grid and sulfate mass. The light brown shading indicates the time of aerosol injections. (b) Time series of the fraction of aerosol mass from each SOM grid and sulfate. The light gray shading indicates the night time hours.

3.3.2.2 TD-CIMS comparison on August 6

Figure 3.3 [THIS FIGURE IS NOT THE FINAL VERSION AS WE ARE WAITING ON UPDATED TD-CIMS DATA] shows the aerosol size distributions from the SMPS and from the model, as well as a comparison between the elemental mass fractions of oxygen, carbon, and sulfur as measured by the TD-CIMS and the corresponding elemental fractions from the model on August 6. Again, the TD-CIMS data are preliminary and likely inaccurate, hence we are waiting on updated data. The model only represents sulfuric acid formation through the OH + SO_2 pathway, so the model could be missing the higher fraction of sulfur measured by the TD-CIMS later in the day on August 6 due to missing other formation pathways for sulfur-containing compounds. While

OH + SO_2 is the dominant reaction pathway for SO_2 in the gas phase (Stockwell and Calvert, 1983), other pathways such as reactions with criegee intermediates, reactions with organic peroxides, multiphase or heterogeneous chemistry in or on droplets and particles, and aqueous-phase oxidation (Ma et al., 2023) are also possible. The lack of representation of these mechanisms could lead to discrepancies between the model and TD-CIMS, and the uncertainties and implications in this work are presented in Section 3.4.

Presuming the TD-CIMS data are accurate, the mass fractions of carbon, oxygen, and sulfur remain relatively invariant throughout the NPF&G event on August 6 (Figure 3.3). The TD-CIMS indicates that approximately one-fifth, two-fifths, and two-fifths of the mass are sulfur, carbon, and oxygen, respectively. The model simulates a similar fraction of sulfur mass prior to the NPF&G event, with the remaining mass consisting mostly of oxygen. Later in the NPF&G event, the model shows the sulfur mass fraction has decreased substantially, and the remaining mass fraction is almost evenly split between oxygen and carbon. The increase in the mass fraction of carbon is expected given the contributions of VOC oxidation products to particle growth, however, this is inconsistent with the TD-CIMS results.

As stated, the discrepancies between the model and the TD-CIMS measurements is likely due to either uncertainties associated with the TD-CIMS measurements or the limited representation of chemistry in the model. Figure 3.3a shows the aerosol size distribution measured by the SMPS on August 6, where there are larger particles (> 200 nm) that appear mainly after 18:00 CDT which could influence the TD-CIMS measurements. While the number of these particles is lower (~10^2-10^3 [cm^{-3}]) than the mode associated with the NPF&G event (~$10^{3.5}$ [cm^{-3}]), the relative mass of each particle is significantly higher (~1000x), therefore, we cannot discount the potential influence of these particles even if the electrical mobility of the larger

particles is lower than the smaller particles. Additionally, the TD-CIMS measures sulfur-containing organics which the model does not simulate. Nevertheless, both the model and the observations highlight the importance of sulfur containing compounds early in the NPF&G event, as well as the importance of organic species for growing particles.

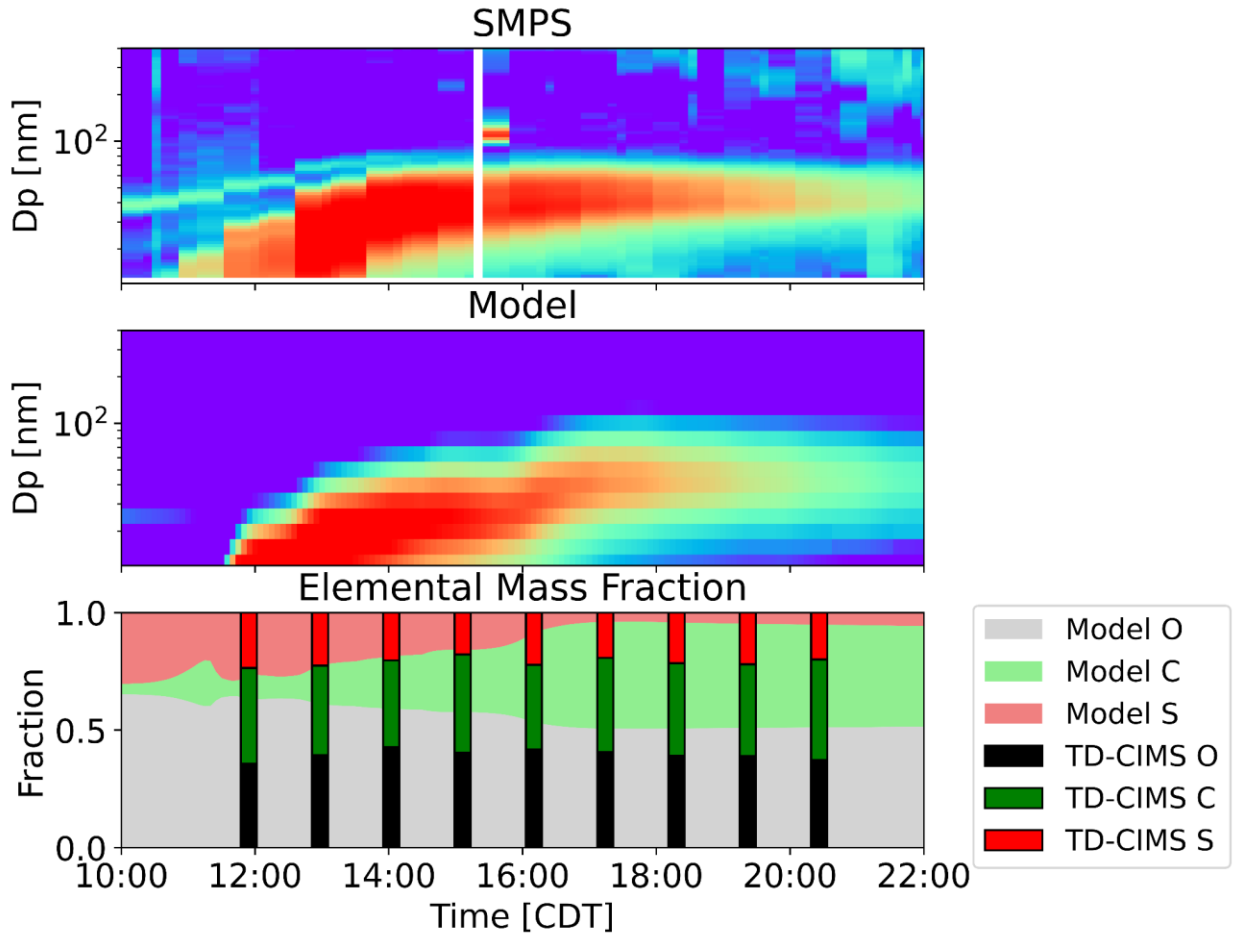

Figure 3.3. (a) [THIS FIGURE IS NOT THE FINAL VERSION AS WE ARE WAITING ON UPDATED TD-CIMS DATA] Aerosol size distribution in the CAGE chamber measured by the SMPS on August 6. (b) Aerosol size distribution from the model on August 6. (c) Vertical bars indicate the mass fraction of oxygen (black), carbon (green), and sulfur (red) measured by the TD-CIMS. The background colors indicate the mass fraction of oxygen (grey), carbon (light green), and sulfur (light red) produced by the model.

3.3.3 Volatility and partitioning of aerosol mass

Figure 3.4a shows a time series of the organic aerosol mass binned by the C*, and, in general, the amount of mass in the particle phase increases with decreasing volatility, consistent with expected mass partitioning behavior (Donahue et al., 2006; Donahue et al., 2011b). During the NPF&G events, the C*=10^{-2} [μg m^{-3}] bin contains the greatest aerosol mass, highlighting the importance of low-volatility organic compounds (LVOCs) for NPF&G events in the CAGE chamber. At night, when seed particles are injected and OH-chemistry slows, the mass in the lowest volatility bin (C*=10^{-3} [μg m^{-3}]) decreases less rapidly than mass in the other bins to be comparable or exceeding the mass in the C*=10^{-2} [μg m^{-3}] bin. This nighttime decrease likely occurs because of the extremely low organic aerosol loading causing an environment that is unfavorable for organic vapors above ~C*= 10^{-1} [μg m^{-3}] to be in the particle phase. Additionally, the low condensation sink causes species to remain in the vapor-phase for longer periods leading to condensation to the chamber walls and no appreciable mass in the C*=10^{-3} [μg m^{-3}] bin.

A unique feature of the CAGE chamber is the removal of ambient particles from the air entering the chamber, which, along with wall losses and instrument sampling, results in an extremely low condensation sink and long aerosol partitioning timescales. Figure 3.4b shows the calculated timescales for aerosol condensation, particle wall losses (D_P = 10 nm), and combined instrument and vapor wall losses. We find the aerosol condensation timescale is much longer than the other timescales, except once NPF&G events have contributed to particle surface area enough to drive down the timescale for condensation (Figure 3.4; Figure B9). This result implies that low-volatility vapors inside the chamber are more often condensing onto the chamber walls or being pulled through the sample flow than contributing to aerosol mass in the chamber. The low-condensation-sink environment of the CAGE chamber underscores the importance of considering

aerosol partitioning and equilibrium timescales, especially as it relates to interpreting NPF&G events and aerosol mass.

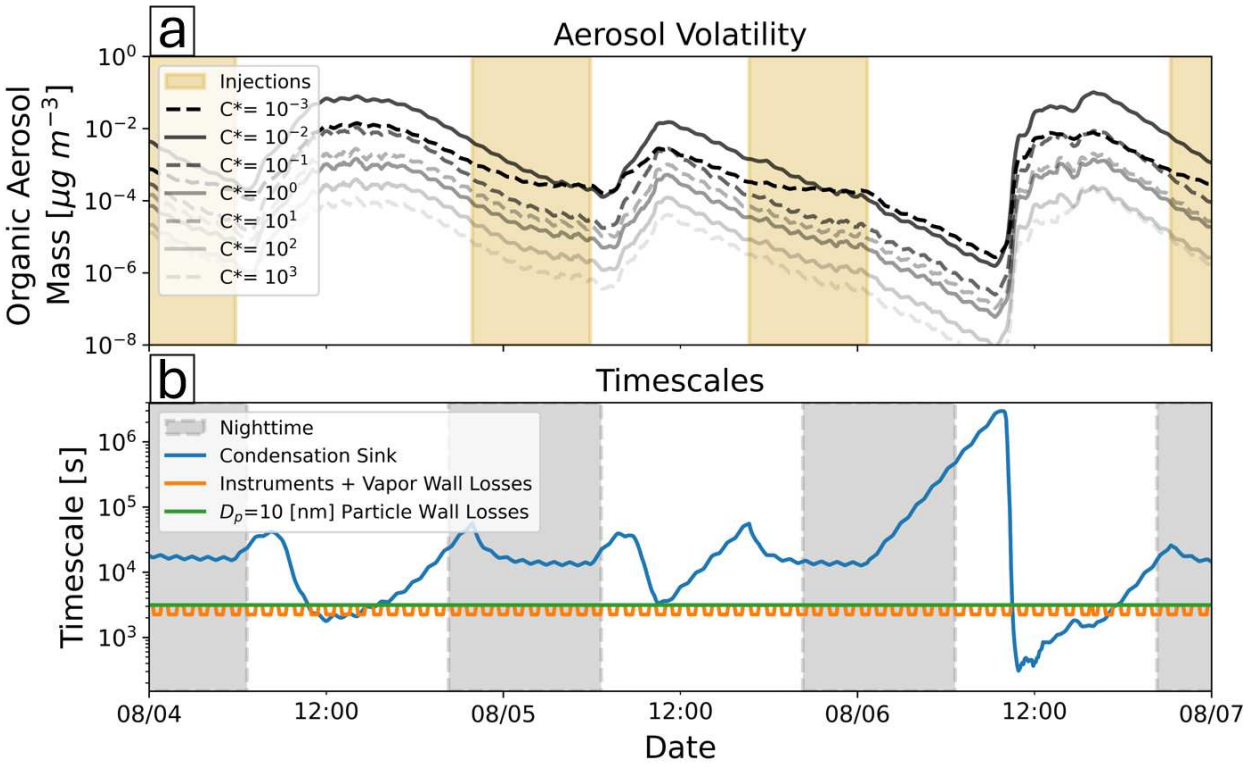

Figure 3.4. (a) Time series of organic aerosol mass in volatility bins ranging from C*=10^{-3} to C*=10^{3} [µg m^{-3}]. Darker shades indicate lower volatility and lighter shades indicate higher volatility. The shaded areas indicate the time of aerosol injections. (b) Calculated timescales in the chamber for condensation (blue), instrumentation and vapor wall losses (orange), and particle wall losses (green).

As discussed in the last paragraph, the CAGE chamber is an environment where aerosol condensation timescales are often longer than other relevant timescales. We find SOA partitioning across a wide range of volatilities, including low volatility organics, is far from equilibrium during NPF&G events, particularly at the start. Figure 3.5 shows 3 h average volatility basis set (VBS) distributions at three different time intervals for the three NPF&G events. For each day, the 'x' symbols indicate the condensed-phase mass that would be present in each volatility bin if the gas-particle system reached equilibrium. Across all NPF&G events and times, our analysis shows that

a portion of potential aerosol mass (i.e., space between the top of the green bars and the 'x') is not being realized due to kinetic limitations of aerosol condensation.

The numbers in the top left of each panel indicate: (1) the averaged total aerosol mass during the 3 h period [μg m^{-3}], (2) the total aerosol mass that would be in the condensed phase at equilibrium (i.e., 'x' symbols) [μg m^{-3}], and (3) the condensation timescale [h]. During all three NPF&G events, the total condensed-phase mass is significantly lower than the equilibrium mass, and the condensation timescales are usually longer than the other chamber timescales (Figure 3.4b) except for during the 13:00-16:00 CST period on August 4 and 6. Notably, the red bars indicate the mass of aerosol sulfate, and they indicate that sulfuric acid is often not reaching thermodynamic equilibrium (which would be fully in the particle phase) prior to the NPF&G events due to the low condensation sink.

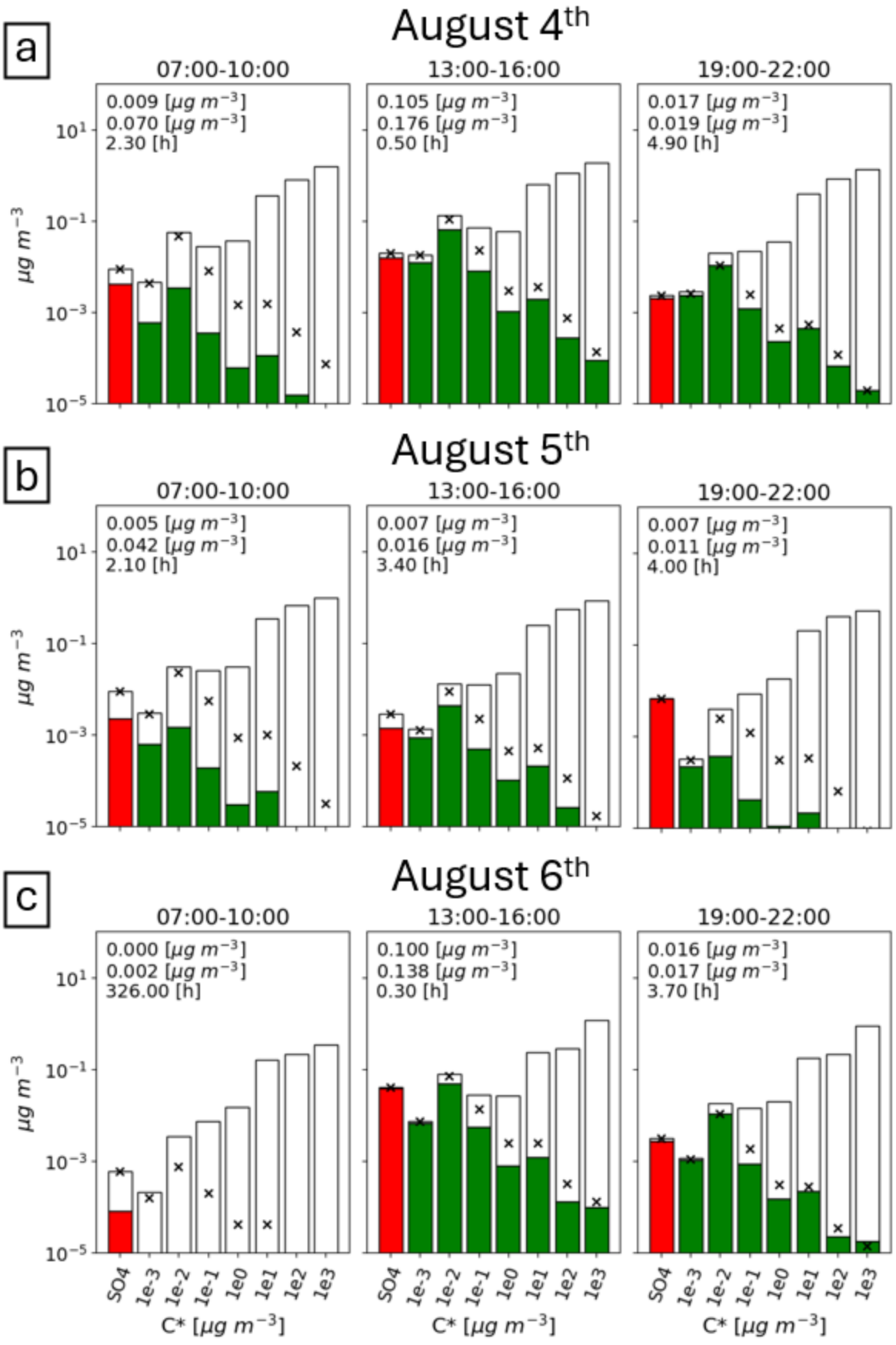
a
August 4th
07:00-10:00
0.009 [μg m−3]
0.070 [μg m−3]
2.30 [h]
13:00-16:00
0.105 [μg m−3]
0.176 [μg m−3]
0.50 [h]
19:00-22:00
0.017 [μg m−3]
0.019 [μg m−3]
4.90 [h]
b
August 5th
07:00-10:00
0.005 [μg m−3]
0.042 [μg m−3]
2.10 [h]
13:00-16:00
0.007 [μg m−3]
0.016 [μg m−3]
3.40 [h]
19:00-22:00
0.007 [μg m−3]
0.011 [μg m−3]
4.00 [h]
c
August 6th
07:00-10:00
0.000 [μg m−3]
0.002 [μg m−3]
326.00 [h]
13:00-16:00
0.100 [μg m−3]
0.138 [μg m−3]
0.30 [h]
19:00-22:00
0.016 [μg m−3]
0.017 [μg m−3]
3.70 [h]
μg m−3
SO4
1e-3
1e-2
1e-1
1e0
1e1
1e2
1e3
C* [μg m−3]

Figure 3.5. (a) Time-averaged volatility distributions during three periods on August 4th. The red bar indicates sulfate mass in the particle phase and the green bars indicate organic mass in the particle phase. The white bars indicate the corresponding mass in the vapor phase. The 'x' symbols indicate the aerosol mass in each volatility bin if the system were to reach equilibrium at ambient temperature. The numbers in the top left of each panel indicate (1) the total modeled aerosol mass, (2) the total aerosol mass at equilibrium, and (3) the average condensation sink timescale over the period. (b) and (c) show the same panels as (a) but for August 5th and August 6th, respectively.

3.3.4 Sensitivity of particle growth and aerosol mass to chamber artifacts

The derived particle growth rates for the three NPF&G events do not perfectly agree between the model and SMPS measurements; however, particle growth rates in the model are sensitive to various assumptions and parameterizations. Figure 3.6 shows the derived particle growth rates for each NPF&G event. The "Base" model simulation overpredicts the particle growth on August 4 by a factor of ~2 (orange bar) relative to observations (black bar). Disabling particle wall losses in the model results in a reduction in particle growth (purple bar), due to increased survival of small particles, which enhances the condensation sink and thus limits the growth of particles, especially at larger sizes, by increasing competition for condensable vapors. In contrast, running the model without vapor wall losses leads to a substantial increase in the particle growth rate on August 4 (yellow bar), due to increased availability of condensable gases. Finally, with particle and vapor wall losses off (light blue), particle growth is similar to the "Base" simulation. The limited change likely reflects the competing effects of increased vapor availability and enhanced particle number, which together maintain a high condensation sink and constrain the overall growth rate.

On August 5, the "Base" simulation and the SMPS-derived particle growth rates agree well. When particle wall losses are turned off, freshly nucleated particles do not grow into the SMPS size range, therefore, no particle growth rate is derived. Alternatively, when vapor wall

losses are turned off, the particle growth rate increases dramatically. Similar to the NPF&G event on August 4, this increase is due to the increased availability of condensable vapors. When both particle and vapor wall losses are disabled, particle growth is approximately double that of the "Base" simulation. For the August 6 event, the particle growth rate from the "Base" simulation is ~1.5 nm h^{-1} higher than the SMPS growth rate. As was the case on August 4, turning particle wall losses off leads to a decrease in the particle growth rate, while turning vapor wall losses off leads to an increase in the particle growth rate. Finally, running the model with particle and vapor wall losses off leads to a particle growth rate similar to the rate derived from the observations.

We tested running the model using the mean temperature and mean relative humidity over the simulation period to test the sensitivity of our results on the diurnal pattern of each variable. We find that running the model with constant temperature leads to a slight increase in particle growth on August 4 and a slight decrease on August 6 (Figure 3.6, green bars). On August 5, there was no particle growth above 10 nm when running with constant temperature. Running the model with constant relative humidity led to small increases and decreases in particle growth (Figure 3.6, dark blue bars). Overall, with the exception of August 5, we find that our results are not sensitive to the diurnal changes in temperature and relative humidity.

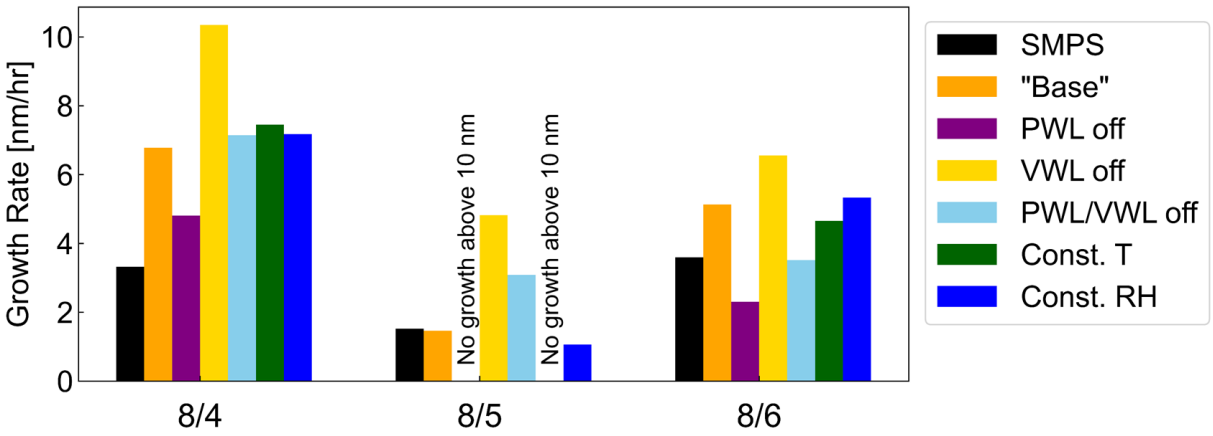

Figure 3.6. Derived particle growth rates for the three NPF&G events from the SMPS (black bars) and from the model. The orange bars indicate the particle growth rates from the "base" case simulation, and the other bars represent the particle growth rates derived from sensitivity simulations.

3.3.5 Implications for potential SOA mass measured in CAGE

Simulations without particle and vapor wall losses have increased number and mass of particles in the CAGE chamber (Figure 3.7 and Figure B10). However, the timescale for particle and vapor losses to the instruments is short enough (2.2 h) to provide the necessary reduction in aerosol loading to have continued NPF&G events. Without instrument pull, the model would likely produce a perpetually growing mode of large particles that would continue to grow and suppress further nucleation from occurring. This highlights a unique quality of some continuous reactor chambers, where sampling the chamber alters the chamber state.

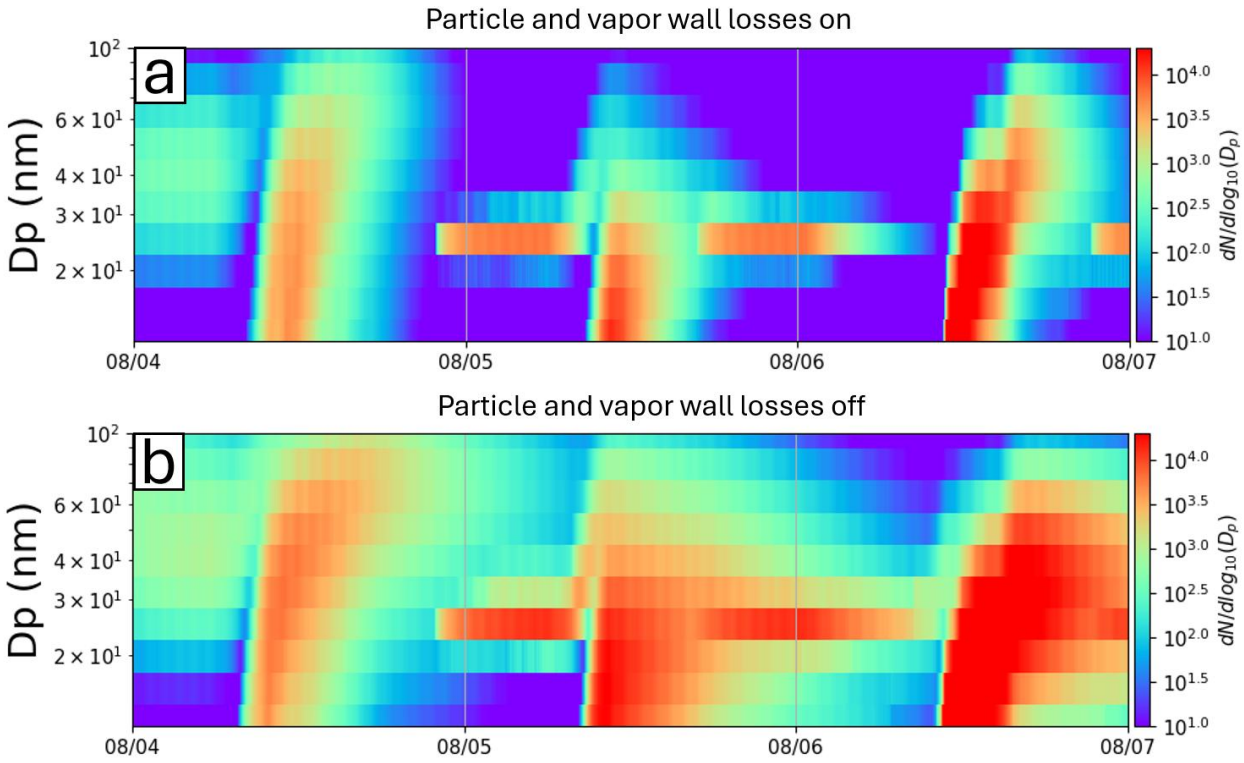

Figure 3.7. (a) Modeled aerosol size distribution from the "base" case. (b) Modeled aerosol size distribution from the simulation with vapor and particle wall losses off.

Our results indicate that particle and vapor wall losses play a significant role in altering the aerosol size distribution in the CAGE chamber. Running the model without particle and vapor wall losses led to a several fold increase in total aerosol mass (Figure B10) at certain times. Quantifying the exact amount of potential SOA mass being lost to the walls and instruments difficult given the confounding timescales for aerosol formation, thermodynamic partitioning, and loss processes, but our modeling results indicate that there is often 0.1-1.0 [μg m^{-3}] of potential aerosol mass being lost to the walls (Figure B10). Additionally, when forced to thermodynamic equilibrium, we find an additional 0.1-1.0 [μg m^{-3}] of aerosol mass that has the potential to contribute to aerosol mass in CAGE (Figure 3.5).

3.4. Uncertainties and limitations

Wall losses: A non-trivial amount of uncertainty in our results stems from properties of the CAGE chamber, principally the rates of vapor and particle wall losses. While work has been done to quantify wall losses in the CAGE chamber (Sirmollo et al., 2021; Zhu et al., 2025) and other similar chambers (Jorga et al., 2023), it remains an open question as to how wall loss rates change based on the environmental conditions in Houson and how the loss rates change over the course of the entire campaign. With the suite of instruments deployed during TRACER-UFI, we cannot fully constrain the wall loss rates, therefore we had to make various assumptions for our modeling work. We derived the first order wall loss rate coefficient for particles in the 60 to 100 nm range by fitting a first order exponential decay function to the total number concentration in the size range during periods with little particle growth. Assuming a $1/D_P$ dependence for particle loss rates, we scaled the particle wall loss rate for all other diameters. While the derived rate of particle losses in the 60 to 100 nm range is likely representative, loss rates for particles outside of that range have greater uncertainty. In other words, we are likely not capturing some of the size dependent characteristics of the particle wall losses in the CAGE chamber, possibly leading to poor model-measurement agreement. Additionally, assuming that the wall loss rate of small particles and vapors is limited by turbulent mixing from the core of the chamber to the edge and not by Brownian Diffusion close to the wall is a limiting factor of this work.

Chamber timescales: Other properties of the CAGE chamber that contribute, to a lesser degree, to the uncertainty of our results are the diffusion timescale through the *gas exchange channel* and any potential losses of particles and vapors between the CAGE chamber and the instruments (e.g., line losses). The rate of gas-exchange between the chamber and the ambient environment is well constrained (Sirmollo et al., 2021). However, we do not account for any potential condensation and re-emission of vapors (e.g., organics and ammonia) throughout the

analysis period in the Teflon filter or in the *gas exchange channel*. While any potential influence of vapor condensation and re-emission in the Teflon filter and *gas exchange channel* is likely to be small, it is a source of potential error in our modeling results. Finally, we have investigated vapor and particle wall losses to the chamber walls, but we have not accounted for losses to the sampling lines. Again, we expect line losses to be limited due to the short distance between the CAGE chamber and the instruments, but we cannot fully account for the potential losses in this work.

TD-CIMS comparison: As stated, the TD-CIMS data presented in this dissertation are likely inaccurate due to issues with data sampling and processing. For our comparison of the mass fraction measured by the TD-CIMS with the model (Figure 3.3c), uncertainty arises both from the TD-CIMS measurements and the model. The primary source of uncertainty in the TD-CIMS measurements is the potential influence of the larger particles (Figure 3.3a) appearing later on August 6 that could potentially influence the mass collected in the instrument. As mentioned, the number of large particles is lower (~10^2-10^3 [cm^{-3}]) than the number in the mode associated with the NPF&G event (~$10^{3.5}$ [cm^{-3}]), however, the large particles have diameters around 200 nm and will have significantly more mass than the particles with diameters around 50 nm. Even with the lower collection efficiency of the TD-CIMS for larger particles, we cannot discount potential influence of the large particles on the mass fractions shown in Figure 3.3c.

In the SOM-TOMAS model, the only reaction pathway for SO_2 is with OH, but there are many other potential pathways to create sulfuric acid, sulfate, and sulfur-containing organic species. Possibly the most important alternative reaction pathway for SO_2 is the reaction of SO_2 with Criegee intermediates to form sulfuric acid. Criegee intermediates have been found to be an important pathway for both sulfuric acid formation and the formation of other sulfur-containing

organics in particles (Mauldin et al., 2012; Chen et al., 2025). Another potentially important pathway for the formation of organosulfate species is through heterogeneous reactions of oxygen-containing species with SO_2, especially if the aerosol is acidic. Chen et al. (2025) also found a variety of organosulfate species in particles, which they postulate were formed from heterogeneous reactions of oxygen-containing species with sulfuric acid. A less clear pathway for SO_2 oxidation is through direct adsorption of SO_2 onto the particle surface where it can then undergo oxidation with either H_2O or O_2; however, this importance of this pathway is difficult to elucidate across different environments given the complexities of heterogeneous chemistry on the surface of particles (Ma et al., 2023). Finally, OH can replace the Cl molecule in NaCl (i.e., sea salt) which can make particles more basic, driving uptake of SO_2 to the particles which then undergoes heterogeneous oxidation to form sulfuric acid. These mechanisms, along with others, are a likely cause for the model-measurement discrepancies, and they are a source of uncertainty when considering our results.

OH concentrations: A source of uncertainty in our modeling results is the use of an OH proxy based on downwelling shortwave radiation. Similar proxies have been used in previous work (Stevens et al., 2012; Pietikäinen et al., 2014; O'Donnell et al., 2023), but these proxies lack any mechanistic chemistry that can influence OH concentrations. We may be missing fluctuations in OH concentrations that could influence NPF&G in the CAGE chamber. We do test scaling the OH concentrations, but this scaling only tests for the sensitivity of our results to the magnitude of OH (i.e., does not test changing the slope in Figure B5).

Nucleation mechanisms: Another source of uncertainty in the model is the nucleation mechanism and scaling of the total nucleation rate. As mentioned, since Houston is a relatively high NO_X environment, we do not include HOM formation. Without HOMs, we do not have

organic nucleation. Therefore, we only use the four inorganic nucleation mechanisms outlined in Dunne et al. (2016). Unfortunately, we did not have measurements of ammonia at the AMF1 site, which would help to better constrain the inorganic nucleation rates. The inclusion of other nucleation mechanisms, such as those based on amines and iodine oxoacids, may have limited the need to scale the total nucleation rate, but more nucleation mechanisms would include further assumptions about the chemical precursors. Nucleation involving amines is potentially important in urban areas (Yu et al., 2012; Johnson and Jen, 2023; Zhao et al., 2024), but without measurements of these species, we cannot constrain such a mechanism relative to others. Additionally, nucleation involving iodine oxoacids can be important in coastal areas (Zhang et al., 2023; Wan et al., 2020), but we again lack the measurement constraints to include this. In other words, scaling the inorganic nucleation rate leads to better model-measurement agreement, but the improvement may not be for the correct reasons. Because of this, we do not draw conclusions about the specific nucleation mechanisms contributing to NPF in the CAGE chamber.

Diffusion of SOM species: The final assumption that leads to uncertainty in our results is the assumption of gas species in the SOM grids not diffusing out of the CAGE reactor through the *gas diffusion channel*. This assumption arises from the lack of measurements of comparable VOC species in the ambient environment, leading us to assume that the ambient environment is the same as the chamber for the species not measured by the PTR-MS. This assumption will affect the results in two ways: (1) there will be times when the chamber has higher concentrations of SOM species than the ambient environment, but those species do not diffuse out leading to increased VOC loading in the chamber; (2) there will be scenarios where ambient concentrations of species in the SOM grids will be higher than those in the chamber, but those vapors will not diffuse into the chamber, leading to lower VOC loading in the chamber relative to the ambient atmosphere. This

assumption is likely to alter results for specific NPF&G events (i.e., too much/little growth or nucleation), but the implications for model bias are likely more limited when looking over longer periods.

3.5. Conclusions

In this work, we present an analysis of the three NPF&G events occurring on August 4, 5, and 6 in the CAGE chamber during the TRACER campaign in Houston, TX. By filtering out ambient particles and allowing ambient vapors to diffuse in, the CAGE chamber provides the unique opportunity to evaluate the NPF&G potential of VOCs in the ambient environment. Our modeling approach provides insight into the dominant contributors to NPF&G in the CAGE chamber, and we test the sensitivity of NPF&G to various assumptions, processes, and parameters.

The model used in this work, SOM-TOMAS, reasonably represents the NPF&G events that occur in the CAGE chamber on August 4, 5, and 6 (Figure 3.1a,b). The model estimates that the majority of organic aerosol mass is derived from trimethylbenzene, toluene, and styrene (Figure 3.2), with trimethylbenzene being the largest contributor due to its high carbon number, SOA yield, and generally elevated concentrations during the analysis period. We find during the night that SOA mass is dominated by ammonium sulfate due to the seed particles injections. Though they are suspect, the TD-CIMS measurements for the NPF&G event on August 6 show relatively invariant fractions of sulfur, oxygen, and carbon (Figure 3.3), whereas the model shows mostly sulfur and oxygen early in the event and carbon and oxygen later in the event. The discrepancy between the model and observations could be due to several factors influencing the measurements and model (see Section 3.3.2.2).

Our analysis of the pertinent timescales in the chamber shows that condensable vapors are lost more quickly to the walls and through instrument sampling than they are to condensing to

particles except for time periods after significant NPF&G has increased the condensation sink (Figure 3.4b). Given the low condensation sink and the relatively short timescales for wall losses and instrument sampling during much of the experimental time period, vapors and particles rarely are partitioned close to thermodynamic equilibrium, although closer during NPF&G events (Figure 3.5). For all three NPF&G events, low-volatility VOCs appear to be the dominant contributor to SOA mass.

We test the sensitivity of particle growth rates in the model to particle and vapor wall losses, temperature, and relative humidity. We find that turning particle wall losses off decreases the particle growth rates for all three days, due to the increased survival of particles to larger sizes which then compete with freshly nucleated particles for condensable vapors (i.e., increase the condensation sink). Conversely, running the model without vapor wall losses led to an increase in particle growth rates due to the increased availability of vapors to drive growth. Running the model without particle and vapor wall losses showed mixed results for the different NPF&G events due to the competing effects of the two processes. Finally, our model results are relatively insensitive to temperature and relative humidity, with the exception of August 5, where the relative humidity in the "base" simulation appears to increase particle growth.

The CAGE chamber is a unique system designed to reflect ambient atmospheric conditions without the ambient aerosol concentrations. The continuous chamber system allows for longer experiments than typical batch chambers, with the potential tradeoffs of compounding chamber wall effects that may alter the results. Further applications of the chamber modeling framework presented in this work will be useful for understanding the conditions under which particles form and grow in different environments.

REFERENCES

Adams, P.J. and Seinfeld, J.H. (2002). Predicting global aerosol size distributions in general circulation models. *Journal of Geophysical Research: Atmospheres* 107 (D19):AAC 4-1-AAC 4-23. doi:10.1029/2001JD001010.

Akherati, A., He, Y., Coggon, M.M., Koss, A.R., Hodshire, A.L., Sekimoto, K., Warneke, C., de Gouw, J., Yee, L., Seinfeld, J.H., Onasch, T.B., Herndon, S.C., Knighton, W.B., Cappa, C.D., Kleeman, M.J., Lim, C.Y., Kroll, J.H., Pierce, J.R., and Jathar, S.H. (2020). Oxygenated Aromatic Compounds are Important Precursors of Secondary Organic Aerosol in Biomass-Burning Emissions. *Environ. Sci. Technol.* 54 (14):8568–8579. doi:10.1021/acs.est.0c01345.

Akherati, A., He, Y., Garofalo, L.A., Hodshire, A.L., Farmer, D.K., Kreidenweis, S.M., Permar, W., Hu, L., Fischer, E.V., Jen, C.N., Goldstein, A.H., Levin, E.J.T., DeMott, P.J., Campos, T.L., Flocke, F., Reeves, J.M., Toohey, D.W., Pierce, J.R., and Jathar, S.H. (2022). Dilution and photooxidation driven processes explain the evolution of organic aerosol in wildfire plumes. *Environ. Sci.: Atmos.* 2 (5):1000–1022. doi:10.1039/D1EA00082A.

Albrecht, B.A. (1989). Aerosols, Cloud Microphysics, and Fractional Cloudiness. *Science* 245 (4923):1227–1230. doi:10.1126/science.245.4923.1227.

Andreae, M.O. and Rosenfeld, D. (2008). Aerosol–cloud–precipitation interactions. Part 1. The nature and sources of cloud-active aerosols. *Earth-Science Reviews* 89 (1):13–41. doi:10.1016/j.earscirev.2008.03.001.

Baccarini, A., Karlsson, L., Dommen, J., Duplessis, P., Vüllers, J., Brooks, I.M., Saiz-Lopez, A., Salter, M., Tjernström, M., Baltensperger, U., Zieger, P., and Schmale, J. (2020).

Frequent new particle formation over the high Arctic pack ice by enhanced iodine emissions. *Nat Commun* 11 (1):4924. doi:10.1038/s41467-020-18551-0.

Bianchi, F., Kurtén, T., Riva, M., Mohr, C., Rissanen, M.P., Roldin, P., Berndt, T., Crounse, J.D., Wennberg, P.O., Mentel, T.F., Wildt, J., Junninen, H., Jokinen, T., Kulmala, M., Worsnop, D.R., Thornton, J.A., Donahue, N., Kjaergaard, H.G., and Ehn, M. (2019). Highly Oxygenated Organic Molecules (HOM) from Gas-Phase Autoxidation Involving Peroxy Radicals: A Key Contributor to Atmospheric Aerosol. *Chem. Rev.* 119 (6):3472–3509. doi:10.1021/acs.chemrev.8b00395.

Bilsback, K.R., He, Y., Cappa, C.D., Chang, R.Y.-W., Croft, B., Martin, R.V., Ng, N.L., Seinfeld, J.H., Pierce, J.R., and Jathar, S.H. (2023). Vapors Are Lost to Walls, Not to Particles on the Wall: Artifact-Corrected Parameters from Chamber Experiments and Implications for Global Secondary Organic Aerosol. *Environ. Sci. Technol.* 57 (1):53–63. doi:10.1021/acs.est.2c03967.

Chen, M., Tong, S., Yu, S., Xu, Y., Lv, X., Zhang, H., Wang, S., and Ge, M. (2025). Impact of the Criegee Intermediate on the Formation of Secondary Organic Aerosols during E-4-Hexen-1-ol Ozonolysis. *J. Phys. Chem. A* 129 (6):1704–1713. doi:10.1021/acs.jpca.4c08028.

Chu, C.-W., Zhai, J., Han, Y., Ye, J., Zaveri, R.A., Martin, S.T., and Hung, H.-M. (2022). New Particle Formation and Growth Dynamics for α-Pinene Ozonolysis in a Smog Chamber and Implications for Ambient Environments. *ACS Earth Space Chem.* doi:10.1021/acsearthspacechem.2c00161.

Clement, A.C., Burgman, R., and Norris, J.R. (2009). Observational and Model Evidence for Positive Low-Level Cloud Feedback. *Science* 325 (5939):460–464. doi:10.1126/science.1171255.

Crump, J.G. and Seinfeld, J.H. (1981). Turbulent deposition and gravitational sedimentation of an aerosol in a vessel of arbitrary shape. *Journal of Aerosol Science* 12 (5):405–415. doi:10.1016/0021-8502(81)90036-7.

Dada, L., Lehtipalo, K., Kontkanen, J., Nieminen, T., Baalbaki, R., Ahonen, L., Duplissy, J., Yan, C., Chu, B., Petäjä, T., Lehtinen, K., Kerminen, V.-M., Kulmala, M., and Kangasluoma, J. (2020). Formation and growth of sub-3-nm aerosol particles in experimental chambers. *Nat Protoc* 15 (3):1013–1040. doi:10.1038/s41596-019-0274-z.

Deng, Y., Inomata, S., Sato, K., Ramasamy, S., Morino, Y., Enami, S., and Tanimoto, H. (2020). Temperature and acidity dependence of secondary organic aerosol formation from α-pinene ozonolysis with a compact chamber system. 24.

Donahue, N.M., Epstein, S.A., Pandis, S.N., and Robinson, A.L. (2011). A two-dimensional volatility basis set: 1. organic-aerosol mixing thermodynamics. *Atmospheric Chemistry and Physics* 11 (7):3303–3318. doi:10.5194/acp-11-3303-2011.

Donahue, N.M., Robinson, A.L., Stanier, C.O., and Pandis, S.N. (2006). Coupled Partitioning, Dilution, and Chemical Aging of Semivolatile Organics. *Environ. Sci. Technol.* 40 (8):2635–2643. doi:10.1021/es052297c.

Dunne, E.M., Gordon, H., Kurten, A., Almeida, J., Duplissy, J., Williamson, C., Ortega, I.K., Pringle, K.J., Adamov, A., Baltensperger, U., Barmet, P., Benduhn, F., Bianchi, F., Breitenlechner, M., Clarke, A., Curtius, J., Dommen, J., Donahue, N.M., Ehrhart, S., Flagan, R.C., Franchin, A., Guida, R., Hakala, J., Hansel, A., Heinritzi, M., Jokinen, T.,

Kangasluoma, J., Kirkby, J., Kulmala, M., Kupc, A., Lawler, M.J., Lehtipalo, K., Makhmutov, V., Mann, G., Mathot, S., Merikanto, J., Miettinen, P., Nenes, A., Onnela, A., Rap, A., Reddington, C.L.S., Riccobono, F., Richards, N.A.D., Rissanen, M.P., Rondo, L., Sarnela, N., Schobesberger, S., Sengupta, K., Simon, M., Sipila, M., Smith, J.N., Stozkhov, Y., Tome, A., Trostl, J., Wagner, P.E., Wimmer, D., Winkler, P.M., Worsnop, D.R., and Carslaw, K.S. (2016). Global atmospheric particle formation from CERN CLOUD measurements. *Science* 354 (6316):1119–1124. doi:10.1126/science.aaf2649.

Fanourgakis, G.S., Kanakidou, M., Nenes, A., Bauer, S.E., Bergman, T., Carslaw, K.S., Grini, A., Hamilton, D.S., Johnson, J.S., Karydis, V.A., Kirkevåg, A., Kodros, J.K., Lohmann, U., Luo, G., Makkonen, R., Matsui, H., Neubauer, D., Pierce, J.R., Schmale, J., Stier, P., Tsigaridis, K., van Noije, T., Wang, H., Watson-Parris, D., Westervelt, D.M., Yang, Y., Yoshioka, M., Daskalakis, N., Decesari, S., Gysel-Beer, M., Kalivitis, N., Liu, X., Mahowald, N.M., Myriokefalitakis, S., Schrödner, R., Sfakianaki, M., Tsimpidi, A.P., Wu, M., and Yu, F. (2019). Evaluation of global simulations of aerosol particle and cloud condensation nuclei number, with implications for cloud droplet formation. *Atmospheric Chemistry and Physics* 19 (13):8591–8617. doi:10.5194/acp-19-8591-2019.

Garofalo, L.A., He, Y., Jathar, S.H., Pierce, J.R., Fredrickson, C.D., Palm, B.B., Thornton, J.A., Mahrt, F., Crescenzo, G.V., Bertram, A.K., Draper, D.C., Fry, J.L., Orlando, J., Zhang, X., and Farmer, D.K. (2021). Heterogeneous Nucleation Drives Particle Size Segregation in Sequential Ozone and Nitrate Radical Oxidation of Catechol. *Environ. Sci. Technol.* 55 (23):15637–15645. doi:10.1021/acs.est.1c02984.

Gordon, H., Kirkby, J., Baltensperger, U., Bianchi, F., Breitenlechner, M., Curtius, J., Dias, A., Dommen, J., Donahue, N.M., Dunne, E.M., Duplissy, J., Ehrhart, S., Flagan, R.C., Frege, C., Fuchs, C., Hansel, A., Hoyle, C.R., Kulmala, M., Kürten, A., Lehtipalo, K., Makhmutov, V., Molteni, U., Rissanen, M.P., Stozkhov, Y., Tröstl, J., Tsagkogeorgas, G., Wagner, R., Williamson, C., Wimmer, D., Winkler, P.M., Yan, C., and Carslaw, K.S. (2017). Causes and importance of new particle formation in the present-day and preindustrial atmospheres. *Journal of Geophysical Research: Atmospheres* 122 (16):8739–8760. doi:10.1002/2017JD026844.

Gryspeerdt, E., Stier, P., and Partridge, D.G. (2014). Satellite observations of cloud regime development: the role of aerosol processes. *Atmos. Chem. Phys.* 14 (3):1141–1158. doi:10.5194/acp-14-1141-2014.

Guo, F., Bui, A.A.T., Schulze, B.C., Yoon, S., Shrestha, S., Wallace, H.W., Sakai, Y., Actkinson, B.W., Erickson, M.H., Alvarez, S., Sheesley, R., Usenko, S., Flynn, J., and Griffin, R.J. (2021). Urban core-downwind differences and relationships related to ozone production in a major urban area in Texas. *Atmospheric Environment* 262:118624. doi:10.1016/j.atmosenv.2021.118624.

He, X.-C., Simon, M., Iyer, S., Xie, H.-B., Rörup, B., Shen, J., Finkenzeller, H., Stolzenburg, D., Zhang, R., Baccarini, A., Tham, Y.J., Wang, M., Amanatidis, S., Piedehierro, A.A., Amorim, A., Baalbaki, R., Brasseur, Z., Caudillo, L., Chu, B., Dada, L., Duplissy, J., El Haddad, I., Flagan, R.C., Granzin, M., Hansel, A., Heinritzi, M., Hofbauer, V., Jokinen, T., Kemppainen, D., Kong, W., Krechmer, J., Kürten, A., Lamkaddam, H., Lopez, B., Ma, F., Mahfouz, N.G.A., Makhmutov, V., Manninen, H.E., Marie, G., Marten, R., Massabò, D., Mauldin, R.L., Mentler, B., Onnela, A., Petäjä, T., Pfeifer, J., Philippov,

M., Ranjithkumar, A., Rissanen, M.P., Schobesberger, S., Scholz, W., Schulze, B., Surdu, M., Thakur, R.C., Tomé, A., Wagner, A.C., Wang, D., Wang, Y., Weber, S.K., Welti, A., Winkler, P.M., Zauner-Wieczorek, M., Baltensperger, U., Curtius, J., Kurtén, T., Worsnop, D.R., Volkamer, R., Lehtipalo, K., Kirkby, J., Donahue, N.M., Sipilä, M., and Kulmala, M. (2023). Iodine oxoacids enhance nucleation of sulfuric acid particles in the atmosphere. *Science* 382 (6676):1308–1314. doi:10.1126/science.adh2526.

He, Y., Akherati, A., Nah, T., Ng, N.L., Garofalo, L.A., Farmer, D.K., Shiraiwa, M., Zaveri, R.A., Cappa, C.D., Pierce, J.R., and Jathar, S.H. (2021). Particle Size Distribution Dynamics Can Help Constrain the Phase State of Secondary Organic Aerosol. *Environ. Sci. Technol.* 55 (3):1466–1476. doi:10.1021/acs.est.0c05796.

He, Y., King, B., Pothier, M., Lewane, L., Akherati, A., Mattila, J., K. Farmer, D., L. McCormick, R., Thornton, M., R. Pierce, J., Volckens, J., and H. Jathar, S. (2020). Secondary organic aerosol formation from evaporated biofuels: comparison to gasoline and correction for vapor wall losses. *Environmental Science: Processes & Impacts* 22 (7):1461–1474. doi:10.1039/D0EM00103A.

He, Y., Lambe, A.T., Seinfeld, J.H., Cappa, C.D., Pierce, J.R., and Jathar, S.H. (2022). Process-Level Modeling Can Simultaneously Explain Secondary Organic Aerosol Evolution in Chambers and Flow Reactors. *Environ. Sci. Technol.* 56 (10):6262–6273. doi:10.1021/acs.est.1c08520.

Hidy, G.M. (2019). Atmospheric Chemistry in a Box or a Bag. *Atmosphere* 10 (7):401. doi:10.3390/atmos10070401.

Hussein, T., Martikainen, J., Junninen, H., Sogacheva, L., Wagner, R., Maso, M.D., Riipinen, I., Aalto, P.P., and Kulmala, M. (2008). Observation of regional new particle formation

in the urban atmosphere. *Tellus B* 60 (4):509–521. doi:https://doi.org/10.1111/j.1600-0889.2008.00365.x.

Jeffries, H.E., Kamens, R.M., and Sexton, K. (2013). Early history and rationale for outdoor chamber work at the University of North Carolina. *Environ. Chem.* 10 (4):349–364. doi:10.1071/EN13901.

Jobson, B.T. and McCoskey, J.K. (2010). Sample drying to improve HCHO measurements by PTR-MS instruments: laboratory and field measurements. *Atmospheric Chemistry and Physics* 10 (4):1821–1835. doi:10.5194/acp-10-1821-2010.

Johnson, J.S. and Jen, C.N. (2023). Role of Methanesulfonic Acid in Sulfuric Acid–Amine and Ammonia New Particle Formation. *ACS Earth Space Chem.* doi:10.1021/acsearthspacechem.3c00017.

Jorga, S.D., Florou, K., Patoulias, D., and Pandis, S.N. (2023). New particle formation and growth during summer in an urban environment: a dual chamber study. *Atmospheric Chemistry and Physics* 23 (1):85–97. doi:10.5194/acp-23-85-2023.

Kirkby, J., Curtius, J., Almeida, J., Dunne, E., Duplissy, J., Ehrhart, S., Franchin, A., Gagné, S., Ickes, L., Kürten, A., Kupc, A., Metzger, A., Riccobono, F., Rondo, L., Schobesberger, S., Tsagkogeorgas, G., Wimmer, D., Amorim, A., Bianchi, F., Breitenlechner, M., David, A., Dommen, J., Downard, A., Ehn, M., Flagan, R.C., Haider, S., Hansel, A., Hauser, D., Jud, W., Junninen, H., Kreissl, F., Kvashin, A., Laaksonen, A., Lehtipalo, K., Lima, J., Lovejoy, E.R., Makhmutov, V., Mathot, S., Mikkilä, J., Minginette, P., Mogo, S., Nieminen, T., Onnela, A., Pereira, P., Petäjä, T., Schnitzhofer, R., Seinfeld, J.H., Sipilä, M., Stozhkov, Y., Stratmann, F., Tomé, A., Vanhanen, J., Viisanen, Y., Vrtala, A., Wagner, P.E., Walther, H., Weingartner, E., Wex, H., Winkler,

P.M., Carslaw, K.S., Worsnop, D.R., Baltensperger, U., and Kulmala, M. (2011). Role of sulphuric acid, ammonia and galactic cosmic rays in atmospheric aerosol nucleation. *Nature* 476 (7361):429–433. doi:10.1038/nature10343.

Krechmer, J.E., Pagonis, D., Ziemann, P.J., and Jimenez, J.L. (2016). Quantification of Gas-Wall Partitioning in Teflon Environmental Chambers Using Rapid Bursts of Low-Volatility Oxidized Species Generated in Situ. *Environ. Sci. Technol.* 50 (11):5757–5765. doi:10.1021/acs.est.6b00606.

Kulmala, M. and Kerminen, V.-M. (2008). On the formation and growth of atmospheric nanoparticles. *Atmospheric Research, 17th International Conference on Nucleation and Atmospheric Aerosols* 90 (2):132–150. doi:10.1016/j.atmosres.2008.01.005.

Li, Q.-Q., Guo, Y.-T., Yang, J.-Y., and Liang, C.-S. (2023). Review on main sources and impacts of urban ultrafine particles: Traffic emissions, nucleation, and climate modulation. *Atmospheric Environment: X* 19:100221. doi:10.1016/j.aeaoa.2023.100221.

Ma, Q., Zhang, C., Liu, C., He, G., Zhang, P., Li, H., Chu, B., and He, H. (2023). A review on the heterogeneous oxidation of SO2 on solid atmospheric particles: Implications for sulfate formation in haze chemistry. *Critical Reviews in Environmental Science and Technology* 53 (21):1888–1911. doi:10.1080/10643389.2023.2190315.

Mauldin III, R.L., Berndt, T., Sipilä, M., Paasonen, P., Petäjä, T., Kim, S., Kurtén, T., Stratmann, F., Kerminen, V.-M., and Kulmala, M. (2012). A new atmospherically relevant oxidant of sulphur dioxide. *Nature* 488 (7410):193–196. doi:10.1038/nature11278.

O'Donnell, S.E., Akherati, A., He, Y., Hodshire, A.L., Shilling, J.E., Kuang, C., Fast, J.D., Mei, F., Schobesberger, S., Thornton, J.A., Smith, J.N., Jathar, S.H., and Pierce, J.R.

(2023). Look Up: Probing the Vertical Profile of New Particle Formation and Growth in the Planetary Boundary Layer With Models and Observations. *Journal of Geophysical Research: Atmospheres* 128 (3):e2022JD037525. doi:10.1029/2022JD037525.

O'Donnell SE, Croft B, Ford B, et al (2025) Going Off Grid: A Comparative Study of the Lagrangian and Eulerian Perspectives of New Particle Formation Events, submitted to Journal of Geophysical Research.

Petters, M.D. and Kreidenweis, S.M. (2007). A single parameter representation of hygroscopic growth and cloud condensation nucleus activity. *Atmospheric Chemistry and Physics* 7 (8):1961–1971. doi:10.5194/acp-7-1961-2007.

Pierce, J.R., Engelhart, G.J., Hildebrandt, L., Weitkamp, E.A., Pathak, R.K., Donahue, N.M., Robinson, A.L., Adams, P.J., and Pandis, S.N. (2008). Constraining Particle Evolution from Wall Losses, Coagulation, and Condensation-Evaporation in Smog-Chamber Experiments: Optimal Estimation Based on Size Distribution Measurements. *Aerosol Science and Technology* 42 (12):1001–1015. doi:10.1080/02786820802389251.

Pietikäinen, J.-P., Mikkonen, S., Hamed, A., Hienola, A.I., Birmili, W., Kulmala, M., and Laaksonen, A. (2014). Analysis of nucleation events in the European boundary layer using the regional aerosol–climate model REMO-HAM with a solar radiation-driven OH-proxy. *Atmos. Chem. Phys.* 14 (21):11711–11729. doi:10.5194/acp-14-11711-2014.

Riccobono, F., Schobesberger, S., Scott, C.E., Dommen, J., Ortega, I.K., Rondo, L., Almeida, J., Amorim, A., Bianchi, F., Breitenlechner, M., David, A., Downard, A., Dunne, E.M., Duplissy, J., Ehrhart, S., Flagan, R.C., Franchin, A., Hansel, A., Junninen, H., Kajos, M., Keskinen, H., Kupc, A., Kürten, A., Kvashin, A.N., Laaksonen, A., Lehtipalo, K., Makhmutov, V., Mathot, S., Nieminen, T., Onnela, A., Petäjä, T., Praplan, A.P., Santos,

F.D., Schallhart, S., Seinfeld, J.H., Sipilä, M., Spracklen, D.V., Stozhkov, Y., Stratmann, F., Tomé, A., Tsagkogeorgas, G., Vaattovaara, P., Viisanen, Y., Vrtala, A., Wagner, P.E., Weingartner, E., Wex, H., Wimmer, D., Carslaw, K.S., Curtius, J., Donahue, N.M., Kirkby, J., Kulmala, M., Worsnop, D.R., and Baltensperger, U. (2014). Oxidation Products of Biogenic Emissions Contribute to Nucleation of Atmospheric Particles. *Science* 344 (6185):717–721. doi:10.1126/science.1243527.

Rosenfeld, D., Andreae, M.O., Asmi, A., Chin, M., de Leeuw, G., Donovan, D.P., Kahn, R., Kinne, S., Kivekäs, N., Kulmala, M., Lau, W., Schmidt, K.S., Suni, T., Wagner, T., Wild, M., and Quaas, J. (2014). Global observations of aerosol-cloud-precipitation-climate interactions. *Reviews of Geophysics* 52 (4):750–808. doi:10.1002/2013RG000441.

Shrestha, S., Yoon, S., Erickson, M.H., Guo, F., Mehra, M., Bui, A.A.T., Schulze, B.C., Kotsakis, A., Daube, C., Herndon, S.C., Yacovitch, T.I., Alvarez, S., Flynn, J.H., Griffin, R.J., Cobb, G.P., Usenko, S., and Sheesley, R.J. (2022). Traffic, transport, and vegetation drive VOC concentrations in a major urban area in Texas. *Science of The Total Environment* 838:155861. doi:10.1016/j.scitotenv.2022.155861.

Sickles, J.E., Ripperton, L.A., Eaton, W.C., and Wright, R.S. (1979). Oxidant-precursor relationships under pollutant transport conditions: outdoor smog chamber study. Volume II. Appendixes. Final report, June 1975-June 1978 (No. PB-80-109135). Research Triangle Inst., Research Triangle Park, NC (USA).

Sirmollo, C.L., Collins, D.R., McCormick, J.M., Milan, C.F., Erickson, M.H., Flynn, J.H., Sheesley, R.J., Usenko, S., Wallace, H.W., Bui, A.A.T., Griffin, R.J., Tezak, M., Kinahan, S.M., and Santarpia, J.L. (2021). Captive Aerosol Growth and Evolution (CAGE) chamber system to investigate particle growth due to secondary aerosol

formation. *Atmospheric Measurement Techniques* 14 (5):3351–3370. doi:10.5194/amt-14-3351-2021.

Smith, J.N., Moore, K.F., McMurry, P.H., and Eisele, F.L. (2004). Atmospheric Measurements of Sub-20 nm Diameter Particle Chemical Composition by Thermal Desorption Chemical Ionization Mass Spectrometry. *Aerosol Science and Technology* 38 (2):100–110. doi:10.1080/02786820490249036.

Stevens, B. and Feingold, G. (2009). Untangling aerosol effects on clouds and precipitation in a buffered system. *Nature* 461 (7264):607–613. doi:10.1038/nature08281.

Stevens, R.G., Pierce, J.R., Brock, C.A., Reed, M.K., Crawford, J.H., Holloway, J.S., Ryerson, T.B., Huey, L.G., and Nowak, J.B. (2012). Nucleation and growth of sulfate aerosol in coal-fired power plant plumes: sensitivity to background aerosol and meteorology. *Atmos. Chem. Phys.* 12 (1):189–206. doi:10.5194/acp-12-189-2012.

Stockwell, W.R. and Calvert, J.G. (1983). The mechanism of the HO-SO2 reaction. *Atmospheric Environment (1967)* 17 (11):2231–2235. doi:10.1016/0004-6981(83)90220-2.

Trump, E.R., Epstein ,Scott A., Riipinen ,Ilona, and and Donahue, N.M. (2016). Wall effects in smog chamber experiments: A model study. *Aerosol Science and Technology* 50 (11):1180–1200. doi:10.1080/02786826.2016.1232858.

Twomey, S. (1974). Pollution and the planetary albedo. *Atmospheric Environment (1967)* 8 (12):1251–1256. doi:10.1016/0004-6981(74)90004-3.

Voisin, D., Smith, J.N., Sakurai, H., McMurry, P.H., and Eisele, F.L. (2003). Thermal Desorption Chemical Ionization Mass Spectrometer for Ultrafine Particle Chemical

Composition. *Aerosol Science and Technology* 37 (6):471–475. doi:10.1080/02786820300959.

Wan, Y., Huang, X., Jiang, B., Kuang, B., Lin, M., Xia, D., Liao, Y., Chen, J., Yu, J.Z., and Yu, H. (2020). Probing key organic substances driving new particle growth initiated by iodine nucleation in coastal atmosphere. *Atmospheric Chemistry and Physics* 20 (16):9821–9835. doi:https://doi.org/10.5194/acp-20-9821-2020.

Westervelt, D.M., Pierce, J.R., and Adams, P.J. (2014). Analysis of feedbacks between nucleation rate, survival probability and cloud condensation nuclei formation. *Atmospheric Chemistry and Physics* 14 (11):5577–5597. doi:https://doi.org/10.5194/acp-14-5577-2014.

Westervelt, D.M., Pierce, J.R., Riipinen, I., Trivitayanurak, W., Hamed, A., Kulmala, M., Laaksonen, A., Decesari, S., and Adams, P.J. (2013). Formation and growth of nucleated particles into cloud condensation nuclei: model–measurement comparison. *Atmospheric Chemistry and Physics* 13 (15):7645–7663. doi:https://doi.org/10.5194/acp-13-7645-2013.

Wiedensohler, A., Cheng, Y.F., Nowak, A., Wehner, B., Achtert, P., Berghof, M., Birmili, W., Wu, Z.J., Hu, M., Zhu, T., Takegawa, N., Kita, K., Kondo, Y., Lou, S.R., Hofzumahaus, A., Holland, F., Wahner, A., Gunthe, S.S., Rose, D., Su, H., and Pöschl, U. (2009). Rapid aerosol particle growth and increase of cloud condensation nucleus activity by secondary aerosol formation and condensation: A case study for regional air pollution in northeastern China. *Journal of Geophysical Research: Atmospheres* 114 (D2). doi:10.1029/2008JD010884.

Williamson, C.J., Kupc, A., Axisa, D., Bilsback, K.R., Bui, T., Campuzano-Jost, P., Dollner, M., Froyd, K.D., Hodshire, A.L., Jimenez, J.L., Kodros, J.K., Luo, G., Murphy, D.M., Nault, B.A., Ray, E.A., Weinzierl, B., Wilson, J.C., Yu, F., Yu, P., Pierce, J.R., and Brock, C.A. (2019). A large source of cloud condensation nuclei from new particle formation in the tropics. *Nature* 574 (7778):399–403. doi:10.1038/s41586-019-1638-9.

Wu, H., Li, Z., Jiang, M., Liang, C., Zhang, D., Wu, T., Wang, Y., and Cribb, M. (2021). Contributions of traffic emissions and new particle formation to the ultrafine particle size distribution in the megacity of Beijing. *Atmospheric Environment* 118652. doi:10.1016/j.atmosenv.2021.118652.

Wu, Z., Hu, M., Yue, D., Wehner, B., and Wiedensohler, A. (2011). Evolution of particle number size distribution in an urban atmosphere during episodes of heavy pollution and new particle formation. *Sci. China Earth Sci.* 54 (11):1772–1778. doi:10.1007/s11430-011-4227-9.

Xiao, M., Hoyle, C.R., Dada, L., Stolzenburg, D., Kürten, A., Wang, M., Lamkaddam, H., Garmash, O., Mentler, B., Molteni, U., Baccarini, A., Simon, M., He, X.-C., Lehtipalo, K., Ahonen, L.R., Baalbaki, R., Bauer, P.S., Beck, L., Bell, D., Bianchi, F., Brilke, S., Chen, D., Chiu, R., Dias, A., Duplissy, J., Finkenzeller, H., Gordon, H., Hofbauer, V., Kim, C., Koenig, T.K., Lampilahti, J., Lee, C.P., Li, Z., Mai, H., Makhmutov, V., Manninen, H.E., Marten, R., Mathot, S., Mauldin, R.L., Nie, W., Onnela, A., Partoll, E., Petäjä, T., Pfeifer, J., Pospisilova, V., Quéléver, L.L.J., Rissanen, M., Schobesberger, S., Schuchmann, S., Stozhkov, Y., Tauber, C., Tham, Y.J., Tomé, A., Vazquez-Pufleau, M., Wagner, A.C., Wagner, R., Wang, Y., Weitz, L., Wimmer, D., Wu, Y., Yan, C., Ye, P., Ye, Q., Zha, Q., Zhou, X., Amorim, A., Carslaw, K., Curtius, J., Hansel, A., Volkamer,

R., Winkler, P.M., Flagan, R.C., Kulmala, M., Worsnop, D.R., Kirkby, J., Donahue, N.M., Baltensperger, U., El Haddad, I., and Dommen, J. (2021). The driving factors of new particle formation and growth in the polluted boundary layer. *Atmospheric Chemistry and Physics* 21 (18):14275–14291. doi:10.5194/acp-21-14275-2021.

Yang, S., Liu, Z., Clusius, P.S., Liu, Y., Zou, J., Yang, Yuan, Zhao, S., Zhang, G., Xu, Z., Ma, Z., Yang, Yang, Sun, J., Pan, Y., Ji, D., Hu, B., Yan, C., Boy, M., Kulmala, M., and Wang, Y. (2021). Chemistry of new particle formation and growth events during wintertime in suburban area of Beijing: Insights from highly polluted atmosphere. *Atmospheric Research* 255:105553. doi:10.1016/j.atmosres.2021.105553.

Yu, H., McGraw, R., and Lee, S.-H. (2012). Effects of amines on formation of sub-3 nm particles and their subsequent growth. *Geophysical Research Letters* 39 (2). doi:10.1029/2011GL050099.

Yu, Q., Fu, N., Lu, J., Zhang, Y., Du, W., and Wang, J. (2025). Atmospheric Amines: Advances in Analytical Techniques, Emission Inventories, Regional Pollution, and Roles in New Particle Formation. *Curr Pollution Rep* 11 (1):31. doi:10.1007/s40726-025-00364-8.

Zaveri, R.A., Easter, R.C., Shilling, J.E., and Seinfeld, J.H. (2014). Modeling kinetic partitioning of secondary organic aerosol and size distribution dynamics: representing effects of volatility, phase state, and particle-phase reaction. *Atmospheric Chemistry and Physics* 14 (10):5153–5181. doi:10.5194/acp-14-5153-2014.

Zhang, X., Cappa, C.D., Jathar, S.H., McVay, R.C., Ensberg, J.J., Kleeman, M.J., and Seinfeld, J.H. (2014). Influence of vapor wall loss in laboratory chambers on yields of

secondary organic aerosol. *Proceedings of the National Academy of Sciences* 111 (16):5802–5807. doi:10.1073/pnas.1404727111.

Zhang, Y., Li, D., He, X.-C., Nie, W., Deng, C., Cai, R., Liu, Yuliang, Guo, Y., Liu, C., Li, Yiran, Chen, L., Li, Yuanyuan, Hua, C., Liu, T., Wang, Z., Wang, L., Petäjä, T., Bianchi, F., Qi, X., Chi, X., Paasonen, P., Liu, Yongchun, Yan, C., Jiang, J., Ding, A., and Kulmala, M. (2023). Iodine oxoacids and their roles in sub-3 nanometer particle growth in polluted urban environments. *EGUsphere* 1–39. doi:10.5194/egusphere-2023-311.

Zhang, Y., Li, D., He, X.-C., Nie, W., Deng, C., Cai, R., Liu, Yuliang, Guo, Y., Liu, C., Li, Yiran, Chen, L., Li, Yuanyuan, Hua, C., Liu, T., Wang, Z., Xie, J., Wang, L., Petäjä, T., Bianchi, F., Qi, X., Chi, X., Paasonen, P., Liu, Yongchun, Yan, C., Jiang, J., Ding, A., and Kulmala, M. (2024). Iodine oxoacids and their roles in sub-3 nm particle growth in polluted urban environments. *Atmospheric Chemistry and Physics* 24 (3):1873–1893. doi:10.5194/acp-24-1873-2024.

Zhao, B., Donahue, N.M., Zhang, K., Mao, L., Shrivastava, M., Ma, P.-L., Shen, J., Wang, S., Sun, J., Gordon, H., Tang, S., Fast, J., Wang, M., Gao, Y., Yan, C., Singh, B., Li, Z., Huang, L., Lou, S., Lin, G., Wang, H., Jiang, J., Ding, A., Nie, W., Qi, X., Chi, X., and Wang, L. (2024). Global variability in atmospheric new particle formation mechanisms. *Nature* 1–8. doi:10.1038/s41586-024-07547-1.

Zhao, B., Shrivastava, M., Donahue, N.M., Gordon, H., Schervish, M., Shilling, J.E., Zaveri, R.A., Wang, J., Andreae, M.O., Zhao, C., Gaudet, B., Liu, Y., Fan, J., and Fast, J.D. (2020). High concentration of ultrafine particles in the Amazon free troposphere produced by organic new particle formation. *Proceedings of the National Academy of Sciences* 117 (41):25344–25351. doi:10.1073/pnas.2006716117.

Zhu, Z., Du, X., and Collins, D.R. (2025). Direct measurement of the growth of small particles in ambient air using captive aerosol chambers. *Atmospheric Environment* 340:120915. doi:10.1016/j.atmosenv.2024.120915.

CHAPTER 4

EFFECTS OF AEROSOL PHASE STATE ON NEW PARTICLE FORMATION AND GLOBAL AEROSOL CONCENTRATIONS[3]

4.1. Introduction

Aerosol particles in the atmosphere are important for the radiative balance of Earth's atmosphere through direct scattering and absorption of radiation (Myhre et al., 2013; Forster et al., 2021) as well as serving as sites for cloud-droplet and ice-crystal formation (Albrecht, 1989; Gryspeerdt et al., 2014; Rosenfeld et al., 2014; Twomey, 1974; Demott et al., 2010). Together, the direct scattering and indirect effects of aerosols on clouds remain the largest uncertainty in global radiative forcing (Forster et al., 2021). By serving as cloud condensation nuclei (CCN), aerosol particles directly affect cloud properties such as albedo, lifetime, and precipitation efficiency (Gryspeerdt et al., 2014; Rosenfeld et al., 2014; Twomey, 1974). In general, particles must have diameters larger than ~50 nm to efficiently interact with solar radiation and influence clouds; in addition, particle composition plays a critical role in determining aerosol radiative and cloud interactions. Therefore, it is important to understand the processes governing aerosol size distributions and composition.

The processes of new particle formation (NPF) and growth (together NPF&G) contributes roughly 50% of cloud level CCN globally (Gordon et al., 2017), and it is the dominant source of global total aerosol number (Gordon et al., 2017; Merikanto et al., 2009). NPF involves the formation of new ~1 nm aerosol particles from gas-phase precursors, primarily through clustering of sulfuric acid with one or more other species such as water (Vehkamäki et al., 2002), ammonia

[3]This chapter to be submitted as: "Effects of aerosol phase state on new particle formation and global aerosol concentrations", Samuel E. O'Donnell, Regina Luu, Manabu Shiraiwa, Chongai Kuang, Ashish Singh, Shantanu H. Jathar, Jeffrey R. Pierce.

(Dunne et al., 2016), amines (Johnson and Jen, 2023; Olenius et al., 2017), low-volatility organics (Riccobono et al., 2014; Kirkby et al., 2016, 2023), or iodine oxoacids (He et al., 2023). Once nucleated, particles are subject to one of two fates: (1) continued growth through vapor condensation or, (2) coagulation with larger particles, thus reducing the number of total particles. Rapid growth of nucleated particles is essential for their contribution to CCN concentrations, as longer residence times at smaller sizes increases the likelihood of being scavenged by larger particles. While sulfuric acid is crucial in particle formation and early growth, concentrations are often insufficient to grow particles to CCN sizes. Consequently, many studies have highlighted the importance of oxidation products of anthropogenic and biogenic volatile organic compounds (VOC) for the rapid growth of freshly nucleated particles (Riipinen et al., 2011, 2012; Roldin et al., 2019; Tröstl et al., 2016; Pierce et al., 2011). This secondary organic aerosol (SOA) is vital for the climatic importance of NPF&G, but the complexities of SOA condensation, chemistry, and thermodynamics makes modeling these processes challenging, especially in 3D regional and global models.

The details of how SOA partitions across different particle sizes is critical for determining how SOA contributes to the growth and survival of freshly formed particles. Under certain conditions, the size-dependent SOA condensation can approach two of the limiting cases shown in Figure 4.1: (1) size-dependent condensation of extremely low-volatility organic compounds (ELVOC; $C^* < 10^{-4}\ \mu g\ m^{-3}$) following Fuchs-corrected aerosol surface area, similar to sulfuric acid, and (2) fast size-dependent Raoult's law-based equilibrium partitioning of semi-volatile organic compounds (SVOC; $0.3 < C^* < 300\ \mu g\ m^{-3}$) to liquid-like particles proportional to the aerosol mass size distribution, similar to aerosol water uptake (Riipinen et al., 2011; Pierce et al.,

2011; Zhang et al., 2012). The first mechanism favors the growth of smaller particles due to their greater surface-area-to-mass ratio, whereas the second favors the growth of larger particles due to their greater mass for equilibrium partitioning. Basic equilibrium partitioning involves several implicit assumptions. First, it assumes that particles are liquid-like and exhibit rapid mixing between the surface to the interior of the particle, such that there are no diffusion-related limitations on the uptake of SVOCs into the particle bulk. Second, it assumes there are no reactions occurring in or on the surfaces of particles, whereby SVOCs can react to form lower-volatility species that will remain in the particles. In this work, we explore some of the effects of particle phase state (i.e., liquid vs. solid) on size-dependent SOA condensation and particle growth.

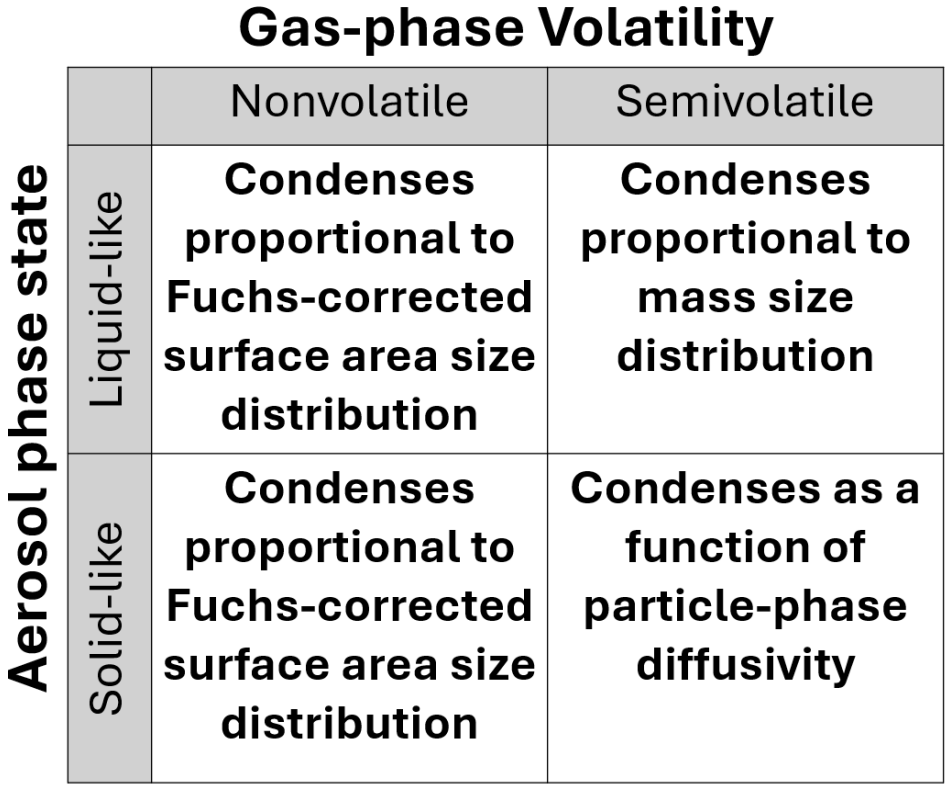

Figure 4.1. Size-dependent condensation behavior for different aerosol phase states (rows) and gas-phase volatilities (columns).

There is a growing body of evidence that organic aerosol particles can exist in more viscous states than liquids, adopting solid-like interiors and glassy exteriors that slow diffusion within the particle (Koop et al., 2011; Reid et al., 2018; Petters et al., 2019). In such cases, diffusion within semi-solid or solid-like particles becomes an additional rate-limiting step for SVOC partitioning, beyond gas-phase production rates and thermodynamic partitioning timescales. Intraparticle diffusion time scales can range from seconds in warm, humid regions to days in cooler, dry regions for 100 nm particles (Luu et al., 2025; Evoy et al., 2019; Riipinen et al., 2012). More viscous phase states effectively reduce the amount of aerosol mass available for equilibrium partitioning by restricting vapor and condensed-phase interactions to near the particle surface (for timescales shorter than the time to diffuse to the center of the particle). Additionally, slow intraparticle diffusion limits the opportunities for heterogeneous and multiphase reactions within particles. As previously discussed, SVOCs partition into liquid-like particles proportional to the aerosol mass size distribution, favoring uptake by larger particles (Figure 4.1, top right). In contrast, because the time scale for intraparticle diffusion is proportional to diameter squared (D_p^2), more solid-like phase states hinder SVOC uptake by larger particles more than by smaller ones. However, this does not mean that size-dependent condensation of SVOCs to solid-like particles converges to the Fuchs-corrected surface area limit. In these cases with semi-solid and solid-like particles the uptake of the small particles relative to the larger particles may be even more favorable than the predicted by the Fuchs-corrected-surface-area limit, but the specific details depend strongly on the particle-phase diffusivity (Figure 4.1, bottom right; Zaveri et al., 2014, 2018; 2022; He et al., 2021; 2025).

While it is currently untenable to represent the details of aerosol size, phase state, mixing, and composition/chemistry, along with the appropriate vapor condensation dynamics in 3D

chemical transport models, studies have leveraged parameterizations to account for these processes. Recent work has developed parameterizations for the accommodation coefficient that account for the effects of particle phase state and vapor volatility on size-dependent SOA condensation behavior, ignoring heterogeneous and condensed-phase chemistry (Shiraiwa and Pöschl, 2021). The accommodation coefficient (α) is used as a scalar to account for observed kinetic limitations of SOA condensation and evaporation on particle surfaces. Shiraiwa and Pöschl (2021) developed the effective accommodation coefficient (α_{eff}) that is similar to α, but accounts for the effective penetration depth of the condensing vapor. The α_{eff} parameter can be incorporated into Fuchs-corrected SOA condensation parameterizations, thus changing the size-dependent SOA condensation behavior.

A growing number of studies have modeled aerosol phase state, viscosity, and SOA equilibrium timescales, while fewer studies have investigated the effects of aerosol phase state on aerosol size distributions. For most of the globe, SOA near the surface appears to be liquid-like, while SOA in dry regions and in the mid- to upper-troposphere appears to be a glassy solids (Luu et al., 2025; Shiraiwa et al., 2017; Zhang et al., 2024). The patterns of aerosol phase state have been found to align with observations, as well as the expected aerosol phase state based on chamber experiments (Zhang et al., 2024; Zaveri et al., 2018). Accounting for aerosol phase state and bulk-diffusion-limited SOA condensation has led to better agreement between measured and modeled aerosol size distributions (Zaveri et al., 2018; He et al., 2021, 2025; Hodshire et al., 2018). Additionally, Zaveri et al. (2022) was able to corroborate experimental findings of diffusion-limited SOA condensation through an analysis of aircraft data and modeling in an urban plume over the Amazon. Importantly, Zaveri et al. (2022) found that the size-dependence of the gas-particle equilibration timescale was important for rapidly growing nucleation mode particles to

sizes at which they could act as cloud condensation nuclei (CCN). Contrarily, He et al. (2025) found little sensitivity of aerosol growth to prescribed aerosol phase state, perhaps due to slow gas-phase chemistry and longer timescales for partitioning in an urban plume relative to chamber experiments. This body of evidence highlights the potential importance of considering the aerosol diffusion limitations for the evolution of aerosol size distributions, but more work is needed to unravel the potential implications for aerosol number, size, and climatic importance.

Given the limited number of studies investigating the effects of diffusion-limited size-dependent SOA condensation on aerosol size distributions in 3D models, this work aims to further investigate some of the implications of size-dependent condensation on aerosol number and size in a global and regional context. In Section 4.2, we introduce the aerosol size distribution measurements used in this work, along with the 3D model to represent aerosol processes in the atmosphere. We also discuss updates to the model incorporating an effective accommodation coefficient parameterization based on Shiraiwa and Pöschl (2021). In Section 4.3, we discuss the global changes in aerosol number, as well as changes from a regional model simulation over the south-central United States. This section concludes with two case studies that illustrate the impact of size-dependent SOA condensation on new particle formation events. In Section 4.4, we discuss the limitations and sources of uncertainty in this work, and in Section 4.5, we discuss the implications and conclusions from this work.

4.2. Methods

4.2.1 Aerosol size distribution measurements

4.2.1.1 Southern Great Plains

Aerosol size distribution measurements were collected from the Atmospheric Radiation Measurement (ARM) Southern Great Plains (SGP) observatory, located in north-central Oklahoma (36.60°N, 97.48°W). The SGP site is primarily surrounded by agricultural land, with intermittent agricultural and rangeland burning, but it is influenced by air masses from a diversity of rural and anthropogenic origins (Liu et al., 2021; Shrivastava et al., 2024; O'Donnell et al., 2025). Organic aerosol (OA) is a significant contributor to submicron aerosol mass at the SGP site, with non-trivial portions of OA attributed to biomass burning during fall, winter, and springtime (Parworth et al., 2015). The data used in this study span from 1 December 2018 to 1 December 2019, in order to capture a full year of aerosol size distributions.

The current generation of the Aerosol Observing System (AOS) has been stationed at the SGP observatory since November 15, 2016, and has been making semi-continuous measurements of particle size distributions from that time to the present. As part of the AOS, a TSI Inc. Model 3938 scanning mobility particle sizer (SMPS) was deployed to measure particles with electrical mobility diameters between 10 and 500 nm across 106 size bins (Singh and Kuang, 2024). Particles entering the AOS SMPS system are given a known charge distribution by a bipolar aerosol charger (TSI Inc. Model 3077A), classified by a long column differential mobility analyzer (DMA; TSI, Inc. Model 3081a) based on their electrical mobility, and finally counted by a condensation particle counter (CPC; TSI Inc. Model 3772) at the given electrical mobility. The measurement cycle for

the SMPS was 5-minutes, and the sample flow was dried to a relative humidity below ~40% using a Nafion dryer (Perma Pure Inc. PD-07018T).

4.2.1.2 CACTI

During the Cloud, Aerosol, and Complex Terrain Interactions (CACTI) field campaign the ARM mobile facility (AMF) was deployed at a site just to the east of the Sierras de Córdoba mountain range of north-central Argentina, from 1 October 2018 through 30 April 2019. Aerosol size distribution measurements were collected using a scanning mobility particle sizer (SMPS; Model 3938; Singh and Kuang, 2024). The SMPS deployed during CACTI is the same model as that used at the SGP observatory, therefore, refer to Section 4.2.1.1 for the details on SMPS operation. For this work, we use the data collected from 1 December 2018 through 1 March 2019, as this period overlaps with our analysis window.

4.2.2 GEOS-Chem-TOMAS model

To simulate aerosol size distributions from 1 December 2018 to 1 December 2019, we used the GEOS-Chem chemical transport model (version 14.3.0, 2024) coupled with the TwO Moment Aerosol Sectional (TOMAS) microphysics module (GC-TOMAS). TOMAS represents particle sizes from 3 nm to 10 μm across 15 size sections. We ran GC-TOMAS at 4° x 5° resolution with 47 vertical levels driven by NASA's Global Modeling and Assimilation Office MERRA-2 meteorology, as well as at 0.25° x 0.3125° resolution with 47 levels (hereafter referred to as nested simulation) over the United States (US) midwest using GEOS Forward Processing (GEOS-FP) meteorology. Output from the 4° x 5° simulation serves as the boundary conditions for the nested simulation. The latitude and longitude bounds for the nested simulations are 110°W to 85°W and 25°N to 45°N. All simulations were initialized using output files from pre-spun-up simulation;

however, we still allow for one month and two weeks of additional spin-up time prior to the analysis period for the 4° x 5° and 0.25° x 0.3125° simulations, respectively.

The TOMAS microphysics package is used to simulate size-resolved aerosol processes and it is set up as 13 logarithmically spaced, mass-quadrupling size sections ranging from 3 nm to 1 μm, with two extra size sections from 1-10 μm. In each size section, the total number of particles is tracked, along with the mass of sulfate, hydrophilic and hydrophobic organic aerosol, internally and externally mixed black carbon, sea salt, dust, nitrate, ammonium, and aerosol water. TOMAS simulates changes in each size section due to nucleation, irreversible sulfate and SOA condensation (see Section 4.2.3), coagulation, primary emissions, and dry and wet deposition. Primary organic aerosol (POA) in GC-TOMAS is assumed to be entirely non-volatile, and SOA condenses using the fixed-yield approach ("simple scheme") from Pai et al. (2020). The inorganic nucleation mechanisms are from Dunne et al. (2016), and the organic nucleation mechanisms are from Riccobono et al. (2014), with the temperature corrections from Yu et al. (2017). In previous work (O'Donnell et al., 2025), we found an improved model to measurement agreement when the organic and total inorganic nucleation rates were scaled up by 100 and 1000, respectively. These scaling factors are likely necessitated by the lack of representing other nucleation pathways, such as those involving amines (Johnson and Jen, 2023; Yu et al., 2012; Olenius et al., 2017), iodine (He et al., 2023; Baccarini et al., 2020), and organics (Zhao, et al., 2024; Kirkby et al., 2016, 2023). The scaling introduces uncertainty to our results, and, because of this, we do not draw conclusions about specific nucleation mechanisms. Further details of the implementation of the nucleation mechanisms can be found in O'Donnell et al. (2025).

GC-TOMAS uses a variety of source-specific emission inventories for gas and aerosol species. The Community Emissions Data System (CEDS) provides anthropogenic emissions of

NO_X, CO, SO_2, NH_3, non-methane VOCs, black carbon, and organic carbon. Biomass burning emissions are from the Quick-Fire Emissions Dataset (QFED) which was found to provide better agreement with observations at the SGP observatory (O'Donnell et al., 2025). The emissions of black carbon and organic aerosol are both source- and size-dependent, following Kodros and Pierce (2017). Sea salt emissions are temperature dependent, following Jaeglé et al. (2011), and emissions of dust are based on the Dust Entrainment and Deposition (DEAD) model from Zender et al. (2003).

4.2.3 Phase state and the effective accommodation coefficient

The accommodation coefficient (α; $0 \leq \alpha \leq 1$) is a scaling factor for the condensation and evaporation rates of vapors to/from particles in the kinetic size regime, and it is often used to account for the observed partitioning rate limitations of SOA (Shiraiwa and Pöschl, 2021, Zaveri et al., 2014). However, treatment of α is generally rudimentary as it often does not have a physical coupling to the kinetic limitations of diffusion within the particle. The effects of particle-phase diffusivity on aerosol condensation are trivial for liquid-like particles that have rapid surface-bulk mixing timescales; however, for glassy or viscous particles, the timescale for a condensing vapor to mix from the surface to the interior of the particles becomes non-negligible. The effective accommodation coefficient (α_{eff}) is functionally similar to α, but it accounts for the kinetic limitations of diffusion within the particles. The details of deriving α_{eff} can be found in Shiraiwa and Pöschl (2021) and Luu et al. (2025), but we will provide an overview here including the necessary details and modifications for inclusion in GC-TOMAS.

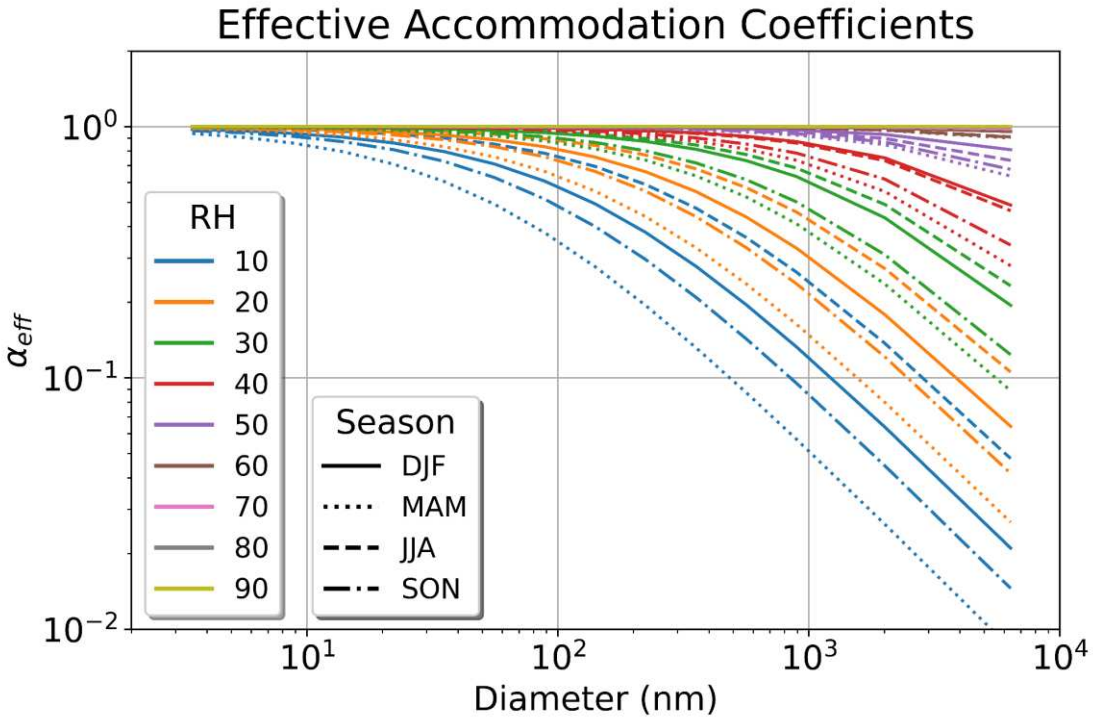

Figure 4.2. Effective accommodation coefficient (α_{eff}) versus particle diameter plotted at different relative humidity values (colors) for the four seasons (line styles). The seasonal values are calculated using the seasonal average volatilities and temperature at the SGP observatory.

To estimate the glass transition temperature (i.e., the temperature at which a particle becomes a glassy semisolid), we use the following parameterization (Li et al., 2020):

$$T_g = 289.10 - 16.50 \times log_{10}(C^0) - 0.29 \times [[log_{10}(C^0)]^2 + 3.23 \times log_{10}(C^0)(O{:}C)] \quad (1)$$

where C^0 is the saturation mass concentration at 298 K for the pure compound, assuming that C^* equals C^0 with ideal mixing conditions. For this work, we assume an $O{:}C$ of 1.5 which is representative of a highly oxidized organic species and is typical for the majority of the troposphere (Aiken et al., 2008; Lambe et al., 2011), and offline calculations show that the effective accommodation coefficient is not very sensitive to $O{:}C$ relative to other parameters. We then

calculate the glass transition temperature for particles that consist of a mixture of pure organic compounds and water using:

$$T_g(\omega_{org}) = \frac{(1-\omega_{org})\times T_{g,w} + (1/k_{GT})\times \omega_{org} T_{g,org}}{(1-\omega_{org}) + (1/k_{GT})\times \omega_{org}} \quad (2)$$

where $T_{g,w}$ is the glass transition temperature of pure water (136 K), k_{GT} is the Gordon-Taylor constant (2.5), and ω_{org} is the organic mass fraction of SOA. ω_{org} is calculated by:

$$\omega_{org} = \left(1 + \frac{\kappa \varphi_w}{\varphi_{SOA}((1/RH)-1)}\right)^{-1} \quad (3)$$

We assume the hygroscopicity parameter (κ) is assumed to be 0.1 which is representative of aged organic species in the atmosphere (Petters and Kreidenweis, 2007; Pringle et al., 2010). Notably, we use a κ representative of only organic species to represent water uptake to particles, despite global mean κ values having been found to be significantly higher (Pringle et al., 2010; Cerully et al., 2015). This assumes that aerosol is entirely externally mixed, and water uptake by inorganic aerosol components does not affect particle phase state. This was done to maintain consistency with Luu et al. (2025), but this assumption will tend to lower aerosol water uptake, increase particle viscosity, and increase the effects of the effective accommodation coefficient. The density of water (φ_w) and the density of SOA (φ_{SOA}) is assumed to be 1.0 and 1.4 g cm^{-3}, respectively.

In order to derive particle viscosity and diffusivity, the Vogel temperature (T_0) must first be calculated. The Vogel temperature is a hypothetical temperature at which viscosity becomes infinite (i.e., completely solid), and it is calculated as follows:

$$T_0 = \frac{39.17 \times T_g(\omega_{org})}{D + 39.17} \quad (4)$$

where D is the fragility parameter and is assumed to be 10 (DeRieux et al., 2018). We can then derive particle viscosity (η; Pa s) using:

$$\eta = EXP\left(-5 + 0.434 \times \frac{T_0 D}{T - T_0}\right) \quad (5)$$

The bulk diffusion coefficient is then calculated using the Stokes-Einstein equation:

$$D_b = \frac{kT}{6\pi a \eta_c} \times \left(\frac{\eta_c}{\eta}\right)^{\xi} \quad (6)$$

where k is the Boltzmann constant ($k = 1.380 \times 10^{-23}$ J/K), η_c is the crossover viscosity ($\eta_c = 1 \times 10^{-3}$ Pa s), a is the hydrodynamic radius of a diffusing species ($a = 0.38$ nm), and ξ is an empirically fit parameter ($\xi = 0.93$; Evoy et al., 2019). Finally, the effective accommodation coefficient (α_{eff}) is derived using:

$$\alpha_{eff} = \alpha_s \frac{1}{1 + \frac{\alpha_s \omega C^0}{4 D_b \rho_p} \times \frac{r_p}{5} \times 10^{-12}} \quad (7)$$

where α_s is the surface accommodation coefficient which we assume to be 1.0, ω is the mean thermal velocity ($\omega = 2 \times 10^4$ cm s^{-1}), C^0 is the volatility of the condensing species, and r_p is the particle radius.

As mentioned, GC-TOMAS uses the "simple scheme" for OA formation. In other words, GC-TOMAS does not explicitly resolve the volatility of either the gas-phase or condensed-phase organics species, therefore, we used seasonally averaged particle- and gas-phase organic volatilities from a GEOS-Chem simulation using the "complex OA scheme" at the SGP observatory (Table 1; Luu et al., 2025). Figure 4.2 shows α_{eff} versus particle diameter using the seasonal averages for volatility and temperature from Table 1 at different relative humidities. To isolate the effects of the average volatility values, Figure C1 shows α_{eff} using a constant temperature of 280.0 K, showing that α_{eff} is substantially higher during DJF than during the other seasons in part due to the higher volatility of the condensed phase (Table 1) at the reference temperature (300 K) leading to less size-dependence. Figure C1 illustrates that the choice of volatilities for particles and gases will have limited impact on our results, with the exception of during the DJF season. While Figure 4.2 uses the seasonal average temperature, the α_{eff} calculation in the GC-TOMAS simulations uses the temperature and relative humidity from MERRA-2 and GEOS-FP in order to resolve the dominant influences on α_{eff}. As mentioned, gas- and particle-phase volatility span many orders of magnitude, therefore, our assumption of spatially and temporally invariant values at 300 K for each is a limitation of this work.

Table 1. Seasonal average particle-phase volatility, gas-phase volatility, and temperature. The volatilities are at the reference temperature of 300 K.

Season	DJF	MAM	JJA	SON
Particle C^* (300K) [μg m^{-3}]	1.15	0.29	0.25	0.37
Vapor C^* (300K) [μg m^{-3}]	45.73	26.69	14.64	29.63
T_{mean} [K]	277.91	288.33	300.07	288.97

GC-TOMAS utilizes a fixed yield approach for irreversible OA condensation, meaning the amount of organic mass that will condense during a model timestep is predetermined. By implementing the effective accommodation coefficient, the total mass of OA being added to the aerosol size distribution is not being altered, rather, the sizes at which mass condenses is altered. This approach is fundamentally unphysical, as, for vapors with a distribution of volatilities, low-volatility vapors will condense according to the Fuchs-corrected surface area while SVOCs will condense according to the mass size distribution for liquid-like particles. In other words, multiple regimes of SOA condensation are happening simultaneously in the real atmosphere, whereas we are forcing regime-specific SOA condensation for all SOA mass. This approach incorporates an updated parameterization of size-dependent condensation based on relative humidity, temperature, and assumed volatilities; however, without explicitly representing the distribution of SOA volatilities, we do not resolve potential spatio-temporal variation in SOA condensation driven by long equilibrium timescales for condensing vapors. In other words, the updated parameterization in GC-TOMAS includes size-dependent condensation, but that size dependent condensation may be occurring upwind or downwind of where it would occur if longer condensation timescales were allowed.

4.3. Results

4.3.1 Changes in global surface level aerosol number

Figure 4.3 shows the global annual-mean surface percent change in the number concentration of particles in the 3-20, 20-80, 80-200, and 200-1000 nm diameter ranges between the simulation with the updated effective accommodation coefficient and the simulation with an accommodation coefficient of 0.65 that is constant across all sizes at all times. Figure 4.3a shows a global decrease in the surface level 3-20 nm size range due to decreases in NPF. The decrease in NPF is driven by increased coagulational losses and increased particle growth rates of small particles to larger sizes, in turn contributing to increases in the condensation and coagulation sinks. The increased particle survival is driven by the effective accommodation coefficient reducing the vapor sink of larger particles (Figure 4.2), thus allowing rapid growth of small particles to sizes where they are less likely to be scavenged by coagulation. As the freshly nucleated particles grow, they increase the condensation sink which then suppresses further NPF from occurring. The changes are especially noticeable in dry regions (e.g., Great Australian desert and southwest United States) where the effective accommodation coefficient has greater differences between small and large particles (Figure 4.2). There are significant increases in the number concentration of 20-80 nm particles (Figure 4.3b) due the increased particle survival into the 20-80 nm size range from the 3-20 nm size range. While the decreases in the concentration of the smallest particles are more spatially homogeneous, the increases in the 20-80 nm size range are concentrated in dry regions where the effects of particle phase state are the most pronounced.

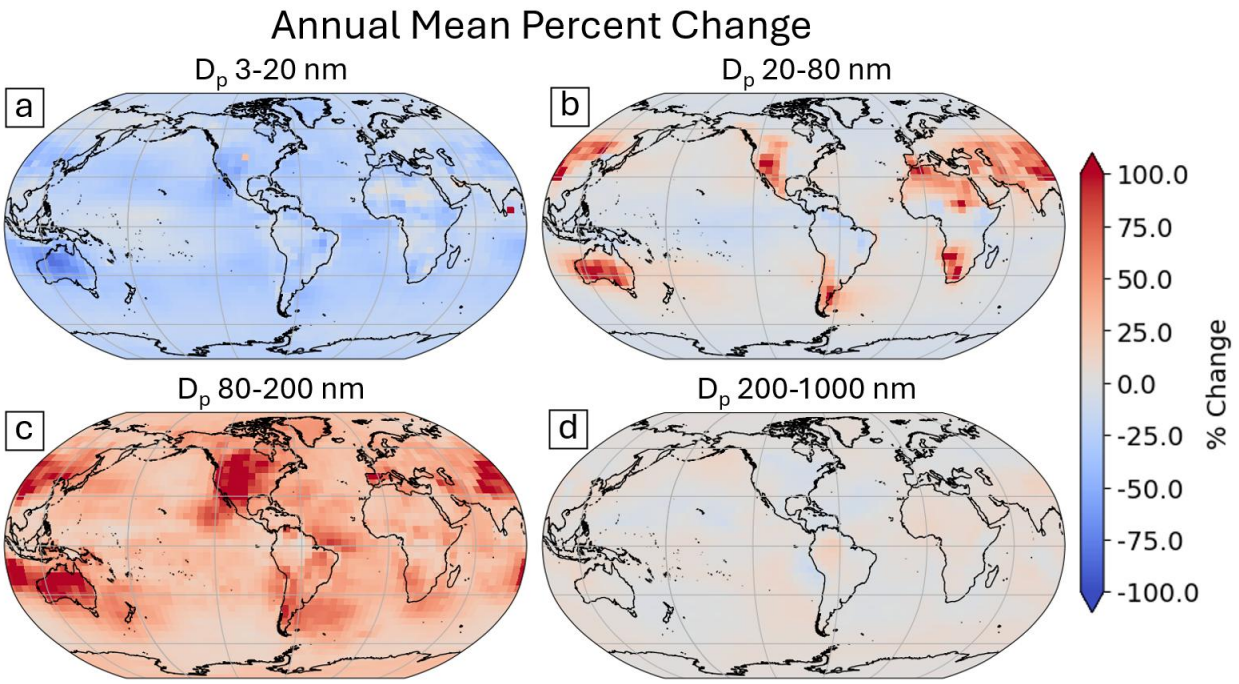

Figure 4.3. Surface maps of the percent change of number between the updated and base simulations for (a) 3-20, (b) 20-80, (c) 80-200, (d) and 200-1000 nm diameter range.

The most significant percent changes in the surface annual mean number concentration are in the 80-200 nm size range. Similar to the 20-80 nm size range, the changes in the 80-200 nm size range generally correspond with the regions of low relative humidity (Figure C2); however, there are increases in regions with higher relative humidity that are likely due to horizontal advection or subsidence (discussed next). The more spatially homogeneous changes are in part due to the 80-200 nm size range maintaining the history of enhanced growth from the 20-80 nm size range as the particles are advected downwind. Notably, the more homogeneous changes in the 3-20 nm size range are partially driven by the more homogeneous changes in the 80-200 which increase the coagulation sink for small particles. The substantial increase in the 80-200 nm size range is driven by the increased survival of freshly nucleated particles growing into this size range from the Aitken mode. Finally, Figure 4.3d shows the percent change in the surface level concentration of 200-

1000 nm particles which shows substantially smaller changes than the other size ranges. Changes in the largest size range are buffered from changes in condensation behavior, as growth from only condensation into this size range takes significantly longer than other processes affecting aerosols in this size range (e.g., coagulation, wet deposition, and emissions).

4.3.2 Vertical changes in global aerosol number

While the surface changes in aerosol number shown in Figure 4.3 generally follow the spatial patterns of relative humidity (Figure C3), there are some changes in regions with high relative humidity, especially in the 80-200 nm size range, that indicate potential changes vertically in the atmosphere. Figure 4.4 shows zonal mean percent changes over the same time period and size ranges as Figure 4.3, and it shows changes principally in the mid-latitude free troposphere. The 3-20 nm size range (Figure 4.4a) changes are consistent with the surface plots showing a general decrease in small particles in the updated simulations, but the most significant decreases are in the descending branch of the Hadley Cell (25° to 35° N, 25° to 35° S; Hadley, 1735; Dima and Wallace, 2003). The subsidence regions generally have lower relative humidity (Figure C3), therefore, the effects of the effective accommodation coefficient are most significant in those regions. The 20-80 nm size range (Figure 4.4b) shows similar spatial changes as the small particles, but with the opposite sign. The updated effective accommodation coefficient causes increases in the Aitken mode number concentration, principally in the regions with large subsidence which partially helps to explain the changes at the surface (Figure 4.3b).

As with the surface changes, the most significant zonal mean changes are in the 80-200 nm size range, which shows a ubiquitous increase in the number of particles (Figure 4.4c). The greatest changes are around the lower descending branch of the Hadley Cell, likely near the top of the planetary boundary layer. The increases in the 80-200 nm size range also extends to the higher

latitudes in the upper atmosphere, corresponding to the decreases in the 3-20 nm number concentration in the same region. Finally, the changes in the 200-1000 nm number concentration are substantially lower than the other size ranges (Figure 4.4d), likely due to other processes driving growth into this size range (i.e., primary emissions other than aerosol condensation.

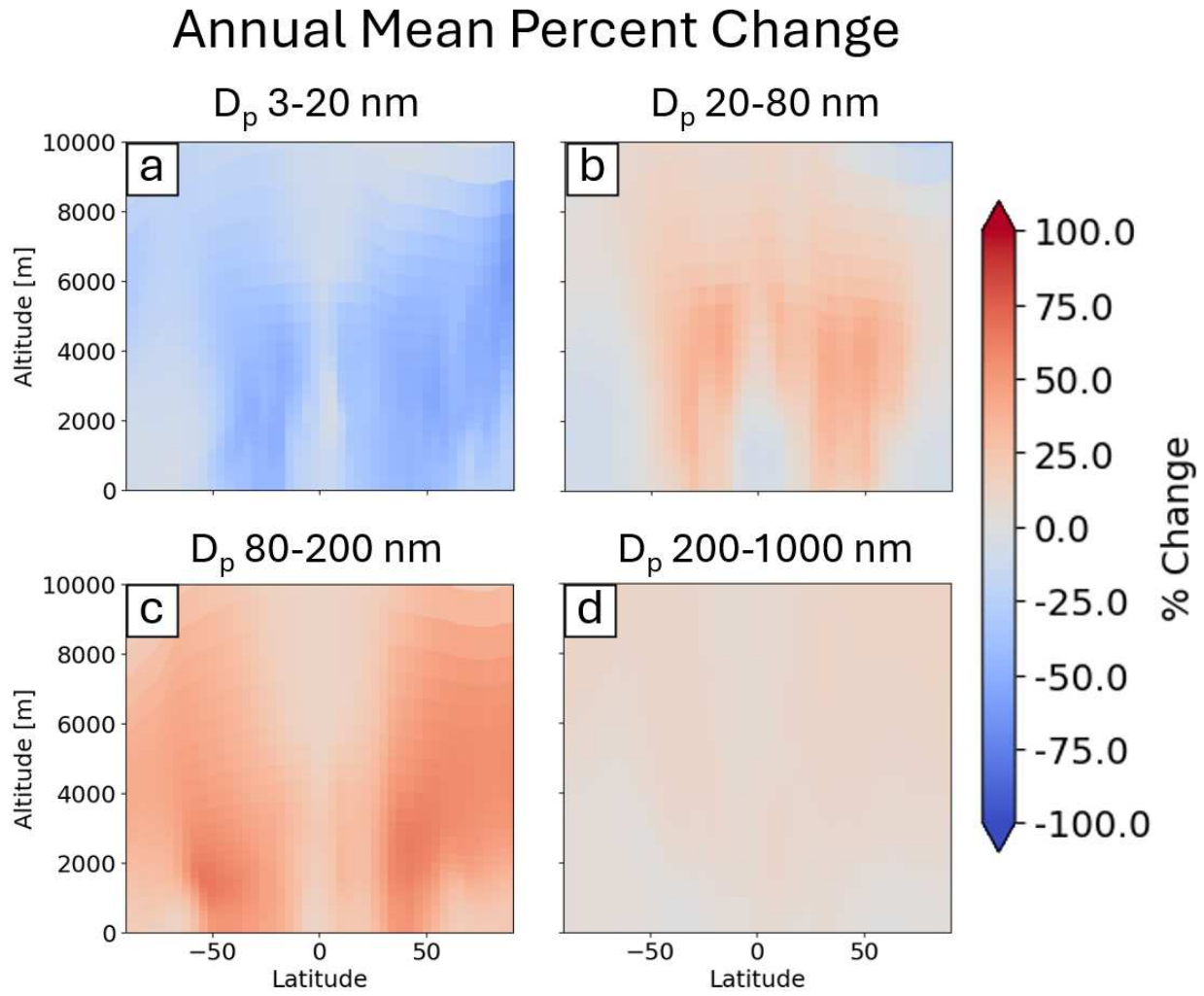

Figure 4.4. Annual zonal mean percent change between the updated simulation and the base simulation for the 3-20 (a), 20-80 (b), 80-200 (c), and 200-1000 (d) nm diameter range.

The aerosol changes in Figure 4.3 and Figure 4.4 illustrate a marked shift in the mean diameter of particles with some regions (e.g., southwest United States) having almost a two-fold increase in 80-200 nm particles in the simulation with the updated effective accommodation

coefficient. Additionally, the updated simulation shows a global decrease in the 3-20 nm number concentration, likely due to decreases in mean nucleation rates, faster growth out of the 3-20 nm size range, and increased coagulation sink. Nucleation rates decrease due to the greater survival of freshly nucleated particles to larger sizes, in turn, suppressing further nucleation from occurring. These results do not indicate that NPF and growth is less important for global aerosol number; contrarily, our results highlight that, even with a modest decrease in NPF frequency, the greater survival of freshly nucleated particles can create significant changes in accumulation mode aerosol. The changes in aerosol number are most pronounced in the dry regions of the atmosphere (Figure C2 and Figure C3) where the effective accommodation coefficient has the greatest size dependence (Figure 4.2).

4.3.3 Seasonal changes in aerosol number

Aerosol processes in the atmosphere, especially NPF and growth, often vary by season, therefore, Figure 4.5 shows the mean surface percent change in the 80-200 nm size range for the four meteorological seasons (winter as DJF, spring as MAM, summer as JJA, and fall as SON). We chose this size range as it had the greatest percent changes (Figure 4.3), and would therefore best highlight the seasonal changes. The greatest changes globally in the 80-200 nm number concentration tend to be in the shoulder seasons (MAM and SON) in the midlatitudes; however, there are persistent changes in all seasons that track with surface relative humidity (e.g., eastern China, southwest United States, and Australia; Figure C2). Notably, there are changes that do not track with surface relative humidity, like the changes extending off the southwest coast of Mexico, potentially the result of the tropical trade winds advecting enhanced number concentrations of particles from North America over the Pacific. The changes could also be attributed to subsidence in the midlatitudes. Additionally, the changes off the southeast coast of Argentina are potentially

the result of advection by westerly winds or vertical subsidence, especially during the MAM and SON seasons.

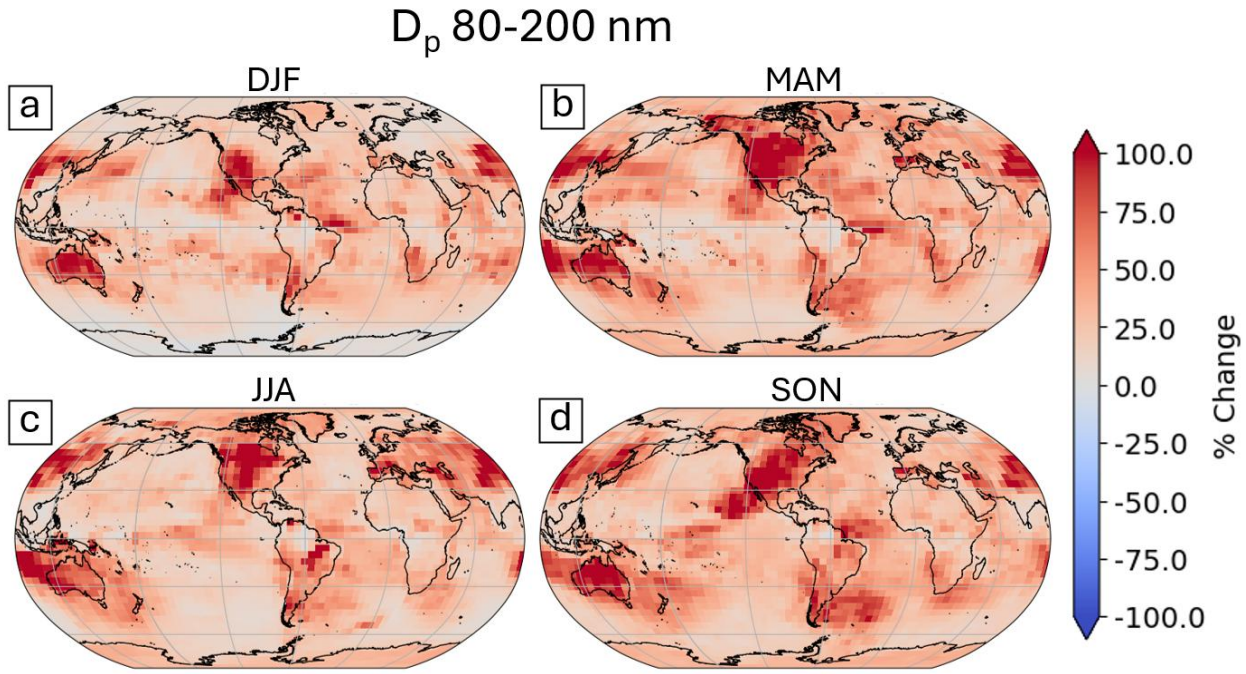

Figure 4.5. Seasonal average maps of the percent change in the surface level number concentration of 80-200 nm particles between the updated simulation and the base simulation.

4.3.4 Regional changes over south-central United States

The results from the nested simulation over the United States agree with the results from the 4° x 5° simulation, both showing a decrease in the surface number concentration of 3-20 nm particles and an increase in 20-80 and 80-200 nm particles concentrations (Figure 4.6). The changes in the 200-1000 nm size range were substantially smaller than the other size ranges, therefore, we have left them out for brevity. The decrease in 3-20 nm particles is generally uniform across the land surface, though, the results show an increase in 3-20 nm particle concentrations over the Gulf of Mexico (Figure 4.6a). In the 20-80 nm size range, the changes are the most

significant over the western portion of the simulation domain (i.e., southern Colorado, New Mexico, and Northern Mexico) where the changes are in excess of 100% (Figure 4.6b). These regions generally have lower relative humidity (~10-40%, Figure C4) than other parts of the domain, therefore, the effects of the updated effective accommodation coefficient are significant. Finally, the 80-200 nm size range shows general increases in number concentration in the updated simulation (Figure 4.6c). The greatest changes are concentrated around Arkansas (US) and the surrounding states, with many other parts of the domain showing significant changes occurring as well.

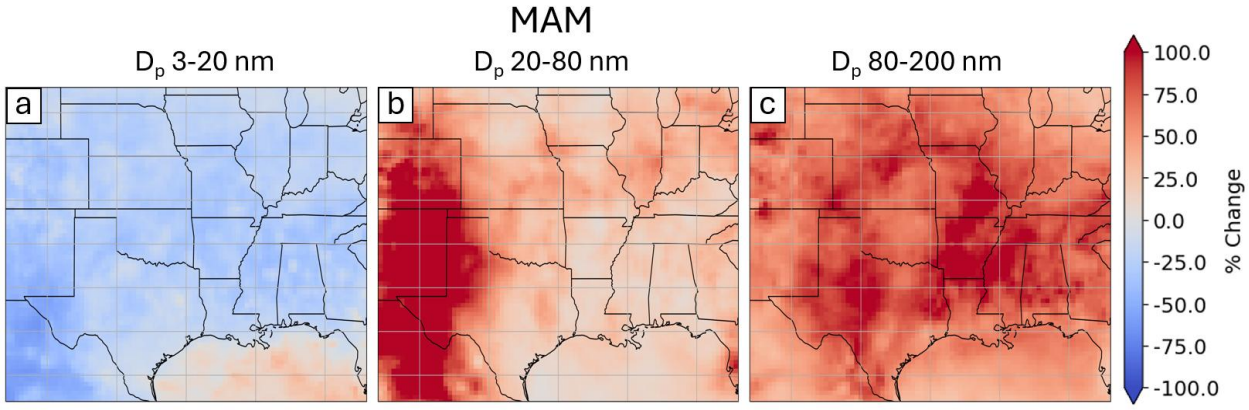

Figure 4.6. Seasonal average (MAM) percent change in surface level aerosol number concentration in the 3-20 (a), 20-80 (b), and 80-200 (c) nm diameter range.

4.3.5 Comparisons with measurements

4.3.5.1 CACTI

Figure 4.7a shows average aerosol size distributions from the 4° x 5° simulations, as well as from the SMPS measured during the CACTI campaign in Argentina. The black-dashed line indicates the size distribution from the SMPS showing a mean diameter of ~40.0 nm and a peak number concentration of ~4500 cm^{-3}. The green line is the average size distribution from the base

model simulation at the AMF site during CACTI. The base model produces an average size distribution with a mean diameter of ~23.0 nm and a peak number concentration of ~4100 cm^{-3}. Finally, the blue line is the average size distribution from the updated simulation with a mean diameter of ~33.0 nm and a peak number concentration of ~5000 cm^{-3}.

The simulation with the updated effective accommodation coefficient shows better agreement in mean diameter as well as closer agreement with the number concentration between 3 and 60 nm. However, the updated simulation overpredicts the number concentration of particles between 60 and 200 nm whereas the base simulation produces an average number concentration in that size range closer to the observations. Notably, changing the effective accommodation coefficient does not change the total amount of SOA mass that will condense in a given timestep, therefore, better model-measurement agreement could potentially be reached by scaling the total amount of primary SOA and SOA precursor. Additionally, errors in the model could arise due to the emissions inventories, deposition parameterization, as well as the lack of aqueous phase chemistry.

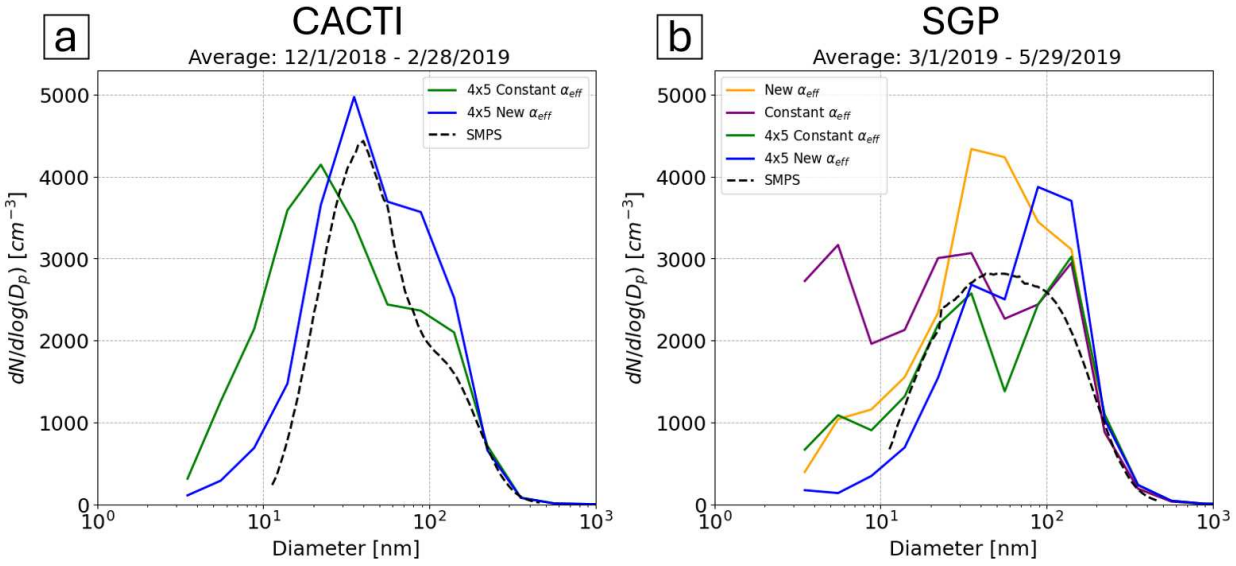

Figure 4.7. (a) Average aerosol size distributions from 1 December 2018 to 28 February, 2019 from the SMPS during CACTI (black dashed line), the "base" 4° x 5° simulation (green line), and the 4° x 5° simulation with the updated effective accommodation coefficient (blue line). (b) Average aerosol size distributions from 3 March 2019 through 29 May 2019 from the SMPS at the SGP site (black line), the "base" 4° x 5° simulation (green line), the updated 4° x 5° simulation (blue line), the "base" 0.25° x 0.3125° simulation (purple line), and the updated 0.25° x 0.3125° simulation (gold line).

4.3.5.2 Southern Great Plains

Figure 4.7b shows a comparison of average aerosol size distributions from four model runs (0.25° x 0.3125° and 4° x 5°; "base" and updated) and the SMPS observations from 3 March 2019 through 29 May 2019. The SMPS aerosol size distribution (black dashed line) has a mode diameter of ~50 nm and a peak number concentration of 2800 cm^{-3}. Both of the 4° x 5° simulations (green and blue lines) show a distinct bimodal distribution, but the updated simulation has substantially more particles in the larger mode. For the nested simulations, the "base" simulation (purple line) aerosol size distribution is trimodal, with peaks at ~5.5, ~30, and ~140 nm. The peak number concentration in each mode in the "base" nested simulation is similar to the unimodal peak in the observations; however, the integrated number of particles is substantially higher than the observations. Finally, the updated nested simulation (gold line) has a similar mean diameter as the observations (dry diameter, $D_p \cong 35$ nm), but the total number of particles in the 20-200 nm size range is overpredicted.

4.3.6 NPF event case studies at SGP

In order to illustrate the effects of the effective accommodation coefficient on NPF&G, we have chosen two representative case studies to examine. For the case studies, we are comparing output from the two nested simulations with SMPS data measured at the SGP observatory.

Notably, the model updates do not necessarily lead to improved agreement with measurements on all days, even with the improvements in the mean size distributions (Figure 4.7); however, we highlight two days (4 April and 22 May 2019) where the updated model shows better agreement with observations.

4.3.6.1 NPF event on 28 April

Figure 4.8 shows a comparison of aerosol size distributions from the SMPS (Figure 4.8a), the "base" model (Figure 4.8b), and the updated model (Figure 4.8c) on 28 April 2019. The measurements show a new mode of particles appearing just before 12:00 CST, which grows over the next two hours. Around 14:00 CST, the number concentration of the growing mode rapidly decreases, indicating a potential shift from an air mass with NPF&G occurring to one where less is occurring. For the remaining several hours, new modes of particles appear and disappear in the 20-50 nm size range, perhaps indicating that NPF&G is occurring inhomogeneously in the region.

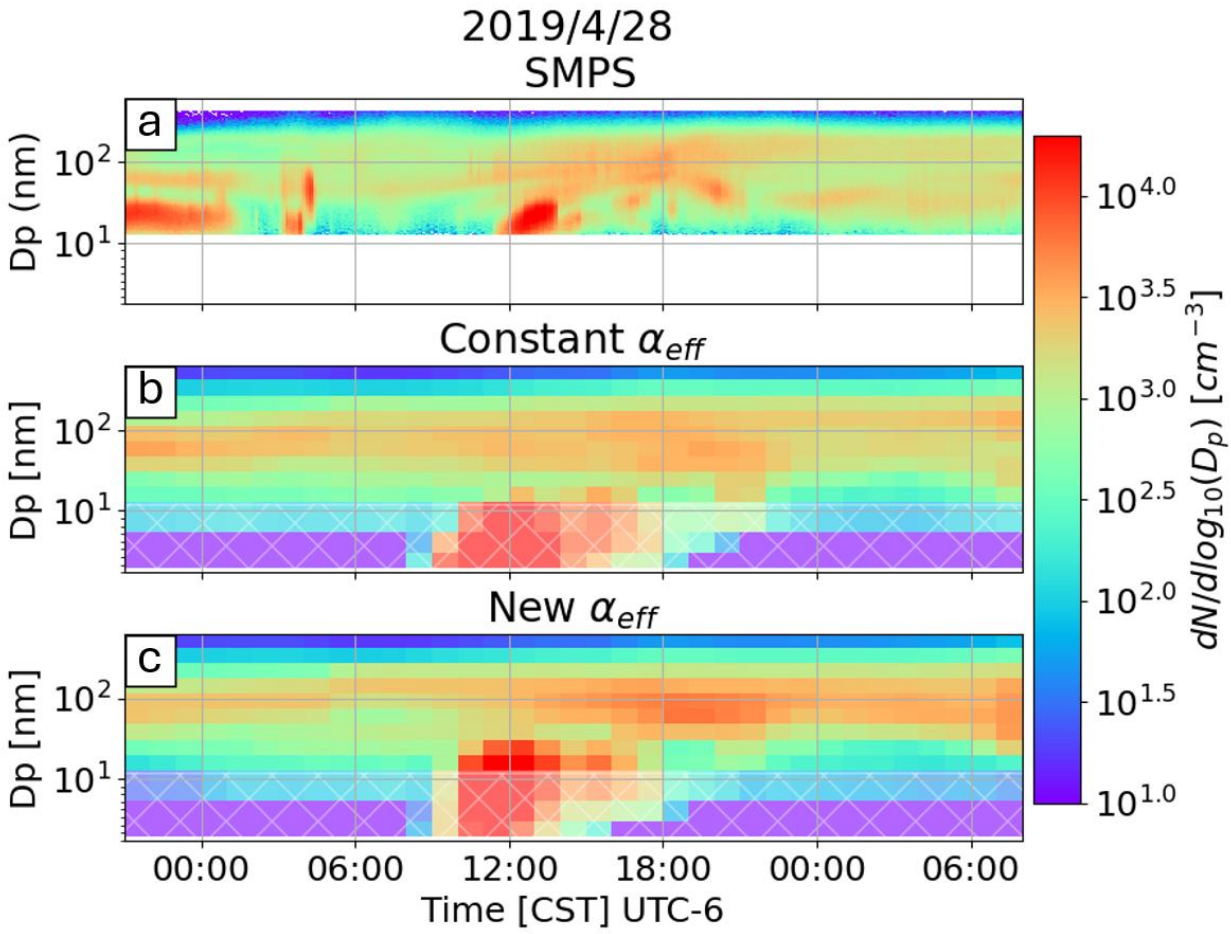

Figure 4.8. (a) Aerosol size distribution measured by the SMPS at the SGP observatory on 28 April 2019. (b) Aerosol size distribution from GC-TOMAS using a constant accommodation coefficient of 0.65. (c) Aerosol size distribution from GC-TOMAS using the updated effective accommodation coefficient. The transparent white patch on the (b) and (c) panels covers the portion of the size distribution not measured by the SMPS in the top panel.

The aerosol size distribution from the "base" model simulation is shown in the middle panel of Figure 4.8. Below ~11 nm, the size distribution is covered by a white patch to indicate the portions of the modeled aerosol size distribution for which there are no corresponding SMPS measurements. The "base" model simulation shows NPF&G starting around 9:00 CST; however, the particles never grow into the size range of the observations. Based on the typical categorization methods employed for NPF&G studies, this day would likely be categorized as a non-event day

(i.e., no NPF&G occurring) in the model unless measurements extended to smaller sizes, whereas the observations indicate a NPF&G event of some sort. The "base" model does show a NPF&G event where the number concentration of particles decreases rapidly after some growth, similar to the observations; however, the modeled NPF&G event does not grow enough compared with the observations. Notably, the "base" simulation does show particles appearing around ~70 nm just after 18:00 CST, which is consistent with the observations.

The bottom panel of Figure 4.8 shows the aerosol size distribution from the simulation with the updated effective accommodation coefficient. As with the "base" simulation, the updated simulation shows NPF&G starting around 9:00 CST; however, the updated simulation shows these particles rapidly growing to sizes larger than 11 nm by 10:00 CST. The modeled NPF&G event grows into the SMPS size range earlier than indicated by the observations, but the particle growth is more consistent with the observations. The observations indicate larger particles appearing after 18:00 CST which is partially captured by both model simulations, but the updated model appears to capture the peak number concentration of the larger particles better.

4.3.6.2 NPF event on 22 May

The second case study (Figure 4.9) is from 22 May 2019, where the observations (Figure 4.9, top panel) shows a NPF&G event with seemingly continuous particle growth but with varying number concentrations in the growing mode. The NPF&G event initially appears in the SMPS size range around 9:00 CST and steadily grows until 12:00 CST. Just after 12:00 CST, the number concentration of the nucleation mode rapidly decreases from ~10^5 [cm^{-3}] to ~10^4 [cm^{-3}]. The new mode of particles continues to grow throughout the rest of the day. Around 22:00 CST, the number concentration of particles in the 30-100 nm size range increases rapidly, perhaps indicative of a shift to an air mass with more intense NPF&G occurring.

The “base” model simulation (Figure 4.9, middle panel) also indicates NPF occurring around the SGP observatory; however, the event timing is delayed and the particle growth is less than the observations indicate. The model shows particles appearing at ~11 nm around 13:00 CST, whereas the SMPS shows particles appearing around 9:00 CST. It is difficult to ascertain if the modeled particles grow due to the lack of a clear growing aerosol mode and concurrent variation in the number concentration of ~20-80 nm particles. The model does show variations in the number of particles throughout the day, perhaps not entirely in alignment with the observations, but still indicative of varying aerosol processes and concentrations on this day.

Finally, the aerosol size distribution from the simulation with updated effective accommodation coefficient (Figure 4.9, lower panel) also shows particles appearing later than the observations, but the particle growth is more consistent with the observations. As with the “base” simulation, the updated model shows particles appearing in the SMPS size range around 13:00 CST, much later than the observations (9:00 CST). The existing aerosol mode prior to the NPF event is shifted to larger sizes, making the new mode associated with the NPF event clearer. The freshly nucleated particles appear to grow around 15:00 CST, and the number concentration of the new aerosol mode decreases after 18:00 CST. The apparent decrease in particle number could be due to coagulation with the larger aerosol mode, or the decrease could be due to a shift in the air mass passing over the SGP site in the model. The elevated number of particles that appears around 22:00 CST in the observations is better captured by the updated simulation, both in terms of number concentration and mode diameter. The particles appear well within the 30-100 nm size range which is consistent with the observations, whereas the particles in the “base” simulation appear at a smaller size.

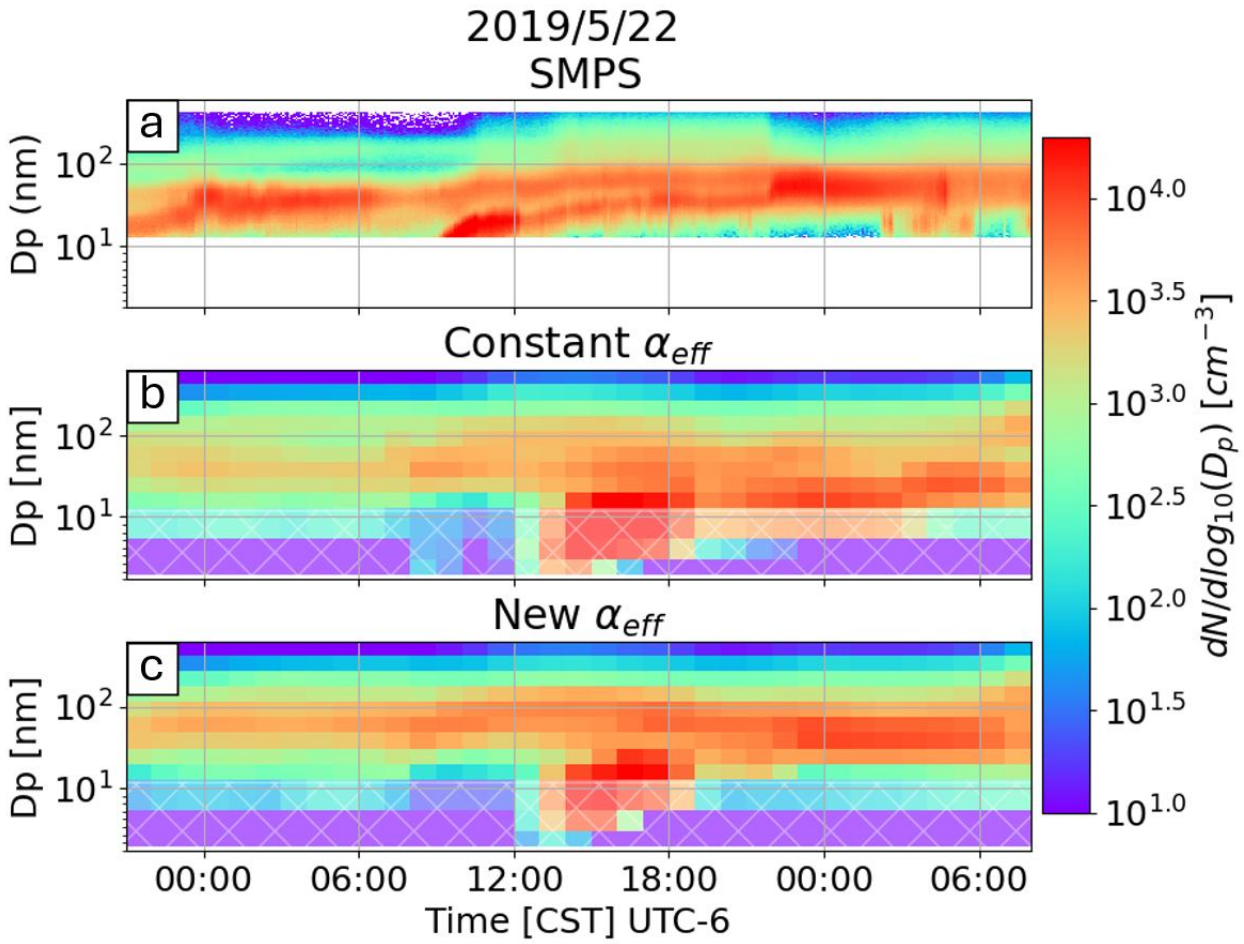

Figure 4.9. (a) Aerosol size distribution measured by the SMPS at the SGP observatory on 22 May 2019. (b) Aerosol size distribution from GC-TOMAS using a constant accommodation coefficient of 0.65. (c) Aerosol size distribution from GC-TOMAS using the updated effective accommodation coefficient. The transparent white patch on the (b) and (c) panels covers the portion of the size distribution not measured by the SMPS in the top panel.

The changes in the aerosol size distributions on 28 April 2019 and 22 May 2019 between the "base" simulation to the updated simulation are consistent with the changes globally and regionally (Figure 4.3, Figure 4.6). Freshly nucleated particles appear to grow more rapidly to larger sizes in the updated simulation. The overall duration and number concentration of the nucleation events are decreased, but the particles that are formed are more likely to grow and increase the number concentration of larger particles. The Aitken and accumulation modes (i.e.,

larger particles) have higher number concentrations of particles, again consistent with the changes seen in the global simulation over the US (Figure 4.6). The updated model appears to improve the representation of aerosol size distributions, both in the mean and for specific NPF events; however, further work is needed to better understand the processes and assumptions that lead to better agreement with observations in the model. Section 4.4 outlines the principal uncertainties in this work, as well as discussion on the implications of various assumptions on the results.

4.4. Uncertainties and Discussion

Organic volatility: The greatest uncertainty in the changes in global aerosol number are from the assumptions made in the effective accommodation coefficient, principally the use of average volatilities for the condensed- and vapor-phase derived at the SGP site for global simulations. Condensed- and vapor-phase volatilities [$\mu g\ m^{-3}$] span many orders of magnitude ($\sim 10^{-5}$ - $10^{5}\ \mu g\ m^{-3}$), therefore, the effective accommodation coefficient parameterization will not capture the specific size dependent condensation behavior for organic species with differing volatilities. The volatilities used in this work should capture the mean condensation behavior of SOA, but this assumption will break down in regions where the mean volatility of organic species is substantially different than SGP. Notably, the greatest changes in aerosol number concentration were generally in the midlatitudes where the SGP values will likely be the most representative. The current configuration of GC-TOMAS does not resolve the volatility of organic species, but this is something that should be explored in the future.

Aerosol hygroscopicity: While we do use constant volatilities, the effective accommodation coefficient is principally dependent on the ambient relative humidity, as water uptake to the aerosol particles drives changes in particle phase state. With this, we assume a constant value of 0.1 for the organic hygroscopicity parameter ($\boldsymbol{\kappa}$), which dictates the assumed

water uptake in the effective accommodation coefficient parameterization. Currently, we do not consider water uptake by inorganic species (e.g., sulfate) in aerosol, which often have higher values of $\boldsymbol{\kappa}$. This assumes that aerosol particles are externally mixed, and this will tend to make particles more solid-like due to less water uptake. The value of $\boldsymbol{\kappa}$ for organic species varies globally (Pringle et al., 2010; Cerully et al., 2015), and our assumption of a $\boldsymbol{\kappa}$ representative of organic species for all aerosol is a limitation. Assuming $\boldsymbol{\kappa}$=0.1 will lead to less water uptake by the aerosol than a higher $\boldsymbol{\kappa}$ that might be more representative of a mixture of aerosol. The lower $\boldsymbol{\kappa}$ will lead to less water uptake, making the particles more solid-like, thus increasing the effects of the effective accommodation coefficient on aerosol condensation. Luu et al. (2024) tested changing $\boldsymbol{\kappa}$ by ±50% and found T/T_g changed by ~5% and ~10% for increasing and decreasing $\boldsymbol{\kappa}$, respectively. Future work should test the assumption of externally mixed aerosol, and include spatially varying $\boldsymbol{\kappa}$ values in order to better resolve water uptake and phase state of aerosol.

Nucleation mechanisms: Another source of uncertainty in this work is associated with the limitations of the nucleation mechanisms in GC-TOMAS. We include the inorganic nucleation mechanisms from Dunne et al. (2016) and the organic-sulfuric acid mechanism from Riccobono et al. (2014), but other nucleation mechanisms have been found to be important in certain environments (Zhao et al., 2024). Additionally, the scaling of the total inorganic (1000x) and organic-sulfuric acid (100x) nucleation rates is potentially necessitated by not resolving other nucleation mechanisms; however, the scaling could also be necessary for the given model architecture. Given the nucleation mechanisms and scaling used in this work, we do not make conclusions about specific nucleation mechanisms. Similar work in the future will benefit from the inclusion of other nucleation mechanisms in order to resolve potential changes throughout the atmosphere.

The assumptions and associated uncertainties discussed in this section ultimately limit the robustness of our conclusions; however, this work still illustrates a novel approach of including aerosol phase state parameterization into a 3D chemistry-aerosol model. The precise changes in the aerosol size distribution over short periods of time at specific locations are likely not well represented. The general shifts in the size distributions (Figure 4.7) as well as the global changes in number concentration (Figure 4.3) align with the theories of kinetically and phase state limited SOA condensation, and future work will do well to explore the many implications of these processes on aerosol populations.

4.5. Conclusions

In this work, we present an analysis of global and regional (south-central U.S.) aerosol number and size distributions using a size-dependent SOA condensation parameterization that accounts for kinetic diffusion limitations in aerosol particles using the GC-TOMAS model. We test the effects of this parameterization on seasonally averaged global aerosol number as well as regional aerosol concentrations over the United States. We also analyze two representative case studies of days where NPF occurs in order to illustrate the effects of the phase state and size-dependent SOA condensation on the growth of freshly nucleated particles.

Using the updated effective accommodation coefficient resulted in increases in the 20-80 nm size range in dry regions, where particles are more likely to be solid-like. Global mean surface concentrations in the 3-20 and 80-200 nm size ranges show more homogeneous decreases and increases, respectively, with the largest changes again occurring in dry regions. The increases in the 80-200 nm size range reflect the persistence of earlier growth in the smaller size ranges (D_p < 80 nm) as the particles advect downwind. These increases increase the coagulation sink for smaller particles, contributing to the more uniform decrease in the 3-20 nm size range. Surface changes in

the 200-1000 nm size range are generally small, as this size range is more affected by other processes than NPF&G. The most significant surface changes occur during the MAM and SON seasons. Zonally averaged changes align with the changes seen at the surface, but the most significant changes occur in regions of large-scale subsidence.

The changes in the nested simulation over the United States align with the changes seen in the 4° x 5°. The reduction in the 3-20 nm size range is relatively uniform, while the increase in the 20-80 nm size range is most significant over the western portion of the simulation domain. The substantial increase in the 20-80 nm size range is likely due to the lower relative humidity and lower temperatures at higher elevations. The 80-200 nm size range shows more uniform increases across the U.S.

When compared to observations, the updated simulations capture the mean aerosol size distribution diameter better than the base simulation. The base 4° x 5° GC-TOMAS simulation underpredicted the mean diameter of particles during the CACTI campaign in DJF, but the updated simulation better agrees with the observations in this regard. The base 0.25° x 0.3125° simulation greatly overpredicted the mean number concentration of nucleation mode particles at the SGP observatory during MAM, while the updated model, again, shows better agreement in terms of mean diameter. GC-TOMAS shows discrepancies with total number in different size ranges, but the mean particle growth appears to be improved. The two case studies show that the updated model simulation produces particle growth in better alignment with the observations, both in terms of the growing nucleation mode as well as the larger diameter modes.

Considering aerosol phase state can improve model representation of aerosol particle growth and production of climate relevant particles. While this work presents an analysis of a diffusion-limited SOA condensation parameterization on aerosol number and size distributions,

there are many future research avenues to explore. Principally, there are many assumptions in this work, such as spatially and temporally constant volatilities and assumed organic hygroscopicity, that can be addressed with further sensitivity simulations. Furthermore, there are many other potential influences on size-dependent particle growth that can constructively or destructively interact with the effects of phase state presented here, such as condensed-phase reactions, gas and aerosol volatility distributions, non-ideal aerosol water uptake, aerosol hygroscopicity, aerosol mixing state, and organic oxidation state. Future work should endeavor to explore the impacts and interactions of these processes on aerosol formation and growth in the atmosphere.

REFERENCES

Aiken AC, DeCarlo PF, Kroll JH, et al (2008) O/C and OM/OC Ratios of Primary, Secondary, and Ambient Organic Aerosols with High-Resolution Time-of-Flight Aerosol Mass Spectrometry. Environ Sci Technol 42:4478–4485. https://doi.org/10.1021/es703009q

Albrecht BA (1989) Aerosols, Cloud Microphysics, and Fractional Cloudiness. Science 245:1227–1230. https://doi.org/10.1126/science.245.4923.1227

Baccarini A, Karlsson L, Dommen J, et al (2020) Frequent new particle formation over the high Arctic pack ice by enhanced iodine emissions. Nat Commun 11:4924. https://doi.org/10.1038/s41467-020-18551-0

Cerully KM, Bougiatioti A, Hite JRJ, et al (2015) On the link between hygroscopicity, volatility, and oxidation state of ambient and water-soluble aerosols in the southeastern United States. Atmospheric Chemistry and Physics 15:8679–8694. https://doi.org/10.5194/acp-15-8679-2015

DeMott PJ, Prenni AJ, Liu X, et al (2010) Predicting global atmospheric ice nuclei distributions and their impacts on climate. Proceedings of the National Academy of Sciences 107:11217–11222. https://doi.org/10.1073/pnas.0910818107

DeRieux W-SW, Li Y, Lin P, et al (2018) Predicting the glass transition temperature and viscosity of secondary organic material using molecular composition. Atmospheric Chemistry and Physics 18:6331–6351. https://doi.org/10.5194/acp-18-6331-2018

Dima, I. M., and J. M. Wallace (2003), On the seasonality of the Hadley cell, J. Atmos. Sci., 60, 1522–1527.

Dunne EM, Gordon H, Kürten A, et al (2016) Global atmospheric particle formation from CERN CLOUD measurements. Science 354:1119–1124. https://doi.org/10.1126/science.aaf2649

Evoy E, Maclean AM, Rovelli G, et al (2019) Predictions of diffusion rates of large organic molecules in secondary organic aerosols using the Stokes–Einstein and fractional Stokes–Einstein relations. Atmospheric Chemistry and Physics 19:10073–10085. https://doi.org/10.5194/acp-19-10073-2019

Forster, P, Storelvmo T, Armour K, et al (2021) The Earth's Energy Budget, Climate Feedbacks, and Climate Sensitivity. In Climate Change 2021: The Physical Science Basis. Contribution of Working Group I to the Sixth Assessment Report of the Intergovernmental Panel on Climate Change. Cambridge University Press, pp. 923–1054, doi: 10.1017/9781009157896.009.

Gordon H, Kirkby J, Baltensperger U, et al (2017) Causes and importance of new particle formation in the present-day and preindustrial atmospheres. Journal of Geophysical Research: Atmospheres 122:8739–8760. https://doi.org/10.1002/2017JD026844

Gryspeerdt E, Stier P, Partridge DG (2014) Satellite observations of cloud regime development: the role of aerosol processes. Atmospheric Chemistry and Physics 14:1141–1158. https://doi.org/10.5194/acp-14-1141-2014

Hadley, G., (1735)*:* Concerning the cause of the general trade-winds. *Phil. Trans.*, ***29*** **,** 58–62.

He X-C, Simon M, Iyer S, et al (2023) Iodine oxoacids enhance nucleation of sulfuric acid particles in the atmosphere. Science 382:1308–1314. https://doi.org/10.1126/science.adh2526

He Y, Akherati A, Nah T, et al (2021) Particle Size Distribution Dynamics Can Help Constrain the Phase State of Secondary Organic Aerosol. Environ Sci Technol 55:1466–1476. https://doi.org/10.1021/acs.est.0c05796

He Y, Bilsback KR, Shrivastava M, et al (2025) Kinetic Modeling of Secondary Organic Aerosol in a Weather-Chemistry Model: Parameterizations, Processes, and Predictions for GOAmazon. ACS EST Air 2:249–263. https://doi.org/10.1021/acsestair.4c00240

Hodshire AL, Palm BB, Alexander ML, et al (2018) Constraining nucleation, condensation, and chemistry in oxidation flow reactors using size-distribution measurements and aerosol microphysical modeling. Atmospheric Chemistry and Physics 18:12433–12460. https://doi.org/10.5194/acp-18-12433-2018

Jaeglé L, Quinn PK, Bates TS, et al (2011) Global distribution of sea salt aerosols: new constraints from in situ and remote sensing observations. Atmospheric Chemistry and Physics 11:3137–3157. https://doi.org/10.5194/acp-11-3137-2011

Johnson JS, Jen CN (2023) Role of Methanesulfonic Acid in Sulfuric Acid–Amine and Ammonia New Particle Formation. ACS Earth Space Chem. https://doi.org/10.1021/acsearthspacechem.3c00017

Kirkby J, Amorim A, Baltensperger U, et al (2023) Atmospheric new particle formation from the CERN CLOUD experiment. Nat Geosci 16:948–957. https://doi.org/10.1038/s41561-023-01305-0

Kirkby J, Duplissy J, Sengupta K, et al (2016) Ion-induced nucleation of pure biogenic particles. Nature 533:521–526. https://doi.org/10.1038/nature17953

Kodros JK, Pierce JR (2017) Important global and regional differences in aerosol cloud-albedo effect estimates between simulations with and without prognostic aerosol

microphysics. Journal of Geophysical Research: Atmospheres 122:4003–4018. https://doi.org/10.1002/2016JD025886

Koop T, Bookhold J, Shiraiwa M, Pöschl U (2011) Glass transition and phase state of organic compounds: dependency on molecular properties and implications for secondary organic aerosols in the atmosphere. Phys Chem Chem Phys 13:19238–19255. https://doi.org/10.1039/C1CP22617G

Lambe AT, Onasch TB, Massoli P, et al (2011) Laboratory studies of the chemical composition and cloud condensation nuclei (CCN) activity of secondary organic aerosol (SOA) and oxidized primary organic aerosol (OPOA). Atmospheric Chemistry and Physics 11:8913–8928. https://doi.org/10.5194/acp-11-8913-2011

Liu J, Alexander L, Fast JD, et al (2021) Aerosol characteristics at the Southern Great Plains site during the HI-SCALE campaign. Atmospheric Chemistry and Physics 21:5101–5116. https://doi.org/10.5194/acp-21-5101-2021

Li Y, Day DA, Stark H, et al (2020) Predictions of the glass transition temperature and viscosity of organic aerosols from volatility distributions. Atmospheric Chemistry and Physics 20:8103–8122. https://doi.org/10.5194/acp-20-8103-2020

Luu R, Schervish M, June NA, et al (2025) Global Simulations of Phase State and Equilibration Time Scales of Secondary Organic Aerosols with GEOS-Chem. ACS Earth Space Chem 9:288–302. https://doi.org/10.1021/acsearthspacechem.4c00281

Merikanto J, Spracklen DV, Mann GW, et al (2009) Impact of nucleation on global CCN. Atmospheric Chemistry and Physics 9:8601–8616. https://doi.org/10.5194/acp-9-8601-2009

Myhre G, Samset BH, Schulz M, et al (2013) Radiative forcing of the direct aerosol effect from AeroCom Phase II simulations. Atmospheric Chemistry and Physics 13:1853–1877. https://doi.org/10.5194/acp-13-1853-2013

Olenius T, Halonen R, Kurtén T, et al (2017) New particle formation from sulfuric acid and amines: Comparison of monomethylamine, dimethylamine, and trimethylamine. Journal of Geophysical Research: Atmospheres 122:7103–7118. https://doi.org/10.1002/2017JD026501

O'Donnell SE, Croft B, Ford B, et al (2025) Going Off Grid: A Comparative Study of the Lagrangian and Eulerian Perspectives of New Particle Formation Events, submitted to Journal of Geophysical Research.

Pai SJ, Heald CL, Pierce JR, et al (2020) An evaluation of global organic aerosol schemes using airborne observations. Atmospheric Chemistry and Physics 20:2637–2665. https://doi.org/10.5194/acp-20-2637-2020

Parworth C, Fast J, Mei F, et al (2015) Long-term measurements of submicrometer aerosol chemistry at the Southern Great Plains (SGP) using an Aerosol Chemical Speciation Monitor (ACSM). Atmospheric Environment 106:43–55. https://doi.org/10.1016/j.atmosenv.2015.01.060

Petters MD, Kreidenweis SM (2007) A single parameter representation of hygroscopic growth and cloud condensation nucleus activity. Atmospheric Chemistry and Physics 7:1961–1971. https://doi.org/10.5194/acp-7-1961-2007

Petters SS, Kreidenweis SM, Grieshop AP, et al (2019) Temperature- and Humidity-Dependent Phase States of Secondary Organic Aerosols. Geophysical Research Letters 46:1005–1013. https://doi.org/10.1029/2018GL080563

Pierce JR, Riipinen I, Kulmala M, et al (2011) Quantification of the volatility of secondary organic compounds in ultrafine particles during nucleation events. Atmospheric Chemistry and Physics 11:9019–9036. https://doi.org/10.5194/acp-11-9019-2011

Pringle KJ, Tost H, Pozzer A, et al (2010) Global distribution of the effective aerosol hygroscopicity parameter for CCN activation. Atmospheric Chemistry and Physics 10:5241–5255. https://doi.org/10.5194/acp-10-5241-2010

Reid JP, Bertram AK, Topping DO, et al (2018) The viscosity of atmospherically relevant organic particles. Nat Commun 9:956. https://doi.org/10.1038/s41467-018-03027-z

Riccobono F, Schobesberger S, Scott CE, et al (2014) Oxidation Products of Biogenic Emissions Contribute to Nucleation of Atmospheric Particles. Science 344:717–721. https://doi.org/10.1126/science.1243527

Riipinen I, Pierce JR, Yli-Juuti T, et al (2011) Organic condensation: a vital link connecting aerosol formation to cloud condensation nuclei (CCN) concentrations. Atmos Chem Phys 11:3865–3878. https://doi.org/10.5194/acp-11-3865-2011

Riipinen I, Yli-Juuti T, Pierce JR, et al (2012) The contribution of organics to atmospheric nanoparticle growth. Nature Geosci 5:453–458. https://doi.org/10.1038/ngeo1499

Roldin P, Ehn M, Kurtén T, et al (2019) The role of highly oxygenated organic molecules in the Boreal aerosol-cloud-climate system. Nat Commun 10:4370. https://doi.org/10.1038/s41467-019-12338-8

Rosenfeld D, Andreae MO, Asmi A, et al (2014) Global observations of aerosol-cloud-precipitation-climate interactions. Reviews of Geophysics 52:750–808. https://doi.org/10.1002/2013RG000441

Shiraiwa M, Li Y, Tsimpidi AP, et al (2017) Global distribution of particle phase state in atmospheric secondary organic aerosols. Nat Commun 8:15002. https://doi.org/10.1038/ncomms15002

Shiraiwa M, Pöschl U (2021) Mass accommodation and gas–particle partitioning in secondary organic aerosols: dependence on diffusivity, volatility, particle-phase reactions, and penetration depth. Atmospheric Chemistry and Physics 21:1565–1580. https://doi.org/10.5194/acp-21-1565-2021

Shrivastava M, Zhang J, Zaveri RA, et al (2024) Anthropogenic Extremely Low Volatility Organics (ELVOCs) Govern the Growth of Molecular Clusters Over the Southern Great Plains During the Springtime. Journal of Geophysical Research: Atmospheres 129:e2024JD041212. https://doi.org/10.1029/2024JD041212

Singh, A, and C Kuang, (2024) Scanning Mobility Particle Sizer (SMPS) Instrument Handbook. U.S. Department of Energy, Atmospheric Radiation Measurement user facility, Richland, Washington. DOE/SC-ARM-TR-147.

Tröstl J, Chuang WK, Gordon H, et al (2016) The role of low-volatility organic compounds in initial particle growth in the atmosphere. Nature 533:527–531. https://doi.org/10.1038/nature18271

Twomey S (1974) Pollution and the planetary albedo. Atmospheric Environment (1967) 8:1251–1256. https://doi.org/10.1016/0004-6981(74)90004-3

Vehkamäki H, Kulmala M, Napari I, et al (2002) An improved parameterization for sulfuric acid–water nucleation rates for tropospheric and stratospheric conditions. Journal of Geophysical Research: Atmospheres 107:AAC 3-1-AAC 3-10. https://doi.org/10.1029/2002JD002184

Yu F, Luo G, Nadykto AB, Herb J (2017) Impact of temperature dependence on the possible contribution of organics to new particle formation in the atmosphere. Atmospheric Chemistry and Physics 17:4997–5005. https://doi.org/10.5194/acp-17-4997-2017

Zaveri RA, Easter RC, Shilling JE, Seinfeld JH (2014) Modeling kinetic partitioning of secondary organic aerosol and size distribution dynamics: representing effects of volatility, phase state, and particle-phase reaction. Atmospheric Chemistry and Physics 14:5153–5181. https://doi.org/10.5194/acp-14-5153-2014

Zaveri RA, Shilling JE, Zelenyuk A, et al (2018) Growth Kinetics and Size Distribution Dynamics of Viscous Secondary Organic Aerosol. Environ Sci Technol 52:1191–1199. https://doi.org/10.1021/acs.est.7b04623

Zaveri RA, Wang J, Fan J, et al (2022) Rapid growth of anthropogenic organic nanoparticles greatly alters cloud life cycle in the Amazon rainforest. Science Advances 8:eabj0329. https://doi.org/10.1126/sciadv.abj0329

Zender CS, Bian H, Newman D (2003) Mineral Dust Entrainment and Deposition (DEAD) model: Description and 1990s dust climatology. Journal of Geophysical Research: Atmospheres 108:. https://doi.org/10.1029/2002JD002775

Zhang Z, Li Y, Ran H, et al (2024) Simulated phase state and viscosity of secondary organic aerosols over China. Atmospheric Chemistry and Physics 24:4809–4826. https://doi.org/10.5194/acp-24-4809-2024

Zhao B, Donahue NM, Zhang K, et al (2024) Global variability in atmospheric new particle formation mechanisms. Nature 1–8. https://doi.org/10.1038/s41586-024-07547-1

CHAPTER 5

CONCLUSIONS AND FUTURE WORK

Motivated by the uncertainty associated with aerosol effects on the global radiation budget, this dissertation endeavors to better constrain the processes of NPF&G in the atmosphere. To that end, this work ranges from using a semi-explicit chemistry and aerosol box model to investigate details of early particle growth from different VOCs, to using a 3D chemical transport model to better understand and interpret how NPF&G events are observed in the atmosphere. From this work, we find the majority of undefined-NPF events at the SGP observatory can be explained as spatially inhomogeneous NPF&G (Chapter 2), the VOCs contributing to potential secondary aerosol processes in the CAGE chamber are primarily anthropogenic (Chapter 3), and including size-dependent vapor condensation based on aerosol phase state improves the representation of aerosol size distributions at several sites around the globe (Chapter 4).

Chapter 2 summary: We used a 3D chemical transport model with online aerosol microphysics, along with a Lagrangian parcel model, to look at NPF&G events from two perspectives: (1) stationary (Eulerian), and (2) following the wind flow (Lagrangian). While previous work has investigated peculiar growth patterns of NPF events (Hakala et al., 2023; Salma et al., 2016) using box models, no approach includes interpolating aerosol size distributions along Lagrangian trajectories to understand NPF&G events. We find that the majority of undefined/class II events (i.e., events with some NPF occurring, but particle growth or number vary greatly in time) can be explained from the Lagrangian perspective, highlighting the plume-like nature of NPF&G events. Given the substantial number of undefined/class II NPF events that occur at many

sites, this work provides a potential avenue for better understanding how these events occur, as well as provide the means to derive meaningful statistics from previously unanalyzable data.

Chapter 2 future work: There are many potential applications of the Eulerian versus Lagrangian comparison framework within 3D models, both for the understanding of NPF&G events and other aerosol and chemistry related problems. For NPF&G, this framework is particularly promising for investigating the condensation and evaporation dynamics of particles and how those microphysical processes manifest in stationary observations. While it seems as though particle shrinkage events can be explained simply through spatial inhomogeneities (Hakala et al., 2023), future work should also focus on how SOA partitioning dynamics influence stationary observations. Additionally, given the task of interpreting real-world observations, an exciting opportunity exists to leverage machine learning (ML) techniques to train an ML model on size distribution output from a 3D model, with the goal of interpreting real-world size distribution observations. Such an approach would depend greatly on the skill of the 3D model used for training, but the potential gains for interpreting stationary size distribution measurements are great, especially for sites close to emissions sources where clear NPF&G events are rare. Finally, this approach can be leveraged to understand how representative an observational site is of the surrounding area. Future work should utilize this framework to characterize existing observation sites as well as future ones.

Chapter 3 summary: In this chapter, a box model with semi-explicit gas-phase chemistry, SOA partitioning thermodynamics, and aerosol microphysics, was used to characterize a novel environmental chamber in Houston Texas during the TRACER campaign. The CAGE chamber filters out ambient particles, allowing only gases to diffuse into the reactor chamber, therefore, the

conditions under which particles form in the chamber are known. The model used in this work was able to produce similar NPF&G events to the ones observed in the chamber, and the model shows most of the SOA in the chamber is derived from anthropogenic VOC oxidation products. This work included many sensitivity tests due to limited observational constraints, and because of this, this work explores many aspects of the CAGE chamber system. While the condensation sink (CS) in the ambient atmosphere plays a critical role in determining the strength of NPF&G, particle and vapor wall losses, in addition to instrument sampling, in the chamber are critical for shaping the aerosol size distribution.

Chapter 3 future work: While the findings from Chapter 3 are relatively limited in their applicability to the ambient atmosphere, there are ways to utilize semi-ambient chambers and modeling to further target specific processes relevant to the real atmosphere. Specifically, the use of two identical chambers (Sirmollo et al., 2021; Zhu et al., 2025; Aktypis et al., 2024) at the same site allows for more targeted perturbations of either injected particles or vapors into one chamber to better understand the sensitivity of aerosol processes to the production rate of condensable vapors or CS. Additionally, semi-ambient chambers that filter out ambient particles could be useful for characterizing the potential sources of secondary aerosol in urban environments as particle loading decreases due to energy transitions. While modeling semi-ambient environmental chambers can be difficult due to the lack of constraints, the utilization of such modeling is potentially impactful as a means to bridge the gap between more controlled chemistry and aerosol chamber experiments and the real atmosphere.

Chapter 4 summary: Given the increasing recognition of the intraparticle diffusion effects on the size-dependent condensation of SVOCs, this chapter investigates modeling size-dependent

condensation effects on global and regional aerosol number and size, as well as the effects on NPF&G events. While we make several simplifying assumptions in this work, the updated model simulation shows substantial increases in the concentration of 20-80 nm particles in regions where particles are expected to have solid-like phase states. Additionally, there are more uniform decreases and increases in the 3-20 nm and 80-200 nm size range as a result of increased survival of small particles leading to an overall increase in the coagulation sink. Size distributions from simulations with size-dependent condensation updates show improvement when compared to average size distributions from south-central United States and north-central Argentina. This work is a preliminary approach to understanding the effects of aerosol phase state on global aerosol number, CCN concentrations, and NPF&G events.

Chapter 4 future work: With a modest investment in model updates, the approach presented in Chapter 4 can be improved to be more physically consistent. As discussed, GC-TOMAS does not resolve the volatility of condensing vapors. While implementing a full volatility distribution for SOA is likely computationally prohibitive in a large-scale 3D model, a simplified approach is likely reasonable, such as an assumed 50/50% split between nonvolatile and SVOC species or a reduced volatility distribution with ~3-4 representative vapor pressure bins. Beyond model updates, future research can further explore the implications of particle phase state on global CCN production and cloud-droplet activation. Additionally, given that Earth's poles have and will warm more than the midlatitudes and tropics, investigating the potential changes on aerosol phase state in these regions could be meaningful. Higher temperature and relative humidity favors less viscous particles, therefore, investigating changes in aerosol phase state due to potential changes in temperature and relative humidity could be of interest from a climate perspective.

Broader future work: There is no realistic scenario in which aerosol particles in the atmosphere will cease to form through the process of NPF&G. Given this, future research on NPF&G in the atmosphere can be guided by questions: **Where**? **How**? and **What**?

Where refers to the need for research in understudied regions where NPF&G is less well understood, such as the upper planetary boundary layer and troposphere, the marine boundary layer, and tropical environments. As shown in this work, the spatial extent of NPF&G events, both horizontally and vertically, are poorly understood, underscoring the need to map NPF&G events in both space and time. Integrating observations from multiple platforms (e.g., ground-based, airborne, and ship) into models will be essential in this effort.

How pertains to the need for research investigating the detailed mechanisms of multicomponent NPF and particle growth. Given the potential for synergistic interactions between multiple precursor vapors during particle formation (Wang et al., 2022), further investigation into these interactions is warranted. Additionally, as discussed in this dissertation, understanding the effects of particle phase state on the aerosol lifecycle and size distribution is of great importance for assessing both climate and human health related impacts.

What addresses the question, "so what?" - why do the aforementioned processes matter and what are their broader impacts? For air quality, this may look like investigating the impacts of NPF&G on air pollution and human health in urban environments. For climate, this may take shape as characterizing parametric and structural uncertainty within climate models to understand how the envelope of uncertainties in aerosol processes propagate in climate predictions. Fundamentally, scientific discovery requires us to ask whether the findings made from addressing the **where** and **how** are impactful to the Earth system. As scientists, we often focus on the **where** and **how**, justified by the **what**, but it is equally important to periodically step back and reexamine the **what**.

REFERENCES

Aktypis A, Sippial DJ, Vasilakopoulou CN, et al (2024) Formation and chemical evolution of secondary organic aerosol in two different environments: a dual-chamber study. Atmospheric Chemistry and Physics 24:13769–13791. https://doi.org/10.5194/acp-24-13769-2024

Hakala S, Vakkari V, Lihavainen H, et al (2023) Explaining apparent particle shrinkage related to new particle formation events in western Saudi Arabia does not require evaporation. Atmospheric Chemistry and Physics 23:9287–9321. https://doi.org/10.5194/acp-23-9287-2023

Salma I, Németh Z, Weidinger T, et al (2016) Measurement, growth types and shrinkage of newly formed aerosol particles at an urban research platform. Atmospheric Chemistry and Physics 16:7837–7851. https://doi.org/10.5194/acp-16-7837-2016

Sirmollo CL, Collins DR, McCormick JM, et al (2021) Captive Aerosol Growth and Evolution (CAGE) chamber system to investigate particle growth due to secondary aerosol formation. Atmospheric Measurement Techniques 14:3351–3370. https://doi.org/10.5194/amt-14-3351-2021

Wang M, Xiao M, Bertozzi B, et al (2022) Synergistic HNO3–H2SO4–NH3 upper tropospheric particle formation. Nature 605:483–489. https://doi.org/10.1038/s41586-022-04605-4

Zhu Z, Du X, Collins DR (2025) Direct measurement of the growth of small particles in ambient air using captive aerosol chambers. Atmospheric Environment 340:120915. https://doi.org/10.1016/j.atmosenv.2024.120915

APPENDIX A

SUPPLEMENT TO: GOING OFF GRID: A COMPARATIVE STUDY OF THE LAGRANGIAN AND EULERIAN PERSPECTIVES OF NEW PARTICLE FORMATION EVENTS

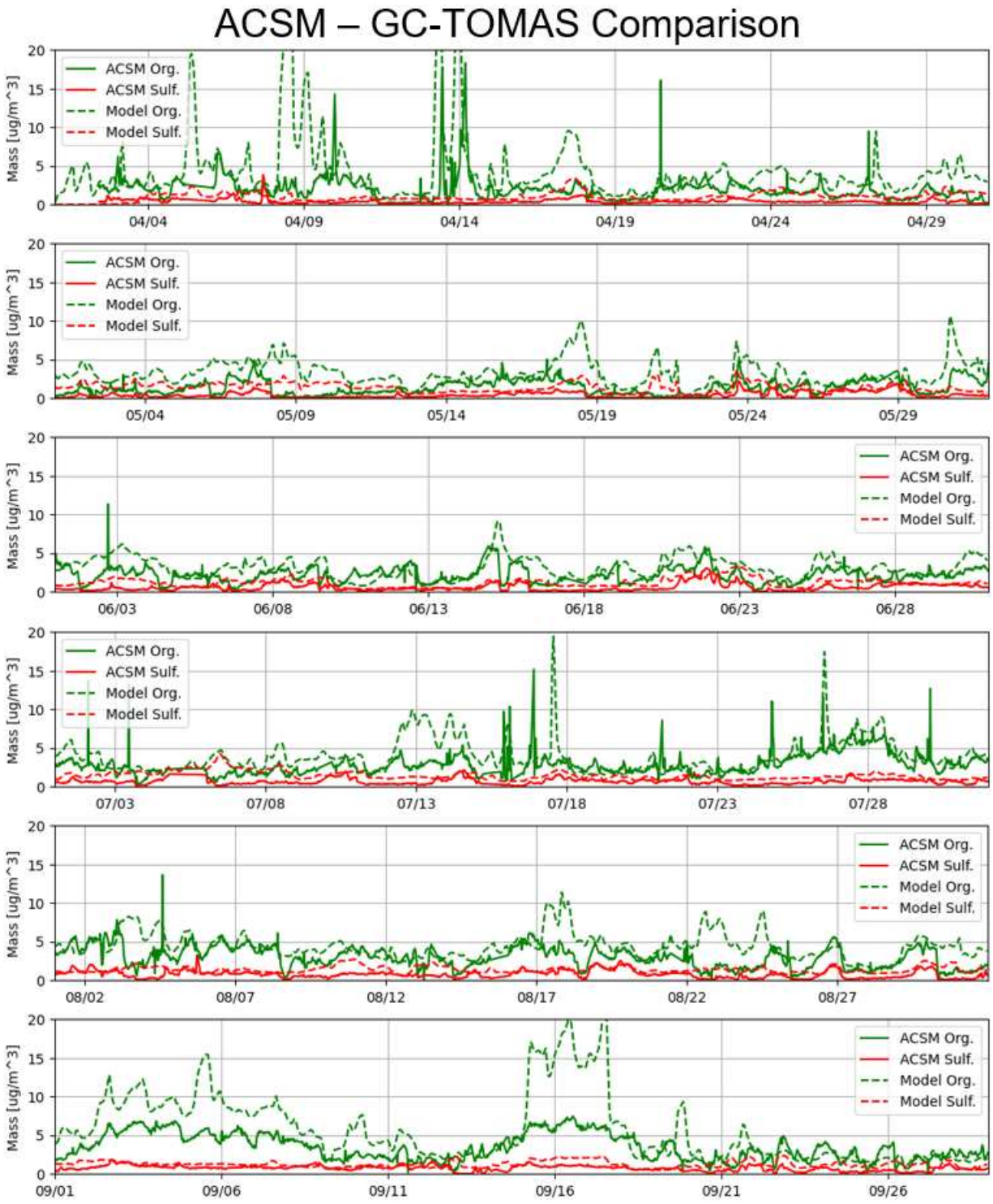

Figure A1. Comparison between the modeled organic and sulfate aerosol mass with the aerosol mass measured by the ACSM at the SGP site. Modeled organic aerosol mass is shown by the green dashed line and the modeled sulfate mass is shown by the red dashed line. The organic aerosol mass measured by the ACSM is shown by the solid green line and the sulfate mass measured by the ACSM is shown by the solid red line.

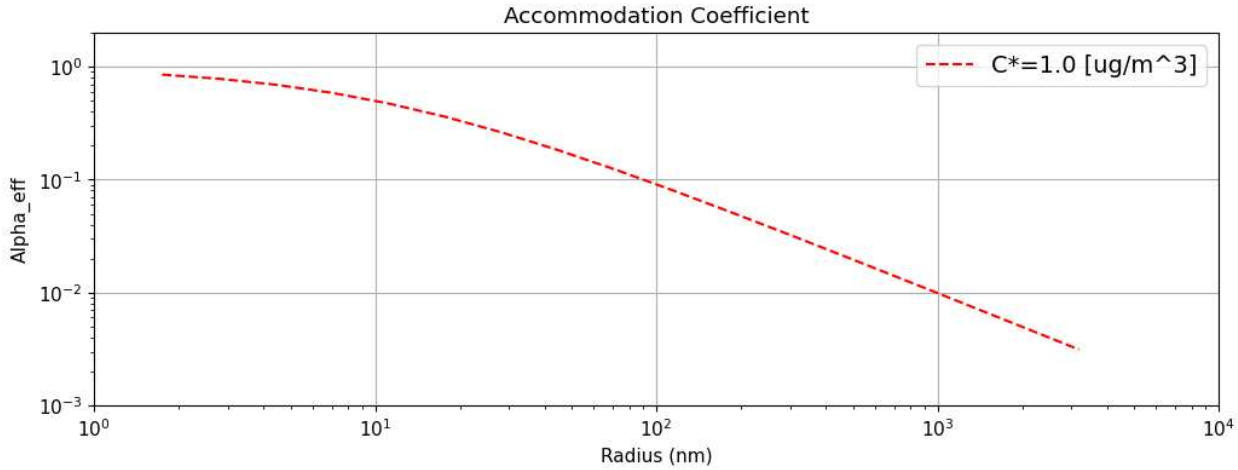

Figure A2. Size dependent accommodation coefficient based on Shiraiwa and Pöschl (2021) for a condensing species with a volatility of 1.0 µg m^{-3} and a particle phase diffusivity of $1.0x10^{-15}$ m^2 s^{-1}.

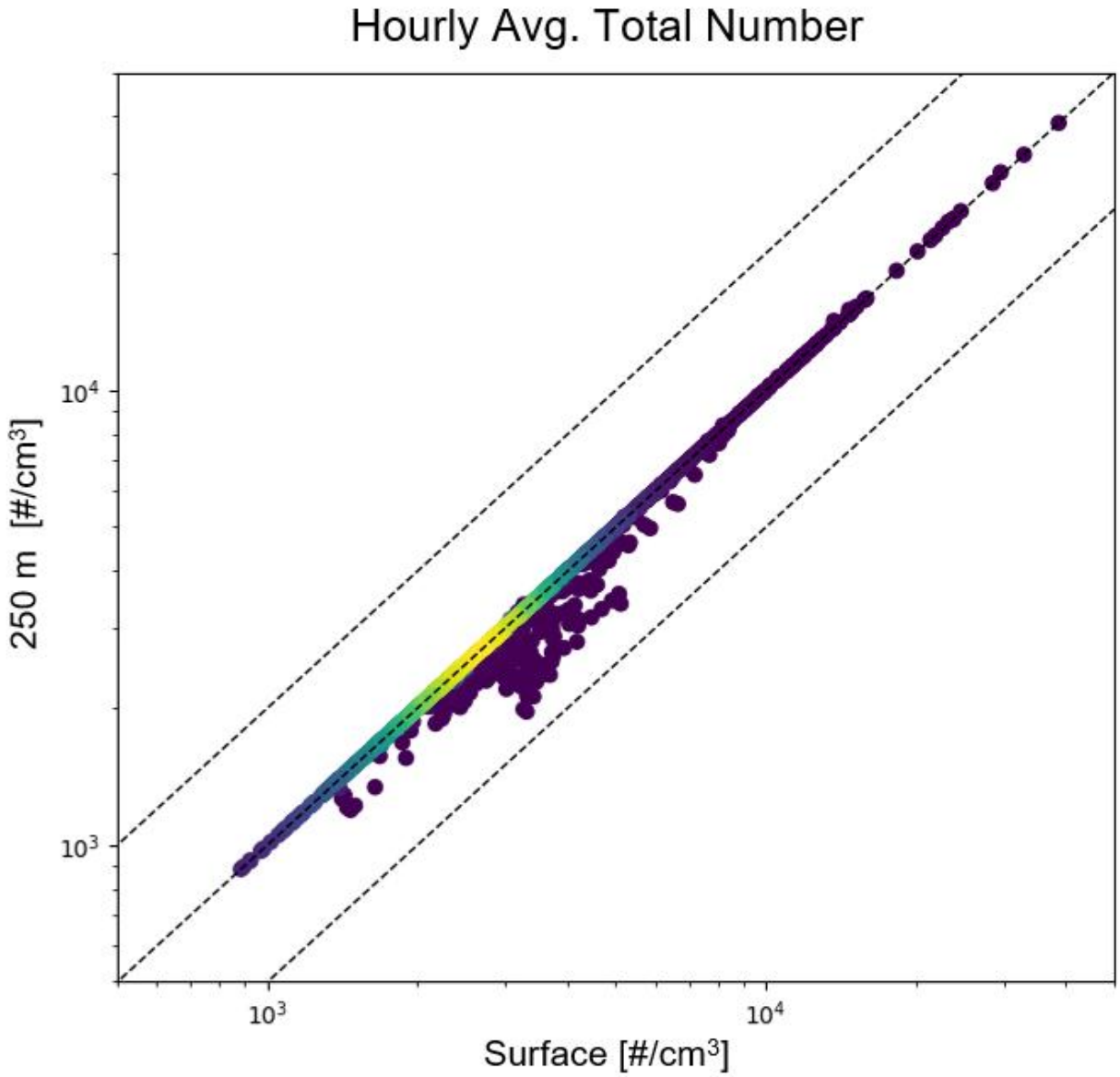

Figure A3. Comparison of the modeled hourly averaged total number concentration between the surface and an altitude of 250 m. The dashed-black lines indicate the 2:1, 1:1, and 1:2 lines.

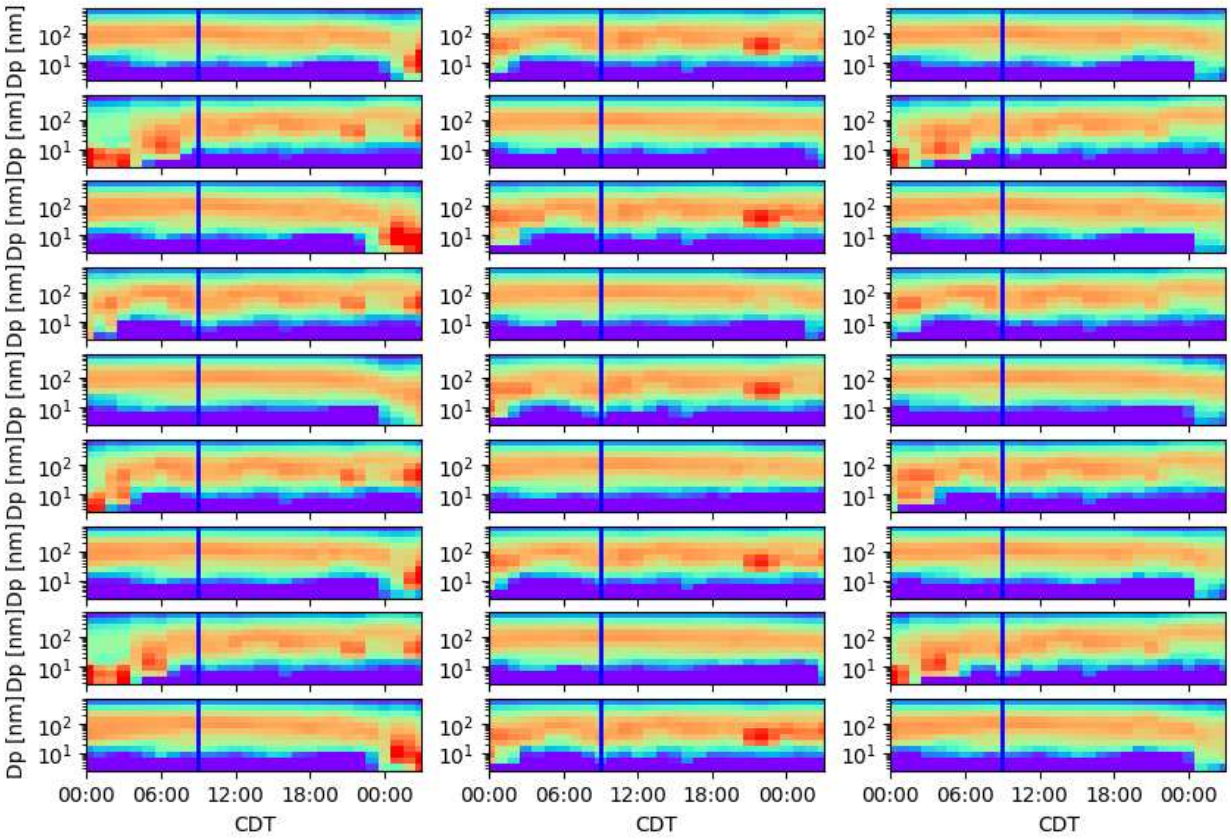

Figure A4. Modeled aerosol size distributions interpolated along the 27 ensemble HYSPLIT trajectories on 6 May 2019. The ensemble forward and backward trajectories were initialized at 9:00 CDT indicated by the blue vertical line.

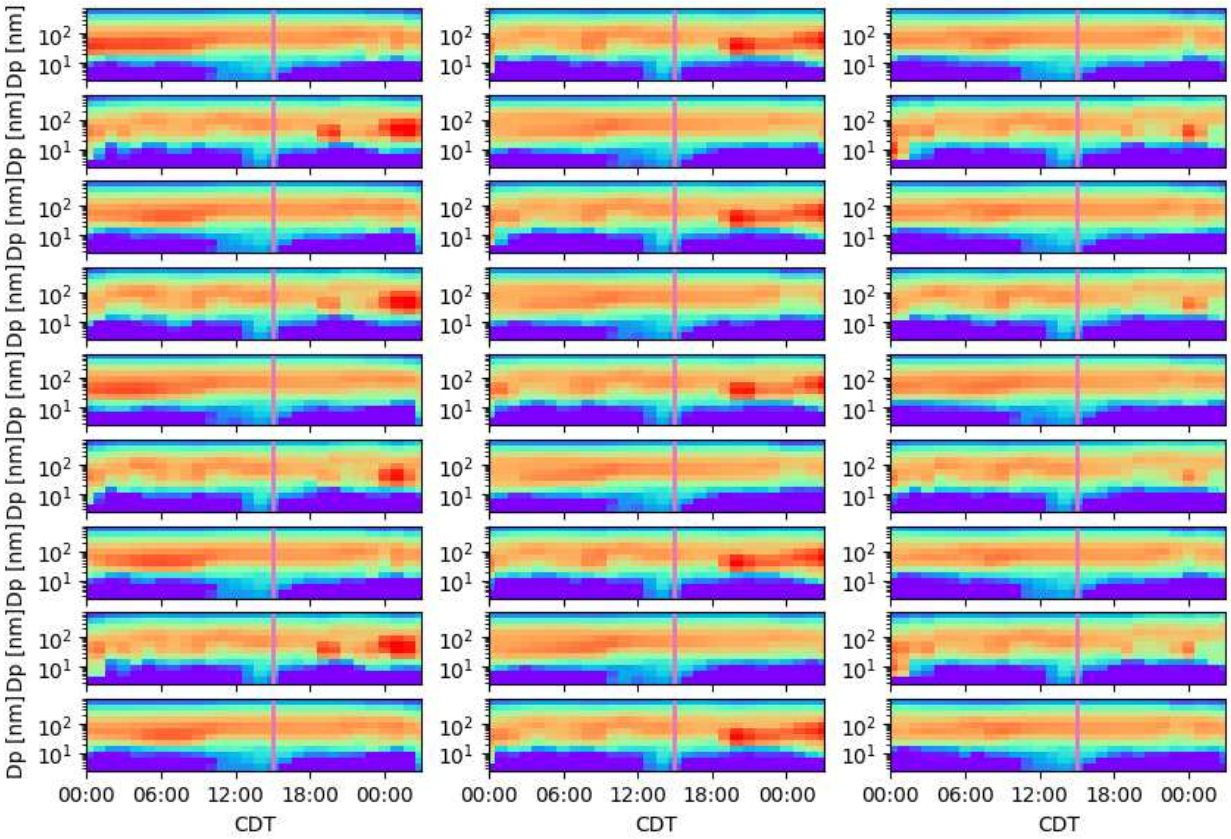

Figure A5. Modeled aerosol size distributions interpolated along the 27 ensemble HYSPLIT trajectories on 6 May 2019. The ensemble forward and backward trajectories were initialized at 15:00 CDT indicated by the pink vertical line.

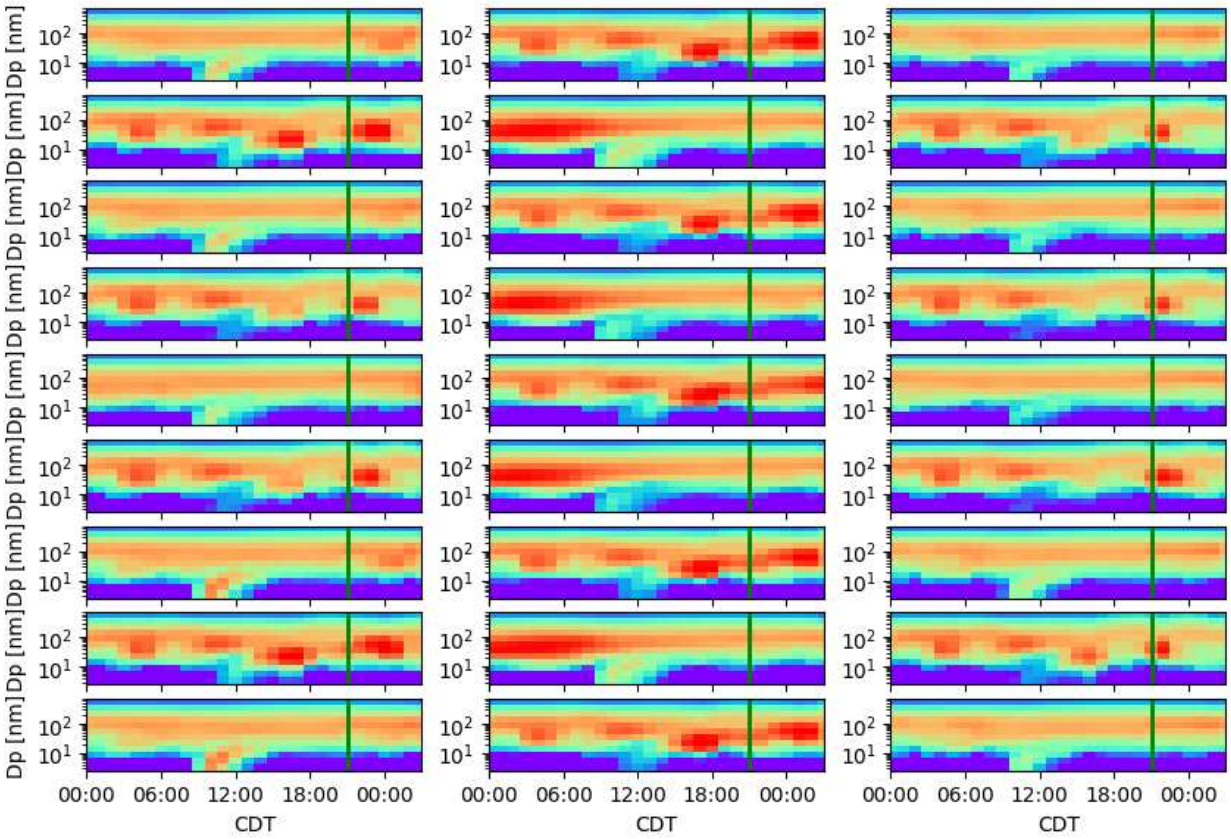

Figure A6. Modeled aerosol size distributions interpolated along the 27 ensemble HYSPLIT trajectories on 6 May 2019. The ensemble forward and backward trajectories were initialized at 21:00 CDT indicated by the green vertical line.

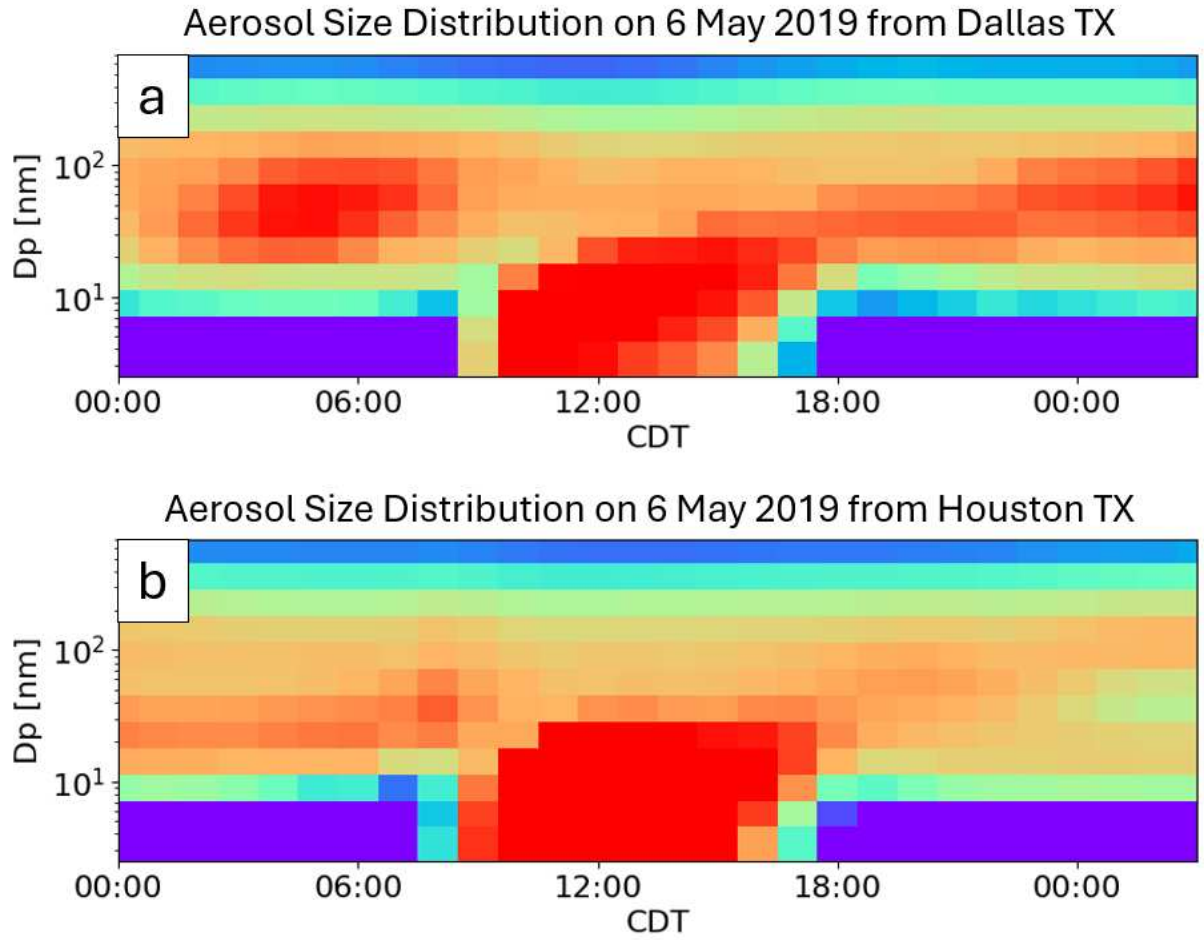

Figure A7. Stationary modeled aerosol size distributions from Dallas, TX (a) and Houston, TX (b) on 6 May 2019.

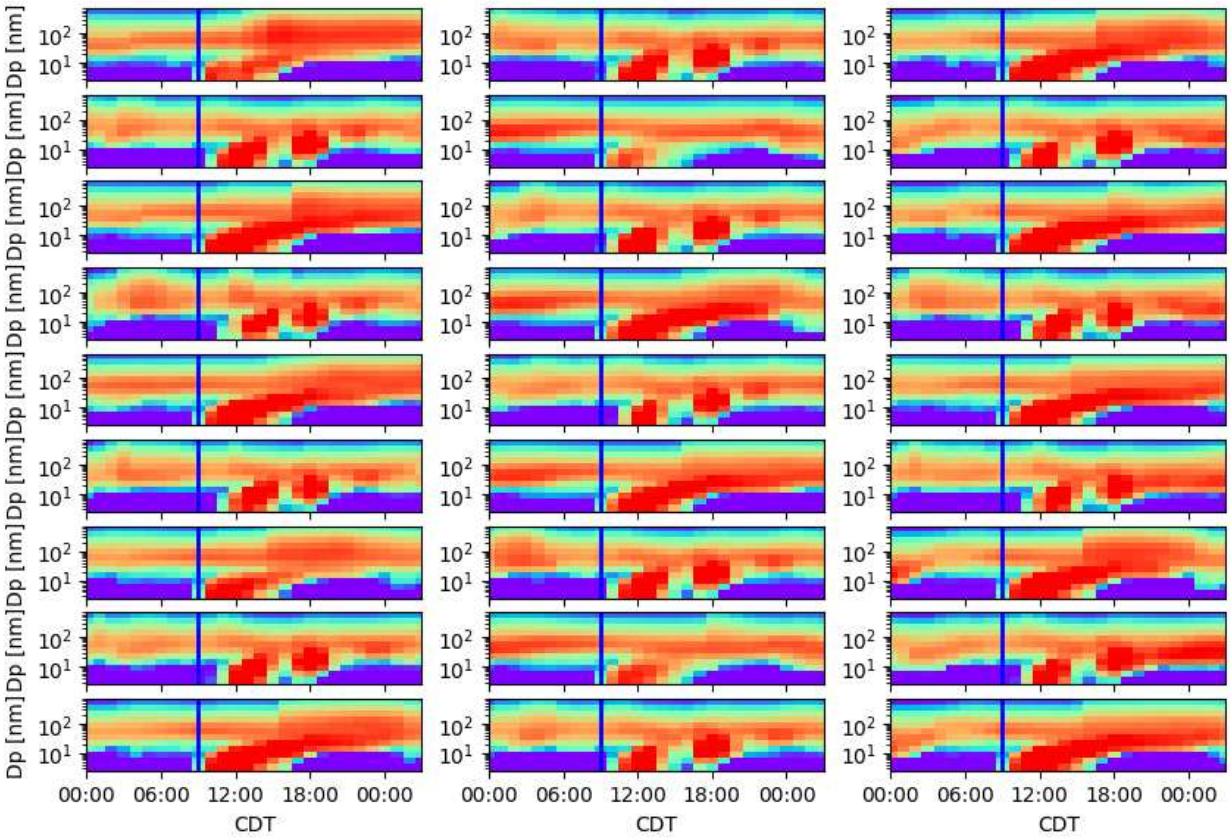

Figure A8. Modeled aerosol size distributions interpolated along the 27 ensemble HYSPLIT trajectories on 15 April 2019. The ensemble forward and backward trajectories were initialized at 9:00 CDT indicated by the blue vertical line.

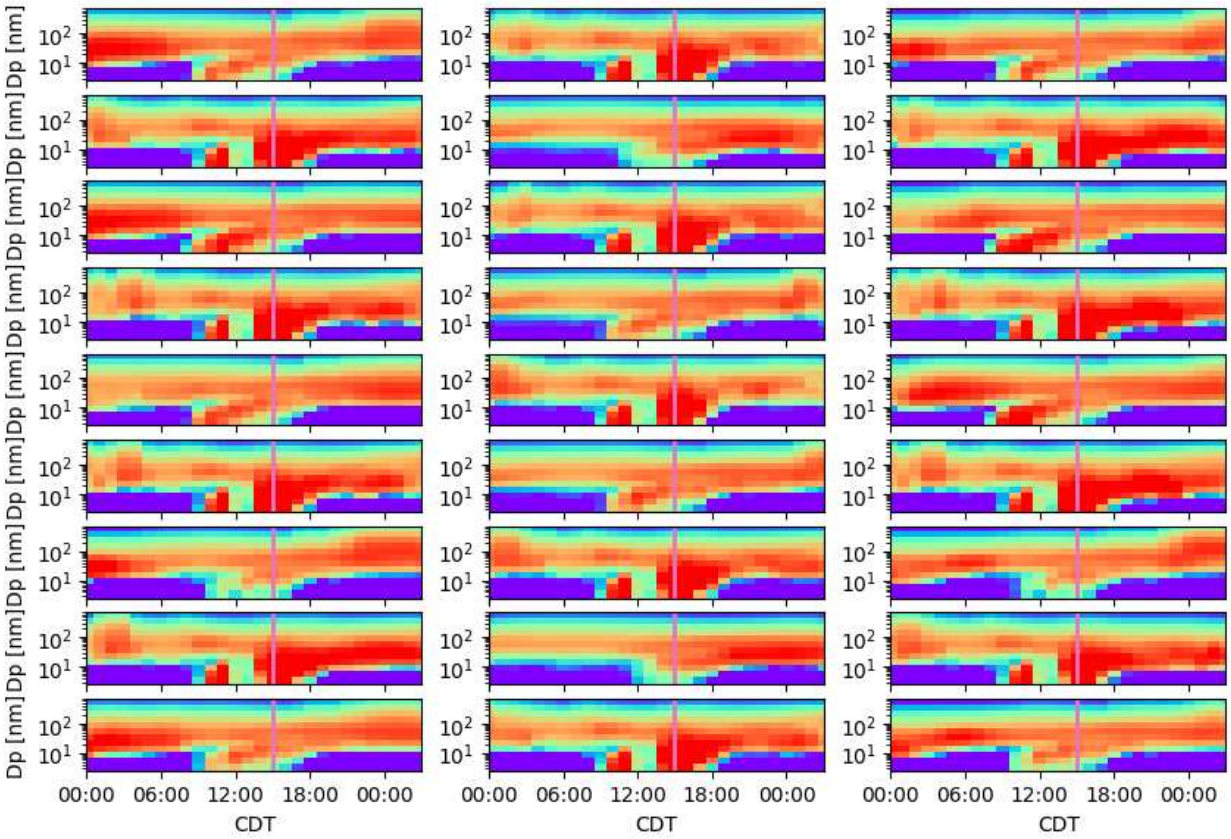

Figure A9. Modeled aerosol size distributions interpolated along the 27 ensemble HYSPLIT trajectories on 15 April 2019. The ensemble forward and backward trajectories were initialized at 15:00 CDT indicated by the pink vertical line.

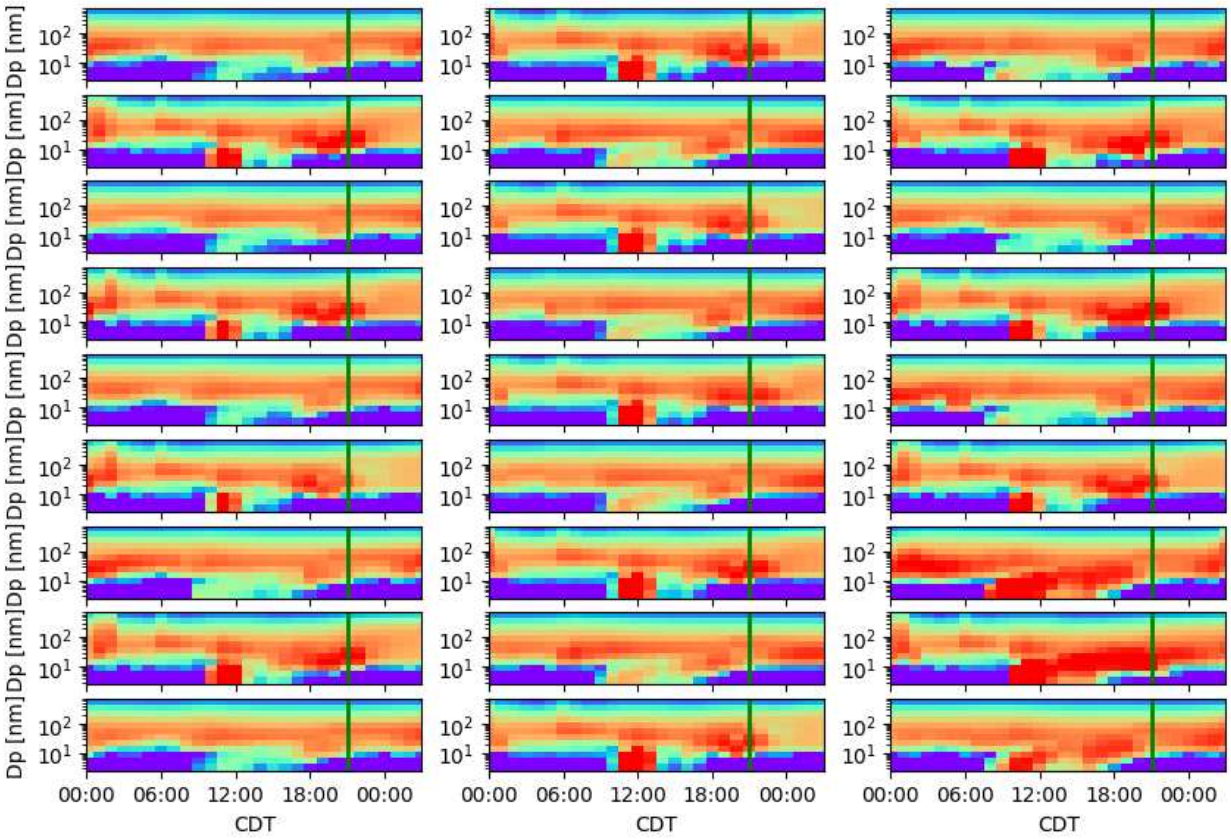

Figure A10. Modeled aerosol size distributions interpolated along the 27 ensemble HYSPLIT trajectories on 15 April 2019. The ensemble forward and backward trajectories were initialized at 21:00 CDT indicated by the green vertical line.

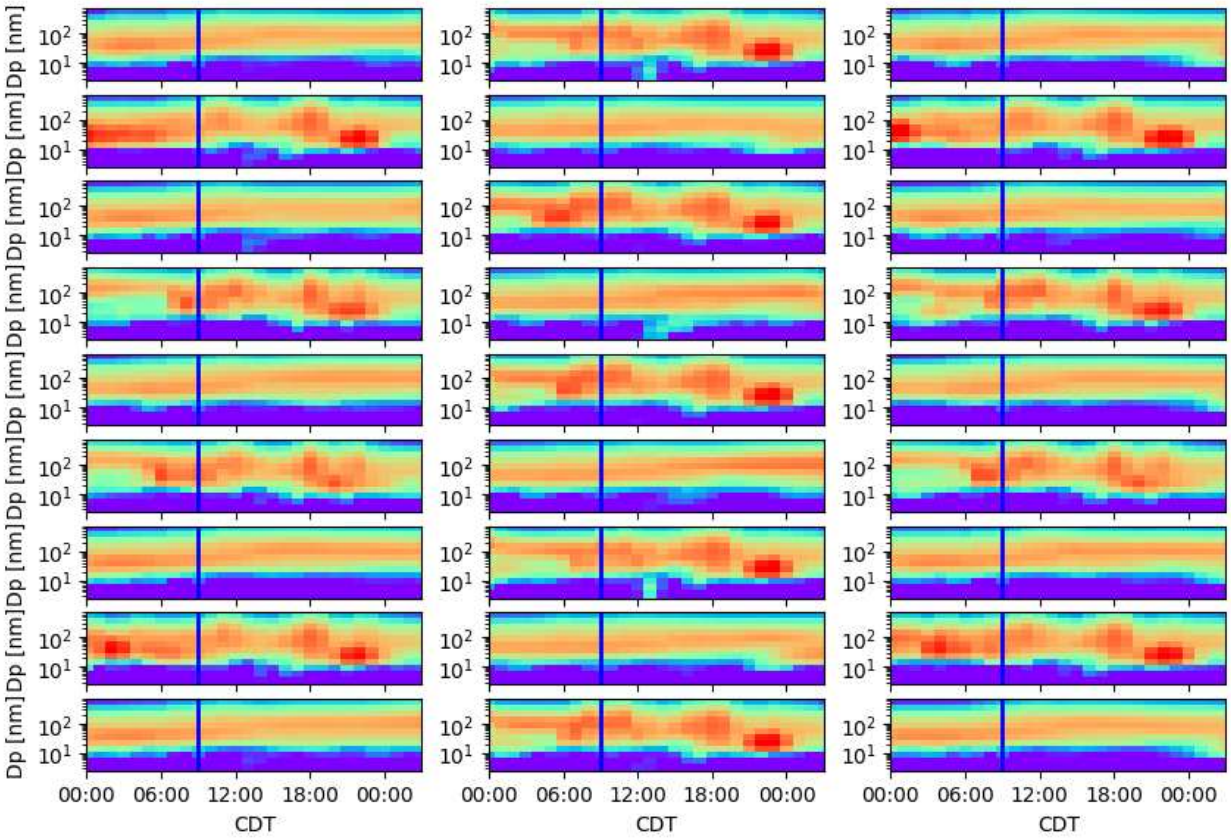

Figure A11. Modeled aerosol size distributions interpolated along the 27 ensemble HYSPLIT trajectories on 13 April 2019. The ensemble forward and backward trajectories were initialized at 9:00 CDT indicated by the blue vertical line.

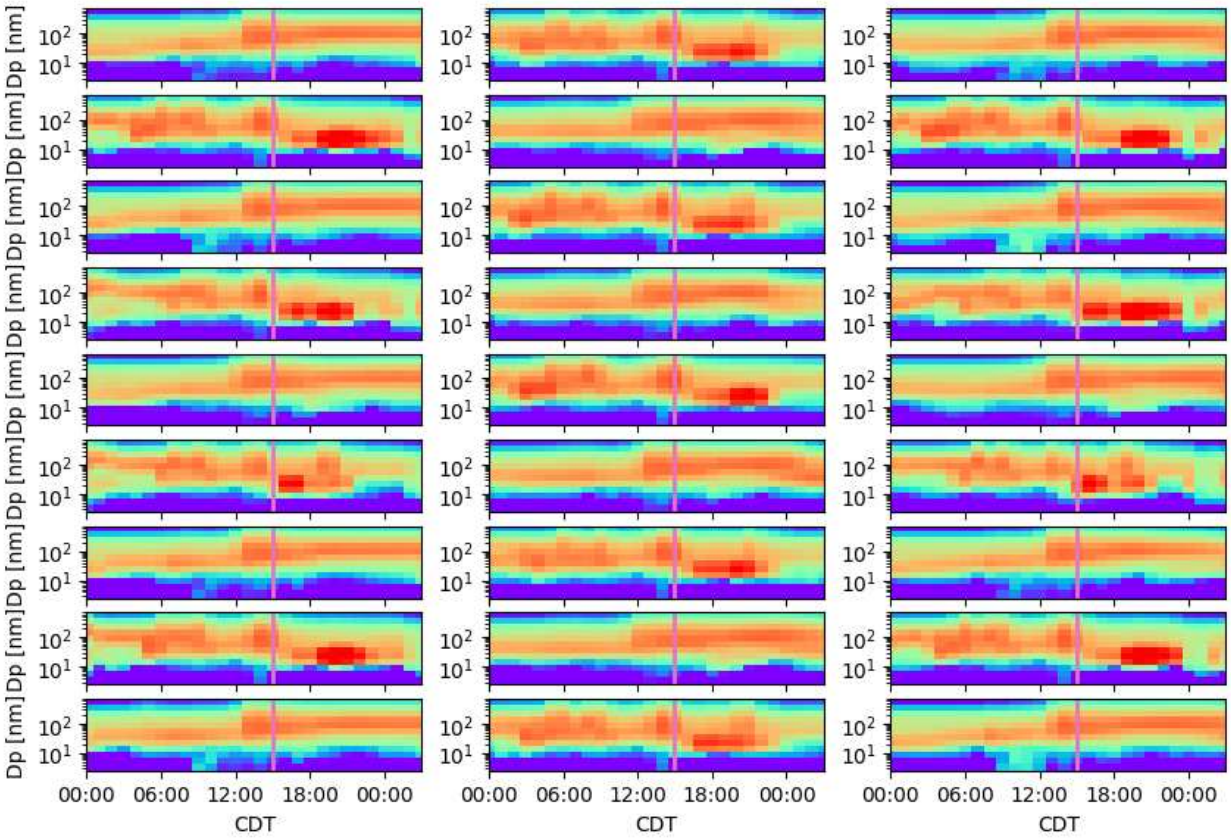

Figure A12. Modeled aerosol size distributions interpolated along the 27 ensemble HYSPLIT trajectories on 13 April 2019. The ensemble forward and backward trajectories were initialized at 15:00 CDT indicated by the pink vertical line.

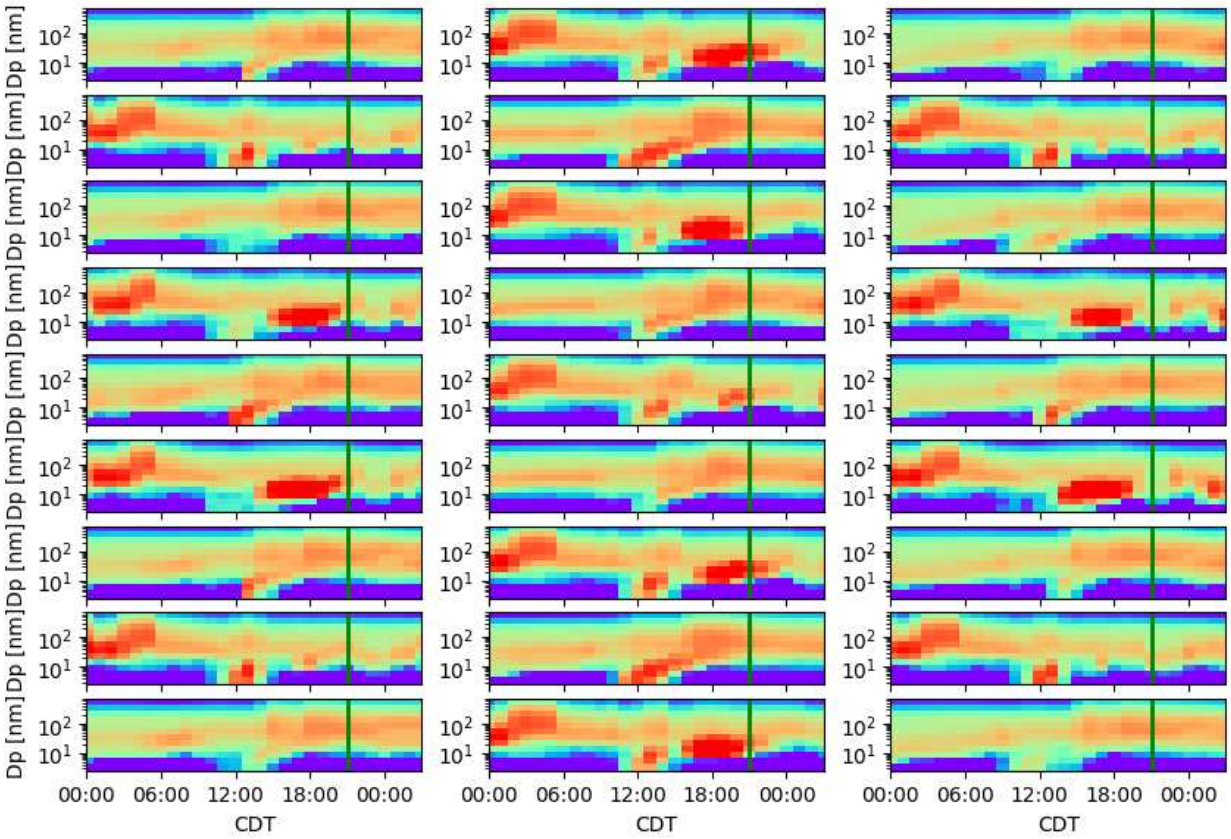

Figure A13. Modeled aerosol size distributions interpolated along the 27 ensemble HYSPLIT trajectories on 13 April 2019. The ensemble forward and backward trajectories were initialized at 21:00 CDT indicated by the green vertical line.

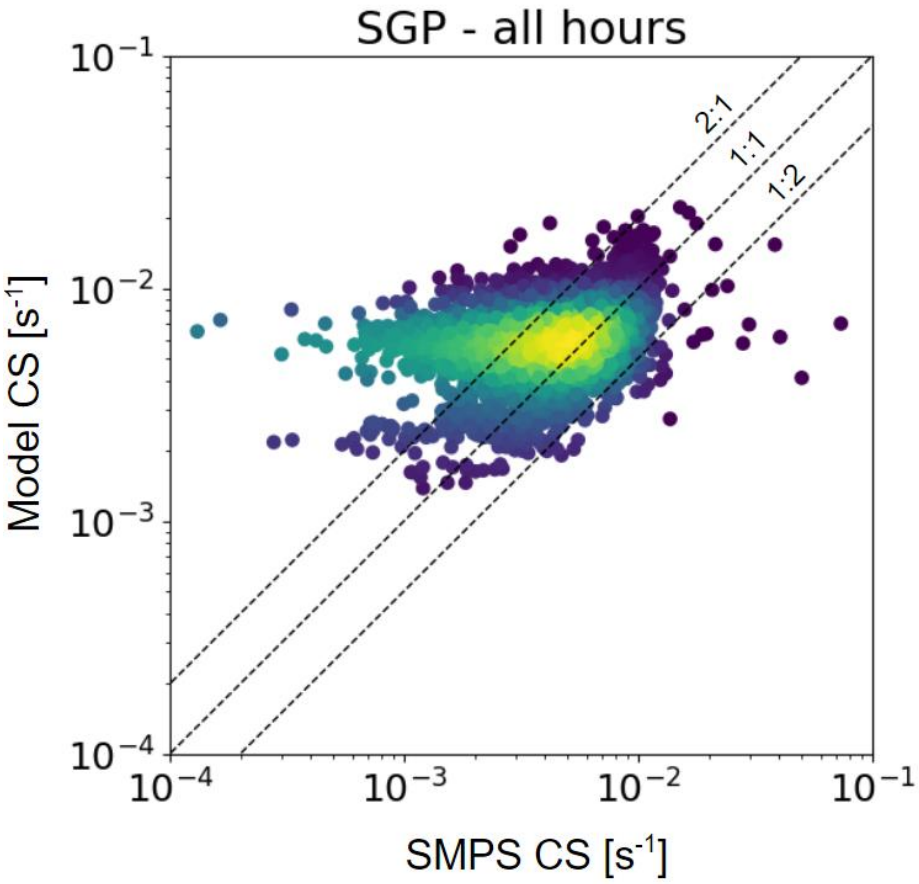

Figure A14. Condensation sink comparison between the SMPS data at the SGP site and the GC-TOMAS model in the SGP grid box.

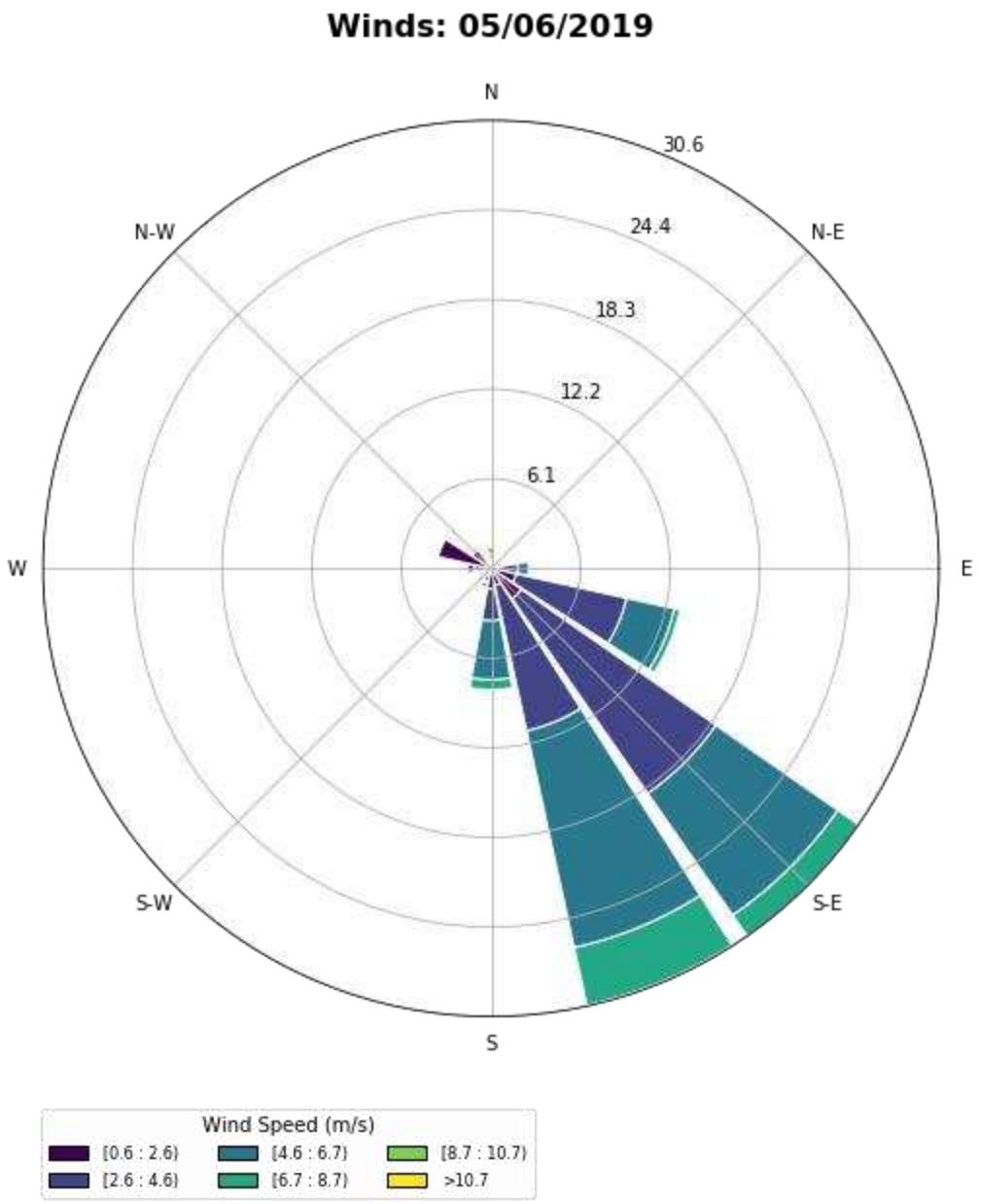

Figure A15. Daily average surface winds at the SGP site on 6 May 2019.

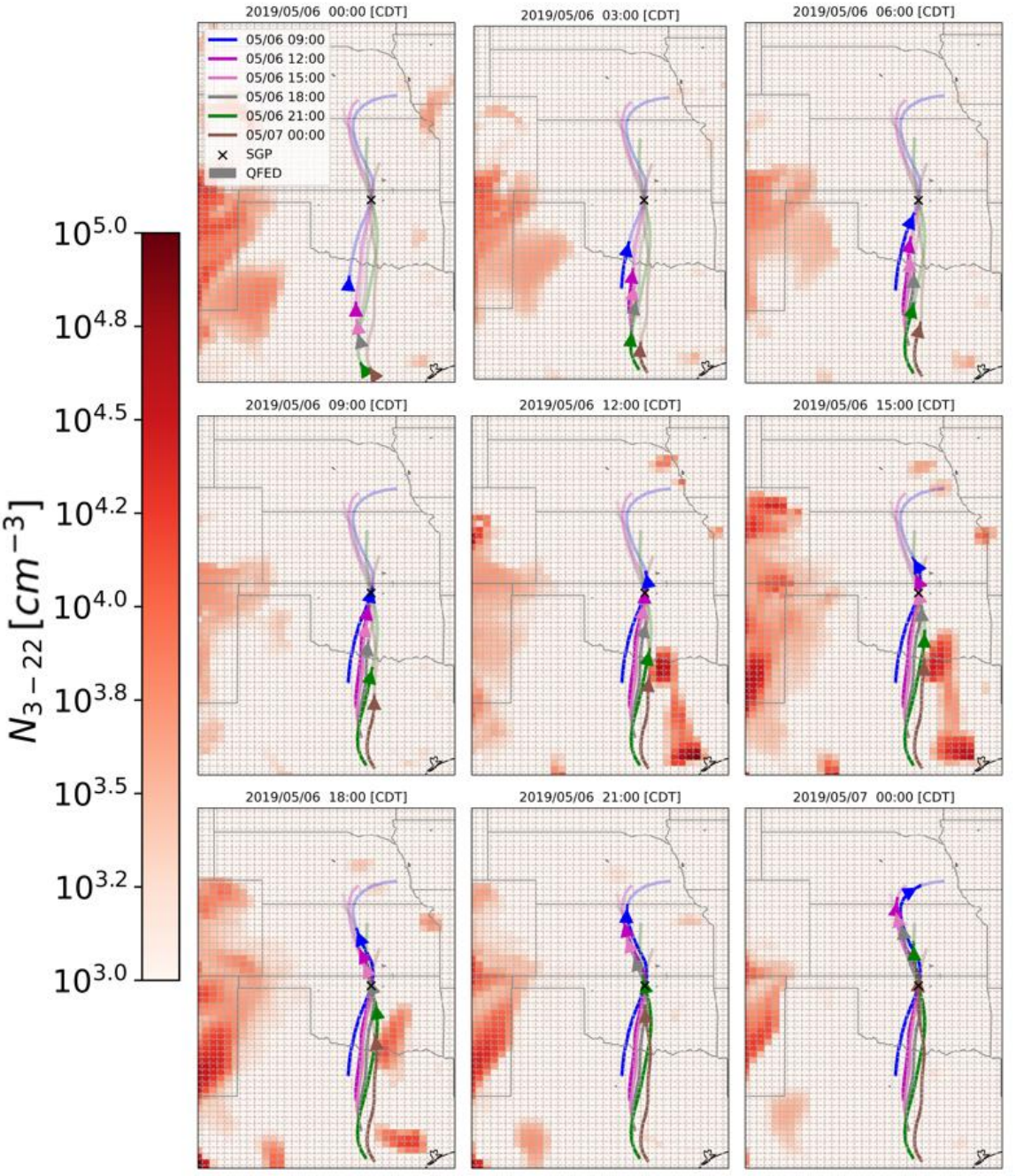

Figure A16. Maps of the 3-22 nm particle number concentration and HYSPLIT trajectories every 3 h on 6 May 2019.

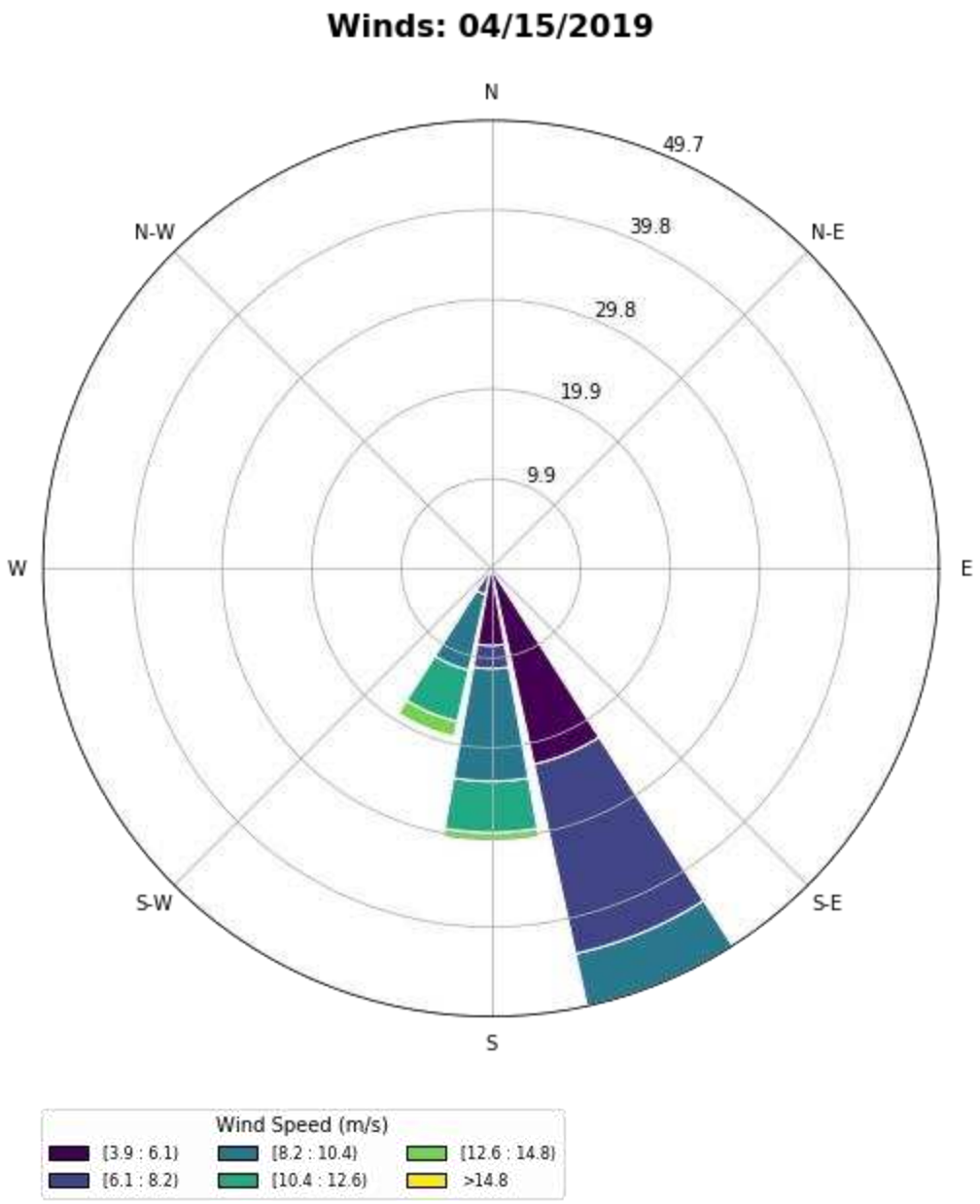

Figure A17. Daily average surface winds at the SGP site on 15 April 2019.

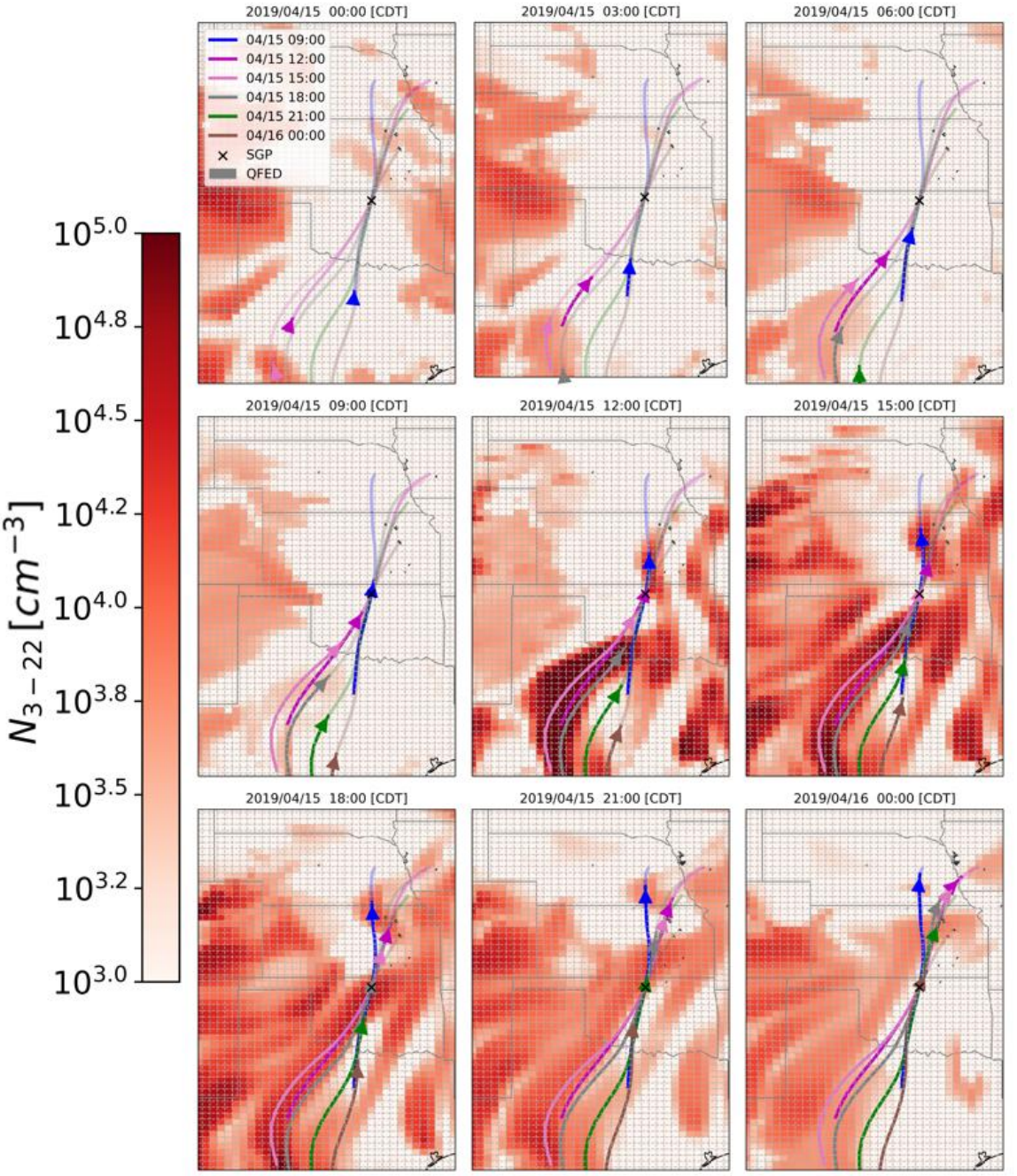

Figure A18. Maps of the 3-22 nm particle number concentration and HYSPLIT trajectories every 3 h on 15 April 2019.

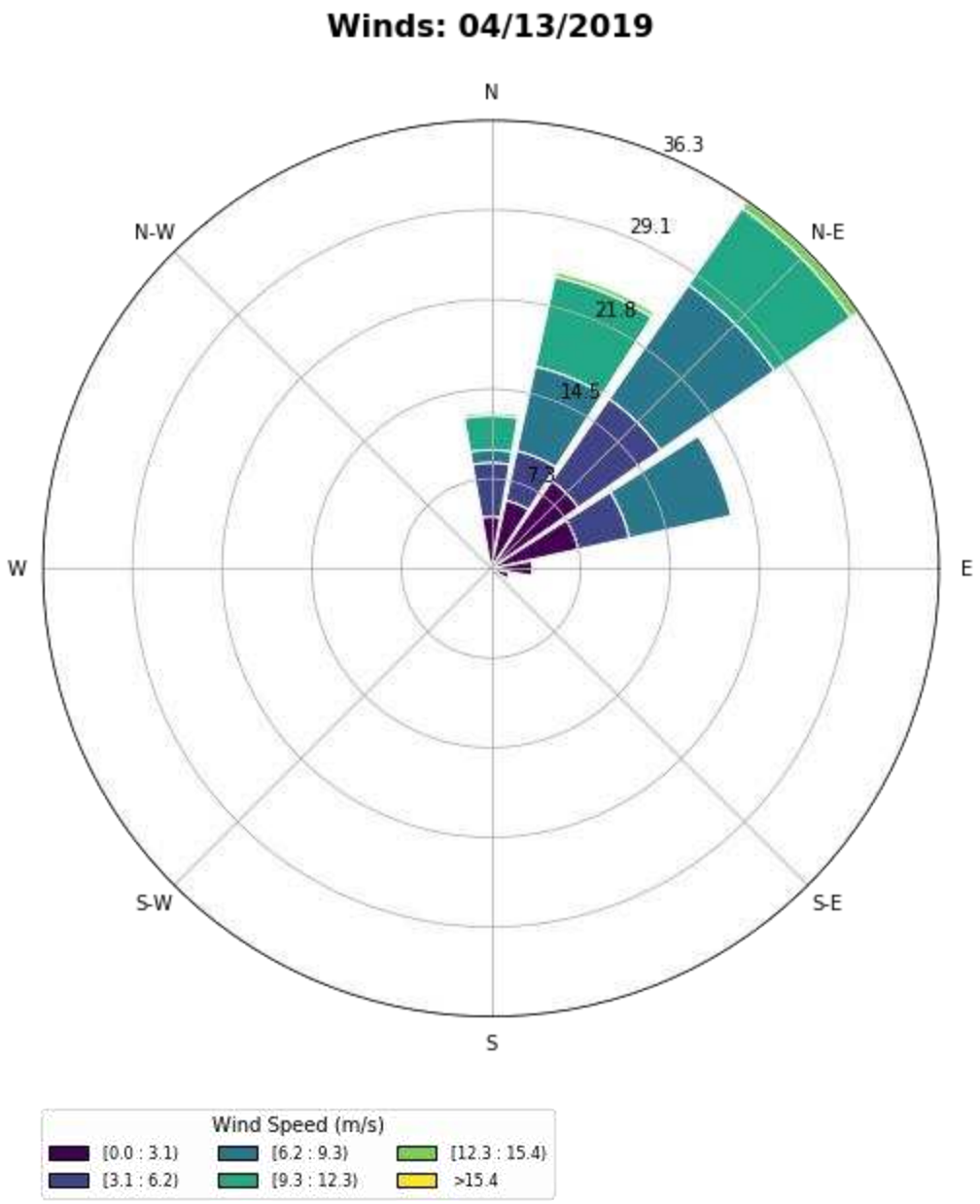

Figure A19. Daily average surface winds at the SGP site on 13 April 2019.

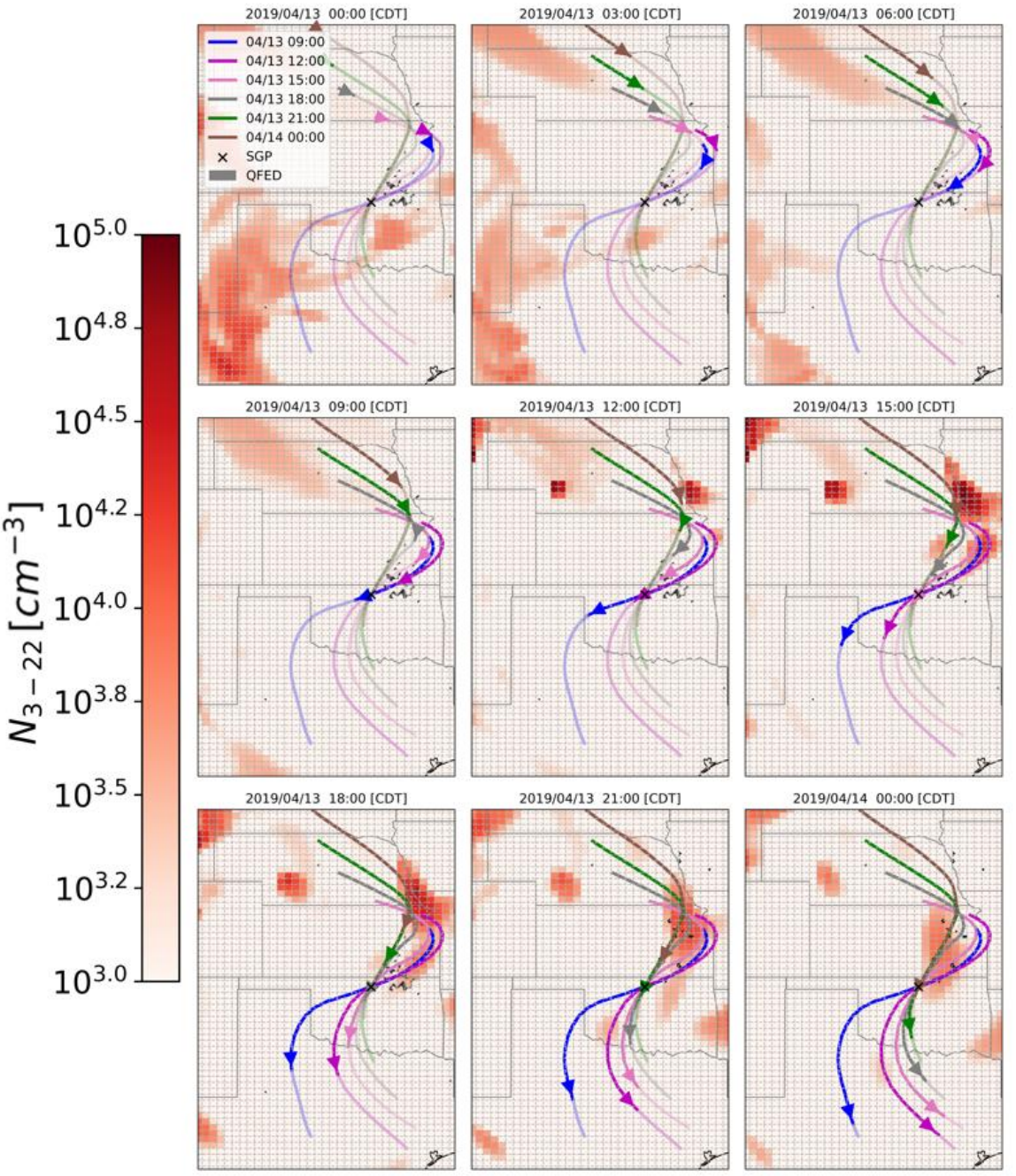

Figure A20. Maps of the 3-22 nm particle number concentration and HYSPLIT trajectories every 3 h on 13 April 2019.

APPENDIX B

SUPPLEMENT TO: PROBING THE POTENTIAL DRIVERS OF NEW PARTICLE FORMATION AND GROWTH DURING TRACER IN HOUSTON, TX

Supplemental Text:

Simple theory of gas-aerosol partitioning in CAGE chamber

The following equations are used to derive the gas/aerosol ratio in the CAGE chamber (see Figure B2).

$$\frac{dA}{dt} = \frac{G}{\tau_{CS}} - \frac{A}{\tau_{pwl}} - \frac{A}{\tau_{inst}} \approx 0 \quad (1)$$

Where G is the mass of low volatility gas in the chamber, A is the aerosol mass, τ_{inst} is the aerosol loss timescale from instruments, τ_{pwl} is the timescale for particle wall losses, and τ_{CS} is the timescale for condensation.

$$\frac{G}{A} = \tau_{CS}\left(\frac{1}{\tau_{pwl}} + \frac{1}{\tau_{inst}}\right) \quad (2)$$

OH Proxy

Stevens et al. 2012:

$$x = log([NO_x]) - 0.195 \quad (3)$$

$$y = \frac{dswrf}{S_0 \cdot T} \quad (4)$$

Where $[NO_x]$ is the mixing ratio of NO_x in ppb, *dswrf* is the downward shortwave radiation flux [W m^{-2}], S_0 is the solar constant at the top of the atmosphere (1370 W m^{-2}), T is the assumed transmittance of a clear atmosphere (0.76).

$$P1 = -0.014x^6 + 0.0027x^5 + 0.1713x^4 - 0.0466x^3 - 0.7893x^2 - 0.1739x + 6.9414 \quad (5)$$

$$P2 = (-1345y^3 + 4002y^2 - 471.8y + 42.72) \times 10^4 \quad (6)$$

Where P1 and P2 are polynomial fits based on NO_x and shortwave radiation. Finally, the OH concentration is calculated from the following:

$$[OH] = 0.82 \cdot 10^{P1 \times log(P2)/6.8} \quad [molec/cm^3] \quad (7)$$

Pietikäinen et al. 2014:

During the day, the OH concentration is calculated as follows:

$$[OH] = 3081.0 \cdot (SWF\downarrow)^{0.8397} \quad \text{[day time]} \tag{8}$$

Where $[OH]$ is in [molecules cm^{-3}] and SWF is the downward shortwave flux [W m^{-2}].

$$[OH] = 6.033 \times 10^{4} \quad \text{[night time]} \tag{9}$$

This work:

$$X = 3081.0 \cdot (SWF\downarrow)^{0.8397} \tag{10}$$

$$[OH] = X + 10 \cdot (X - 6.033 \times 10^{4}) \quad \text{[day time]} \tag{11}$$

$$[OH] = 2.67 \times 10^{5} \quad \text{[night time]} \tag{11}$$

X is the OH concentration directly from Pietikäinen et al., (2014), and Eqn. 11 scales the OH concentration up to be of a similar magnitude to the OH concentration from the Stevens et al., (2012) proxy. The goal was to have OH concentrations be of a similar magnitude to the Stevens et al., (2012), but with the functional response as the Pietikäinen et al., (2014) proxy.

Figures:

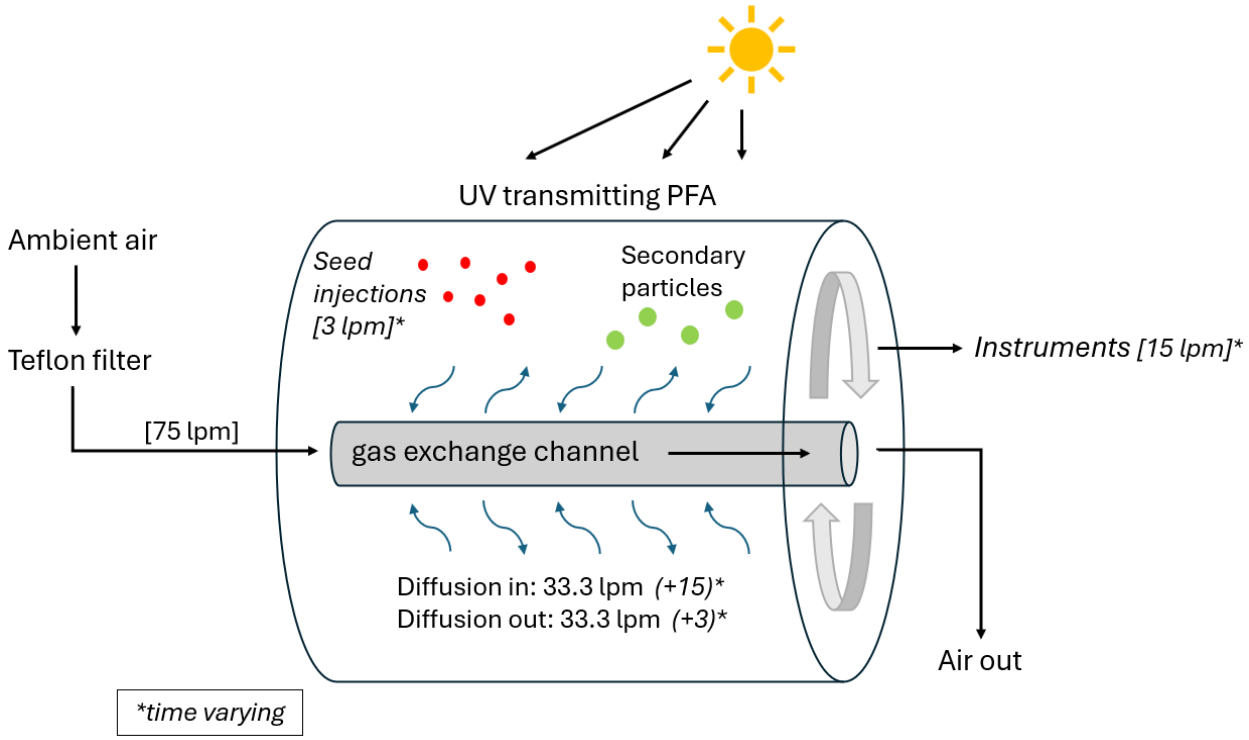

Figure B1. Schematic representation of the CAGE chamber. Processes that are not continuous in time are indicated with a * and italics.

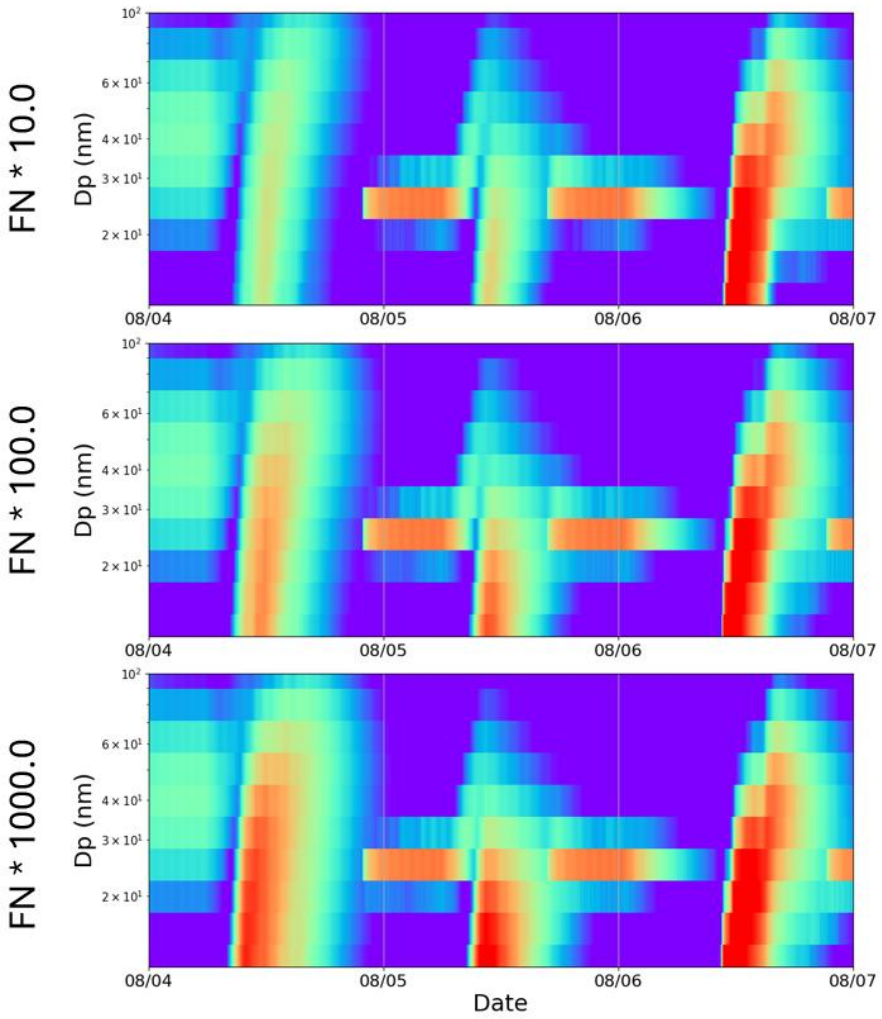

Figure B2. Modeled aerosol size distributions from tests scaling the total nucleation rate. The top panel shows the results from scaling nucleation by 10.0, the middle panel shows scaling nucleation by 100.0, and the bottom panel shows scaling nucleation by 1000.0.

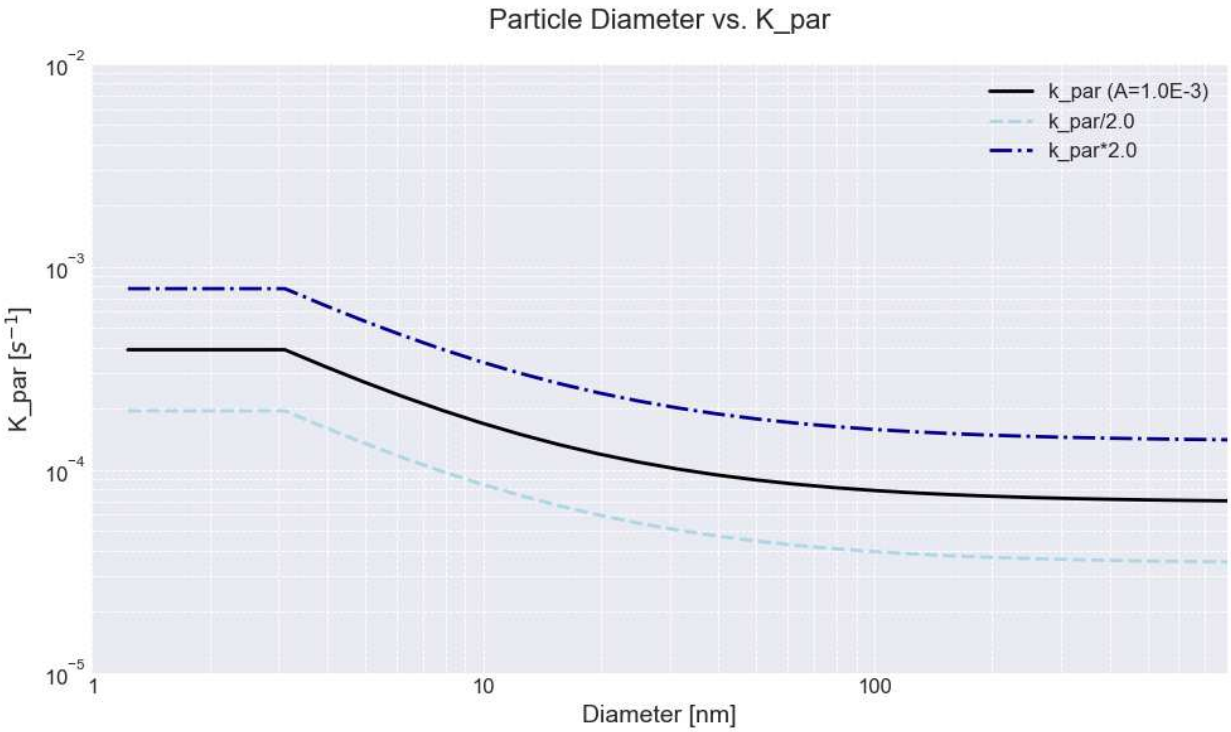

Figure B3. Size dependent particle wall loss rates derived for the CAGE chamber. The black line is the curve used in the base simulations, and the blue curves are sensitivity cases where wall loss rates are scaled up and down by 2.

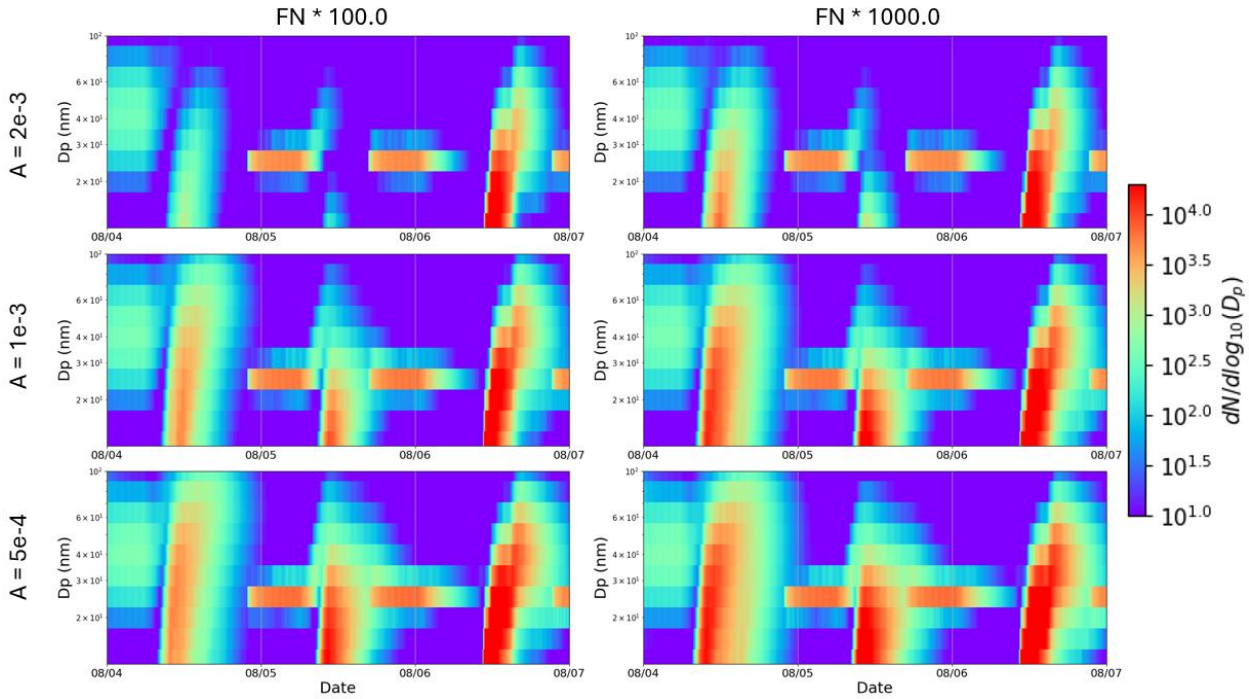

Figure B4. Modeled aerosol size distributions from sensitivity simulations where we perturbed the vapor and particle wall loss rates and the nucleation rate scalar.

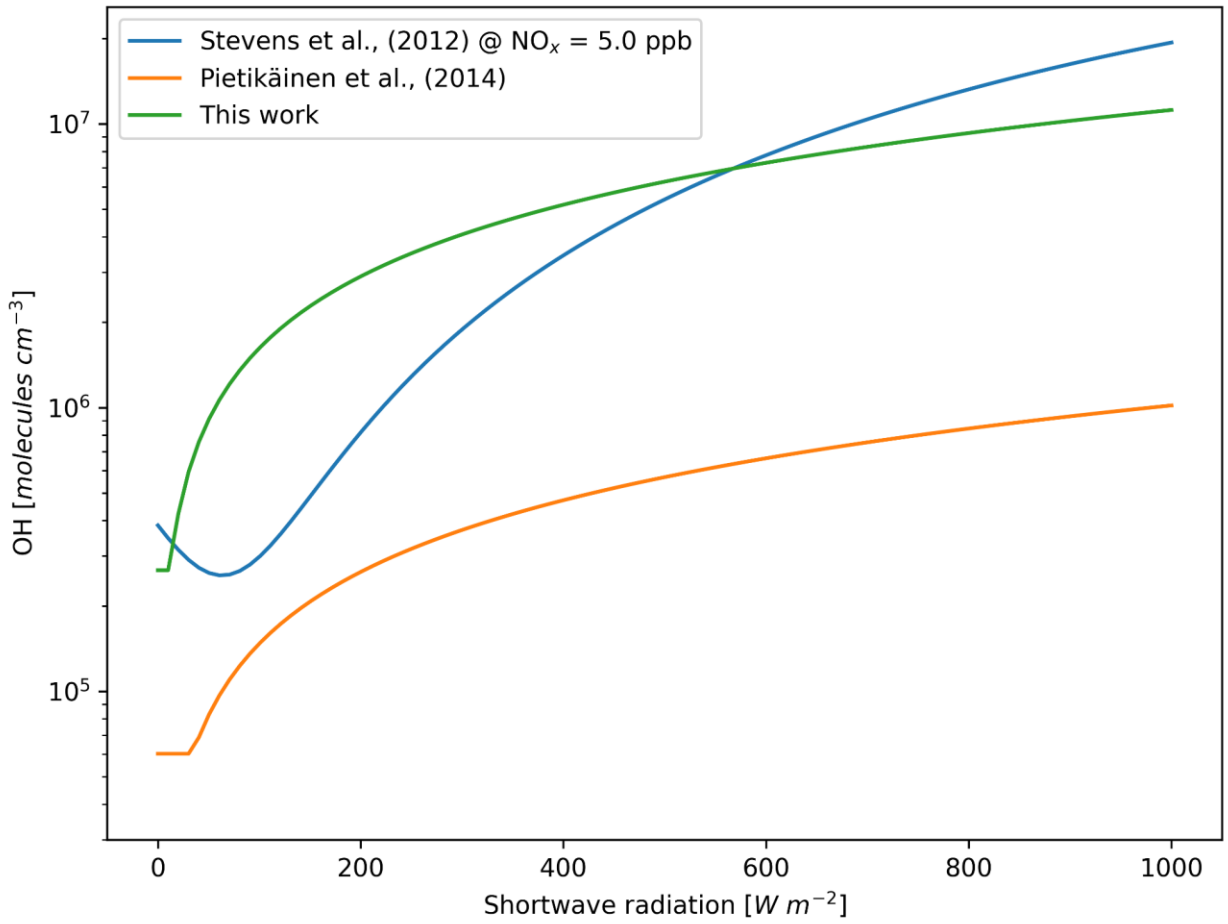

Figure B5. Comparison of shortwave radiation (x-axis) and hydroxyl radical concentrations (OH) (y-axis) from three proxy calculations. The blue line represents the OH concentration derived from the Stevens et al., (2012) proxy with NOx concentrations set to 5 [ppb]. The orange line represents the OH concentration derived from the Pietikainen et al., (2014) proxy. Finally, the green line represents the OH proxy used in this work.

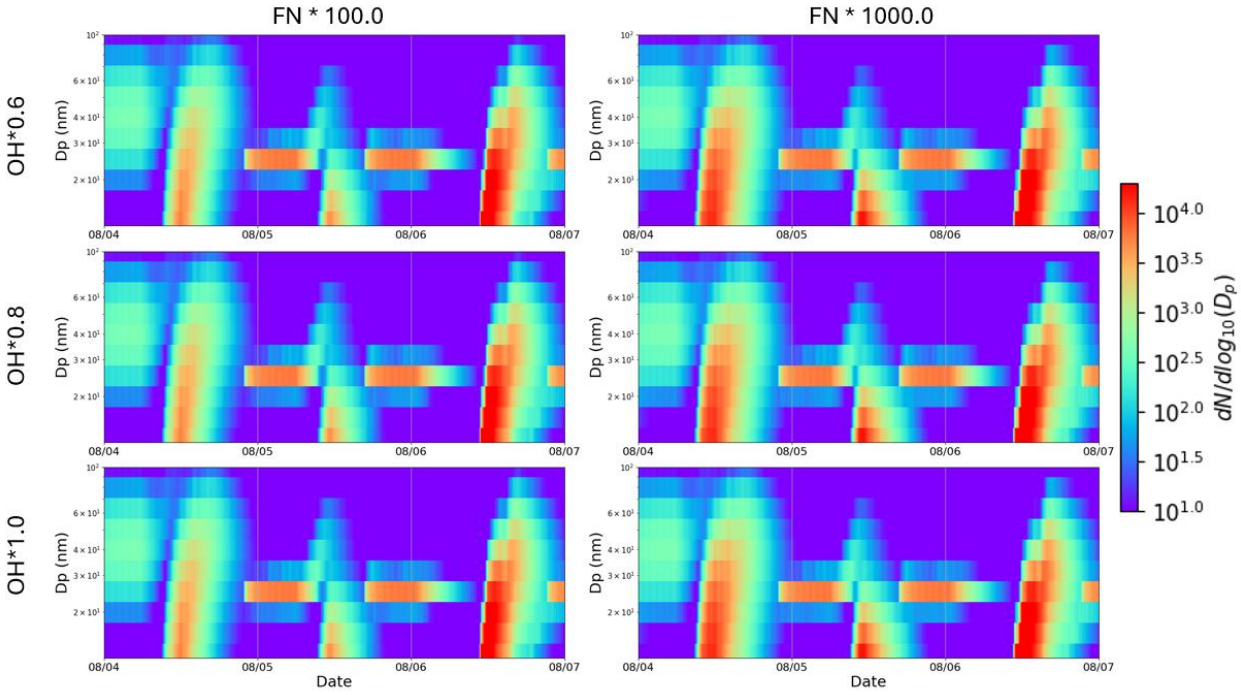

Figure B6. Modeled aerosol size distributions from sensitivity simulations perturbing the hydroxyl radical (OH) and nucleation rate scalar.

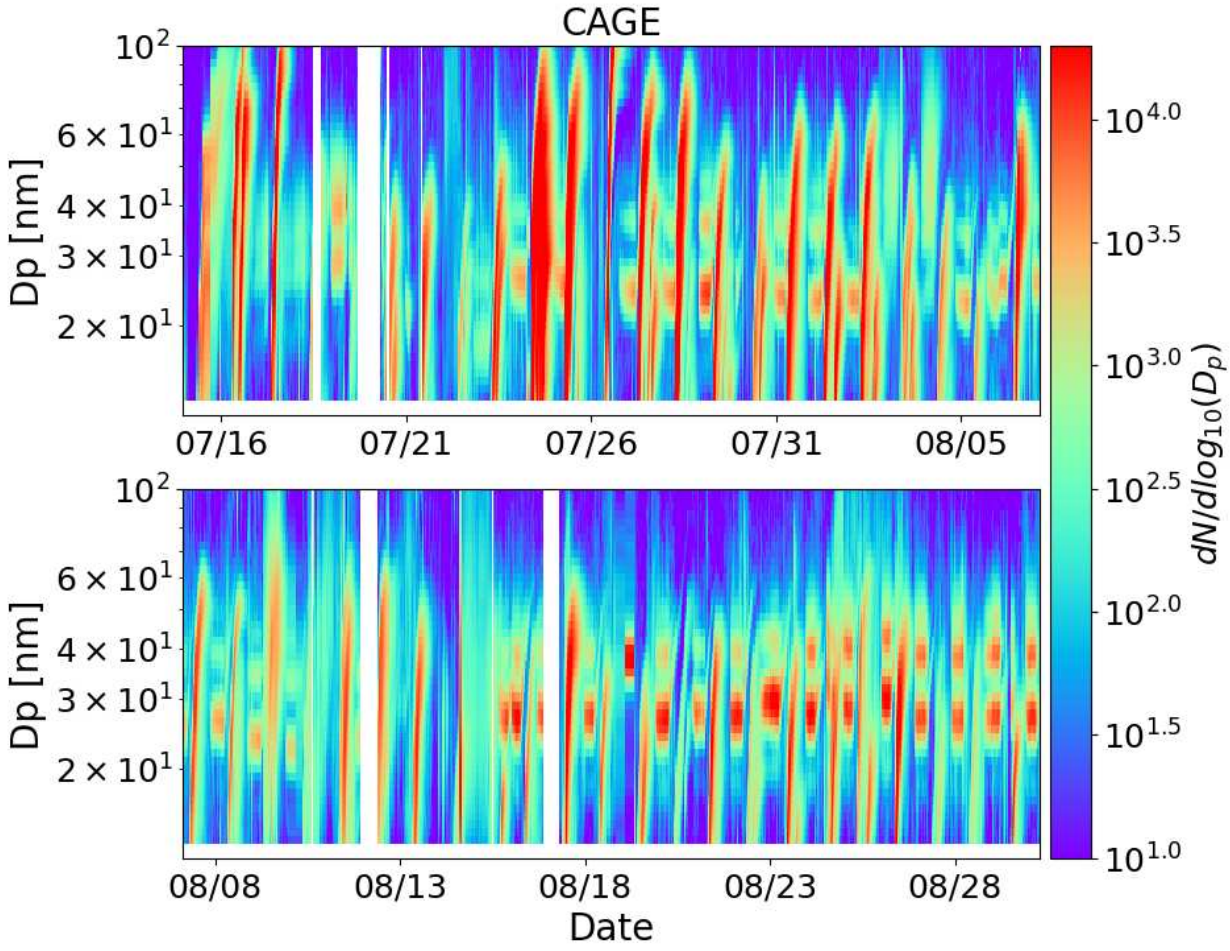

Figure B7. Aerosol size distribution measured in the CAGE chamber during the entire TRACER-UFI campaign.

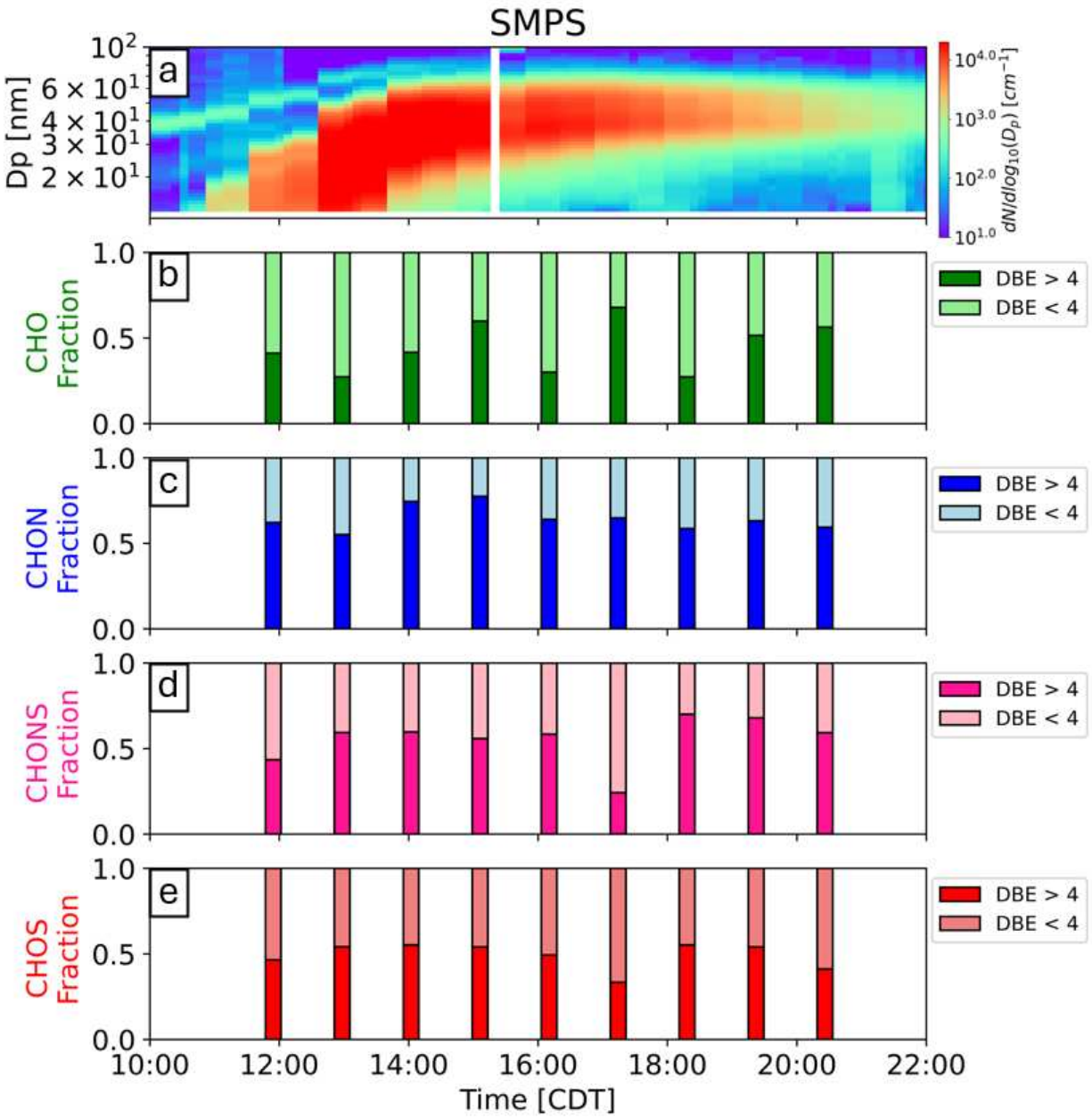

Figure B8. (a) Aerosol size distribution from the SMPS on August 6. (b) CHO, (c) CHON, (d) CHONS, and (e) CHOS classes separated by DBE greater than 4 (aromatic) and less than 4 (aliphatic).

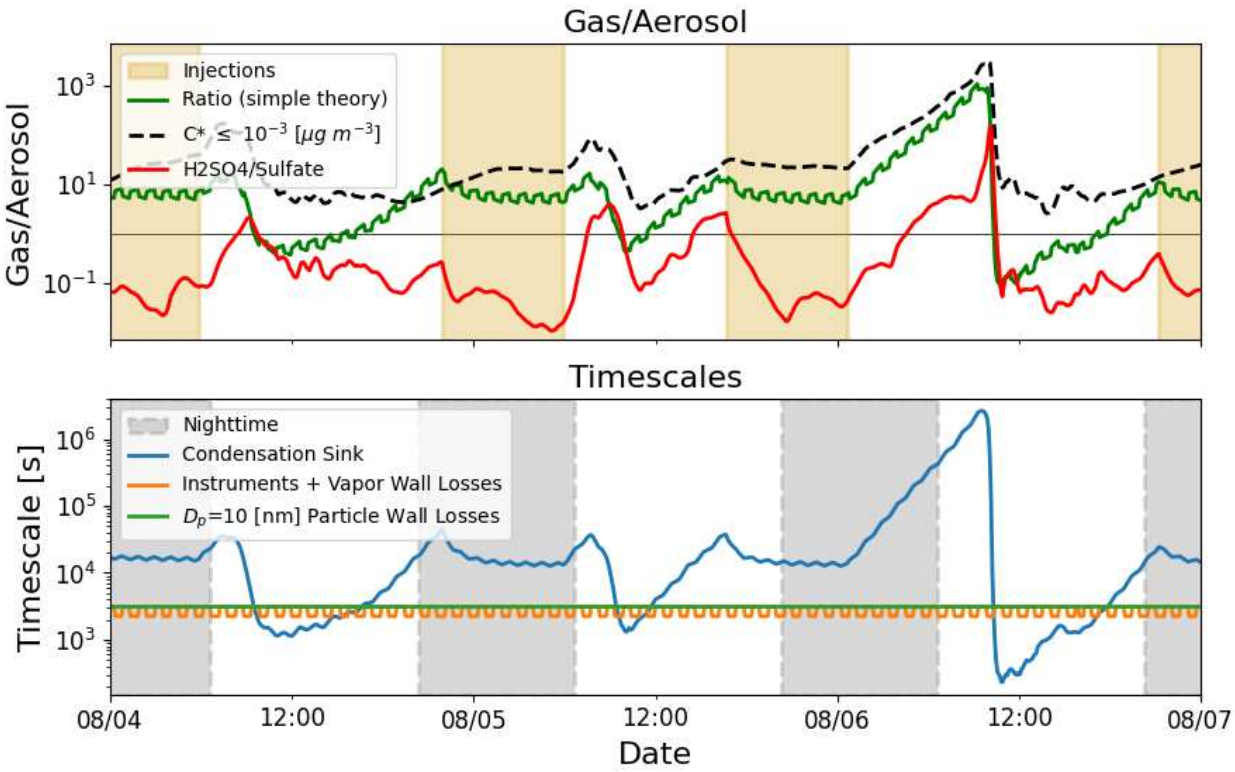

Figure B9. Time series of the ratio of mass in the gas-phase to mass in the condensed-phase. The black line indicates the ratio for organic species with a saturation vapor pressure below 10^{-3} [μg m^{-3}], the red line represents the gas/aerosol ratio of sulfuric acid and sulfate, and the green line represents the gas/aerosol ratio derived using Equation 2. The times of aerosol injections are shaded in light gray. (b) Time series of the different timescales affecting the gas/aerosol ratio.

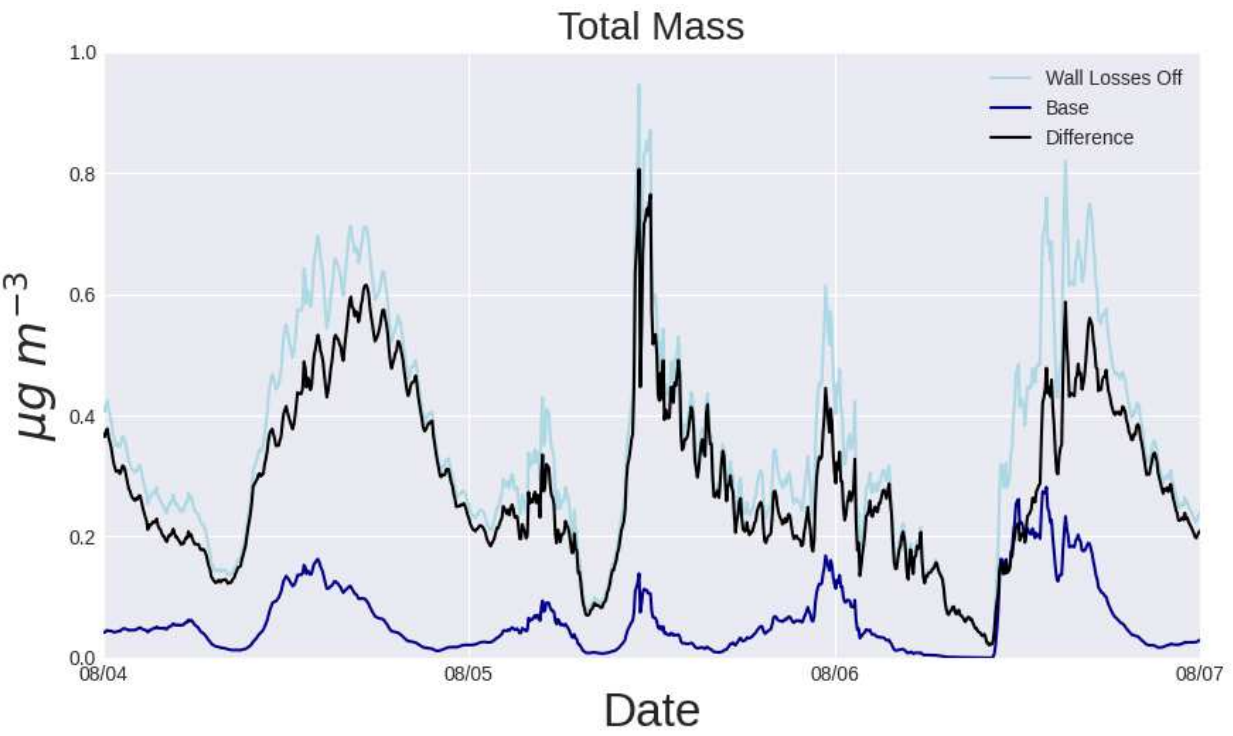

Figure B10. Time series of total aerosol mass (organic and inorganic) from the "base" simulation (dark blue line) and from the simulation with vapor and particle wall losses off (light blue line). The difference in total mass between the two simulations is indicated by the black line.

VOC class	ΔLVP	P_1	P_2	P_3	P_4	mFRAG	k_{OH}
benzene	1.582	0.075	0.004	0.899	0.022	0.845	1.22×10^{-12}
toluene	1.550	0.003	0.001	0.996	0.001	0.263	5.63×10^{-12}
xylenes	1.571	0.296	0.323	0.350	0.031	0.080	2.31×10^{-11}
isoprene	2.245	0.576	0.053	0.356	0.016	0.015	1.00×10^{-10}
α-pinene	1.503	0.454	0.251	0.247	0.048	0.236	5.23×10^{-11}

Table B1. We use the high NO_X parameters from Bilsback et al. (2023), accounting for various chamber artifacts (PWL+V2PWL+VWL in Bilsback et al., 2022). See section 3.2.2.2 in the main text for descriptions of each parameter.

APPENDIX C

SUPPLEMENT TO: EFFECTS OF AEROSOL PHASE-STATE ON NEW PARTICLE FORMATION AND GLOBAL AEROSOL CONCENTRATIONS

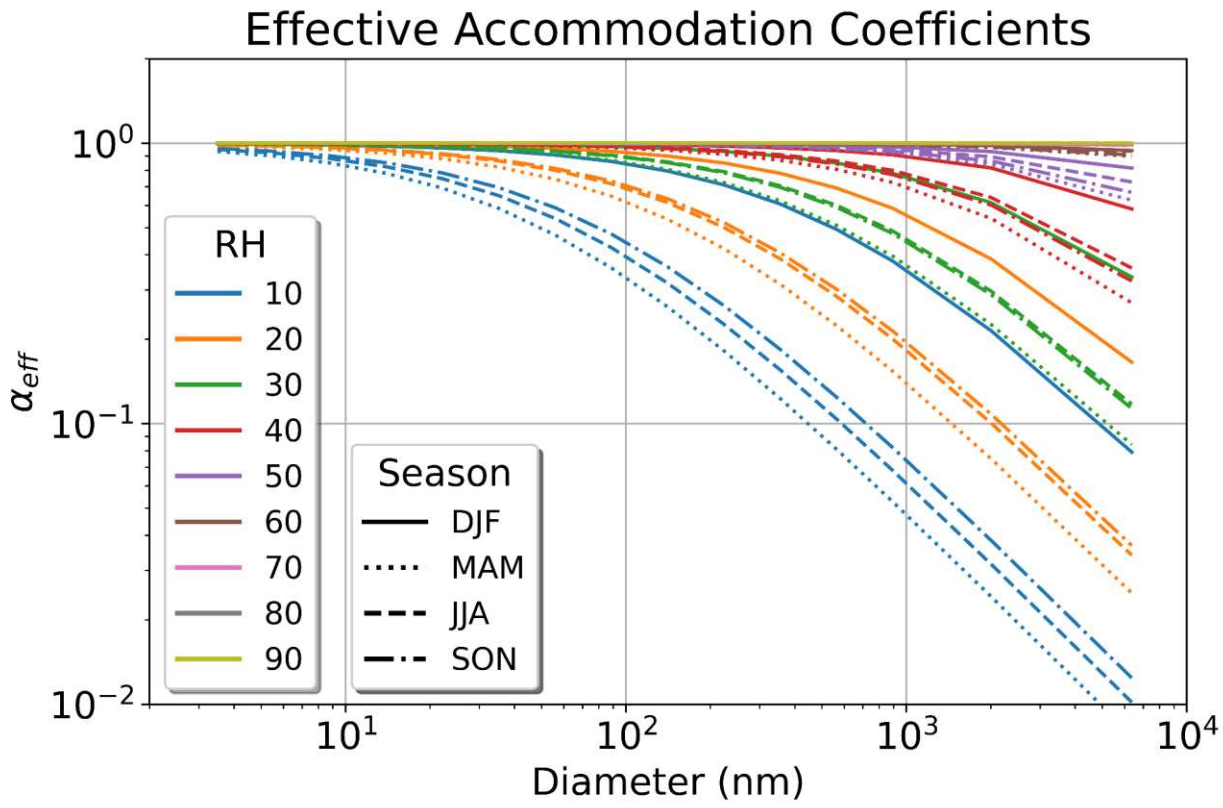

Figure C1. Effective accommodation coefficient (α_{eff}) versus particle diameter plotted at different relative humidity values (colors) for the four seasons (line styles), but calculated at 280.0 K instead of the seasonally averaged temperature.

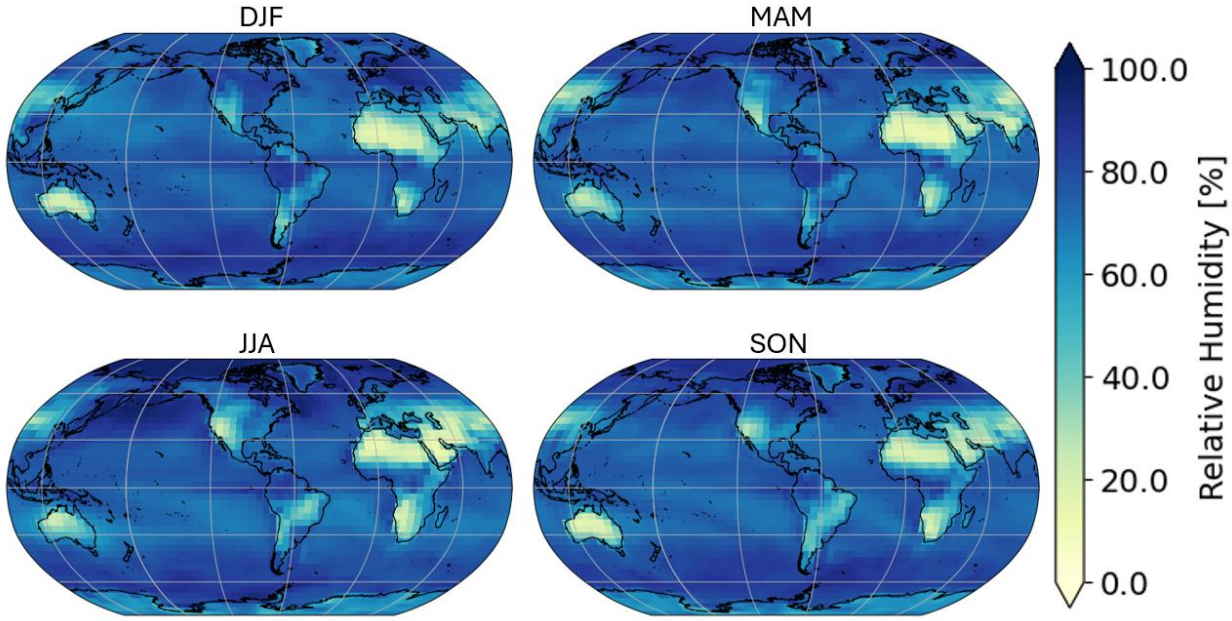

Figure C2. Mean seasonal relative humidity at the surface.

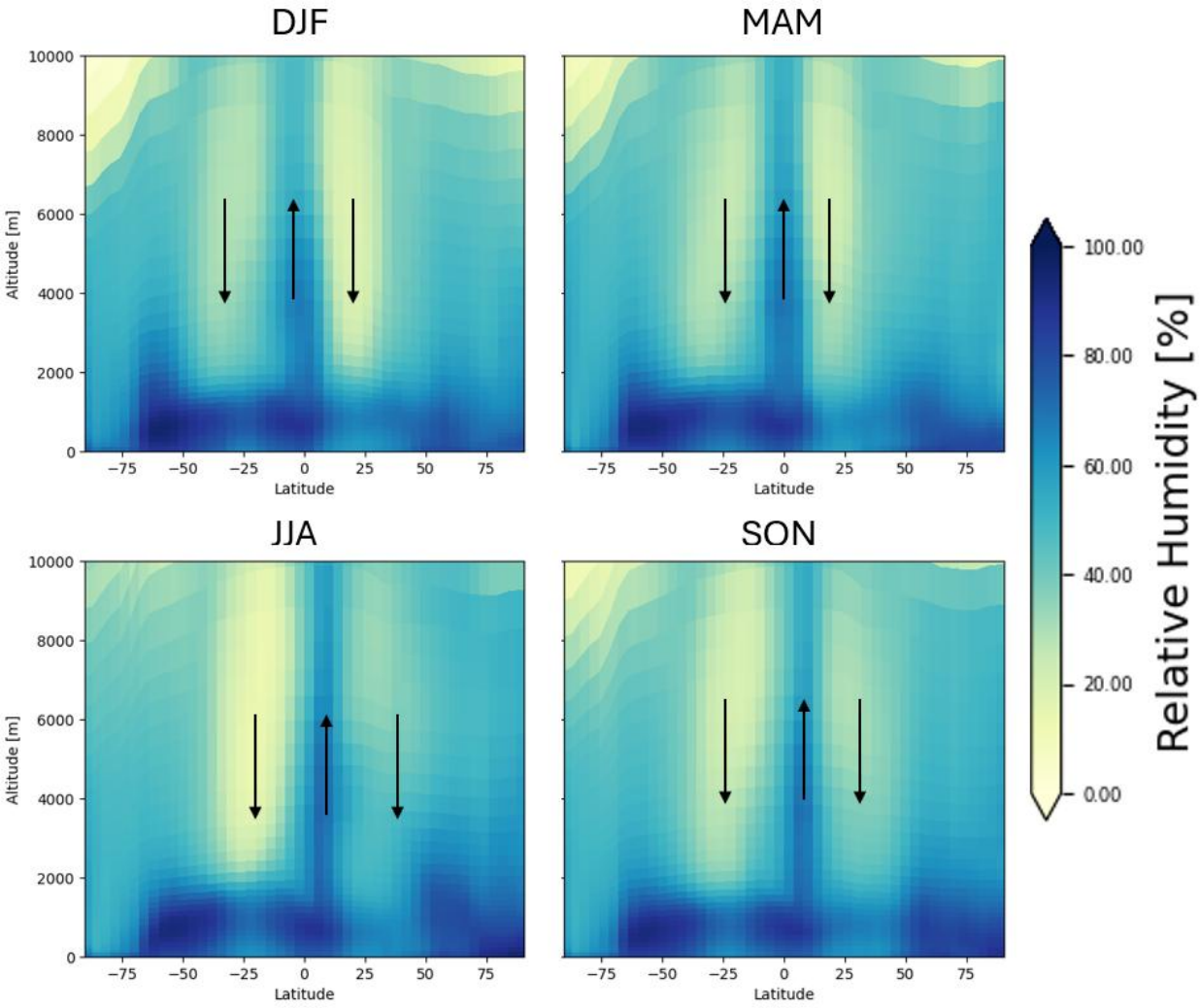

Figure C3. Zonal mean seasonal relative humidity.

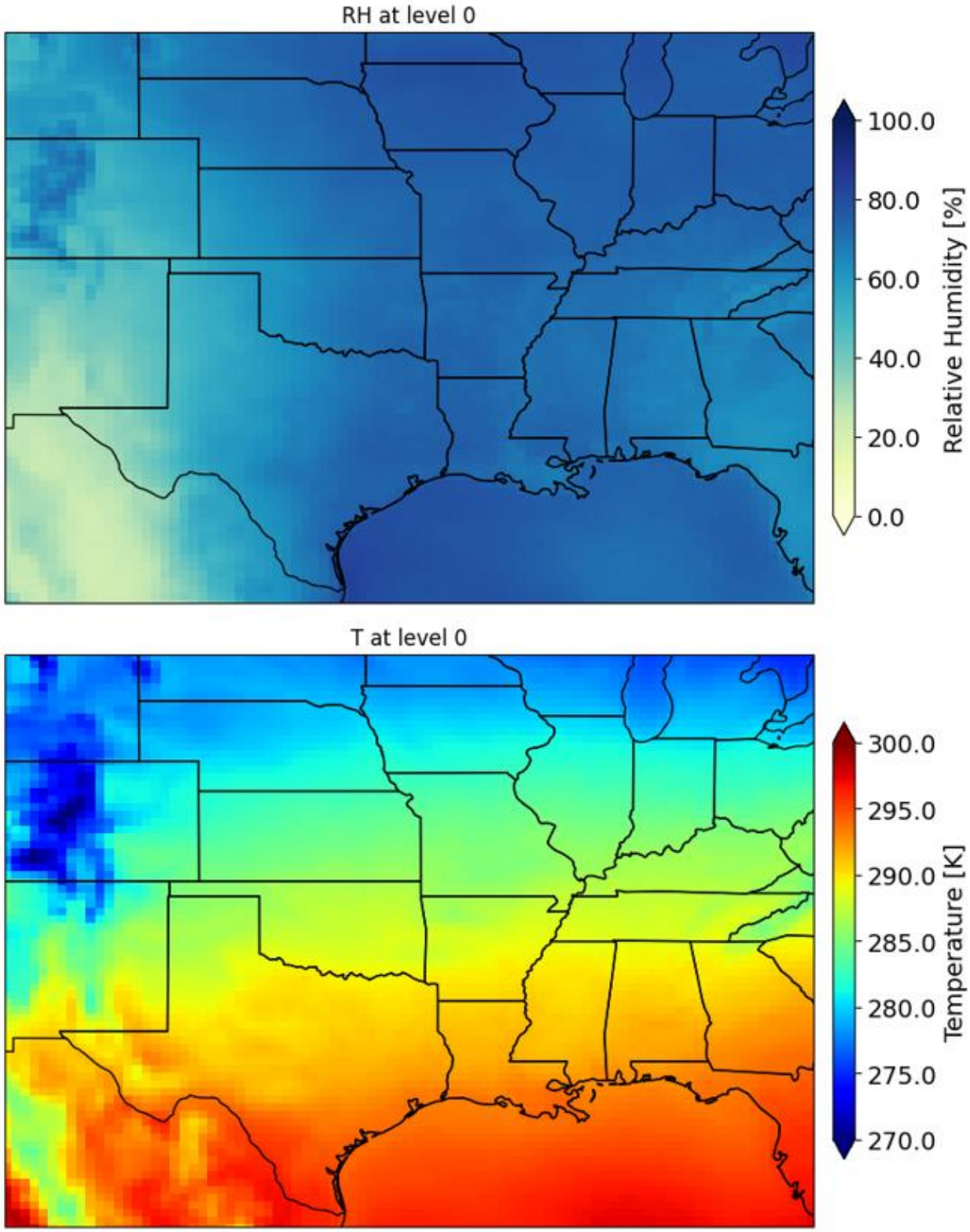

Figure C4. top panel: Mean surface relative humidity during MAM. bottom panel: Mean surface temperature during MAM.